Technische Universität München
TUM School of Natural Sciences

Characterization and Identification of Micro- and Nanoplastic by Raman Microspectroscopy, Scanning Electron Microscopy, Field-Flow Fractionation and Chemometrics

Christian W. Schwaferts

Vollständiger Abdruck der von der TUM School of Natural Sciences der Technischen Universität München zur Erlangung des akademischen Grades eines

Doktors der Naturwissenschaften (Dr. rer. nat.)

genehmigten Dissertation.

Vorsitzende: Priv.-Doz. Dr. Natalia P. Ivleva
Prüfer der Dissertation:

1. Prof. Dr. Martin Elsner
2. Prof. Dr. Michael Schuster
3. Prof. Dr. Thilo Hofmann

Die Dissertation wurde am 24.03.2022 bei der Technischen Universität München eingereicht und durch die TUM School of Natural Sciences am 10.08.2022 angenommen.

„Dem Anwenden muss das Erkennen vorausgehen.“

– Max Planck

Danksagungen

Ich möchte an dieser Stelle PD Dr. Natalia P. Ivleva und Prof. Dr. Martin Elsner für die Betreuung meiner Doktorarbeit danken und, dass ich stets mit guten Ratschlägen, inspirierenden Gesprächen und Lösungsansätzen unterstützt wurde. Ich bin insbesondere dankbar, dass ihr mir die Möglichkeit gegeben habt, dieses faszinierende Thema frei und auch eigenen Vorstellungen folgend zu bearbeiten und auf mehreren Konferenzen zu präsentieren. Ich habe in dieser Zeit sehr viel gelernt.

Ganz besonders danken will ich auch Dr. Elisabeth von der Esch und Dr. Philipp Anger, an deren Seite ich an der Mikroplastik-Thematik geforscht habe. Mit euch war es eine Freude, Erfolge zu feiern, und eine Erleichterung, stressige Phasen durchzustehen. Philipp, von dir habe ich die praktischen Aspekte in der Mikroplastik-Analytik gelernt und Eli, du hast mich stets dazu angespornt und motiviert das Beste aus dieser Arbeit herauszuholen.

Weiterhin möchte ich meinen Kollegen der Raman- und REM-Gruppe Oleksii Morgaienko, Irina Beer, Ruben Weiss und Oliver Jakob danken. Ihr habt unser Labor mit einer freundlichen und kollegialen Atmosphäre gefüllt und es war immer schön, mit euch zu Forschen oder auch mal eine Auszeit zu nehmen.

Ich möchte auch allen meinen Koautoren meinen Dank für die erfolgreiche Zusammenarbeit ausdrücken. Hierunter ganz besonders meinem Bruder Patrick Schwaferts, der mich auch über das Manuskript hinausgehend stets mit statistischer Expertise bereichert hat.

Den von mir betreuten Studierenden Monika Pointner, Lisa Beese, Maximilian Huber und Marcel Klotz gilt ebenso mein Dank. Ihr habt durch eure Lernbereitschaft und fleißige Mitarbeit mir die Praktika zur Freude gemacht und zur Dissertation und dem Forschungsprojekt wichtige Beiträge geleistet.

Großen Dank möchte ich auch allen Mitgliedern des Instituts für Wasserchemie und Chemische Balneologie ausdrücken. Insbesondere Prof. Dr. Reinhard Nießner, dessen große Erfahrung und Weitblick meine Arbeit bereichert hat. Zudem danke ich auch Julia Neumair, Julia Klüpfel, Lisa Göpfert, Katharina Sollweck, Dr. Karin Wieland, Eva Krois, Jessica Beyerl, Philipp Streich, Andreas Auerhammer, David Glöckler und Markus Weber, dank denen unsere „Kaffeedusche“ immer einen Besuch wert war. Weiterhin danke ich Christine Beese, Cornelia Popp, Sebastian Wiesemann, Roland Hoppe und insbesondere Christine Benning, von der ich außerordentlich viel über die Arbeit am Elektronenmikroskop gelernt habe.

Nicht zuletzt danke ich Vanessa Sogne und Dr. Florian Meier der Postnova Analytics GmbH für die großartige Zusammenarbeit, die fruchtbaren Diskussionen und die Unterstützung bei den experimentellen Arbeiten. Dadurch habt ihr zum Erfolg dieser Doktorarbeit beigetragen.

Abstract

Nanoplastic contamination is an emerging issue with the potential to negatively human health and the environment. For a reliable risk assessment, suitable analytical methods are necessary. However, established techniques from microplastic (MP) analysis face limitations, due to the small sizes and low masses of nanoparticles. On the other hand, current techniques for nanoparticle characterization do not allow for a chemical identification of the polymer, which is essential for a quantitative characterization. The presented thesis aims to solve this analytical challenge by developing new methods for Raman microspectroscopy (RM) in combination with scanning electron microscopy (SEM), field-flow fractionation (FFF), and chemometrics.

As an initial step, a critical review presents the state of the art in nanoplastic analysis, including a discussion of the methodological gap and the techniques that can potentially be adapted from nanoparticle analysis and MP analysis. This results in a roadmap laying out the requirements and possible techniques for each step of the nanoplastic analysis. It begins with the analytical question and sample treatment, discusses methods for particle separation, visualization, and physical characterization, and addresses the chemical identification of nanoplastic.

In a second step, the lower size limit of RM, combined with SEM, for the analysis of MP and nanoplastic was evaluated and demonstrated to be applicable down to the theoretical diffraction limit at around 0.25 µm. This was experimentally tested for spherical and irregular, fragmented particles, as they are expected in the environment. Following this qualitative assessment of lower particle size limits for MP/sub-MP analysis, quantification of particle number and size distribution on the Raman filter was approached. Here, a key challenge is to enable a statistically sound determination of the MP number and the MP/non-MP ratio, respectively. This was solved by delineating a particle-by-particle measurement algorithm based on window sampling, for which the bias and standard deviation of random and systematic window placement was investigated using simulated filters. Results show that random window sampling prevents the introduction of bias. It is, however, accompanied by an increased standard deviation. Furthermore, increasing the size of the windows also increases the bias or standard deviation for systematic and random windows, respectively. To obtain a confidence interval (CI) even though the total particle number is unknown, a bootstrap method is used. This approach enables an *on-the-fly* measurement algorithm where first, a smaller increment of particles/windows is measured and analyzed. Subsequently, the CI of the data up to this point is estimated by bootstrap, and it is assessed whether the error margin and error probability are below an acceptance criterion, in which case the measurement can be stopped, else it is continued with the next increment of particles. This *on-the-fly* procedure will enable that an optimal end-point is found such that no measurement time is wasted.

In a third step, RM was online-coupled to FFF by developing an optical tweezer-based flow-cell in order to facilitate automated nanoplastic analysis, which does not rely on image analysis, but instead on particle separation followed by chemical characterization. The setup was validated for particles in the size range from 200 nm to 10 µm, concentrations in the order of 1 mg/L (10^9 particles L^{-1}), and different

material (polymers and inorganic). Using two variants of FFF (asymmetric flow field-flow fractionation & centrifugal field-flow fractionation), it was shown that the online-coupling can be implemented for multiple particle separation techniques. Thus, the optimal technique can be selected based on their respective advantages and disadvantages. In addition to the chemical identification by the novel RM flow-cell, physical characterization of the particles was performed by a UV and multi angle light scattering (MALS) detector, providing the particle size distribution. Thus, the foundation for a multi-detector system has been laid, which will enable a comprehensive nanoplastic analysis, as well as the application to a broader set of particulate samples.

Zusammenfassung

Die neuartige Problemstellung der Nanoplastik-Belastung ist von Bedeutung, weil Nanoplastik im Verdacht steht, Gesundheit und Umwelt negativ zu beeinflussen. Um eine belastbare Risikobewertung zu ermöglichen, sind belastbare analytische Methoden zur chemischen Identifizierung und Quantifizierung notwendig. Allerdings sind die etablierten Techniken der Mikroplastik (MP)-Analytik in Bezug auf kleine Partikelgrößen und -massen limitiert. Ebenso sind vorhandene Techniken für die Nanopartikelcharakterisierung nicht in der Lage, eine chemische Identifizierung zu gewährleisten, welche für eine korrekte Quantifizierung essentiell ist. Die vorliegende Arbeit hat zum Ziel, diese analytische Herausforderung durch die Entwicklung neuer Methoden für die Raman-Mikrospektroskopie (RM) in Kombination mit Rasterelektronenmikroskopie (REM), Feldflussfraktionierung (FFF) und Chemometrie zu lösen.

Zu Beginn wurde ein kritischer Übersichtsartikel publiziert, der zum einen den Stand der Technik der Nanoplastikanalytik darstellt und weiterhin eine Diskussion beinhaltet, die methodologische Lücken und Techniken, die aus bestehender Nanopartikel- und MP-Analytik adaptiert werden können, adressiert. Dieser Artikel entwirft somit einen Fahrplan, der die Problemstellungen und möglichen Techniken für jeden einzelnen Schritt in der Nanoplastik-Analytik thematisiert. Dies beginnt bei der analytischen Fragestellung und Probenaufbereitung, geht über Methoden zur Partikeltrennung, Bildgebung und physikalischen Charakterisierung, und umfasst schließlich die chemische Identifizierung der Partikel.

Anschließend wurde die untere Größenbegrenzung der RM, ergänzt durch REM, für die Analytik von Mikro- und Nanoplastik untersucht und seine Anwendbarkeit bis hinab zum theoretischen Diffraktionslimit bei ca. 0.25 µm experimentell demonstriert. Dies wurde für sphärische und irreguläre, fragmentierte Partikel, wie sie in der Umwelt zu erwarten sind, getestet. Nach dieser qualitativen Untersuchung zu unteren Grenzen einer mikrospektroskopischen Größenidentifizierung und chemischen Charakterisierung wurde die Quantifizierung von Partikeln auf den Ramanfiltern thematisiert. Ein Hauptproblem ist hier die Gewährleistung einer statistisch belastbaren Bestimmung von MP-Anzahl und dem Verhältnis von MP zu nicht-MP. Dies wurde gelöst, indem ein Messalgorithmus für individuelle Partikel basierend auf Window Sampling formuliert wurde. Anhand von simulierten Ramanfiltern wurde der Fehler (Bias) und die Standardabweichung für den Fall untersucht, dass Fensterpositionen, innerhalb derer Partikel ausgezählt und charakterisiert werden, zufällig oder systematisch gewählt werden. Es zeigte sich, dass zufällige Fenster einen Bias verhindern, allerdings bringen diese eine erhöhte Standardabweichung mit sich. Zudem wurde gezeigt, dass wenige große Fenster, im Gegensatz zu vielen kleinen, diesen Bias bzw. erhöhte Standardabweichung verstärken. Da die notwendige Gesamtpartikelanzahl nicht bekannt ist, um ein Konfidenzintervall (CI) zu berechnen, wurde eine Bootstrapmethode implementiert. In diesem *on-the-fly* Messalgorithmus wird zunächst ein kleines Inkrement der Partikel/Fenster gemessen und ausgewertet. Mit diesen Daten wird durch Bootstrap das entsprechende CI geschätzt und daraus abgeleitet, ob es unterhalb eines bestimmten Akzeptanzkriteriums liegt. Ist dies der Fall, wird die Messung beendet, andernfalls wird ein weiteres Inkrement charakterisiert, bis die Gesamtheit der ausgezählten Partikel die gewünschte statistische Sicherheit ermöglicht. Somit ermöglicht dieser *on-the-fly*-Algorithmus die Bestimmung eines optimalen Endpunktes, so dass keine Messzeit verschwendet wird.

In einem letzten Projekt wurde eine Nanoplastik Analyse verfolgt, die Partikelzahl und -größenverteilung nicht aufgrund von Bild-basierter RM charakterisiert, sondern basierend auf Partikelgrößentrennung und daran anschließender chemischer Identifizierung. Hierzu wurde RM online an die FFF gekoppelt, indem eine Flusszelle auf Basis des Optical Tweezer-Effekts entwickelt wurde. Dieses Setup wurde für Partikelgrößen von 200 nm bis 10 µm, Partikelgehalte in der Größenordnung von 1 mg/L (10^9 Partikel L^{-1}) und verschiedene Materialien (polymerisch und anorganisch) validiert. Anhand von zwei Varianten der FFF (Asymmetrischer-Fluss-Feldflussfraktionierung & Zentrifugale Feldflussfraktionierung) wurde gezeigt, dass diese Onlinekopplung für verschiedene Partikeltrenntechniken eingesetzt werden kann, wobei die Wahl der jeweiligen Methode gemäß ihrer jeweiligen Vor- und Nachteile getroffen werden kann. Durch den Einsatz eines UV- und multi angle light scattering (MALS)-Detektors kann eine physikalische Charakterisierung der Partikel hinsichtlich ihrer Größenverteilung erreicht werden. Zusammen mit der neuen RM-Flusszelle wurde nun der Grundstein für ein Multidetektorsystem gelegt, das eine umfassende Nanoplastikanalytik, sowie die Anwendung für eine Bandbreite anderer partikulärer Proben ermöglichen kann.

List of Publications

Publications Included in this Thesis

- **Christian Schwaferts**, Reinhard Niessner, Martin Elsner, Natalia P. Ivleva, „Methods for the Analysis of Submicrometer- and Nanoplastic Particles in the Environment“, *Trends in Analytical Chemistry* **2019**, 112, 52–65, DOI: 10.1016/j.trac.2018.12.014
- **Christian Schwaferts**, Vanessa Sogne, Roland Welz, Florian Meier, Thorsten Klein, Reinhard Niessner, Martin Elsner, Natalia P. Ivleva, „Nanoplastic Analysis by Online Coupling of Raman Microscopy and Field-Flow Fractionation Enabled by Optical Tweezers“, *Analytical Chemisty* **2020**, 92, 5813–5820, DOI: 10.1021/acs.analchem.9b05336
- **Christian Schwaferts**, Patrick Schwaferts, Elisabeth von der Esch, Martin Elsner, Natalia P. Ivleva, „Which particles to select, and if yes, how many? Subsampling methods for Raman microspectroscopic analysis of very small microplastic“, *Analytical and Bioanalytical Chemistry* **2021**, 413, 3625–3641, DOI: 10.1007/s00216-021-03326-3

Further Publications

- **Christian Schwaferts**, Martin Elsner and Natalia P. Ivleva, „Analytische Methoden für die Detektion und Quantifizierung von Mikroplastik in diversen Matrices“, *131. VDLUFA Kongressband* **2019**, VDLUFA Schriftenreihe Band 76/2019, VDLUFA Verlag, Darmstadt, ISBN: 978-3-941273-26-9
- Elisabeth von der Esch, Maria Lanzinger, Alexander J. Kohles, **Christian Schwaferts**, Jana Weisser, Thomas Hofmann, Karl Glas, Martin Elsner and Natalia P. Ivleva, „Simple Generation of Suspensible Secondary Microplastic Reference Particles via Ultrasound Treatment“ *Frontiers in Chemistry* **2020**, 8, 169, DOI: 10.3389/fchem.2020.00169
- Sarah Brunschweiger, Emile Tabu Ojong, Jana Weisser, **Christian Schwaferts**, Martin Elsner, Natalia P. Ivleva, Roland Haseneder, Thomas Hofmann, Karl Glas, „The effect of clogging on the long-term stability of different carbon fiber brushes in microbial fuel cells for brewery wastewater treatment“, *Bioresource Technology Reports* **2020**, 11, 100420, DOI: 10.1016/j.biteb.2020.100420
- Hannes K. Imhof , Mohammed Al-Azzawi, Astrid Bartonitz, Sebastian Beggel, Joerg E. Drewes, Martin Elsner, Elisabeth von der Esch, Karl Glas, Natalia P. Ivleva, Simone Kefer, Oliver Knoop, Horst-Christian Langowski, Oliver Miesbauer, Julia Reichel, **Christian Schwaferts**, Jana Weisser, Juergen P. Geist, „Der Eintrag von Mikroplastik in Lebensmittel und die Aquatischen Umwelt und seine Folgen – aktuelle Fragen und Antworten.“, *Mitteilungen der Fachgruppe Umweltchemie und Ökotoxikologie* **2020**, 2, 26. Jahrgang, ISSN: 1618-3258

- Oliver Knoop, **Christian Schwaferts**, Mohammed M.S.M. Al-Azzawi, Marco Kunaschk, Matin Funck, Jochen Türk, Florian Meier, Martin Elsner, Natalia P. Ivleva, Jörg E. Drewes, „Analytik von Mikro- und Submikro-Plastikpartikeln aus Wasserproben: Status Quo und Ausblick“ *KW Korrespondenz Wasserwirtschaft* **2021**, 3, 14. Jahrgang, 138–146, DOI: 10.3243/kwe2021.03.001

Oral Presentations

- **Christian Schwaferts**, Reinhard Niessner, Martin Elsner, Natalia P. Ivleva, „Raman-Mikrospektroskopie von Submikrometer-Plastikpartikeln“, *Umwelt* **2018**, Münster, 09.–12.09.2018

- **Christian Schwaferts**, Vanessa Sogne, Roland Drexel, Florian Meier, Thorsten Klein, Reinhard Niessner, Martin Elsner, Natalia P. Ivleva, „Kopplung von Asymmetrischer Fluss Feldflussfraktionierung und Raman-Mikrospektroskopie für die Analyse von Submikrometer-Plastik“, *ANAKON* **2019**, Münster, 25.–28.03-2019

- **Christian Schwaferts**, Martin Elsner, Natalia P. Ivleva, „Analytische Methoden für die Detektion und Quantifizierung von Mikroplastik in diversen Matrices“, *131. VDLUFA Kongress* **2019**, Gießen, 10.–12.09.2019

- **Christian Schwaferts**, Vanessa Sogne, Roland Drexel, Florian Meier, Thorsten Klein, Reinhard Niessner, Martin Elsner, Natalia P. Ivleva, „Online coupling of Raman microscopy and field-flow fractionation enabled by optical tweezers for nanoplastic analysis“, *20th International Symposium on Field- and Flow-Based Separations, FFF2020* **2020**, Vienna, Austria, 23.–27.02.2020

- **Christian Schwaferts**, Vanessa Sogne, Roland Drexel, Florian Meier, Thorsten Klein, Reinhard Niessner, Martin Elsner, Natalia P. Ivleva, „Nanoplastik-Charakterisierung mittels einer Online-Kopplung von Raman-Mikrospektroskopie und Feldflussfraktionierung“, *Wasser* **2021**, Online, 10.–12.05.2021

Poster Presentations

- **Christian Schwaferts**, Reinhard Niessner, Martin Elsner, Natalia P. Ivleva, „Detection and identification of submicrometer plastic particles using Raman-microspectroscopy and scanning electron microscopy“, *Analytica Conference* **2018**, Munich, 10.–13.04.2018

- **Christian Schwaferts**, Reinhard Niessner, Martin Elsner, Natalia P. Ivleva, „Detektion und Identifizierung von Subµ-Plastikpartikeln mit Raman-Mikrospektroskopie“, *Wasser* **2018**, Papenburg, 07.–09.05.2018

- **Christian Schwaferts**, Reinhard Niessner, Martin Elsner, Natalia P. Ivleva, „Detection and Identification of Submicrometer Plastic Particles using Raman-Microspectroscopy and Scanning Electron Microscopy“, *ANAKON* **2019**, Münster, 25.–28.03-2019
- **Christian Schwaferts**, Reinhard Niessner, Martin Elsner, Natalia P. Ivleva, „Detektion und Identifizierung von Subµ-Plastikpartikeln mit Raman-Mikrospektroskopie“, *Wasser* **2019**, Erfurt, 27.–29.05.2019
- **Christian Schwaferts**, Vanessa Sogne, Roland Welz, Florian Meier, Thorsten Klein, Reinhard Niessner, Martin Elsner, Natalia P. Ivleva, „Nanoplastic analysis by Raman microscopy on-line coupled to field-flow fractionation via optical tweezers“, *SETAC* **2020**, Dublin, 04.–07.05.2020.
- **Christian Schwaferts**, Patrick Schwaferts, Elisabeth von der Esch, Martin Elsner, Natalia P. Ivleva, „How many particles to identify with Raman microspectroscopy? Subsampling methods for very small microplastic particles“, *Wasser* **2021**, Online, 10.–12.05.2021

Declaration of Contribution

Methods for the Analysis of Submicrometer- and Nanoplastic Particles in the Environment

Christian Schwaferts, Reinhard Niessner, Martin Elsner and Natalia P. Ivleva,

Trends in Analytical Chemistry **2019**, 112, 52–65, DOI: 10.1016/j.trac.2018.12.014

This article reviews the state of the art of environmental nanoplastic analysis and discusses methodological approaches and techniques that can be adapted from adjacent fields, specifically microplastic and engineered nanoparticles, as well as instrumental analytical chemistry. C.S. performed the literature search on these fields. The methods were grouped according to different steps/tasks in the full analytical process. These were sample preparation (including chemical treatment, preconcentration, and separation techniques), light scattering techniques for particle sizing, imaging/visualization, and chemical identification (spectroscopy, gas-chromatography-mass-spectrometry). All of those were integrated in a roadmap for the analytical process. C.S. performed the structuring of the manuscript. The discussed methods were compiled in comprehensive tables and complemented with figures illustrating the application ranges. C.S. created these tables and figures. The review contains a critical discussion, which defines the methodological gap, highlights current challenges, and gives prospects for future solutions. C.S. wrote the manuscript and implemented the peer-reviewer's comments. M.E., R.N., and N.I. supervised and reviewed the work.

Which particles to select, and if yes, how many? Subsampling methods for Raman microspectroscopic analysis of very small microplastic

Christian Schwaferts, Patrick Schwaferts, Elisabeth von der Esch, Martin Elsner and Natalia P. Ivleva,

Analytical and Bioanalytical Chemistry **2021**, 413, 3625–3641, DOI: 10.1007/s00216-021-03326-3

In this work, subsampling schemes for MP particles on filters by RM analysis were investigated. Based on the challenge that, for decreasing particle size, the optimal random sampling is no longer available because the total particle number will be unknown, window sampling is assessed via simulated filters. C.S. planned the simulations and performed initial runs, P.S. implemented the R-code. Filters exhibiting two types of spatial structure were generated: a uniform distribution and a structure, where the particles tend towards the center. Those were analyzed with two types of window patterns: random windows and systematic windows, which cover the filter (almost) comprehensively. It was shown that systematic windows have the risk of generating a biased result, whereas random windows are bias-free but have an increased standard deviation. It was further shown that having few large windows instead of many small windows (with equal total area) results in an increase of the bias in systematic windows and an increase in the standard deviation of random windows, respectively. C.S. performed the analysis of the data together with P.S.. The goal of subsampling on the Raman filter is to obtain a number of particles that have to be analyzed such that the result satisfies certain precision requirements (error margin, error probability). To assess the precision of the result, a confidence interval (CI) needs to be available. In random sampling, the CI can be calculated based on an urn model without replacement. For window sampling, however, it is unavailable. Hence, a bootstrap method was used to estimate the CI for such a RM measurement. The bootstrap CIs were assessed by comparing their error margin to those of the simulated filters (which were known, as they could be analyzed multiple times). Here, it was seen that the bootstrap CIs gave a conservative estimation of the error standard deviations and also that bootstrap on systematic windows lost the advantage over random windows of reduced standard deviation. Ergo, random windows can clearly be recommended, especially since the bias of systematic windows could be detrimental to the bootstrap algorithm. C.S. performed the analysis of the data together with P.S.. Finally, an *on-the-fly* RM measurement protocol is proposed based on window sampling and a bootstrap estimation. Here, increments of particles analyzed by RM and the results are instantly used to estimate the bootstrap CI, which then informs the decision to either stop or continue the measurement. With that, an optimal measurement time can be achieved. C.S. projected the algorithm and wrote the manuscript. P.S. contributed the theoretical statistical formalization of random sampling, window sampling and bootstrap. E.E. contributed to the conception of the study and reviewed the manuscript. M.E. and N.I. supervised and reviewed the work.

Nanoplastic Analysis by Online Coupling of Raman Microscopy and Field-Flow Fractionation Enabled by Optical Tweezers

Christian Schwaferts, Vanessa Sogne, Roland Welz, Florian Meier, Thorsten Klein, Reinhard Niessner, Martin Elsner and Natalia P. Ivleva,

Analytical Chemisty **2020**, 92, 5813–5820, DOI: 10.1021/acs.analchem.9b05336

This study describes the development and characterization of the online-coupling of Raman microspectroscopy (RM) to field-flow fractionation (FFF) via an optical trapping-based flow-cell. R.W. constructed the prototype of the flow-cell and C.S. performed the experiments to elucidate and characterize the working principle of the flow-cell. It was concluded that on the cell bottom, a 2D optical trap is formed, which retains particles to ensure sufficient interaction with the Raman laser to generate a strong signal. This laser-optical focussing solves the issues with low sensitivity of typical Raman flow-cells. Subsequently, C.S. and V.S. performed a thorough validation of the on-line coupling, demonstrating the application range for particles of different materials, sizes in the range from 200 nm – 5 µm, and concentrations of $\sim$ 1 mg/L (10^9 particles L^{-1}). Further, a periodic particle release was implemented, to ensure that the separation information is preserved, and the hyphenation of RM to two types of FFF (Asymmetric-flow FFF and Centrifugal FFF) was demonstrated. To this end, an initial test on monodisperse particles was performed, which was followed by the separation of different mixtures. C.S. performed the data analysis and created the figures. In the results, it is shown that the separated particles can be attributed to their chemical composition in a time-resolved manner. It is even possible to detect particles that can not be separated well. These spectroscopic data are combined with the physical characterization of the commercially available detectors, which enables particle detection and sizing. This results in a comprehensive multidetector analysis of nanoplastic particles. C.S. concieved of the study and wrote the manuscript. F.M., T.K., R.N., M.E and N.I. supervised the study and reviewed the work.

Contents

Chapter 1

Introduction

1.1 What is Microplastic?

1.1.1 Definitions

Microplastic (MP) are particles from synthetic polymers that are classified according to their size[1–4]. MP is defined as plastic particles in the size range of 1 µm – 1 mm, whereas particles between 1 mm and 5 mm are called large MP, to incorporate the historical size definition, which initially extended into the millimeter range[5]. Particles below 1 µm are called nanoplastic and sometimes an additional distinction between subµ-plastic (100 nm – 1 µm) and nanoplastic (< 100 nm) is made[2,4]. Moreover, MP is commonly differentiated according to its origin. Particles that are produced for a specific application with these dimensions (e.g. abrasives in cosmetics) are termed *primary* MP, whereas particles resulting from the fragmentation of large plastic debris in the environment, due to various stressors, are called *secondary* MP[1,2].

These two criteria are most common in MP studies. However, this analyte is vastly more complex, which is not reflected in this reduced definition. Moving towards harmonization and comparability of data, it is important that the relevant characteristics of MP are clearly understood and documented. To this end, the following categories have been suggested: chemical composition, physical state, solubility in water, size, shape, color and origin[4]. Other authors have proposed an even more general approach by eliminating the categorical nature of the common data reporting, where sizes, shapes and polymer types are presented in distinct categories. It should rather be reported as a fitted function for the size distribution, the ratios of the *xyz* dimensions of the MP and the density, replacing the polymer type[6].

1.1.2 The Omnipresent Contaminant

Synthetic polymers are an essential part of our lives. They offer the generation of wealth and a high standard of living for a broad population. This is reflected in the huge production capacity of polymers, which lies in the megaton range[7]. It is, however, also the case that a substantial part of these plastics end up in the environment – a problem that is also in the megaton range[8]. The marine environment is the

first point of observation for this contamination, which now appears globally, due to the interconnected nature of our production and waste treatment pathways[8,9] as well as the food chain[10,11].

Plastic reaches the aquatic environments via waste water treatment plants (WWTP)[9] and rivers[8], where it is exposed to diverse stressors, ranging from ultraviolet (UV) light to mechanical forces, that effect the fragmentation to MP[12] and nanoplastic[13–15]. The main entry path into terrestrial systems[16] is via sewage sludge from WWTPs[17], mulch foils[18], and tire wear[19,20]. Some studies also document airborne MP[21].

The harmfulness[22] of MP is hypothesized to be based on its particulate nature itself and also on the various additives, which are blended into the material. Furthermore, MP can function as a vector for pollutants and pathogenic microorganisms and viruses[1,2]. However, studies that quantify the effects of MP produce partly contradicting results, ranging from none to severe effects[23–25]. This emphasizes the need for improved and harmonized analytical techniques that provide the data for reliable studies enabling regulatory agencies to tackle this issue.

1.1.3 Analytical Tools for Microplastic

1.1.3.1 The Analytical Question

Every analytical measurement starts with a question: What is the quantity of interest? Only if this question is clearly defined, a sensible and suitable analytical method can be applied. This is especially true for a diverse analyte such as MP with its multitude of properties and characteristics (see Section 1.1.1), of which only a subset will constitute the required parameters for each individual study. These considerations must start with the investigated system, such as surface waters, sediments, organisms, or food samples, and sampling must take into account the required characteristics of the MP, which are relevant in the study (e.g. environmental fragments, fibers, or tire wear). In terms of chemical identification, the general decision between total mass of MP in a sample vs. a detailed particle size distribution needs to be made. Here, the trade-off is that measurements of the mass content are comparatively quick, whereas microspectroscopic techniques provide a large degree (such as particle sizes or distribution) of information at the cost of longer measurement times[3].

1.1.3.2 Sampling and Sample Treatment

The sampling procedure depends on the investigated system. Water samples from aquatic environments are typically sampled volume-reduced (i.e. the particulate matter is taken from the water sample on-site, typically by filtration or nets)[5], whereas sediments are sampled in bulk[3]. Proper planning is very important and includes aspects of sampling points and sample size, which effect the reliability and representativeness of the study[26]. Furthermore, contamination control is of utmost importance, since plastic is a ubiquitous material in every laboratory. It is not only present in material and equipment, but also in clothing and gloves. Thus, using a laminar flow box is virtually obligatory[3,27].

Most samples will exhibit a relatively low concentration of MP and contain a large amount of inhibiting matrix, thus, a sample treatment is necessary. Matrix can be composed of organic and inorganic matter, which, in most cases, will have to be removed before any subsequent analysis can be performed. In Raman microspectroscopy (RM), the natural fluorescence of organic matter (e.g. from carotenoids or chlorophyll) is orders of magnitude larger than the Raman signal[2], emphasizing the need for its removal. Only in few, rare cases (e.g. drinking or tap water) can the sample be directly processed for chemical identification, e.g. by filtration onto a filter for Fourier-transform infrared (FT-IR) microspectroscopy or RM.

The removal of organic matrix can be performed by a variety of protocols. The list comprises acid (HNO_3, 65 %), alkaline (NaOH, KOH, dilute, e.g. 1 M or concentrated, e.g. 10 M), oxidative (H_2O_2 (30 %), Fenton's reagent (Fe(II) + H_2O_2), O_3), or enzymatic treatments[28–30]. Further, some laboratories employ sodium dodecyl sulfate and ultrasonic treatment[31], the latter of which should be avoided, though, since MP is shown to break down to smaller fragments under the influence of ultrasound[32,33].

Aggressive chemicals can cause morphological changes of the MP particles[34]. For instance, alkaline treatments affect polymers that are prone to hydrolysis, such as polyamide[28]. Other studies report a leaching of fluorescence markers by acids, bases, or H_2O_2[35]. For nanoplastic, most of the common treatments showed to cause agglomeration[35]. Enzymatic treatments offer a less harsh alternative, which can avoid many of the abovementioned sample alterations. The disadvantage of the enzymatic treatment, however, is its long processing time of about 2 weeks[30]. It has to be noted that among different studies, different efficacies and prevalences for the treatment protocols are reported. Thus, it is advisable for new studies to perform a preliminary validation of the treatment on the stability of the particles, taking into account the plastic types, sample characteristics, and sizes in question.

To remove inorganic matrix, as present in e.g. sediment samples, a common technique is density separation[2], for which the Munich Microplastic Sediment Separator (MPSS) can be employed. The MPSS is a stirred container, in which 6 kg sample and 30 L $ZnCl_2$ solution are stirred to a slurry and then sedimented. Due to the density of the separating solution ($ZnCl_2$: 1.6 – 1.7 g/mL), the lighter plastic particles float on top and sediment remains at the bottom. A ball valve facilitates the decanting of the top layer, which can be further treated, e.g. by filtration[36]. Next to $ZnCl_2$, other solutions like NaCl (1.2 g/mL), $CaCl_2$ (1.3 g/mL), NaI (1.8 g/mL), or sodium polytungstate (1.4 g/mL, up to 3.1 g/mL) can be used. The density of the respective salt solutions determines whether denser polymers like polyoxymethylene (POM) can be separated, as well. In many cases, a trade-off has to be made, as e.g. NaCl is inexpensive and non-toxic, but does not separate all polymer types (e.g. PVC, POM), whereas sodium polytungstate has a higher density, but is quite expensive, and $ZnCl_2$ is a good compromise of cost and density, but is toxic and dangerous to the environment and needs special care when used[2].

1.1.3.3 Chemical Identification and Quantification

The treated sample has to be subjected to an identification step to ensure the correct quantification of the mass and/or number of MP among the total sample. This step is essential, since a distinction between

natural particles and plastic particles has to be made because (i) any physical separation cannot be assumed to be perfect and (ii) some samples are not subjected to a separation.

In the early stages of MP analysis, studies relied on a visual inspection alone, in some cases using a light microscope, due to simplicity and cost-effectiveness. Particles are sorted by optical criteria like color and shape[5]. This approach, however, has been heavily criticized, since polymer particles exhibit a multitude of morphologies and, when altered by environmental influences, can be visually indistinguishable from natural particles. This results in a large risk of false positives[5,37].

Therefore, a chemical identification and quantification has been established, for which mainly two analytical chemical approaches have been applied: (i) mass-based thermoanalytical methods, which pyrolytically fragment the sample and analyze the indicative molecules by gas-chromatography/mass-spectrometry and (ii) particle-based vibrational spectroscopic methods, in which molecular vibrations are excited by infrared light (FT-IR) or monochromatic, visible light (inelastic scattering, Raman effect). These methods enable the unambiguous identification of the polymer and in some cases the additives, which results in far less error concerning the MP attribution compared to an approach based on visual identification alone[1,2,38].

The thermoanalytical methods primarily comprise two variants: pyrolysis-gas-chromatography-mass-spectrometry (Py-GC-MS) and thermo-extraction-desorption-gas-chromatography-mass-spectrometry (TED-GC-MS). Both identify the polymer type (and additives) by detecting thermal decomposition products (desorbed molecules, respectively) by GC-MS and deliver an output based on the total mass content of MP in the whole sample.

With Py-GC-MS, isolated particles are subjected to a temperature program, which first desorbs volatile organic compounds and pollutants at app. 350 °C and then pyrolyzes the particle at app. 600 °C – 700 °C. The polymer type is identified by comparison of the pyrogram with a validated database of known polymers[39,40]. Polar polymers may require the presence of a reactant, i.e. thermochemolysis, for proper pyrolyzation and chromatographic separation (e.g. hydrolysis or methylation)[41]. Mass quantification is performed by external calibration[42] with a limit of detection (LOD) of 0.01 – 1 µg, which is strongly dependent on the polymer type[43].

TED-GC-MS, on the other hand, uses a thermogravimetric analysis unit (TGA), in which the sample is pyrolyzed and volatile fragments are collected on a solid-phase adsorber, which is subsequently analyzed by thermodesorption-GC-MS[44]. This method requires a validation of the polymer types in question[45], in which polyethylene poses a particular challenge[46]. TED-GC-MS also enables the analysis of tire wear[47]. By the use of the TGA unit, a larger sample size can be processed (up to 100 mg, compared to 5 mg in Py-GC-MS). Quantification is also performed by external calibration, and LODs range from 0.5 µg – 2.5 µg[3]. An automated instrumentation[48] enables a fast and simple analysis even in the presence of a matrix[46].

Another established group of methods for the chemical identification and quantification of MP is based on vibrational spectroscopy. Here, vibrational transitions in the molecules are excited, resulting in a characteristic *fingerprint* spectrum. This enables an unambiguous identification of the polymer. FT-IR

detects the absorption of infrared light, whereas RM detects the inelastic scattering of visible, (near) IR, and UV laser light.

FT-IR is used for MP analysis with two variants. Attenuated-total-reflection-FT-IR (ATR-FT-IR) is chosen for the manual identification of single MP particles. Due to the manual handling of the particles, there is a practical size limitation[2] of around 500 µm. Smaller particles can be identified with FT-IR microscopes (µ-FT-IR), which provide chemical imaging of complete filters by utilizing focal-plane-arrays (FPA). Thus, a larger number of particles can be analyzed[33,49]. This creates a very large dataset, for which an automated data processing/analysis is necessary[50]. The result of the measurement comprises the characterization of single particles in terms of size, shape, and chemical identity down to 10 µm[2,38]. Moreover, the spectroscopic analysis can also identify additives in the polymer, like softeners or stabilizers[51].

RM is a combination of Raman spectroscopy and optical microscopy, which uses lasers in the visible, near-IR, or UV spectrum. Hence, it can give a better lateral resolution. This enables the analysis of MP down to 1 µm (and below)[1,2]. It also effects a higher precision when analyzing smaller particles[51,52]. RM can identify additives, including pigments, together with the polymer type. However, fluorescent samples (containing e.g. chlorophyll or carotenoids) inhibit the spectrum acquisition, since fluorescence is orders of magnitude stronger than the Raman effect. This can be avoided by either removing organic matrix or photobleaching, i.e. irradiating the sample with the Raman laser to decompose the fluorescent components[2]. A great advantage of RM is its insensitivity to water, which permits the analysis in a flow-cell, as performed in this thesis, or the analysis of biota samples.

Spectra acquisition in RM is performed on individual points, thus, for each particle, one spectrum is recorded. For automation and quantification, this implies that, initially, an optical microscope image is acquired and processed by image recognition[53], giving the coordinates of all particles. From these, a subset for analysis is selected[26], which is then targeted by the RM and measured. This subset needs to be large enough to satisfy the quality requirements for the analysis. Then, database matching provides the particle identity and gives a chemically correlated size distribution of up to 7000 particles[54]. The automated routines enable the analysis of larger numbers of particles, which give more reliable data and remove operator bias[26].

These advances in the RM analysis of MP, together with automation routines, have increased the particle numbers that can be measured. Consequently, smaller and smaller particle size ranges are being targeted so that the transition from MP to nanoplastic is emerging as a new frontier in the global plastic contamination issue with a new set of methodological challenges.

1.2 Nanoplastic: The New Frontier

1.2.1 Why Bother?

Nanoplastic is expected in the environment, since the plastic particle contamination is mainly sourced from the fragmentation of large plastic debris[13–15]. These fragmentation processes can be mechanical[55] or by UV radiation[15]. Initially, the main focus was on MP so that only in recent years, interest in smaller and smaller particles has led to the emergence of a dedicated focus on nanoplastic. Hence, research on the topic is still scarce. Nonetheless, a study showed the presence of nanoplastic in personal care products[56], others confirmed the presence of nanoplastic in the Atlantic ocean[57] and in snow[58], and it was also shown that MP could be fragmented to nanoplastic by biota[59].

Concerning the size definition of nanoplastic, there are currently two approaches: On the one hand, the whole nanometer range from 1 nm – 1000 nm is called nanoplastic, based on the consideration that particles in this size range exhibit colloidal behavior[60]. On the other hand, a distinction is made between the sizes of 1 nm – 100 nm and 100 nm – 1000 nm, which are denoted nanoplastic and subµ-plastic, respectively[4]. The latter incorporates the size definitions for nanomaterials by the European Commission, which defines an object with at least one dimension smaller than 100 nm as a nanomaterial[61]. This thesis will use the term nanoplastic to address plastic particles in the whole nanometer range. Occasionally, a distinction in two classes will be useful and will be made in appropriate places.

The decreasing size of nanoplastic particles effects a very large surface to volume ratio and, consequently they will display a different behavior in the environment and organisms compared to MP. Concurrently, from the analysis of MP size distributions and the resulting power law[6], an exponential increase in the particle numbers can reasonably be assumed for nanoplastic. Some knowledge can be drawn from engineered nanoparticles as well as MP research[62,63], however, there are distinct differences between the MP and nanoplastic[64]. Indeed, in the environment, nanoplastic displays colloidal behavior[60], and will, hence, stay dispersed, unlike MP, which tends to settle[64]. It also has a propensity for heteroaggregation with natural organic and inorganic matter[65–67]. Moreover, its large surface area implies an increased potential for the leaching of additives[64] and the sorption of organic pollutants[68]. In an organism, the loaded particles can release the pollutants more effectively and pose a toxicological threat, as was shown for polychlorinated biphenyls in daphniae[69].

Nanoplastic showed effects on biota[70], hence while the scientific community discusses whether MP is of toxicological relevance[23–25], the risk that nanoplastic bears may be greater due to its smaller size. In this regard, acute toxicity tests on biofilms indicated toxicity for nano-sized particles (100 nm), where larger particles (0.5 µm – 9 µm) showed no effects[71]. Other reports showed that nanoplastic is able to penetrate the blood-brain barrier[11,72], disturb[73] and transfer through[74] lipid membranes, persist over multiple generations in the organism[75], or exhibits trophic transfer[10,11]. Recently, the accumulation in plants has also been reported[76].

In the light of these new effects, properties, and behaviors that are to be expected of nanoplastic particles, it is all the more important to provide analytical techniques and methods that are capable of providing reliable data on this emerging analyte. Dependable conclusions to approach this issue can only be derived and detailed knowledge be achieved with a suitable methodological toolset available.

1.2.2 The New Analytical Challenge – Knowledge Gap

The most vital aspect of the analysis of the plastic contamination issue is the chemical identification of the particles, to avoid false positives[5,37] (Section 1.1.3). For nanoplastic, the particles can not even be observed optically, which accentuates the need for chemical identification. Furthermore, although somewhat counterintuitive, the expected exponential increase in particle numbers[6] is accompanied by lower mass contents, due to the dependency of the mass to the third power of the diameter d^3. Hence, analytical techniques appropriate for nanoplastic have to provide chemical information and also have to exhibit low limits for size detection or low limits of detection in terms of mass determination.

As a consequence, we face a methodological gap in analysis when approaching the nanoplastic size range. The established techniques for MP particle analysis hit their size limit in the low micrometer range. Since the particle-based spectroscopic techniques, µ-FT-IR and RM, are integrated into a microscope, their size range is determined by the diffraction limit, which, in turn, depends on the parameters of the optical components and the observed wavelengths. Hence, this limit is placed at ca. 10 µm for IR radiation and (according to the state of the art) ca. 1 µm for RM, which uses visible light[2,51]. Aside from spectroscopic techniques, there are thermoanalytical techniques, which are also established for the analysis of MP. Here, the resulting information is a total mass content. So, these techniques are not subject to size limitations[42,45]. They do, however, require a sufficient LOD to enable the analysis of the exponentially decreasing mass fraction of nanoplastic, which needs to be alleviated by a preconcentration step[57,77].

Here, the focus is put on the spectroscopic techniques, specifically RM, since these give a higher degree of information on the size distribution and morphology on the level of individual particles. In addition, RM can, in principle, provide this analysis on particles even in the subµ-range, giving access to optical characterization of a part of the nanoplastic range and pushing the need to change the instrumental approach down to a lower size threshold. This high degree of data is especially relevant for research, since this challenging analyte needs to be understood well before regulatory action and fast routine analysis with reduced information content can be implemented.

So far, the focus of this introduction has been on methods for MP analysis that are able to chemically identify the particle. On the other hand, there is a wide range of knowledge on engineered nanoparticles (ENP) in the environment and techniques for their physical rather than chemical analysis[78–81]. For instance, light scattering techniques or electron microscopy are some of the most common and routinely used representatives. Ergo, there are some methods that can possibly be transferred to the analysis of nanoplastic. However, most of the techniques for nanoparticles only offer a physical particle characterization, usually in terms of particle number, size, particle size distribution (PSD), or morphology.

There are no methods that can provide the crucial chemical identification, yet. Furthermore, since ENPs are mostly inorganic, the techniques for nanoparticles that actually give chemical information do so on an elemental basis, like ICP-MS[81], and are not sufficient for the identification of polymer type and distinction of the carbon-based polymer particles from natural organic matter.

Consequently, new approaches in the analytical methodology need to be established. This, on the one hand, can be achieved by pushing the limits of the established methods down to cover (part of) the nanoplastic range. On the other hand, different techniques, which offer characterization for different aspects of inquiry (e.g. Raman spectroscopy for chemical identification and light scattering for physical size characterization) can be combined to close the current methodological gap. This can be relevant for exploring the very small size range of nanoplastic, as established ENP techniques have the capability to analyze these nanoparticles. Furthermore, many of the relevant techniques for the analysis of nanoplastic and even very small MP are microscopy- or imaging-based and are facing issues with measurement times, which scale with the data points required for reliable quantification of the exponentially increasing particle numbers. Hence, an optimization towards representativity, high-throughput, and automatization will be necessary.

1.2.3 State of the Art

In recent years, the analysis of nanoplastic has become an emergent topic of interest. At the beginning of the thesis (October 2017), however, there was a very limited number of studies pertaining to this issue. The earliest reviews proposed sources and effects of nanoplastic based on knowledge from polymeric nanoparticles (mostly polystyrene latices)[82]. Knowledge was extrapolated from the environmental behavior of ENPs onto MP to estimate the behavior of nanoplastic[62].

The earliest investigations on the topic demonstrated that, indeed, nanoplastic is formed from larger plastic debris by different fragmentation mechanisms. Gigault et al. exposed plastic, collected at a beach, to solar radiation and analyzed the resulting nanoplastic by dynamic light scattering (DLS) and transmission electron microscopy (TEM)[13]. Subsequently, Lambert et al. showed that also typical polymers from single use consumer products fragment to nanoplastic by UV irradiation[14,15]. Actually detecting nanoplastic was restricted to few studies. One showed the existence of primary (i.e. specifically produced) nanoplastic in facial scrubs by scanning electron microscopy (SEM) and spectroscopic methods (FT-IR, X-ray photoelectron spectroscopy, XPS)[56]. Another study confirmed the presence of nanoplastic in the Atlantic Ocean by Py-GC-MS, after ultrafiltration preconcentration (factor of 100)[57]. Furthermore, it has been documented that plastic particles fragment to nanoplastic in biota, i.e. the Antarctic krill (*Euphausia superba*), which has a strong mastication apparatus[59].

Concerning the environmental behavior of nanoplastic, first model studies were performed on polystyrene latices, documenting heteroaggregation behavior with natural organic matter and inorganic colloids[65,66,83]. The analytics applied in these studies were mainly based on DLS and SEM.

Regarding the abovementioned methodological gap in the analytical methods, the need to push the application range of RM down to smaller MP particle sizes has been discussed in earlier reviews[26,84]. And in principle, the use of RM on nanostructured objects is theoretically possible[85] and was performed e.g. in a microtechnological application, in which 300 nm wide silicon strips were laterally profiled with a resolution of 140 nm by RM with 1.3 N.A. objective and UV laser (364 nm)[86]. Another application showed the spectrum acquisition of a 40 nm PS latex bead with a 1.25 N.A. Raman tweezer setup (730 nm, 120 mW)[87]. However, the application of RM on environmental plastic particles has not been shown in the nanometer size range. Reports are limited to micrometer-sized particles, with the smallest particles detected ranging from 5 µm to 10 µm in the respective studies[31,51,88,89].

Moreover, the automation for the quantification of MP with RM is an important advance to be made[26], since the manual particle analysis is very time consuming and labor intensive[88]. It further enables the measurement of greater numbers of particles, which increases the reliability of the data and removes operator bias[26]. However, the development of such automated routines for MP is still in progress[53], except for some commercial RM control softwares, which offer sequential analysis of measurement points[90,91]. Considerations on the particle selection have, consequently, also been limited to windows with areas that could reasonably be analyzed. These windows are placed in an arbitrary[89] or somewhat structured[38] pattern. Hence, automation needs to be advanced to enable the optimal – random[26,92–94] – particle selection.

Py-GC-MS as particle size-independent technique (see above) was shown to be able to identify nanoplastic in a model application with a 100 nm PS latex[77] and in the detection of nanoplastic in the Atlantic ocean[57]. These studies, however, needed to apply a preconcentration by either a crossflow ultrafiltration (factor 200) or a dead-end ultrafiltration (factor 100), respectively. The second established thermoanalytical method for MP analysis, TED-GC-MS[45], has not been investigated for nanoplastic yet, but might benefit from the greater sample volume, if the reduced sensitivity compared to Py-GC-MS is alleviated. XPS has also been used for nanoplastic identification[56,95] by the specific binding energies of the orbitals giving insight in the molecular structure[96]. Current applications of XPS, however, are based on reference matching – an identification of an unknown environmental sample needs to be performed yet. Furthermore, since the method observes bonding energies of the orbitals, an unambiguous identification of many polymers might be difficult to achieve.

Field-flow fractionation (FFF) coupled to online detectors as particle separation and characterization technique has the potential to provide an analysis on particles of a wide size range. Indeed, asymmetric-flow field-flow fractionation coupled to UV and multi-angle light scattering (AF4-UV-MALS) was shown to be able to investigate irregular and polydisperse nanoplastic particles[97] and to process nanoplastic (PS beads) after chemical digestion of biological matrix[98]. Mintenig et al. showed that offline Py-GC-MS after AF4-UV-MALS characterization can be performed[77]. Chemical identification on the eluting fraction, especially online-coupled, is rare and has not been implemented for nanoplastic. The commercially available ICP-MS detector[99] and an organic carbon detector (OCD)[100] are only able to provide elemental information on the sample and lack the specific structure elucidation required for nanoplastic identification.

Nanoparticle analysis techniques that give physical characterization were used as well. Here, TEM and SEM were both used to visualize (mainly primary) nanoplastic particles and derive a PSD[60,66]. Similarly, the commercially available DLS[66,83] and nanoparticle tracking analysis (NTA)[14,15] were used to provide size information and, in the case of DLS, the zeta potential. Further microscopic approaches were used for the detection of nanoplastic: Fluorescence microscopy and confocal laser scanning microscopy (CLSM) could be used to track the translocation of particles in the organism[59,101]. It was also emphasized that the leaching of the fluorophore has to be accounted for[102]. Such an approach, however, might not be feasible for environmental plastic, since it is not fluorescent.

Among the nanoparticle techniques, there are some that give chemical structure information. Scanning probe microscopy (SPM) approaches were combined with Raman spectroscopy to tip-enhanced Raman spectroscopy (TERS)[103–105] and IR spectroscopy with atomic force microscopy-IR spectroscopy (AFM-IR)[106–108], providing vibrational spectroscopy with size limits of ca. 10 nm and 50 nm, respectively. Additionally, the sub-diffraction photothermal IR spectroscopy/Raman spectroscopy[109] could offer chemical identification in the subµ range. These techniques have not been used for nanoplastic analysis and need to be validated for this application. They also need to account for the high measurement times and the resulting representativity issues in particle selection.

1.2.4 How to Achieve Nanoplastic Analysis? – Goal of the Thesis

The new nanoplastic issue and its potentially negative impact on health and the environment makes advances in method development imperative. This thesis aims to close the methodological gap as described above (Section 1.2.2).

Since this field of inquiry is newly emerging, as a first step, a critical overview of the state of the art, the established techniques in MP that can be adapted, and the techniques from ENP analysis that can benefit the nanoplastic characterization is performed. Here, possible pathways for enabling nanoplastic analysis with regard to the abovementioned demands (Section 1.2.2) are discussed and critically evaluated. Then, a roadmap for a comprehensive nanoplastic analysis including sample treatment, preconcentration, separation, and characterization is laid out.

Subsequently, technical solutions aiming at closing the methodological gap based on RM due to the abovementioned advantages (Section 1.2.2) are developed. These solutions aim at tackling the nanoplastic size range from two directions: Starting with methods of MP analysis, it is the aim to decrease the lower bound of the application range and, secondly, to ensure statistically sound quantification even of these small particles. In a third part, the nanoplastic size range is approached from the other end: combining established nanoparticle techniques, specifically FFF, with Raman spectroscopy.

In the first part, the size limit of RM is pushed down to the subµ range, as estimated by the theoretical description of the diffraction limit of around 0.25 µm, depending on the wavelength of the laser and the numerical aperture of the instrument[85]. Hence, the presented work aims at illustrating the applicability of

RM down to the theoretical limit and combining the RM analysis with high resolution imaging by SEM to provide appropriate morphological characterization.

A second part of this thesis accompanies this effort by developing a measurement algorithm for the particle-by-particle approach of RM. This is realized by employing chemometric methods, specifically Theory of Sampling[92–94], for a window-based particle selection and an error estimation by a bootstrap method[110]. Hereby, a statistically sound quantification for the automated analysis of very small MP and nanoplastic is pioneered.

In the third part, the combination of FFF, a suitable technique for nano-sized particles (and small microparticles), with RM for chemical identification is realized for the first time. For this coupling, a flow-cell has been developed that allows the online-coupling of Raman spectroscopy to FFF-UV-MALS, enabling an automatable multi-detector setup, which provides particle detection (UV), size characterization (MALS), and chemical identification (Raman) in one run. Moreover, two variants of FFF (asymmetric-flow FFF, AF4 & centrifugal FFF, CF3) with their respective advantages and disadvantages (see Section 2.3) are used[a] to enable a specific and modular analysis of the individual sample. This technique aims to pave the path towards nanoplastic analysis with the potential for the application to a much broader set of particulate samples.

References

1. Ivleva, N. P. Chemical Analysis of Microplastics and Nanoplastics: Challenges, Advanced Methods, and Perspectives. *Chemical Reviews* **2021**, *121*, 11886–11936.
2. Ivleva, N. P.; Wiesheu, A. C.; Niessner, R. Microplastic in Aquatic Ecosystems. *Angewandte Chemie, International Edition* **2017**, *56*, 1720–1739.
3. Braun, U.; Jekel, M.; Gerdts, G.; Ivleva, N. P.; Reiber, J. Diskussionspapier Mikroplastik-Analytik: Probenahme, Probenaufbereitung und Detektionsverfahren. **2018**.
4. Hartmann, N. B.; Hüffer, T.; Thompson, R. C.; Hassellöv, M.; Verschoor, A.; Daugaard, A. E.; Rist, S.; Karlsson, T.; Brennholt, N.; Cole, M.; Herrling, M. P.; Hess, M. C.; Ivleva, N. P.; Lusher, A. L.; Wagner, M. Are We Speaking the Same Language? Recommendations for a Definition and Categorization Framework for Plastic Debris. *Environmental Science & Technology* **2019**, *53*, 1039–1047.
5. Hidalgo-Ruz, V.; Gutow, L.; Thompson, R. C.; Thiel, M. Microplastics in the marine environment: a review of the methods used for identification and quantification. *Environmental Science & Technology* **2012**, *46*, 3060–3075.
6. Kooi, M.; Koelmans, A. A. Simplifying Microplastic via Continuous Probability Distributions for Size, Shape, and Density. *Environmental Science & Technology Letters* **2019**, *6*, 551–557.
7. PlasticsEurope Plastics: The facts 2018. **2018**.

[a] Generally, AF4 is better suited for small particles below 100 nm and CF3 can also be applied to the low micrometer range (ca. 10 nm – 20 µm) and can separate according to particle density[111].

8. Jambeck, J. R.; Geyer, R.; Wilcox, C.; Siegler, T. R.; Perryman, M.; Andrady, A.; Narayan, R.; Law, K. L. Marine pollution. Plastic waste inputs from land into the ocean. *Science* **2015**, *347*, 768–771.

9. Murphy, F.; Ewins, C.; Carbonnier, F.; Quinn, B. Wastewater Treatment Works (WwTW) as a Source of Microplastics in the Aquatic Environment. *Environmental Science & Technology* **2016**, *50*, 5800–5808.

10. Chae, Y.; An, Y.-J. Effects of micro- and nanoplastics on aquatic ecosystems: Current research trends and perspectives. *Marine Pollution Bulletin* **2017**, *124*, Special Issue: Hong Kong Conference 2016, 624–632.

11. Mattsson, K.; Johnson, E. V.; Malmendal, A.; Linse, S.; Hansson, L.-A.; Cedervall, T. Brain damage and behavioural disorders in fish induced by plastic nanoparticles delivered through the food chain. *Scientific Reports* **2017**, *7*, 11452.

12. Ter Halle, A.; Ladirat, L.; Gendre, X.; Goudouneche, D.; Pusineri, C.; Routaboul, C.; Tenailleau, C.; Duployer, B.; Perez, E. Understanding the Fragmentation Pattern of Marine Plastic Debris. *Environmental Science & Technology* **2016**, *50*, 5668–5675.

13. Gigault, J.; Pedrono, B.; Maxit, B.; Ter Halle, A. Marine plastic litter: The unanalyzed nano-fraction. *Environmental Science: Nano* **2016**, *3*, 346–350.

14. Lambert, S.; Wagner, M. Characterisation of nanoplastics during the degradation of polystyrene. *Chemosphere* **2016**, *145*, 265–268.

15. Lambert, S.; Wagner, M. Formation of microscopic particles during the degradation of different polymers. *Chemosphere* **2016**, *161*, 510–517.

16. Rillig, M. C.; Lehmann, A.; de Souza Machado, A. A.; Yang, G. Microplastic effects on plants. *The New Phytologist* **2019**, *223*, 1066–1070.

17. Ng, E.-L.; Huerta Lwanga, E.; Eldridge, S. M.; Johnston, P.; Hu, H.-W.; Geissen, V.; Chen, D. An overview of microplastic and nanoplastic pollution in agroecosystems. *The Science of the Total Environment* **2018**, *627*, 1377–1388.

18. Astner, A.; Hayes, D.; O'Neill, H.; Evans, B.; Pingali, S.; Urban, V.; Young, T. Mechanical formation of micro- and nano-plastic materials for environmental studies in agricultural ecosystems. *Science of The Total Environment* **2019**, *685*, 1097–1106.

19. Kole, P. J.; Löhr, A. J.; van Belleghem, F. G. A. J.; Ragas, A. M. J. Wear and Tear of Tyres: A Stealthy Source of Microplastics in the Environment. *International Journal of Environmental Research and Public Health* **2017**, *14*, 1265.

20. Wagner, S.; Hüffer, T.; Klöckner, P.; Wehrhahn, M.; Hofmann, T.; Reemtsma, T. Tire wear particles in the aquatic environment - A review on generation, analysis, occurrence, fate and effects. *Water Research* **2018**, *139*, 83–100.

21. Dris, R.; Gasperi, J.; Saad, M.; Mirande, C.; Tassin, B. Synthetic fibers in atmospheric fallout: A source of microplastics in the environment? *Marine Pollution Bulletin* **2016**, *104*, 290–293.

22. Toussaint, B.; Raffael, B.; Angers-Loustau, A.; Gilliland, D.; Kestens, V.; Petrillo, M.; Rio-Echevarria, I. M.; van den Eede, G. Review of micro- and nanoplastic contamination in the food chain. *Food Additives & Contaminants. Part A, Chemistry, Analysis, Control, Exposure & Risk Assessment* **2019**, *36*, 639–673.

23. Burton, G. A. Stressor Exposures Determine Risk: So, Why Do Fellow Scientists Continue To Focus on Superficial Microplastics Risk? *Environmental Science & Technology* **2017**, *51*, 13515–13516.

24. Hale, R. C. Are the Risks from Microplastics Truly Trivial? *Environmental Science & Technology* **2018**, *52*, 931.

25. Kramm, J.; Völker, C.; Wagner, M. Superficial or Substantial: Why Care about Microplastics in the Anthropocene? *Environmental Science & Technology* **2018**, *52*, 3336–3337.

26. Anger, P. M.; von der Esch, E.; Baumann, T.; Elsner, M.; Niessner, R.; Ivleva, N. P. Raman microspectroscopy as a tool for microplastic particle analysis. *Trends in Analytical Chemistry* **2018**, *109*, 214–226.

27. Zarfl, C. Promising techniques and open challenges for microplastic identification and quantification in environmental matrices. *Analytical and Bioanalytical Chemistry* **2019**, *411*, 3743–3756.

28. Dehaut, A.; Cassone, A.-L.; Frère, L.; Hermabessiere, L.; Himber, C.; Rinnert, E.; Rivière, G.; Lambert, C.; Soudant, P.; Huvet, A.; Duflos, G.; Paul-Pont, I. Microplastics in seafood: Benchmark protocol for their extraction and characterization. *Environmental Pollution* **2016**, *215*, 223–233.

29. Hurley, R. R.; Lusher, A. L.; Olsen, M.; Nizzetto, L. Validation of a Method for Extracting Microplastics from Complex, Organic-Rich, Environmental Matrices. *Environmental Science & Technology* **2018**, *52*, 7409–7417.

30. Löder, M. G. J.; Imhof, H. K.; Ladehoff, M.; Löschel, L. A.; Lorenz, C.; Mintenig, S.; Piehl, S.; Primpke, S.; Schrank, I.; Laforsch, C.; Gerdts, G. Enzymatic Purification of Microplastics in Environmental Samples. *Environmental Science & Technology* **2017**, *51*, 14283–14292.

31. Enders, K.; Lenz, R.; Stedmon, C. A.; Nielsen, T. G. Abundance, size and polymer composition of marine microplastics $\geq$ 10 µm in the Atlantic Ocean and their modelled vertical distribution. *Marine Pollution Bulletin* **2015**, *100*, 70–81.

32. Von der Esch, E.; Lanzinger, M.; Kohles, A. J.; Schwaferts, C.; Weisser, J.; Hofmann, T.; Glas, K.; Elsner, M.; Ivleva, N. P. Simple Generation of Suspensible Secondary Microplastic Reference Particles via Ultrasound Treatment. *Frontiers in Chemistry* **2020**, *8*, 169.

33. Löder, M. G. J.; Gerdts, G. In *Marine Anthropogenic Litter*, Bergmann, M., Gutow, L., Klages, M., Eds.; Springer International Publishing: Cham, 2015, pp 201–227.

34. Al-Azzawi, M. S. M.; Kefer, S.; Weißer, J.; Reichel, J.; Schwaller, C.; Glas, K.; Knoop, O.; Drewes, J. E. Validation of Sample Preparation Methods for Microplastic Analysis in Wastewater Matrices—Reproducibility and Standardization. *Water* **2020**, *12*, 2445.

35. Rist, S.; Baun, A.; Hartmann, N. B. Ingestion of micro- and nanoplastics in Daphnia magna - Quantification of body burdens and assessment of feeding rates and reproduction. *Environmental Pollution* **2017**, *228*, 398–407.

36. Imhof, H. K.; Schmid, J.; Niessner, R.; Ivleva, N. P.; Laforsch, C. A novel, highly efficient method for the separation and quantification of plastic particles in sediments of aquatic environments. *Limnology and Oceanography: Methods* **2012**, *10*, 524–537.

37. Lenz, R.; Enders, K.; Stedmon, C. A.; Mackenzie, D. M. A.; Nielsen, T. G. A critical assessment of visual identification of marine microplastic using Raman spectroscopy for analysis improvement. *Marine Pollution Bulletin* **2015**, *100*, 82–91.

38. Huppertsberg, S.; Knepper, T. P. Instrumental analysis of microplastics-benefits and challenges. *Analytical and Bioanalytical Chemistry* **2018**, *410*, 6343–6352.

39. Fries, E.; Dekiff, J. H.; Willmeyer, J.; Nuelle, M.-T.; Ebert, M.; Remy, D. Identification of polymer types and additives in marine microplastic particles using pyrolysis-GC/MS and scanning electron microscopy. *Environmental Science. Processes & Impacts* **2013**, *15*, 1949–1956.

40. Dekiff, J. H.; Remy, D.; Klasmeier, J.; Fries, E. Occurrence and spatial distribution of microplastics in sediments from Norderney. *Environmental Pollution* **2014**, *186*, 248–256.

41. Käppler, A.; Fischer, M.; Scholz-Böttcher, B. M.; Oberbeckmann, S.; Labrenz, M.; Fischer, D.; Eichhorn, K.-J.; Voit, B. Comparison of µ-ATR-FTIR spectroscopy and py-GCMS as identification tools for microplastic particles and fibers isolated from river sediments. *Analytical and Bioanalytical Chemistry* **2018**, *410*, 5313–5327.

42. Fischer, M.; Scholz-Böttcher, B. M. Simultaneous Trace Identification and Quantification of Common Types of Microplastics in Environmental Samples by Pyrolysis-Gas Chromatography-Mass Spectrometry. *Environmental Science & Technology* **2017**, *51*, 5052–5060.

43. Braun, U.; Altmann, K.; Bannick, C. G.; Becker, R.; Bitter, H.; Bochow, M.; Dierkes, G.; Enders, K.; Eslahian, K. A.; Fischer, D. Status Report: Analysis of Microplastics — Sampling, Preparation and Detection Methods within the Scope of the Bmbf Research Focus Plastics in the Environment: Sources, Sinks, Solutions. **2020**.

44. Dümichen, E.; Braun, U.; Senz, R.; Fabian, G.; Sturm, H. Assessment of a new method for the analysis of decomposition gases of polymers by a combining thermogravimetric solid-phase extraction and thermal desorption gas chromatography mass spectrometry. *Journal of Chromatography A* **2014**, *1354*, 117–128.

45. Dümichen, E.; Eisentraut, P.; Bannick, C. G.; Barthel, A.-K.; Senz, R.; Braun, U. Fast identification of microplastics in complex environmental samples by a thermal degradation method. *Chemosphere* **2017**, *174*, 572–584.

46. Dümichen, E.; Barthel, A.-K.; Braun, U.; Bannick, C. G.; Brand, K.; Jekel, M.; Senz, R. Analysis of polyethylene microplastics in environmental samples, using a thermal decomposition method. *Water Research* **2015**, *85*, 451–457.

47. Eisentraut, P.; Dümichen, E.; Ruhl, A. S.; Jekel, M.; Albrecht, M.; Gehde, M.; Braun, U. Two Birds with One Stone—Fast and Simultaneous Analysis of Microplastics: Microparticles Derived from Thermoplastics and Tire Wear. *Environmental Science & Technology Letters* **2018**, *5*, 608–613.

48. Duemichen, E.; Eisentraut, P.; Celina, M.; Braun, U. Automated thermal extraction-desorption gas chromatography mass spectrometry: A multifunctional tool for comprehensive characterization of polymers and their degradation products. *Journal of Chromatography A* **2019**, *1592*, 133–142.

49. Tagg, A. S.; Sapp, M.; Harrison, J. P.; Ojeda, J. J. Identification and Quantification of Microplastics in Wastewater Using Focal Plane Array-Based Reflectance Micro-FT-IR Imaging. *Analytical Chemistry* **2015**, *87*, 6032–6040.

50. Primpke, S.; Lorenz, C.; Rascher-Friesenhausen, R.; Gerdts, G. An automated approach for microplastics analysis using focal plane array (FPA) FTIR microscopy and image analysis. *Analytical Methods* **2017**, *9*, 1499–1511.

51. Käppler, A.; Fischer, D.; Oberbeckmann, S.; Schernewski, G.; Labrenz, M.; Eichhorn, K.-J.; Voit, B. Analysis of environmental microplastics by vibrational microspectroscopy: FTIR, Raman or both? *Analytical and Bioanalytical Chemistry* **2016**, *408*, 8377–8391.

52. Cabernard, L.; Roscher, L.; Lorenz, C.; Gerdts, G.; Primpke, S. Comparison of Raman and Fourier Transform Infrared Spectroscopy for the Quantification of Microplastics in the Aquatic Environment. *Environmental Science & Technology* **2018**, *52*, 13279–13288.

53. Anger, P. M.; Prechtl, L.; Elsner, M.; Niessner, R.; Ivleva, N. P. Implementation of an open source algorithm for particle recognition and morphological characterisation for microplastic analysis by means of Raman microspectroscopy. *Analytical Methods* **2019**, *11*, 3483–3489.

54. Von der Esch, E.; Kohles, A. J.; Anger, P. M.; Hoppe, R.; Niessner, R.; Elsner, M.; Ivleva, N. P. TUM-ParticleTyper: A detection and quantification tool for automated analysis of (Microplastic) particles and fibers. *PLOS ONE* **2020**, *15*, e0234766.

55. Ekvall, M. T.; Lundqvist, M.; Kelpsiene, E.; Šileikis, E.; Gunnarsson, S. B.; Cedervall, T. Nanoplastics formed during the mechanical breakdown of daily-use polystyrene products. *Nanoscale Advances* **2019**, *1*, 1055–1061.

56. Hernandez, L. M.; Yousefi, N.; Tufenkji, N. Are There Nanoplastics in Your Personal Care Products? *Environmental Science & Technology Letters* **2017**, *4*, 280–285.

57. Ter Halle, A.; Jeanneau, L.; Martignac, M.; Jardé, E.; Pedrono, B.; Brach, L.; Gigault, J. Nanoplastic in the North Atlantic Subtropical Gyre. *Environmental Science & Technology* **2017**, *51*, 13689–13697.

58. Materić, D.; Kasper-Giebl, A.; Kau, D.; Anten, M.; Greilinger, M.; Ludewig, E.; van Sebille, E.; Röckmann, T.; Holzinger, R. Micro- and Nanoplastics in Alpine Snow: A New Method for Chemical Identification and (Semi)Quantification in the Nanogram Range. *Environmental Science & Technology* **2020**, *54*, 2353–2359.

59. Dawson, A. L.; Kawaguchi, S.; King, C. K.; Townsend, K. A.; King, R.; Huston, W. M.; Bengtson Nash, S. M. Turning microplastics into nanoplastics through digestive fragmentation by Antarctic krill. *Nature Communications* **2018**, *9*, 1001.

60. Gigault, J.; Halle, A. T.; Baudrimont, M.; Pascal, P.-Y.; Gauffre, F.; Phi, T.-L.; El Hadri, H.; Grassl, B.; Reynaud, S. Current opinion: What is a nanoplastic? *Environmental Pollution* **2018**, *235*, 1030–1034.

61. Commission, E. Commission recommendation of 18 October 2011 on the definition of nanomaterial (2011/696/EU). *Official Journal of the European Communities: Legis* **2011**, *L 275*, 38–40.

62. Hüffer, T.; Praetorius, A.; Wagner, S.; von der Kammer, F.; Hofmann, T. Microplastic Exposure Assessment in Aquatic Environments: Learning from Similarities and Differences to Engineered Nanoparticles. *Environmental Science & Technology* **2017**, *51*, 2499–2507.

63. Mitrano, D. M.; Wick, P.; Nowack, B. Placing nanoplastics in the context of global plastic pollution. *Nature Nanotechnology* **2021**, 1–10.

64. Gigault, J.; El Hadri, H.; Nguyen, B.; Grassl, B.; Rowenczyk, L.; Tufenkji, N.; Feng, S.; Wiesner, M. Nanoplastics are neither microplastics nor engineered nanoparticles. *Nature Nanotechnology* **2021**, 1–7.

65. Cai, L.; Hu, L.; Shi, H.; Ye, J.; Zhang, Y.; Kim, H. Effects of inorganic ions and natural organic matter on the aggregation of nanoplastics. *Chemosphere* **2018**, *197*, 142–151.

66. Oriekhova, O.; Stoll, S. Heteroaggregation of nanoplastic particles in the presence of inorganic colloids and natural organic matter. *Environmental Science: Nano* **2018**, *5*, 792–799.

67. Chen, W.; Ouyang, Z.-Y.; Qian, C.; Yu, H.-Q. Induced structural changes of humic acid by exposure of polystyrene microplastics: A spectroscopic insight. *Environmental Pollution* **2018**, *233*, 1–7.

68. Velzeboer, I.; Kwadijk, C. J. A. F.; Koelmans, A. A. Strong sorption of PCBs to nanoplastics, microplastics, carbon nanotubes, and fullerenes. *Environmental Science & Technology* **2014**, *48*, 4869–4876.

69. Jiang, R.; Lin, W.; Wu, J.; Xiong, Y.; Zhu, F.; Bao, L.-J.; You, J.; Ouyang, G.; Zeng, E. Y. Quantifying nanoplastic-bound chemicals accumulated in Daphnia magna with a passive dosing method. *Environmental Science: Nano* **2018**, *5*, 776–781.

70. Mattsson, K.; Hansson, L.-A.; Cedervall, T. Nano-plastics in the aquatic environment. *Environmental Science. Processes & Impacts* **2015**, *17*, 1712–1721.

71. Miao, L.; Hou, J.; You, G.; Liu, Z.; Liu, S.; Li, T.; Mo, Y.; Guo, S.; Qu, H. Acute effects of nanoplastics and microplastics on periphytic biofilms depending on particle size, concentration and surface modification. *Environmental Pollution* **2019**, *255*, 113300.

72. Kashiwada, S. Distribution of Nanoparticles in the See-through Medaka (Oryzias latipes). *Environmental Health Perspectives* **2006**, *114*, 1697–1702.

73. Rossi, G.; Barnoud, J.; Monticelli, L. Polystyrene Nanoparticles Perturb Lipid Membranes. *The Journal of Physical Chemistry Letters* **2014**, *5*, 241–246.

74. Zhao, J.; Stenzel, M. H. Entry of nanoparticles into cells: the importance of nanoparticle properties. *Polymer Chemistry* **2018**, *9*, 259–272.

75. Zhao, L.; Qu, M.; Wong, G.; Wang, D. Transgenerational toxicity of nanopolystyrene particles in the range of μg L^{-1} in the nematode Caenorhabditis elegans. *Environmental Science: Nano* **2017**, *4*, 2356–2366.

76. Sun, X.-D.; Yuan, X.-Z.; Jia, Y.; Feng, L.-J.; Zhu, F.-P.; Dong, S.-S.; Liu, J.; Kong, X.; Tian, H.; Duan, J.-L., et al. Differentially charged nanoplastics demonstrate distinct accumulation in Arabidopsis thaliana. *Nature Nanotechnology* **2020**, *15*, 755–760.

77. Mintenig, S. M.; Bäuerlein, P. S.; Koelmans, A. A.; Dekker, S. C.; van Wezel, A. P. Closing the gap between small and smaller: Towards a framework to analyse nano- and microplastics in aqueous environmental samples. *Environmental Science: Nano* **2018**, *5*, 1640–1649.

78. Laborda, F.; Bolea, E.; Cepriá, G.; Gómez, M. T.; Jiménez, M. S.; Pérez-Arantegui, J.; Castillo, J. R. Detection, characterization and quantification of inorganic engineered nanomaterials: A review of techniques and methodological approaches for the analysis of complex samples. *Analytica Chimica Acta* **2016**, *904*, 10–32.

79. Lin, P.-C.; Lin, S.; Wang, P. C.; Sridhar, R. Techniques for physicochemical characterization of nanomaterials. *Biotechnology Advances* **2014**, *32*, 711–726.

80. Zänker, H.; Schierz, A. Engineered nanoparticles and their identification among natural nanoparticles. *Annual Review of Analytical Chemistry* **2012**, *5*, 107–132.

81. Tiede, K.; Boxall, A. B. A.; Tear, S. P.; Lewis, J.; David, H.; Hassellov, M. Detection and characterization of engineered nanoparticles in food and the environment. *Food Additives & Contaminants, Part A* **2008**, *25*, 795–821.

82. Koelmans, A. A.; Besseling, E.; Shim, W. J. In *Marine Anthropogene Litter*; Springer: 2015, pp 325–340.

83. Chen, C.-S.; Le, C.; Chiu, M.-H.; Chin, W.-C. The impact of nanoplastics on marine dissolved organic matter assembly. *Science* **2018**, *634*, 316–320.

84. Araujo, C. F.; Nolasco, M. M.; Ribeiro, A. M. P.; Ribeiro-Claro, P. J. A. Identification of microplastics using Raman spectroscopy: Latest developments and future prospects. *Water Research* **2018**, *142*, 426–440.

85. Zoubir, A., *Raman imaging: Techniques and applications*; Springer Series in Optical Sciences, Vol. 168; Springer: Berlin, Heidelberg, 2012.

86. Poborchii, V.; Tada, T.; Kanayama, T. High-spatial-resolution Raman microscopy of stress in shallow-trench-isolated Si structures. *Applied Physics Letters* **2006**, *89*, 233505.

87. Ajito, K.; Torimitsu, K. Single Nanoparticle Trapping Using a Raman Tweezers Microscope. *Applied Spectroscopy* **2002**, *56*, 541–544.

88. Imhof, H. K.; Ivleva, N. P.; Schmid, J.; Niessner, R.; Laforsch, C. Contamination of beach sediments of a subalpine lake with microplastic particles. *Current Biology* **2013**, *23*, R867–R868.

89. Imhof, H. K.; Laforsch, C.; Wiesheu, A. C.; Schmid, J.; Anger, P. M.; Niessner, R.; Ivleva, N. P. Pigments and plastic in limnetic ecosystems: A qualitative and quantitative study on microparticles of different size classes. *Water Research* **2016**, *98*, 64–74.

90. Oßmann, B. E.; Sarau, G.; Holtmannspötter, H.; Pischetsrieder, M.; Christiansen, S. H.; Dicke, W. Small-sized microplastics and pigmented particles in bottled mineral water. *Water Research* **2018**, *141*, 307–316.

91. Schymanski, D.; Goldbeck, C.; Humpf, H.-U.; Fürst, P. Analysis of microplastics in water by micro-Raman spectroscopy: Release of plastic particles from different packaging into mineral water. *Water Research* **2018**, *129*, 154–162.

92. Gy, P. Sampling of discrete materials – a new introduction to the theory of sampling: I. Qualitative approach. *Chemometrics and Intelligent Laboratory Systems* **2004**, *74*, 7–24.

93. Gy, P. Sampling of discrete materials: II. Quantitative approach – sampling of zero-dimensional objects. *Chemometrics and Intelligent Laboratory Systems* **2004**, *74*, 25–38.

94. Pitard, F. F., *Theory of Sampling and Sampling Practice*; CRC Press: 2019.

95. Lu, S.; Zhu, K.; Song, W.; Song, G.; Chen, D.; Hayat, T.; Alharbi, N. S.; Chen, C.; Sun, Y. Impact of water chemistry on surface charge and aggregation of polystyrene microspheres suspensions. *Science of the Total Environment* **2018**, *630*, 951–959.

96. Foerch, R.; Beamson, G.; Briggs, D. XPS valence band analysis of plasma-treated polymers. *Surface and Interface Analysis* **1991**, *17*, 842–846.

97. Gigault, J.; El Hadri, H.; Reynaud, S.; Deniau, E.; Grassl, B. Asymmetrical flow field flow fractionation methods to characterize submicron particles: Application to carbon-based aggregates and nanoplastics. *Analytical and Bioanalytical Chemistry* **2017**, *409*, 6761–6769.

98. Correia, M.; Loeschner, K. Detection of nanoplastics in food by asymmetric flow field-flow fractionation coupled to multi-angle light scattering: Possibilities, challenges and analytical limitations. *Analytical and Bioanalytical Chemistry* **2018**, *410*, 5603–5615.

99. Nischwitz, V.; Gottselig, N.; Missong, A.; Meyn, T.; Klumpp, E. Field flow fractionation online with ICP-MS as novel approach for the quantification of fine particulate carbon in stream water samples and soil extracts. *Journal of Analytical Atomic Spectrometry* **2016**, *31*, 1858–1868.

100. Missong, A.; Holzmann, S.; Bol, R.; Nischwitz, V.; Puhlmann, H.; V Wilpert, K.; Siemens, J.; Klumpp, E. Leaching of natural colloids from forest topsoils and their relevance for phosphorus mobility. *The Science of the Total Environment* **2018**, *634*, 305–315.

101. Dawson, A.; Huston, W.; Kawaguchi, S.; King, C.; Cropp, R.; Wild, S.; Eisenmann, P.; Townsend, K.; Bengtson Nash, S. Uptake and depuration kinetics influence microplastic bioaccumulation and toxicity in Antarctic Krill (Euphausia superba). *Environmental Science & Technology* **2018**, *52*, 3195–3201.

102. Schür, C.; Rist, S.; Baun, A.; Mayer, P.; Hartmann, N. B.; Wagner, M. When Fluorescence Is not a Particle: The Tissue Translocation of Microplastics in Daphnia magna Seems an Artifact. *Environmental Toxicology and Chemistry* **2019**, *38*, 1495–1503.

103. Yeo, B.-S.; Amstad, E.; Schmid, T.; Stadler, J.; Zenobi, R. Nanoscale Probing of a Polymer-Blend Thin Film with Tip-Enhanced Raman Spectroscopy. *Small* **2009**, *5*, 952–960.

104. Schmid, T.; Opilik, L.; Blum, C.; Zenobi, R. Nanoscale chemical imaging using tip-enhanced Raman spectroscopy: A critical review. *Angewandte Chemie, International Edition* **2013**, *52*, 5940–5954.

105. Kumar, N.; Mignuzzi, S.; Su, W.; Roy, D. Tip-enhanced Raman spectroscopy: Principles and applications. *EPJ Techniques and Instrumentation* **2015**, *2*, 1538.

106. Dazzi, A.; Saunier, J.; Kjoller, K.; Yagoubi, N. Resonance enhanced AFM-IR: A new powerful way to characterize blooming on polymers used in medical devices. *International Journal of Pharmaceutics* **2015**, *484*, 109–114.

107. Dazzi, A.; Prater, C. B.; Hu, Q.; Chase, D. B.; Rabolt, J. F.; Marcott, C. AFM-IR: Combining atomic force microscopy and infrared spectroscopy for nanoscale chemical characterization. *Applied Spectroscopy* **2012**, *66*, 1365–1384.

108. Dazzi, A.; Prater, C. B. AFM-IR: Technology and Applications in Nanoscale Infrared Spectroscopy and Chemical Imaging. *Chemical Reviews* **2017**, *117*, 5146–5173.

109. Furstenberg, R.; Kendziora, C. A.; Papantonakis, M. R.; Nguyen, V.; McGill, R. A. In *Next-Generation Spectroscopic Technologies V*, ed. by Druy, M. A.; Crocombe, R. A., SPIE: 2012; Vol. 8374, pp 293–302.

110. Tibshirani, R. J.; Efron, B. An introduction to the bootstrap. *Monographs on Statistics and Applied Probability* **1993**, *57*, 1–436.

111. Contado, C. Field flow fractionation techniques to explore the “nano-world”. *Analytical and Bioanalytical Chemistry* **2017**, *409*, 2501–2518.

Chapter 2

Relevant Techniques for the Thesis

2.1 Raman Microspectroscopy

Raman spectroscopy and especially its surface-analytical variant, Raman microspectroscopy (RM) has seen an immense increase in popularity in the last decades[1] and is now a broadly utilized technique for chemical identification and structure determination due to a variety of advantages. Among those are its easy sample preparation, non-destructive nature, the insensitivity to water, which enables the analysis of aqueous and living samples. Furthermore, the use of different laser sources in the visible spectrum provides a tunable excitation and better resolution than infrared spectroscopy (IR). Hence, RM finds many applications on topics covering environmental science (e.g. MP, aerosols), geology, art & archaeology (e.g. pigments), medicine (analysis of biomolecules, bacteria, cells, tissue, ...), process analysis (e.g. electronics, catalysis, nuclear industry), pharmaceutics, or forensics[2,3].

The following chapter introduces fundamental aspects of Raman spectroscopy. These fundamentals and a more in-depth and elaborated view of the matter can be found in the excellent books by Schrader[4], McCreery[5], Ferraro et al.[6], Smith & Dent[3], or Popp & Mayerhöfer[2].

2.1.1 Theory

2.1.1.1 Vibration

IR and Raman spectroscopy are vibrational spectroscopies, which excite molecular vibrations. These are directly connected to the specific structure of the molecule and characteristic functional groups. A basic model can be developed from Hooke's law, which describes vibrations by the force of replacement $F = -k \cdot x$, where k is the force constant of the bond and x is the displacement from an equilibrium position. With $F = m \cdot a$ it can be resolved to

$$\nu = \frac{1}{2\pi}\sqrt{\frac{k}{\mu}} \tag{2.1.1}$$

wherein

$$\mu = \frac{m_1 \cdot m_2}{m_1 + m_2} \tag{2.1.2}$$

is the reduced mass, m_1, m_2 are the masses of the bonded atoms and ν is the frequency of the vibration. Vibrational frequencies ν can be converted to wavenumbers $\tilde{\nu}$ and wavelengths λ by the correlation $\tilde{\nu} = \frac{\nu}{c} = \frac{1}{\lambda}$ and c, the speed of light. The energy E of this system is approximated in quantum mechanics by the harmonic oscillator

$$E = h\nu(v + \frac{1}{2}) \tag{2.1.3}$$

where h is Planck's constant and v is the quantum number. To better include the inequivalency of the transition energies and the border cases of dissociation and incompressibility for small displacement, it is modelled by an anharmonic oscillator:

$$E = hc\omega_e(v + \frac{1}{2}) + hc\chi_e\omega_e(v + \frac{1}{2})^2 + \dots \tag{2.1.4}$$

where ω_e is the wavenumber corrected for anharmonicity, and $\chi_e\omega_e$ indicates the magnitude of anharmonicity.

Since energy levels in the harmonic oscillator are equidistant, the selection rule is $\Delta v = \pm 1$ resulting in only basic vibrations. For the anharmonic oscillator, it is $\Delta v = \pm 1, \pm 2, \pm 3, \dots$, which also allows for overtones. Further, the selection rules for IR and Raman spectroscopy imply that the vibration has to change the dipole or the polarizability, respectively.

The population of the energy levels is described by the Maxwell-Boltzmann distribution, from which the ratio of two levels can be written as

$$\frac{P_{v=1}}{P_{v=0}} = e^{\frac{-\Delta E}{kT}} \tag{2.1.5}$$

where $-\Delta E$ is the energy difference between the two states, k is Boltzmann's constant, and T is the absolute temperature. This ratio determines the intensities of different transitions in Raman spectroscopy (Stokes and Anti-Stokes bands, respectively, see below).

Vibrations transiently change the structure of the molecule, hence, the symmetry of the molecule determines – and allows to predict – the normal modes of molecular vibrations. Furthermore, the symmetry of any normal mode determines if it is strong or weak in IR or Raman, respectively. For molecules with an inversion symmetry, there even is the rule of mutual exclusion, stating that modes are either IR or Raman active. The vibrational modes appear in different types (e.g. stretching, in-plane and out-of-plane bending, skeleton vibrations) and can be attributed to complete molecules (fingerprint, < 1500 cm^{-1}) or functional groups (e.g. carboxylic acid, or phenyl group)[4,6].

The fact that functional groups tend to vibrate (almost) independently of the rest of the molecules in what is known as group vibrations is vital for the interpretation of the spectra of polymers. Since, polymers typically consists of many thousands of atoms and (non-linear) molecules have 3N-6 normal modes, it would be impossible to analyze the spectrum of a polymer. However, due to the fact that polymers

consist of repeating units, this complexity is reduce to a manageable spectrum. Thus, the spectrum is dominated by vibrations of repeating units, which absorb/scatter in phase[7].

2.1.1.2 Raman Spectroscopy

Vibrational spectroscopy is mainly performed in two variants: infrared spectroscopy (IR) and Raman spectroscopy[a]. These two are considered to be complementary as they excite different vibrations, depending on their symmetry. Different instrumental approaches are pursued to excite and measure the respective vibrational spectra. IR is based on the irradiation of molecules with light of the same wavelength as the vibrational transitions (Figure 2.1, left). The spectrum is recorded by the absorption of these wavelengths from the light source. In contrast, Raman spectroscopy utilizes the inelastic scattering of visible light so that vibrational spectra are acquired as the difference of the incoming wavelength and the scattered light, which is red/blue-shifted by the transition of the molecular vibrations. This effect was first discovered by Sir Chandrasekhra Venkata Raman in 1928[9].

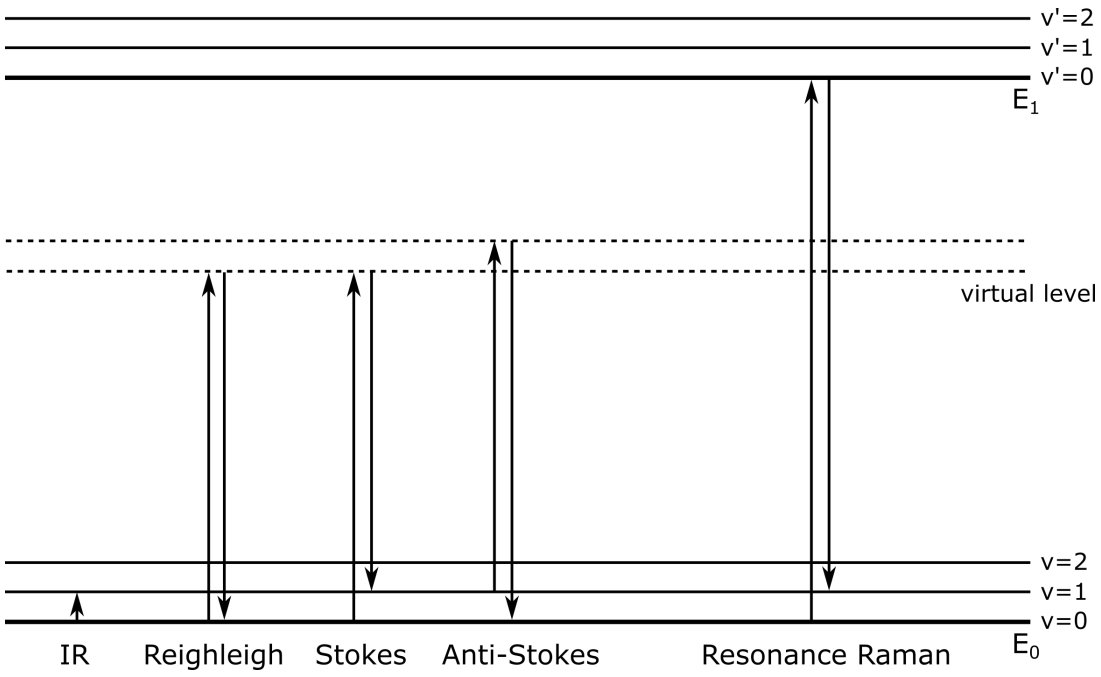

Fig. 2.1: Energy diagram (arbitrary y-axis scale) illustrating the transitions for IR absorption, Raman Scattering in the form of Rayleigh, Stokes & Anti-Stokes and Resonance Raman.

For the scattering effects, the system can be treated as if it interacted with a virtual energy level to which it is excited (Figure 2.1). In elastic, Rayleigh, scattering, the excited state on the virtual level relaxes to the ground state and emits a photon with the same wavelength as the initial photon. In Raman scattering, the system relaxes to an excited vibrational state (e.g. $v = 1$), thus, the emitted photon has a lower energy. The difference equals the energy of the transition of the vibrational states. This form of inelastic

[a] This thesis focuses on IR and Raman spectroscopy. There are more techniques that excite vibrational states, such as photoacoustic spectroscopy, electron energy loss spectroscopy, inelastic electron tunneling spectroscopy, or inelastic neutron scattering[8].

scattering is termed Stokes scattering. It is also possible for the scattering photon to excite a molecule that occupies an excited vibrational state (e.g. $v = 1$) and when the system relaxes to the vibrational ground state (e.g. $v = 0$) , the emitted photon has a higher energy. The difference also equals the energy of the transition. This mode is called Anti-Stokes scattering and since it transitions from excited vibrational states, the ratio of intensity of the Stokes and Anti-Stokes signal can give information on the occupation of the vibrational levels, from which the temperature of the system can be calculated (equation 2.1.5). If the incident laser wavelength matches with the energy of electronic transitions of a molecule in the sample, Resonance Raman occurs, which gives a much stronger Raman signal[6].

The intensity of the two spectroscopies correlate with the concentration of the sample, hence, they can be used for quantification. Here, IR spectroscopy follows the Lambert-Beer law

$$A = log\frac{I}{I_0} = \epsilon cd \tag{2.1.6}$$

where, I_0 and I denote the intensities of the incident and transmitted beams, respectively, ϵ is the molecular absorption coefficient, c is the concentration of the sample and d is the cell length. It has to be noted that the Lambert-Beer law loses linearity for high concentrations c. Contrary to this exponential correlation, Raman spectroscopy follows a linear correlation with regard to the concentration c:

$$I = K(\nu) \cdot A(\nu) \cdot \nu^4 \cdot I_0 \cdot J(\nu) \cdot c \tag{2.1.7}$$

where $K(\nu)$ describes the overall spectrometer response, $A(\nu)$ is the self-absorption of the medium, ν is the frequency of the scattered radiation, I_0 is the intensity of the incident radiation, $J(\nu)$ is a molar scattering parameter, and c is the concentration of the sample. From this equation, it can be seen that also the wavelength of the laser has a critical impact on the signal intensities. This is especially relevant when utilizing infrared-lasers (see Section 2.1.2)[6].

2.1.2 Instrumentation

RM is the combination of Raman spectroscopy with an optical microscope, which enables spatially resolved chemical analysis of various samples. Most RM instruments comprise the following main components[2,10,11]:

1. Excitation source, i.e. laser
2. Microscope unit, which also acquires optical images
3. Filter that removes Rayleigh scattering and stray light
4. Spectrograph that disperses light on a grating
5. Detector, i.e. CCD camera
6. Control/processing unit, i.e. computer

Figure 2.2 shows the general setup of a RM, in which the sample is optically imaged by the microscope and also irradiated with the excitation laser. This setup collects backscattered photons through the microscope objective. Raman scattering passes through a filter, which eliminates the excitation wavelengths and enters the spectrometer, in which it is diffracted on a grating with different densities of lines for the respective resolution. Thus, the light is split by wavelength and is detected on a charge-coupled device (CCD).

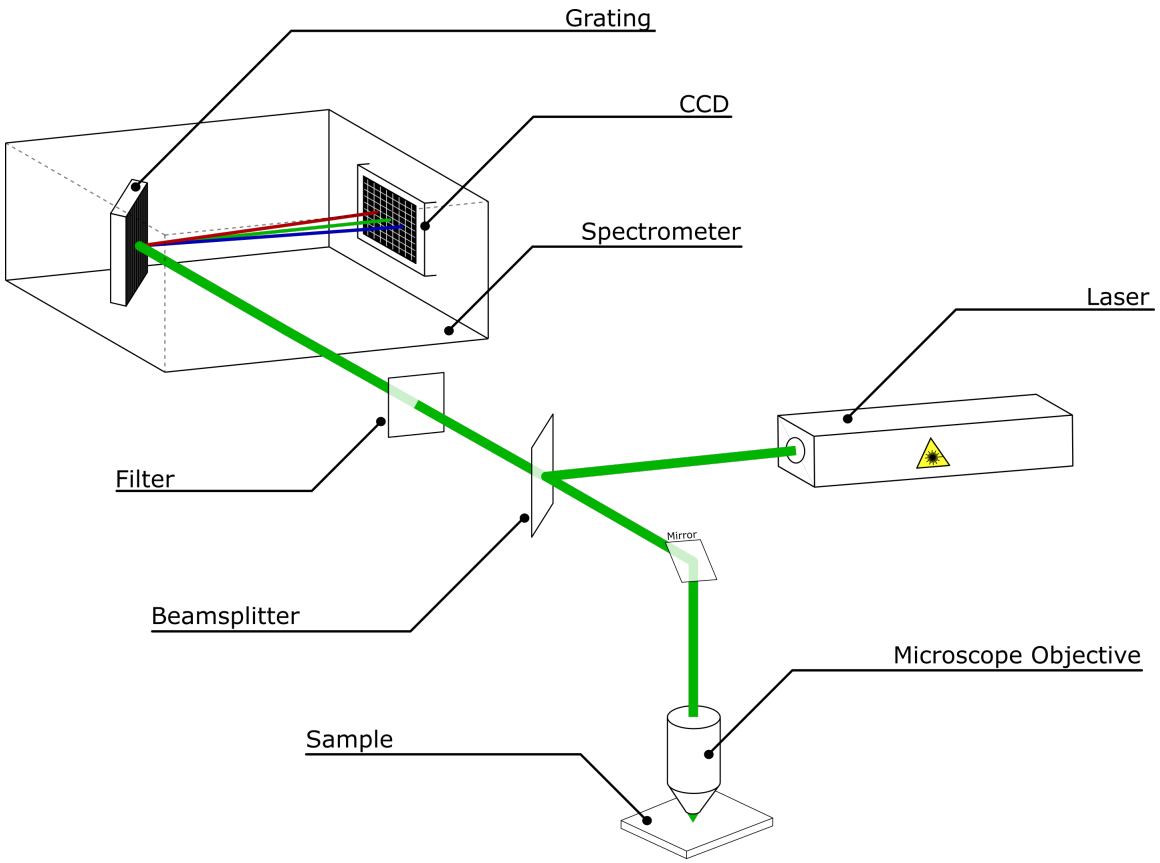

Fig. 2.2: Schematic setup of a Raman microspectroscope. A laser provides the excitation irradiation, which is directed via beamsplitter and through a microscope onto the sample. Raman backscattering is collected by the microscope objective and guided through the beamsplitter and filter into the spectrometer. There, it is diffracted on a grating, which disperses the wavelengths onto a CCD detector.

Laser Since their implementation almost 50 years ago, lasers have been the basis for the broad application of Raman spectroscopy, as they provide the required light intensity to off-set the low yield of the Raman scattering. Today, very efficient lasers are available and many wavelengths can be applied for analysis. Longer wavelengths (e.g. 785 nm) suffer from reduced intensities, as they correlate with ν^4 (equation 2.1.7). However, they can enable the analysis in samples, which would fluoresce, if analyzed with visible light lasers (e.g. 532 nm). UV lasers also circumvent fluorescence and their smaller wavelength can increase spatial resolution (see Section 2.1.3), however their instrumental implementation requires special care (e.g. special mirrors).

Filter Since the Raman scattering is much weaker than the elastic scattering ($\sim 10^{-6}$), this Rayleigh scattering would obstruct the Raman signal. Thus, a filter needs to be used, which blocks the wavelength of the excitation laser. Mainly, two types are utilized: Edge filters are long pass optical filters, which transmit all wavelengths above a certain cut-off (e.g. 534 nm for 532 nm excitation). Second, notch filters only reject a sharp line (the excitation wavelength). Thus, notch filters allow the acquisition of Anti-Stokes bands.

Microscope In RM, Raman spectroscopy is integrated in a microscope. Here, regular and inverted microscopes are used and can be operated in reflectance or transmission mode. Further, optical components such as darkfield, polarized light, or fluorescence excitation can be added as well. There are also many different objectives for specific tasks, which have different magnifications, numerical apertures (N.A.), or specific characteristics, such as water immersion or coverslip correction. Thus, a versatile visualization is available. Raman microscopes are typically confocal microscopes, in which a pinhole eliminates light from other planes than the focal plane. This improves the axial resolution (the lateral resolution is also improved to a minor degree), which enables precise 2D and 3D mapping of samples. The size of the pinhole opening determines the axial resolution and the signal intensity. A large pinhole decreases resolution but gives a stronger signal[10,12,13].

Spectrometer The spectrometer analyzes the Raman scattering by wavelength. In it, the grating is the central component, diffracting light depending on its wavelength λ (and angle). Thus, a transposition of spectral into spatial information takes place. This spatial information is then detected by a CCD camera. The diffraction on the grating follows the grating formula

$$\sin\alpha + \sin\beta = k \cdot n \cdot \lambda \tag{2.1.8}$$

where α is the incoming angle, β the output angle, k the order of diffraction, and n the line (groove) density, in grooves/mm (mm^{-1}). Most commonly, the first order of diffraction (k = 1) is taken into account.

There are different line densities available (e.g. 300 mm^{-1} – 1800 mm^{-1}), where more grooves per mm result in a higher spectral resolution. With high line density or longer path-length, the spectral region becomes rather large. Hence, the spectrum has to be acquired in several windows (intervals of the observed wavenumber region). To achieve this, the grating can be rotated.

Detector Detection in a RM system is performed on a CCD camera chip (*charge coupled device*) due to the fact that CCDs are already optimized for use in the visible range (as well as UV and near IR). CCDs are arrays of pixels, which generate charge depending on the incoming light intensity. Furthermore, Electron Multiplying CCDs (EM-CCD) can be used to improve signal intensity due to low Raman scattering. This leads to faster integration, which is especially useful for imaging.

2.1.3 Lateral & Axial Resolution

When aiming at analyzing subµ- and nanoplastic by RM, the limiting factor for the smallest particle size is the optical resolution of the microscope, since it determines which single particles can be targeted by the Raman laser. This resolution is determined by the diffraction limit.

The lateral resolution is determined by the laser spot size, which, in turn, depends on the wavelength λ and the characteristics of the instrument, i.e. the numerical aperture $N.A.$. The size is approximated by an airy disc, whose diameter is $d_{\mathrm{Laser}} = \frac{1.22\lambda}{N.A.}$. For example, with a green laser of $\lambda = 532\,\mathrm{nm}$ and a 100 $\times$ magnification objective with a numerical aperture of $N.A. = 0.9$ the laser spot size is $d_{\mathrm{Laser}} = 0.72\,\mu\mathrm{m}$. The actual spot size, of course, deviates from the theoretical one due to imperfections in the setup and can be experimentally analyzed by a line scan across the sharp border of a test material (e.g. silicon)[14].

Aside the laser spot size, it is obvious that the criterion of when two (infinitesimal) points can be discerned influences the resolution. Figure 2.3 shows some examples for such criteria. The Rayleigh criterion puts the resolution at half the laser diameter ($r_{\mathrm{Rayleigh}} = \frac{0.61\lambda}{N.A.}$). The 80 %-criterion demands that the intensity between the two points is less than 80 % of the maximum ($r_{80\,\%} = \frac{0.42\lambda}{N.A.}$). Finally, the Sparrow criterion only requires that the first and second derivative of the intensity of the combined peak is zero ($r_{\mathrm{Sparrow}} = \frac{0.33\lambda}{N.A.}$). The resulting resolutions for the above mentioned example setup ($\lambda = 532\,\mathrm{nm}$, $N.A. = 0.9$) would then equate to $r_{\mathrm{Rayleigh}} = 0.31\,\mu\mathrm{m}$, $r_{80\,\%} = 0.25\,\mu\mathrm{m}$ and $r_{\mathrm{Sparrow}} = 0.20\,\mu\mathrm{m}$, respectively.

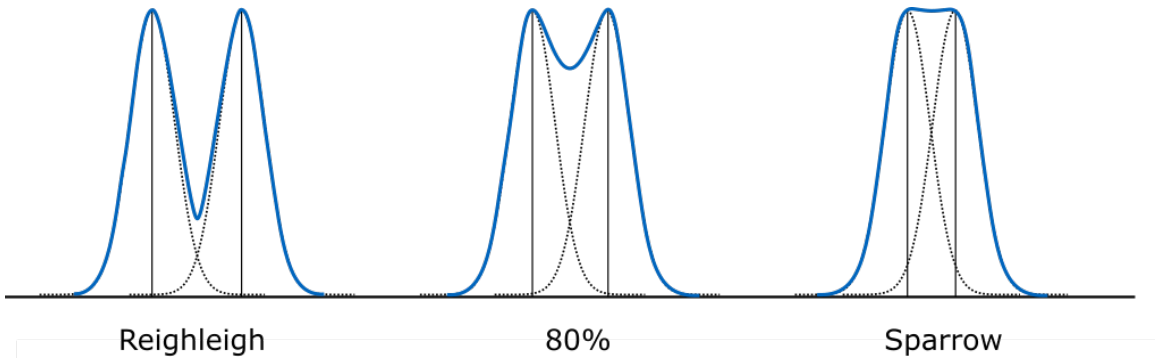

Fig. 2.3: Different resolution criteria for optical diffraction. Two infinitesimal points can be discerned by the (a) Rayleigh criterion, (b) 80 %-criterion, (c) Sparrow criterion.

Although the lateral resolution is most important in this thesis, the axial resolution also plays an important role. This is, again, determined by the airy approximation, where the sampling depth is $d_{\mathrm{axial}} = \frac{4n\lambda}{N.A.}$, where n is the refractive index of the sample. This axial resolution is most improved by the confocal pinhole, which eliminates out-of-plane scattering[2,12–14].

2.1.4 Raman Tweezers

During the treatment of particles in the low micrometer and nanometer range, the optical tweezer effect can occur. This effect was first published in 1970 by Arthur Ashkin[15] and describes the radiation pressure on micrometer-sized particles. In other terms, a force is exerted on microscopic objects due to the momentum transfer of photons onto the particles in a highly focused laser beam. The focussing is usually achieved by a microscope objective of a high numerical aperture.

In this setup the particle is subject to two forces caused by the light. On the one hand, there is the scattering force $F_{scatter}$, which propels the particle in the direction of light propagation and is a result of the forward momentum of the photons. Second, the optical gradient force F_{grad} directs the particles towards the point of highest light intensity. Thus, for a laser spot with a Gaussian intensity profile, the force is directed to the center of the focal point. The force is dependent on the gradient of the intensity, thus a high numerical aperture objective is necessary. In the case that the gradient force is larger than the scattering force, the particle will be pulled into the focal volume of the beam[16], thus, creating a stable 3D trap (single-beam gradient force optical trap). This application is called „optical tweezers“ following its first report by Ashkin in 1986[17].

There are different approaches to describe and model the gradient force. Each applies in one of three regimes, depending on the size ratio of the particle d and the laser wavelength λ. If $d \gg \lambda$, the ray optics approximation can be used, in which the force is modelled by a series of reflections on the particle (inner/outer) surface[18]. When $d \ll \lambda$, the particles are considered as point dipole, which interacts with the electric field of the light (dipole approximation)[19]. However, when the particle size is in the same order of magnitude as the wavelength of the laser ($d \sim \lambda$), those models are not sufficient. In this case, the precise interaction of the electromagnetic wave with the particle has to be considered[20].

The possibility of manipulating microscopic objects brought forward a plethora of applications for optical tweezers ranging from nanoparticles, proteins, biophysics, to microorganisms or cells[20–22]. Moreover, since RM and optical tweezers both utilize visible lasers and a microscope objective, it is possible to collect a Raman spectrum from trapped particles, which is then called Raman Tweezers. This too has found a variety of applications, such as spectroscopy of nanoparticles[23] or blood cells[24]. It has been used in an even more elaborate way, when trapped cells are identified by Raman spectroscopy and then pushed into different eluent streams, thus causing a separation (Raman activated cell sorting)[25].

2.2 Scanning Electron Microscopy

Electron microscopy (EM) images samples by their interaction with electrons rather than with photons as in optical microscopy. Thereby, several differences arise. Primarily the resolution is much higher, as it is no longer bound to the wavelength of visible light. Here we focus on scanning electron microscopy (SEM) instead of the other popular variant, transmission electron microscopy (TEM). The attainable resolutions are in the range of 2 – 5 nm for SEM and 0.1 nm for TEM. In this work, SEM will complement the Raman microscopic analysis, as it can provide a much better resolution and illustrate many otherwise unobtainable, morphological details. This chapter will discuss the basic principles and instrumentation of SEM. The fundamentals and a deeper elaboration of the matter can be found in the textbooks by Michler[26], Zhou et al.[27], Ul Hamid[28], and Goldstein et al.[29].

2.2.1 Principle of SEM

In SEM, the imaging is performed by scanning an electron beam over the sample surface (as opposed to transmitting the beam through a thinly sliced sample in TEM). This scanning of the sample causes a variety of interactions of the electrons, which give different emissions. Figure 2.4 illustrates some of them. The various emissions can be collected by their respective detectors (Section 2.2.2.3). It has also to be noted that the electron beam focus diameter is in the size range of nanometers, whereas the interacting electrons penetrate into a bulb-like volume with dimensions in the micrometer-range, which constitutes the critical factor for lateral resolution.

Secondary electrons (SE) are caused by the interaction of the primary beam with the electron cloud of the atoms of the sample, where electrons from the outer shells are ejected. These electrons have lower energies than the incident beam and typically are generated in regions close to the sample surface. Moreover, SEs can have different sources. If they result from the primary beam at the point of incidence, they are called SE_1. It is also possible that backscattering electrons, which have spread in the sample, cause a SE to emit, which is then called SE_2 and consequently results in worse resolution. Finally, SEs can occur by the interaction of BSEs with the walls of the SEM sample chamber. These are SE_3 and occur as noise.

Backscattered electrons (BSE) are elastically scattered electrons of the primary beam that penetrate into the sample and are directed out through the surface again, usually by interacting with multiple atoms. Therefore, they typically emit from deeper regions of the sample, which implies that they do not necessarily re-emit from the incident point of the primary beam. BSEs are defined by their energy, which has to be larger than 50 eV. The backscattering efficiency correlates with the square of the atomic number effecting that heavier metals in the sample give brighter signal.

X-ray emission can occur when the primary electrons knock out electrons from the atom shell, which then constitutes an exited ionic state of the atom (cation). When this state relaxes, characteristic radiation is emitted. If the missing electrons come from the inner shell, the resulting high-energy photons are X-rays,

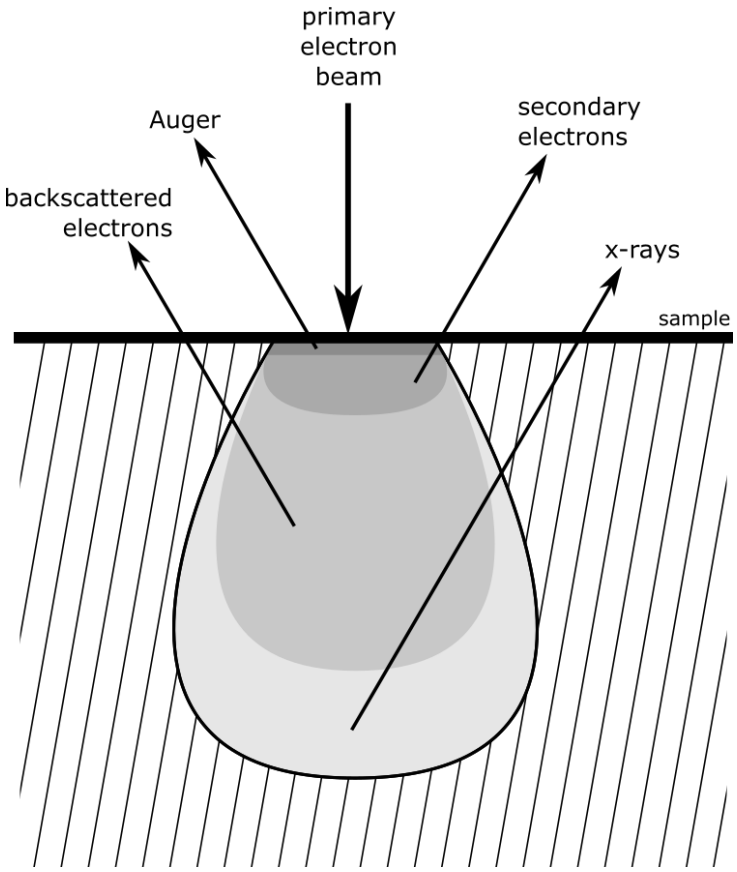

Fig. 2.4: Sample interaction volume and selected emissions by electron irradiation in electron microscopy. The primary electron beam meets the sample at the incident spot and penetrates into the matter, where the different interactions occur at different depths.

which can be used to perform elemental analysis on the sample. If an outer shell electron is knocked out, the photon is in the visible range, this is then called cathodoluminescence. Another effect to note is the emission of an Auger electron, which is ejected instead of a photon carrying the transition energy[26,28].

The resolution of a SEM depends on both the spot of the focussed electron beam and on the penetration depth. The minimal diameter d_0 of the spot can be approximated by[26]

$$d_0 = \left(\frac{4 \cdot I_0}{\pi^2 \cdot R} \right)^{\frac{1}{2}} \cdot \frac{1}{\alpha_0} \tag{2.2.1}$$

where I_0 is the beam current, R is the gun brightness, and α_0 is the aperture angle. This implies that smaller currents or a larger brightness R gives better resolution. The gun brightness includes the diameter of the beam output of the gun and the scale of the demagnification by the condenser lenses. Thus, the type of the cathode plays a critical role (see Section 2.2.2.1).

The penetration depth depends on the electron energy and the atomic number of the sample material and effects the range of the electron interaction in/with the sample. This, in turn determines the visual information, i.e. a high penetration depth provides information on the inner parts of the specimen at the cost of the surface structure (see Figure 2.4).

2.2.2 Instrumentation

This and the next section will give a brief survey of the general setup of a SEM and its detectors. The electron source and optics are within the so called electron column, detectors and sample are placed in the sample chamber. Both are connected to a (in some cases, two) vacuum system.

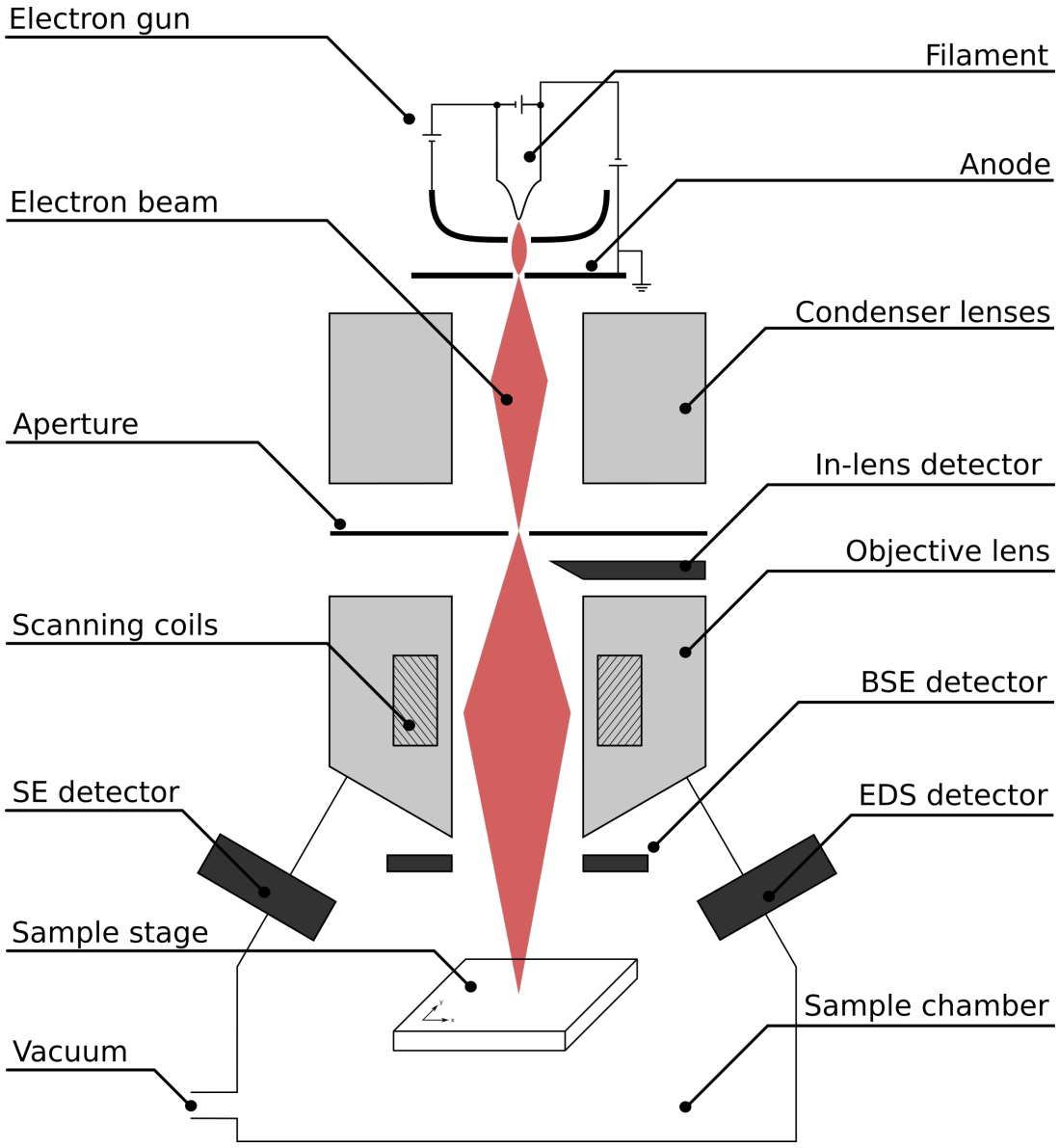

Fig. 2.5: Schematic setup of a SEM comprising the column including electron gun and electron optics, sample chamber and detectors (SE: secondary electron; BSE: backscattered electron; EDS: energy dispersive spectroscopy)

2.2.2.1 Electron Gun

The electron gun is the source of the electron beam. Here electrons are emitted from a cathode and accelerated towards an anode. The potential pulling out the electrons (in SEM up to ca. 30 kV) that is applied to the wire is called *bias voltage*. The size of the electron emitter tip determines the beam size

at the anode, also called the crossover-point. Over time, the guns have been improved, as the older thermionic W-filament is a simple bent fiber, whereas the more modern FE guns are microscopically sharp tips, with a source radius of only $\sim 0.1 - 1$ µm.

There are two types of guns: thermionic or field emission (FE). Thermionic electron guns (W-filament & LaB_6) are heated electrically to high temperatures (> 2000 °C) so that electrons are excited enough to leave the metal and can be accelerated by an anode. FE guns use the tunneling effect, which occurs at the extremely fine tips, where the local electric field becomes very strong. In Schottky emitters the effect of the strong local field and a ZrO-coating on a W single crystal is combined with a medium temperature ($\sim$ 1500 °C), which is in itself too low for electron emission. Cold field emission guns, on the other hand, are entirely based on the tunneling effect at the tip and work at room temperature[26,28].

2.2.2.2 Electron Optics

In SEM, the electron beam from the gun has to be demagnified so that a narrow spot is formed on the sample for appropriately high resolution (see Figure 2.5). This is achieved by the use of electron optics, i.e. electromagnetic lenses. These have an impact on the electron beam by a magnetic field, which can be varied in strength by the electric current. Electromagnetic lenses are composed of a copper coil in a circular iron casing, through the center of which the electron beam runs. The magnetic field is located in the center bore. Here, the perpendicular components of the magnetic field deflect the off-axis electrons towards the beam direction (helically), effecting the electron beam to be (mostly) collimated.

The general setup (Figure 2.5) of the SEM comprises condenser lenses, an objective lens, an aperture, scanning coils, and aberration correction (specific fine improvements are omitted for brevity). Here, the reader is, again, referred to the literature[26–29]. Condenser lenses reduce (i.e. demagnify) the beam diameter in a way comparable to optical lenses. The objective lens is the last lens before the sample, which focusses the beam and has a different geometry to accommodate the sample below. The required demagnification depends on the beam diameter provided by the gun. Thermionic guns produce a wider beam, which usually requires three condenser lenses. The smaller beam from FE guns usually only needs two. The beam passes an aperture, which has small holes of different diameter ($\sim 5 - 500$ µm) to reduce lens effects (e.g. spherical aberration) and to control the spot size and beam current. Scanning coils deflect the beam in the *xy*-direction to scan over the imaged area of the sample.

For appropriate focussing, some aberrations have to be accounted for. Spherical aberration occurs due to a radially inhomogeneous magnetic field in the lens, which focusses the beam in a disk rather than a in point. It can be controlled by a small aperture after the objective lens, which blocks off-axis electrons that would form the disc. Chromatic aberration is caused by fluctuations in the acceleration voltage, i.e. electron velocities and is a critical factor when working with small acceleration voltages. Astigmatism is the result of an inhomogeneous field in the lenses due to instrument imperfections or contamination and causes the focus to split along two axes. Thus, the image is distorted in one direction and moves to a perpendicular direction, when the focus is changed. It is corrected by a stigmator, which is directly placed in the objective lens and is able to apply a field on specific segments[26,28].

2.2.2.3 Detectors

Connected to the bottom of the column is the sample chamber, in which the sample is placed and the different detectors are located. These detectors are each suited to collect specific emissions from the interaction of the primary electron beam and the sample.

The most common type of detector for SEs is the Everhardt-Thornley (ET) detector, a scintillator-photomultiplier. Here, the scintillator is placed close to the sample to collect electrons at an angle of ~ 30 °. The entrance is shielded by a Faraday cage onto which a voltage is applied. A positive voltage (+250 V) pulls in SEs and a negative voltage (-50 V) deflects SEs so that only BSEs are collected. However, common SEMs have dedicated BSE detectors. It has to be noted that at positive voltages, the image contains influences of both SEs and BSEs. Finally, photons from the scintillator are guided into the photomultiplier tube, which amplifies the signal. From there on, the data is processed and the image is generated.

Since the ET detector collects direct SEs from the sample but also BSEs and indirect SEs from the interaction of BSE with distant spots on the sample (SE_2) or the instrument itself (SE_3), the resolution of the image is degraded. This can be prevented by the use of *in-lens* SE detectors, which are placed in the column, above the objective lens. They allow that the sample can be placed very close to the exit of the electron beam at the objective lens so that its magnetic field only allows SEs to enter back up in the column. This excludes much of the noise that would be collected on the ET detector and results in a higher resolution and better sensitivity for surface layers[28].

The BSE detector consists of a semiconductor (solid state) diode, which is typically divided into several sub-panels. Those create a current when the high-energy BSEs hit. Scattering probability is highest in the upward direction, thus, the BSE detector has a circular geometry and is placed below the pole piece of the column so that the electron beam passes the center of the detector and low angle BSE are detected[26,28].

Energy dispersive spectroscopy (EDS), alternatively called energy dispersive X-ray spectroscopy (EDX), enables chemical (i.e. elemental) characterization. The primary beam causes X-ray radiation (see Section 2.2.1), which can be either characteristic radiation originating from the transition of electronic levels or continuous radiation, resulting from the deceleration of the primary beam. Instrumentally, the EDS detector is moved close to the sample and collects X-rays through a collimator and an electron trap, which eliminate stray X-rays and electrons, respectively. Then, the radiation passes a beryllium window and is detected on a semiconductor (usually, Li-doped silicon or Si drift detectors), on which the photon generates a specific current that can be correlated to the energy of the X-ray. Finally, the number of incidents can be used to quantify the specific elements in the sample[27–29].

2.2.3 Special Techniques

SEM is a versatile imaging technique, which has become relevant for many disciplines from fundamental research to industry. Thus, it is not surprising that many special techniques were developed to analyze samples with specific requirements, such as biological samples. In this section, a small selection, comprising low vacuum SEM, Cryo-EM, and RISE, will be discussed.

2.2.3.1 Low Vacuum SEM

Low vacuum SEM or environmental SEM (ESEM^{TM}) enables the analysis of samples that would suffer from high vacuum and charging effects, like biological specimens or polymers without coating. Here a gas atmosphere is introduced into the sample chamber, which alleviates pressure of high vacuum and reduces charging due to the ionization of the gas (positive), which equilibrates the negative charge on the sample surface. In low vacuum mode, however, the ET detector can not be applied. Thus, another detector, which is based on cascade ionization by the SEs, is used. Here, the resolution becomes also dependent on the gas pressure since high pressures broaden the primary beam, but on the other hand it increases the intensity of the ion cascade. The operator needs to fine tune the parameters to suit the respective sample[26].

2.2.3.2 Cryogenic SEM

Cryogenic (scanning) electron microscopy (Cryo-SEM) offers the ability to analyze the structure of complex biological or environmental samples, as it is present in the actual system. It also avoids shrinking effects or destruction of e.g. cells. To this end, the sample suspension is deposited on a Cu-C TEM grid, the excess is wiped off and the sample is then plunged into liquid ethane. This coolant is chosen, as it has a high heat capacity and its thermal conductivity is much larger than liquid nitrogen (ethane: $\sim$ 15000 K/s, N_2: 500 K/s). Thus, sufficiently fast cooling is provided (> 10^5K/s). This step is performed on specific plungers, which comprise a weighted rod, onto which the TEM grid is fixed, and then dropped into the coolant. This fast cooling is essential to ensure that the water in the sample vitrifies to amorphous ice rather than crystallizing. Thus, no expansion takes place and damage to e.g. cells is prevented. Afterwards, the grid is transferred to liquid nitrogen for storage and subsequently inserted to the SEM sample chamber on a cooled sample stage. Here, ice can be sublimated by a controlled temperature increase. SEM imaging can be performed as usual[30–33].

2.2.3.3 Correlated Raman Imaging and Scanning Electron Microscopy

The combination of Raman and SEM gives detailed information on a multitude of samples by providing high resolution visualization by SEM and structural information by vibration spectroscopy and even the potential for elemental analysis by EDS. An integrated solution has been developed, which avoids the

necessity of transporting the sample between instruments. This technique is termed Raman imaging and scanning electron microscopy, RISE microscopy. There are two possibilities to realize this coupling: (i) by precise movement of the SEM stage to the microscopy objective, which is placed in the chamber, next to the other detectors, or (ii) by utilizing a mirror that focusses the laser onto the sample under the pole piece. For this application, the RM instrumentation has to be functional in vacuum[34,35].

2.3 Field-flow Fractionation

Among separation techniques, field-flow fractionation (FFF) appears as prevalent technique for particle separation, as it does not require a stationary phase. Thus, no principal size restrictions are imposed on the analyte, which enables size ranges of e.g. 1 nm – 10 µm for asymmetric-flow field-flow fractionation (AF4) or 10 nm – 20 µm for centrifugal field-flow fractionation (CF3)[36]. This qualifies this method for the analysis of very small MP and nanoplastic[37], for which there are, otherwise, not many alternatives to tackle this entire size range. Thus, this section will briefly lay out the fundamentals of FFF, which will be relevant for the studies of this thesis. More elaborate treatments can be found in the following sources[36,38–40].

2.3.1 Theory

The general setup of FFF (Figure 2.6) comprises a flow channel with a flat geometry, in which a carrier fluid passes longitudinally with a flow rate that guarantees laminar flow. Further, a perpendicular separation force is applied (uniformly) over the channel length, which can be of different nature. These range from popular types such as hydrodynamic (i.e. by a cross-flow, AF4), thermal, or gravity, to more experimental variants like electrical, dielectrophoretic, magnetic, or photophoretic[36,41].

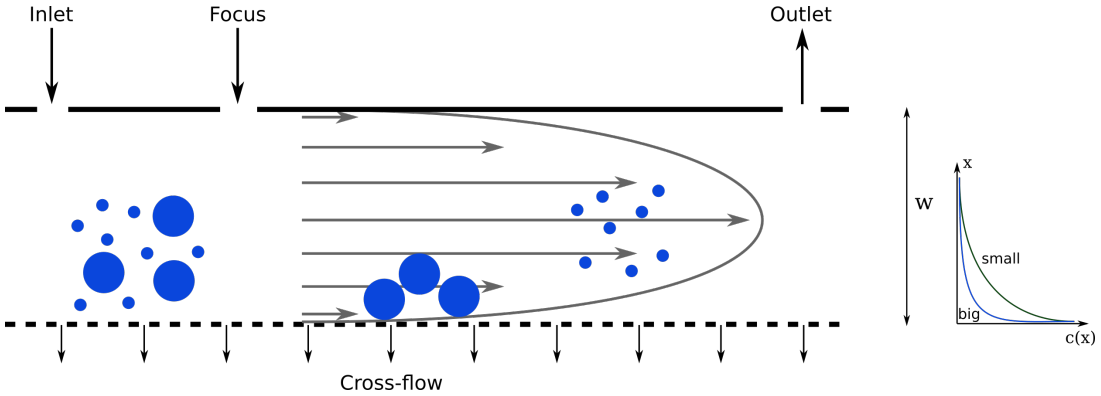

Fig. 2.6: Schematic setup of an AF4. Particles are injected via the inlet and focussed by keeping the particles in place using the focus stream. A pump, which removes solvent through the permeable bottom, the accumulation wall, creates the separation field. Separated particles elute via the outlet. To the right is a schematic plot of the concentration profiles of small and big particles. The small particles have higher concentration to the center of the channel, which causes the separation[42].

A force equilibrium occurs between the separating force U on the particle (e.g. liquid cross-flow) and its diffusivity D (Brownian motion). Due to the parabolic profile of the flow velocities in the laminar

flow, this equilibrium correlates with D and, thus, effects the location of the particles with regard to the accumulation wall according to

$$c(x) = c_0 \cdot e^{-\frac{x}{\lambda^{\mathsf{FFF}} w}} \tag{2.3.1}$$

with c_0 the concentration at the accumulation wall, $c(x)$ the concentration at distance x perpendicular to the accumulation wall, w the channel thickness, and λ^{FFF} the retention parameter. Figure 2.6, on the right, illustrates two schematic concentration profiles for small and large particles. Their resulting equilibrium position determines the retention of the particles, as those less affected by the separating force U are located closer to the center of the stream where the laminar flow has larger flow velocities, which, in turn, elute the particles faster. Thus, a spatial dependency of the particle properties is transformed into a temporal one.

The correlating retention parameter expresses the force equilibrium by

$$\lambda^{\mathsf{FFF}} = \frac{D}{U \cdot w} \tag{2.3.2}$$

which takes different forms, depending on the type of FFF. For asymmetric flow FFF (AF4)[36], centrifugal FFF (CF3)[43], and thermal FFF (ThF3)[36], these are, respectively:

$$\lambda^{\mathsf{AF4}} = \frac{D \cdot V^0}{V_c \cdot w^2} \tag{2.3.3}$$

$$\lambda^{\mathsf{CF3}} = \frac{kT}{m_{eff} G w} \tag{2.3.4}$$

$$\lambda^{\mathsf{ThF3}} = \frac{D}{D_T \frac{dT}{dx} w} \tag{2.3.5}$$

where V_c is the cross-flow velocity, V^0 is the volume of the channel (i.e. void volume), k is Boltzmann's constant, T the temperature, $m_{eff} = m\frac{\Delta\rho}{\rho_s}$, with m the particle mass, ρ_s the particle density, $\Delta\rho$ the difference between particle density and carrier density, further, $G = \omega^2 r$ is the centrifugal acceleration, with ω the angular velocity of the rotor and r its radius. D_T is the thermal diffusion coefficient, $\frac{D_T}{D}$ is the Soret coefficient, and $\frac{dT}{dx}$ is the Temperature gradient. From these, the hydrodynamic diameter d_H for AF4, mass and density, m and ρ for CF3, and the Soret coefficient $\frac{D_T}{D}$ for ThF3, can be calculated.

The retention parameter λ^{FFF} is obtained in the experiment from the observable retention ratio

$$R = \frac{V^0}{V^r} = \frac{t^0}{t^r} \tag{2.3.6}$$

where V^0 is the void volume, V^r the solvent volume that eluted until the analyte exits the channel, t^0 is the void time (i.e. elution time of unretained particle), t^r is the retention time of the analyte. This ratio R correlates to λ^{FFF} by

$$R = 6\lambda^{\mathsf{FFF}} \left(\coth \frac{1}{2\lambda^{\mathsf{FFF}}} - 2\lambda^{\mathsf{FFF}} \right) \tag{2.3.7}$$

which can be approximated by $R = 6\lambda^{\mathsf{FFF}}$ for sufficiently strong retention ($V^r > 6V^0$) and spherical particles. Thus, the separation experiment can be related to the characteristic properties of the analyte.

E.g. in AF4, the diffusivity D is obtained, which can be converted to the hydrodynamic diameter of the particles by the Stokes-Einstein equation

$$d_H = \frac{kT}{3\pi\eta D} \tag{2.3.8}$$

where η is the viscosity of the solvent[38,39,44,45].

2.3.2 Working Principle

The working principle of FFF will be discussed on the example of AF4, as the general process bears sufficient commonalities. Differences to CF3 will be noted in Section 2.3.2.2

2.3.2.1 Asymmetrical-Flow Field-Flow Fractionation

Commercial FFF instruments are equipped with a solvent supply and degasser, eliminating dissolved gases and bubbles, which would be detrimental to the operation of the separation. The carrier fluid is transported by HPLC pumps into the separation channel by the inlet port (see Figure 2.6), through which the sample suspension is injected as well. This can be done either by manual injection into a valve or by an autosampler.

The AF4 channel has a trapezoidal shape, which gets narrower towards the outlet, and its height is determined (and varied) by spacers with heights available in the range of 100 µm – 500 µm. The bottom of the channel (accumulation wall) is delimited by a porous ceramic frit, onto which a nanofiltration membrane is placed, allowing the passage of solvent and dissolved (small) molecules but retains particulate matter. The flow through the bottom membrane is called cross-flow and is usually performed by syringe pumps, which enable a precise and constant flow.

An experiment has different phases. First, a focus step, in which the sample is injected, while a second flow of carrier solvent, which enters through another port, several centimeters down-stream of the inlet, counteracts the injection stream. This results in the particles retaining their position, while excess solvent is removed by the cross-flow through the membrane. Hence, the sample is collected at the beginning of the channel. The actual position of the particle cloud along the channel depends on the specific flow rates of the individual pumps.

In the second step, the relaxation step, the whole sample is now in the channel, but the focus flow is left active, so the particles still don't elute. Now, equilibration of the forces can take place and each particle type is located at its respective x position. If this phase is kept too short, the separation is not optimal and larger amounts of sample are lost in the void peak (see below).

Finally, in the elution step, the focus flow is stopped and the elution takes place at a constant carrier flow. During this step, the cross-flow is set to a predefined flow-rate profile, which has to be optimized for the individual sample. Typically, the cross-flow is either set to a constant value, a linear, or an exponential

decay. Ergo, in the process of elution, first, a void peak will occur, which contains dissolved small ions and sample that has not achieved equilibrium. Then, particles will pass the channel in the order from small to large. This order is present in normal mode elution, which is valid for particles smaller than $\sim$ 1 µm (the actual transition depends on the sample and the flow rates). Larger particles are subject to steric mode elution. Here, they are sufficiently large to be affected by the force field in a way that they are in contact with the accumulation wall. Hence, larger particles reach further in the channel, where they experience higher flow velocities. This effects an inverse order of elution, where large particles elute first[36,38,39].

The AF4 channel permits two types of preconcentration of the sample. Since the particles are held in the channel during the injection phase by the focus flow, while solvent is removed by the cross-flow, it is possible to inject a larger sample volume and gather all particles in the starting point of elution. This, however, is limited by the amount of particles, since a too high concentration degrades the quality of the fractogram and also generates loss of particles on the membrane[46]. Secondly, the slot-outlet technique enables an enrichment after separation, where at the end of the channel, a portion of the stream is removed by a separate valve (via the overpressure valve). This is based on the principle that particles are located at the accumulation wall at the bottom. Thus, solvent can be pumped from the top without loss of analyte, thereby increasing the detector signal[47].

The separated particle fractions exit the channel by the outlet valve and pass a series of online-coupled detectors for characterization. Details on detectors are given in Section 2.3.3. Finally, the fractions are either discharged in a waste container and the characterization data evaluated, or the fractions can be collected for offline analysis and storage.

2.3.2.2 Centrifugal Field-Flow Fractionation

CF3 follows an analogous principle, where the separation channel is in a centrifuge. Eluent and sample are introduced via a rotational valve at the central axis of the rotor. Since no solvent can be eliminated through the accumulation wall, the injection and relaxation phases differ from AF4. Here, the sample is injected in the rotating channel and the solvent flow is stopped during the relaxation phase. Hence, flow is only switched on for the elution phase again. This has the effect that no preconcentration in the injection step is possible. The separation is caused by the gravitational/centrifugal field, whose intensity is controlled by the rotation speed of the centrifuge. This variant of FFF displays a similar elution order with small particles eluting before larger ones, but also particles with lower density before those with higher density (see Section 2.3.1). Steric inversion occurs analogously to AF4 but might be more relevant, since the size range of CF3 covers larger particles (10 nm – 20 µm)[36].

2.3.3 Detectors

Following the separation, a detection of the particles in the eluent has to take place. For FFF, as for e.g. liquid chromatography or size exclusion chromatography, detectors of different kind are online-coupled

to the separation system, which give the chromatogram/fractogram. There is a wide range of online detectors for FFF, which give a variety of information on the fractions. Coupling (several) detectors to FFF is commonly termed *hyphenation* (e.g. AF4-UV-MALS). The following brief mention of some detectors is by no means exhaustive, but rather aimed at the problems, which are relevant to this thesis. For a detailed list of detector possibilities and ongoing research in coupling techniques, the reader is referred to current reviews[36,42,45].

2.3.3.1 Concentration Detectors

Commercial FFF systems are often equipped with at least one detector that functions as indicator of a passing fraction. Here, the common choice is either a UV detector or a refractive index (RI) detector, which either detects the absorbance of a UV lamp emission or the change in refractive index, respectively. Both detectors exhibit a concentration dependency of the signal[42]. Although UV detectors – as applied in the setup of this thesis – are typically suggested as concentration detector, because the absorbance of UV follows the Lambert-Beer correlation $A = \log \frac{I}{I_0} = \epsilon c d$ (see Section 2.1.1.2). However, this is only applicable in select cases, since the absorption is also affected by diffraction (turbidity) and the wavelength-dependent extinction coefficient, which varies with different samples[38].

2.3.3.2 Size Characterization

One of the major features of hyphenated detectors is the instrumental determination of the particle size, which is commonly performed by light scattering[48]. Size detectors complement the theoretical size calculation from the retention parameter (Section 2.3.1) to account for deviations from the idealized models[38,45]. Here, both dynamic and static light scattering are applied, however, static light scattering, in the form of multi angle light scattering (MALS) is the predominantly applied technique. Dynamic light scattering (DLS) is based on the correlation of light fluctuation to the Brownian motion, from which the hydrodynamic diameter d_H can be derived. MALS, on the other hand, observes the angular profile of the scattering intensity, which depends on the particle size. Via suitable models, this size (i.e. the diameter of gyration d_g, which can be transformed into the geometric diameter by[49] $d_{geo} = d_g/0.775$) can be derived from the signal intensities of a set of detectors at different angles[38].

Ideally, the scattering at a 0° angle needs to be investigated. However, this is experimentally impossible, since a detector can't be placed in this position. Thus, MALS uses many angles, from which the 0° intensity can be extrapolated by a curve fit. This can be derived from the basic light scattering relationship,

$$\frac{R_\theta}{Kc} = M_w \cdot P(\theta) \tag{2.3.9}$$

assuming sufficiently low concentrations, which is reasonable in a FFF fraction[50], where θ is the scattering angle, R_θ is the Rayleigh ratio, K is an optical constant, c is the concentration, M_w is the molecular weight by mass of the polymer, and $P(\theta)$ is the particle scattering function. This function $P(\theta)$ is

approximated by different terms for different systems, such as small particles (ca. < 100 nm, in which they are considered isotropic scatterers), for spheres, or random coils (typically polymer conformation).

Using the simplified approximation[50]

$$P(\theta) = 1 - \left(\frac{16\pi^2}{3\lambda^2}\right) \cdot r_g^2 \cdot \sin^2(\theta/2) \tag{2.3.10}$$

where λ is the wavelength of the incident light source, a combined expression

$$\frac{R_\theta}{Kc} = M_w \cdot \left(1 - \left(\frac{16\pi^2}{3\lambda^2}\right) \cdot r_g^2 \cdot \sin^2(\theta/2)\right) \tag{2.3.11}$$

is achieved, which can be plotted by setting $\sin^2(\theta/2)$ as the x-axis and R_θ/Kc as the y-axis. This plot is called Debye plot and represents a linearization, in which the intercept equals M_w and the slope $-16\pi^2 M_w r_g^2/3\lambda^2$, from which d_g is received. There are different possibilities to plot the MALS data aside the Debye plot, such as the Zimm or Berry plot, which plot the inverse of equation 2.3.11 or the square root of the inverse, respectively. These different plots aim to provide a more accurate representation for different types of particles. E.g. the Debye plot works well for spheres, whereas the Zimm plot is recommended for small particles (< 40 nm), or the Berry plot for random coils[50]. Ultimately, evaluating the MALS data requires the fine-tuning of the modelling and extrapolation, which includes the careful selection of the angles to include in the evaluation.

2.3.3.3 Further Detection Methods

As stated above, FFF detection is a multi-method approach, hence, there is a wide choice in characterization methods exceeding the ones mentioned here. Of especial note is the elemental analysis by techniques like inductively-coupled plasma mass-spectrometry (ICP-MS), inductively-coupled plasma optical emission spectroscopy (ICP-OES), or graphite furnace atom absorption spectroscopy (GF-AAS)[38]. Of those elemental techniques, ICP-MS is the most common detector that has been established and commercialized[51,52]. Additionally, single particle ICP-MS (spICP-MS) was online coupled to FFF for nanoparticle analysis, as well[45].

Aside from the hyphenated techniques, collecting fractions of the separated sample (automatically or manually) enables the offline analysis by virtually any technique that can process particle suspensions. Noteworthy is the use of electron microscopy to provide visualization of the separated particles, as well as confirmation of the size characterization either by MALS or by the retention parameter[36,38,42].

2.4 Concluding Remarks

These techniques in this thesis have been chosen due to their complementary advantages (and limitations). RM provides chemical information and identification on the samples accompanied by optical

imaging (> 1 µm) in a non-destructive way and with easy sample preparation. However, the optical microscopy is almost insufficient for the resolution of nanoplastic. Thus, SEM is combined, which provides high-resolution visualization of even the smallest nanoparticles (> 2 nm). Similar to RM, SEM offers rather simple sample preparation, when applied for micro-/nanoplastic. But as they both work on individual particles, measurement times are quite long. Typically, samples for SEM need to be electrically conductive to prevent charging effects. However, for small plastic particles, the use of FE-guns and the low-pressure mode can facilitate the visualization without metal coating. In addition, samples for SEM – unlike RM – need to be dry to be put in the vacuum chamber. Thus the investigation of biological samples is preferrably performed by RM or by low vacuum SEM. FFF and its detectors complement the two, as they analyze the particles(1 nm – $\sim$ 20 µm) in bulk (Chapter 7.3). Therefore, measurements are much faster, however, no chemical identification is provided. One has to keep in mind that the validation of FFF protocols for new samples requires the optimization of many parameters, such as flow rates, channel components, solvents, or relaxation and injection steps[44]. This makes FFF very labour intensive in the initial phase (as well as maintenance). Finally, while the cost of all three is rather high, they do, on the other hand, provide a high degree of information, which is very important when approaching a new analyte such as nanoplastic. Further developments toward routine analysis, which include faster and more specific (thus cheaper) analyses, will be an important task down the road, once the proof-of-concepts have been presented.

References

1. Niessner, R. Analytical Chemistry: Current Trends in Light of the Historic Beginnings. *Angewandte Chemie, International Edition* **2018**, *57*, 14328–14336.
2. Popp, J.; Mayerhöfer, T., *Micro-Raman Spectroscopy: Theory and Application*; De Gruyter: Berlin, Boston, 2020.
3. *Modern Raman Spectroscopy: A Practical Approach, Second Edition*; John Wiley & Sons: 2019.
4. *Infrared and Raman Spectroscopy*; Schrader, B., Ed.; John Wiley & Sons: 1995.
5. *Raman Spectroscopy for Chemical Analysis*; McCreery, R. L., Ed.; John Wiley & Sons: 2000.
6. *Introductory Raman Spectroscopy*, Second Edition; Ferraro, J. R., Nakamoto, K., Brown, C. W., Eds.; Academic Press: San Diego, 2003.
7. Bower, D. I.; Maddams, W. F., *The Vibrational Spectroscopy of Polymers*; Cambridge Solid State Science Series; Cambridge University Press: 1989.
8. Sheppard, N. The historical development of experimental techniques in vibrational spectroscopy. *Handbook of Vibrational Spectroscopy* **2006**.
9. Raman, C. V.; Krishnan, K. S. A new type of secondary radiation. *Nature* **1928**, *121*, 501–502.
10. Dhamelincourt, P. In *Handbook of Vibrational Spectroscopy*; American Cancer Society: 2006.
11. Skoog, D. A.; Holler, F. J.; Crouch, S. R., *Principles of instrumental analysis*; Cengage learning: 2017.

12. Everall, N. J. Confocal Raman microscopy: common errors and artefacts. *The Analyst* **2010**, *135*, 2512–2522.

13. Everall, N. Optimising image quality in 2D and 3D confocal Raman mapping. *Journal of Raman Spectroscopy* **2014**, *45*, 133–138.

14. Zoubir, A., *Raman imaging: Techniques and applications*; Springer Series in Optical Sciences, Vol. 168; Springer: Berlin, Heidelberg, 2012.

15. Ashkin, A. Atomic-Beam Deflection by Resonance-Radiation Pressure. *Physical Review Letters* **1970**, *25*, 1321–1324.

16. Neuman, K. C.; Block, S. M. Optical trapping. *Review of Scientific Instruments* **2004**, *75*, 2787–2809.

17. Ashkin, A.; Dziedzic, J. M.; Bjorkholm, J. E.; Chu, S. Observation of a single-beam gradient force optical trap for dielectric particles. *Optics Letters* **1986**, *11*, 288–290.

18. Ashkin, A. Forces of a single-beam gradient laser trap on a dielectric sphere in the ray optics regime. *Biophysical Journal* **1992**, *61*, 569–582.

19. Gordon, J. P. Radiation Forces and Momenta in Dielectric Media. *Physical Review A* **1973**, *8*, 14–21.

20. Optical tweezers and their applications. *Journal of Quantitative Spectroscopy and Radiative Transfer* **2018**, *218*, 131–150.

21. Nussenzveig, H. M. Cell membrane biophysics with optical tweezers. *European Biophysics Journal* **2018**, *47*, 499–514.

22. Dhakal, K. R.; Lakshminarayanan, V. Optical tweezers: fundamentals and some biophysical applications. *Progress in Optics* **2018**, *63*, ed. by Visser, T. D., 1–31.

23. Ajito, K.; Torimitsu, K. Single Nanoparticle Trapping Using a Raman Tweezers Microscope. *Applied Spectroscopy* **2002**, *56*, 541–544.

24. Bankapur, A.; Zachariah, E.; Chidangil, S.; Valiathan, M.; Mathur, D. Raman Tweezers Spectroscopy of Live, Single Red and White Blood Cells. *PLOS ONE* **2010**, *5*, 1–11.

25. Song, Y.; Yin, H.; Huang, W. E. Raman activated cell sorting. *Current Opinion in Chemical Biology* **2016**, *33*, 1–8.

26. Michler, G. H., *Electron microscopy of polymers*; Springer Laboratory; Springer: Berlin and Heidelberg, 2008.

27. Zhou, W.; Wang, Z. L., *Scanning microscopy for nanotechnology: Techniques and applications*; Springer: New York, NY, 2007.

28. Ul-Hamid, A., *A Beginners' Guide to Scanning Electron Microscopy*; Springer International Publishing: Cham, 2018.

29. Goldstein, J. I.; Newbury, D. E.; Michael, J. R.; Ritchie, N. W.; Scott, J. H. J.; Joy, D. C., *Scanning Electron Microscopy and X-Ray Microanalysis*, 4th ed. 2018; Springer New York: New York, NY, 2018.

30. Dobro, M. J.; Melanson, L. A.; Jensen, G. J.; McDowall, A. W. In *Cryo-EM Part A Sample Preparation and Data Collection*, Jensen, G. J., Ed.; Methods in Enzymology, Vol. 481; Academic Press: 2010, pp 63–82.

31. Passmore, L.; Russo, C. In *The Resolution Revolution: Recent Advances In cryoEM*, Crowther, R., Ed.; Methods in Enzymology, Vol. 579; Academic Press: 2016, pp 51–86.

32. Erlandsen, S.; Lei, M.; Martin-Lacave, I.; Dunny, G.; Wells, C. High Resolution CryoFESEM of Microbial Surfaces; CryoFESEM of Microbes; Stanley Erlandsen et al. *Microscopy and Microanalysis* **2003**, *9*, 273.

33. Luo, H.; Scriven, L.; Francis, L. F. Cryo-SEM studies of latex/ceramic nanoparticle coating microstructure development. *Journal of Colloid and Interface Science* **2007**, *316*, 500–509.

34. Wille, G.; Schmidt, U.; Hollricher, O. In *Confocal Raman Microscopy*, Toporski, J., Dieing, T., Hollricher, O., Eds.; Springer International Publishing: Cham, 2018, pp 559–580.

35. Cardell, C.; Guerra, I. An overview of emerging hyphenated SEM-EDX and Raman spectroscopy systems: Applications in life, environmental and materials sciences. *Trends in Analytical Chemistry* **2016**, *77*, 156–166.

36. Contado, C. Field flow fractionation techniques to explore the “nano-world”. *Analytical and Bioanalytical Chemistry* **2017**, *409*, 2501–2518.

37. Mintenig, S. M.; Bäuerlein, P. S.; Koelmans, A. A.; Dekker, S. C.; van Wezel, A. P. Closing the gap between small and smaller: Towards a framework to analyse nano- and microplastics in aqueous environmental samples. *Environmental Science: Nano* **2018**, *5*, 1640–1649.

38. Baalousha, M.; Stolpe, B.; Lead, J. R. Flow field-flow fractionation for the analysis and characterization of natural colloids and manufactured nanoparticles in environmental systems: A critical review. *Journal of Chromatography A* **2011**, *1218*, 4078–4103.

39. Wahlund, K.-G. Flow field-flow fractionation: Critical overview. *Journal of Chromatography A* **2013**, *1287*, 97–112.

40. Schimpf, M. E.; Caldwell, K.; Giddings, J. C., *Field-flow fractionation handbook*; Wiley-Interscience: New York and Chichester, 2000.

41. Kononenko, V. L.; Giddings, J. C.; Myers, M. N. On the possibility of photophoretic field-flow fractionation. *Journal of Microcolumn Separations* **1997**, *9*, 321–327.

42. Wagner, M.; Holzschuh, S.; Traeger, A.; Fahr, A.; Schubert, U. S. Asymmetric Flow Field-Flow Fractionation in the Field of Nanomedicine. *Analytical Chemistry* **2014**, *86*, 5201–5210.

43. Giddings, J.; Karaiskakis, G.; Caldwell, K. D.; Myers, M. N. Colloid characterization by sedimentation field-flow fractionation: I. Monodisperse populations. *Journal of Colloid and Interface Science* **1983**, *92*, 66–80.

44. Gigault, J.; Zhang, W.; Lespes, G.; Charleux, B.; Grassl, B. Asymmetrical flow field-flow fractionation analysis of water suspensions of polymer nanofibers synthesized via RAFT-mediated emulsion polymerization. *Analytica Chimica Acta* **2014**, *819*, 116–121.

45. Wang, Y.; Cuss, C.; Shotyk, W. Application of asymmetric flow field-flow fractionation to the study of aquatic systems: Coupled methods, challenges, and future needs. *Journal of Chromatography A* **2020**, *1632*, 461600.

46. Hassellöv, M.; Lyvén, B.; Haraldsson, C.; Sirinawin, W. Determination of Continuous Size and Trace Element Distribution of Colloidal Material in Natural Water by On-Line Coupling of Flow Field-Flow Fractionation with ICPMS. *Analytical Chemistry* **1999**, *71*, 3497–3502.

47. Prestel, H.; Niessner, R.; Panne, U. Increasing the sensitivity of asymmetrical flow field-flow fractionation: Slot outlet technique. *Analytical Chemistry* **2006**, *78*, 6664–6669.

48. Xu, R. Light scattering: A review of particle characterization applications. *Particuology* **2015**, *18*, 11–21.

49. Schwaferts, C.; Sogne, V.; Welz, R.; Meier, F.; Klein, T.; Niessner, R.; Elsner, M.; Ivleva, N. P. Nanoplastic Analysis by Online Coupling of Raman Microscopy and Field-Flow Fractionation Enabled by Optical Tweezers. *Analytical Chemistry* **2020**, *92*, 5813–5820.

50. Andersson, M.; Wittgren, B.; Wahlund, K.-G. Accuracy in Multiangle Light Scattering Measurements for Molar Mass and Radius Estimations. Model Calculations and Experiments. *Analytical Chemistry* **2003**, *75*, 4279–4291.

51. Meermann, B. Field-flow fractionation coupled to ICP–MS: separation at the nanoscale, previous and recent application trends. *Analytical and Bioanalytical Chemistry* **2015**, *407*, 2665–2674.

52. Pornwilard, M.-M.; Siripinyanond, A. Field-flow fractionation with inductively coupled plasma mass spectrometry: past, present, and future. *Journal of Analytical Atomic Spectrometry* **2014**, *29*, 1739–1752.

Chapter 3

Methods for the Analysis of Submicrometer- and Nanoplastic Particles in the Environment

Reference

Christian Schwaferts, Reinhard Niessner, Martin Elsner and Natalia P. Ivleva, *Trends in Analytical Chemistry* **2019**, 112, 52–65, https://doi.org/10.1016/j.trac.2018.12.014, https://www.sciencedirect.com/science/article/pii/S0165993618304631.

Permission statement

The author of this Elsevier article retains the right to include it in a thesis or dissertation, provided it is not published commercially. For more information, please visit: https://www.elsevier.com/about/our-business/policies/copyright#Author-rights.

Abstract

Nanoplastic is an emerging topic of relevance in environmental science. The analytical methods for microplastic have a particle size limit of a few micrometers so that new methods have to be developed to cover the nanometer range. This contribution reviews the progress in environmental nanoplastic analysis and critically evaluates which techniques from nanomaterial analysis may potentially be adapted to close the methodological gap. A roadmap is brought forward for the whole analytical process from sample treatment to particle characterization. This includes a critical review of (i) methods for analyte extraction and preconcentration from various environmental matrices; (ii) methods for the separation of the nanoplastic into specific size fractions; (iii) light scattering techniques and various types of microscopy to characterize the particle fractions; (iv) chemical identification of particles to validate the obtained data. For these methods, we will discuss prospects and limitations to develop analytical protocols for specific sampling scenarios.

3.1 Introduction

Environmental plastic and especially microplastic (MP) pollution is a topic of great public concern. In recent years, questions concerning even smaller particles, so called nanoplastic, have emerged and

are of pressing interest, especially since it has been identified in facial scrubs[1] and in marine surface waters[2]. MP is defined as particles in the size range from 1 µm to 5 mm, nanoplastic ranges from 1 nm to 100 nm and the sizes between 100 nm to 1 µm are called subµ-plastic[3]. This classification adheres to the European Commission's definitions for engineered nanoparticles (ENPs)[4]. However, there is still debate on the size classes for nanoplastic, with an alternative that defines the whole nanometer range (1 nm – 1000 nm) as nanoplastic[5]. Furthermore, MP is separated into primary MP, which comprises particles that were produced for a specific purpose (e.g. for cosmetics), and secondary MP, which is generated from larger plastic debris by fragmentation[3]. This classification could be applied to subµ- and nanoplastic as well, denoting e.g. a polystyrene (PS) latex or nanometer-sized plastic particles in cosmetics as primary nanoplastic. Particles that originate from larger pieces by fragmentation in the environment would, then, be classified as secondary nanoplastic. This topic, thereby, creates a cross-section with nanoparticle science, because nanoplastic particles are in principle polymeric nanoparticles. It is, however, well placed in the field of environmental plastic analysis, since it is part of the whole plastic contamination problem. The debate on what actually is comprised by „plastic", thereby meaning „synthetic polymer" (including associated additives), is still ongoing. Usually, particle size and, implicitly, the prerequisite that the particle is insoluble in water are the core determinants for plastic particle analysis. However, this excludes important aspects like the chemical composition (polymer type, additives, ageing) or whether particles made of modified polymers of natural origin (e.g. natural rubbers in tire wear) can be assigned to „plastic". For more details on a definition and categorization framework for plastic debris, the reader is referred to a recent publication of Hartmann et al.[6].

These distinctions have to be kept in mind, when defining the analytical question for specific sample scenarios. In MP analysis, the sampling and sample treatment of MP is accomplished with respect to the system that is probed. Nets or sieving are applied for aquatic systems[7], density separation for sediments[8,9], and chemical digestion for food or biota samples[3,10], in the latter two, MP particles are then collected on filters. The size cut-off of these methods, however, only covers the micrometer range (except for membrane filtration, see Section 3.2.2.1). This is illustrated in Figure 3.1. Hence, for subµ- and nanoplastic there is a need for sampling that retains such small particles.

Following the sampling and sample treatment, there is the determination of the MP particle size and number – alternatively, the mass content – and the identification of the polymer. To that end, there are (i) techniques that combine microscopic and spectroscopic analysis and (ii) thermoanalytical methods[3,10,11]. In spectroscopy, MP can be measured on a particle by particle basis with attenuated total reflection Fourier transform-infrared spectroscopy (ATR-FT-IR)[10] [10], where MP particles (usually larger than 500 µm) are handpicked. Smaller particles are collected on filters and identified with focal plane array micro-FT-IR (FPA-FT-IR)[10,12] [10,12] or Raman microspectroscopy (RM)[13–15] with particle sizes down to 10 µm and 1 µm, respectively. Thermoanalytical MP detection, on the other hand, provides polymer and additive characterization and quantifies by mass content of MP in a sample. Its limits of detection (LODs) depend on the polymer type and are in the range of nanograms to micrograms[16–18].

It has to be kept in mind that the mass of the particle decreases with the third power of its diameter d^3. The orders of magnitude of the particle diameter d in m and particle mass m in g (assuming a density

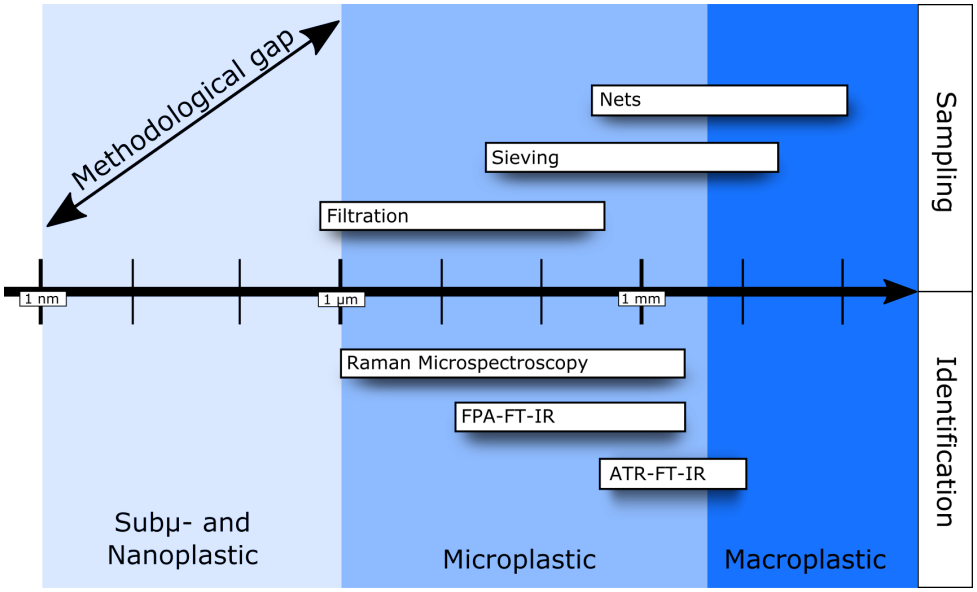

Fig. 3.1: The analysis of MP is established for particles down to 1 µm. Below, there is a methodological gap.

of 1) follow the correlation $\log m = 3 \log d + 6$. It gives the masses of e.g. 10 µm, 100 nm and 10 nm particles as 10^{-9} g = 1 ng, 10-15 g = 1 fg and 10-1 g = 1 ag, respectively. This demonstrates the steep decrease of the particle mass and can be connected to the particle number, which, in turn, increases with d^3. This means that, with fixed mass, one 100 µm plastic particle (m = 1 µg) is equivalent to a thousand 10 µm, a million 1 µm, a billion 100 nm and a trillion 10 nm particles. From this consideration it can be concluded that, although unintuitive, subµ- and nanoplastic can constitute high particle numbers and, at the same time, low masses in a sample (e.g.[1,2,19]).

Hence, techniques would have to provide low particle size detection limits or low LODs in terms of mass to detect subµ- and nanoplastic in environmental samples. The size ranges for MP identification are plotted in Figure 3.1, showing that for subµ- and nanoplastic they have hit a limit. So have the thermoanalytical methods with LODs that are too high for the low masses of subµ- and nanoplastic that we could expect in the environment.

This illustrates that for the analysis of subµ- and nanoplastic we are facing a methodological gap. When entering the nanometer size range, a new approach in the analytical methodology must be taken. This concerns specific characteristics, like particle size distribution (PSD) or morphology and the chemical identity, for which techniques that detect in the nanometer range will be needed. In addition, an appropriate sample treatment, especially, a preconcentration and also a separation step to properly isolate the particles, will be an essential part of the required protocol.

The established methods for MP analysis, however, have the potential to be adapted for the analysis of subµ- and nanoplastic particles by combining them to other techniques. Such combinations, like preconcentration to solve LOD issues or light scattering-based techniques that give a PSD to solve the problem of representativeness in techniques for single particle analysis, could alleviate their limitations. Furthermore, there is much knowledge on the analysis of ENPs in the environment that may potentially

be harnessed to close this methodological gap. A seminal paper by Hüffer et al. discussed similarities and differences that may help the understanding of micro- and nanoplastic particles[20]. Especially when regarding methods that concern particle characterization, there are many techniques for the analysis of ENPs that have been established[20–24]. Some of them may be transferred to nanoplastic analysis, mainly techniques that characterize particles by their geometry, like dynamic light scattering (DLS) or electron microscopy (EM). However, since ENPs are mostly inorganic and nanoplastic is mainly carbon-based, the identification of the chemical composition of the particle will require new protocols. Subµ- and nanoplastic, as is usual in MP analysis, needs an identification of the particle composition in terms of the polymer type (e.g. polyethylene (PE), PS) instead of just an elemental analysis to provide a reliable characterization of the environmental sample.

Furthermore, first studies demonstrated the fragmentation of larger particles into subµ- and nanoplastic. The tests were performed either on MP particles that were collected from the ocean[25] or pristine consumer products[26,27]. Two distinct steps in the formation of small plastic particles have been determined. First, a surface erosion of small, nano-sized particles. Second, fragmentation of the parent particles into equally sized smaller MP particles. The focus of other studies has been the propensity of subµ- and nanoplastic to form heteroaggregates with organic and inorganic matter[28]. Primary nanoplastic beads and the dissolved organic content in seawater was studied, to show that nanoplastic accelerates the coagulation of dissolved organic matter to particulate organic matter[29].

These findings emphasize the great difference between ENPs and primary subµ- and nanoplastic beads compared to secondary subµ- and nanoplastic, which is likely to occur in the environment. Due to their fragmented nature, they will exhibit irregular shape, surface morphologies and charges than synthetic subµ- and nanoplastic beads, on which many studies concerning the topic have been based. Here it is also important to mention their heteroaggregation behavior, which contrasts MP. The challenge for method development will be to accommodate for the properties that will be inherent to environmental subµ- and nanoplastic particles.

Here we want to review the techniques that have already been applied in subµ- and nanoplastic studies (search was conducted using Web of Science and Google Scholar with the search terms „nanoplastic“, „nano- and microplastic“ and „analysis“, amongst others, including publications until august 2018) and present techniques from ENP analysis that we think may have a potential for subµ- and nanoplastic research. We will critically discuss their applicability and project a roadmap for the whole analytical process in environmental systems.

3.2 Sample Preparation

Since the plastic contamination can be found in very diverse locations, the analytical process begins with the clarification of the question that is to be answered (plastic particle number, size and PSD or mass of plastic particles per mass or volume of sample), which, in turn, depends on the sample to be analyzed. Samples can range from drinking water to food, environmental waters, sediments, biota tissue, to WWTP in-/effluents, which have greatly different contents of matrix that accompanies the plastic particles.

Plastic is an omnipresent material in our live. Therefore, there is a strong risk of sample contamination during sampling and sample handling, which shows that proper particle contamination measures have to be taken. Tools and setups should be made from non-polymer materials to avoid a systematic contamination of the sample. Also, contamination due to airborne particles and synthetic fibers from clothing needs to be prevented by the use of laminar flow benches. However, it seems unlikely to completely avoid plastic in all components, therefore, a thorough blank value and recovery evaluation of the method should be performed.

3.2.1 Digestion of Matrix

When choosing methods for sample treatment, characterization, and identification, in order to obtain the required information on the sample, in many cases it will be necessary to remove the matrix, in order to enable the technique to analyses the particles. This means organic matrix like tissue, organisms, or natural organic matter (NOM) has to be removed. Depending on the treatment, some inorganic particles may be removed as well, e.g. carbonate-based sediments with acid treatment.

A multitude of approaches for the digestion of organic matrix have been applied in ENP[21] and MP[3] analysis, some of which have also been utilized for nanoplastics[30]. These approaches comprise acid treatment, usually 65 % nitric acid[30,31], sometimes in combination with 30 % hydrogen peroxide[32,33] and alkaline treatment with sodium hydroxide[30,34,35]. Additionally, a mild enzymatic protocol with Proteinase K can be used for tissue decomposition[30,32].

The treatment must not alter the plastic particles, therefore care has to be taken when choosing the sample treatment protocol. Homogenization may damage the plastic particles. Also, it has been shown with optical microscopy and DLS that acid, alkaline and H_2O_2 treatment cause aggregation of the particles, most likely due to the strong change in ionic strength of the solution[30]. Enzymatic treatment is milder and has been demonstrated to cause no[32] or less[30] aggregation with the particles (fluorescent, 100 nm, PS). Further, harsh treatments (acid, alkaline, H_2O_2) can, in some cases, negatively influence the fluorescence signal of labelled plastic particles (e.g. in toxicology studies)[30,33]. In many studies a proper validation of the digestion is lacking. It is, however, very important to find a sufficiently mild protocol that does not alter the plastic particles and stabilizes them against aggregation. If, on the other hand, information on the particle morphology and aggregation state is not required by the analytical question, this step can be reduced to a mere recovery test for quantification. For quantification of

fluorescent particles, a recovery test concerning the stability of the fluorophore should be performed to evaluate a specific treatment[33].

3.2.2 Preconcentration

Even though large amounts of plastic pollution are present in the environment[36], the mass of subµ- and nanoplastic particles is probably very low[2,19]. Therefore, for most types of sample, a preconcentration step is inevitable. There are several different methods, from which may be chosen, depending on the sample and the following characterization and identification (Table 3.1).

3.2.2.1 Membrane Filtration

The process of filtration is very common for MP analysis, where e.g. the whole micrometer range of particles can be sampled on a filter membrane for spectroscopic analysis[3,37,38]. Membrane filters from different materials (e.g. aluminum oxide, ceramics, or polycarbonate) are commercially available with pore sizes in the range of several µm to 0.01 µm. It has to be noted that the use of polymeric membranes could introduce plastic contamination to the sample. It should also be kept in mind that the size fraction in the filtrate is usually smaller than the nominal pore size. Membrane filters need to be handled very delicately to avoid damaging of the membrane, which would compromise the size cut-off. When using filters with small pore sizes, especially below 0.1 µm, they exhibit very low flow rates, which effects the sample volume that can realistically be filtered. This volume decreases with decreasing pore size (e.g. 25 mL with 0.4 µm pores[39] or 0.1 mL with 0.01 µm pores[1]). This needs to be considered when deciding on a treatment protocol for a large sample volume, especially when planning for environmental samples, which may contain high amounts of organic content in relation to the plastic particles, for which ultrafiltration (UF) could be a preferable alternative. On the other hand, since subµ- and nanoplastic in the environment is expected to occur in heteroaggregates with organic matter (Section 3.1) membrane filtration could retain and enable an imaging of those aggregates.

Membrane filtration in a five-step sequence of the pore sizes 25 µm, 2.5 µm, 0.45 µm and two times 0.1 µm has been performed for the isolation of PE nanoplastic particles (24 nm – 52 nm) from facial scrubs[1]. This filtration cascade helped to avoid a fast clogging of the pores.

3.2.2.2 Ultrafiltration

UF uses nano-porous membranes that have a molecular weight cut-off in the range of 10 – 100 kDa (which roughly corresponds to 5 – 50 nm). They are employed either in a stirred cell[2], a centrifugal field[40] or in cross-flow mode (also called tangential flow)[41], in which the suspension flow is cycled past a parallel membrane, to prevent its blockage. As opposed to the methodologically similar dialysis[42], the filtration is performed by applying pressure to facilitate the flow of the filtrate, which increases its operation speed.

A stirred cell with a molecular weight cut-off of 10 kDa has been used to concentrate (factor 50) the subµ- and nanoplastic fraction (< 1.2 µm) of artificially fragmented MP particles[25] and a marine water sample (factor 100)[2]. Cross-flow UF with a cut-off between 40 and 60 kDa has been evaluated as preconcentration (factor 200) step for asymmetric flow field flow fractionation (AF4) with PS beads in the range of 50 nm – 1000 nm[41]. This indicates that Cross-flow UF is a method with high potential for the processing of environmental samples, because it is able to process large volumes of water, in the m^3 range. It is also very gentle because it does not eliminate all the solvent, therefore particle loss and sample alteration or aggregation are minimized[21,43]. It has to be added that AF4 is also able to preconcentrate to some extent by creating a focusing flow that collects up to 50 mL of the sample at the beginning of the flow channel[44,45].

3.2.2.3 Ultracentrifugation

Centrifugation and ultracentrifugation (UC) can be used to sediment particles from suspensions into a pellet. For subµ- and especially nanoplastic, the higher centrifugal forces of UC, which are in the range of 10^5 g, will be required to affect the smaller plastic particles, which bring the inherent difficulty of densities close to that of water. This technique is readily available and simple to use, but has the caveat that it only processes smaller sample volumes, in the range of 10 – 100 mL, which limits its applicability for environmental water samples. UC collects all particles in the pellet without separation, irrespective of whether they are plastic, or originate from the (in)organic environmental matrix. Additionally, the high centrifugal forces or stress from redispersing the pellet may alter the sample by forming aggregates or damaging plastic particles[21,42,46]. However, these drawbacks might be irrelevant in an analytical protocol that is independent of the morphology of the sample, like pyrolysis gas chromatography mass spectrometry (Py-GC-MS) that destroys the sample anyway.

Employing density gradient UC[47], on the other hand, may provide a separation of plastic particles and matrix with higher densities, e.g. sediment[48]. This, however, will require a preceding digestion of organic matrix, which would otherwise be contained in the same fraction as the plastic particles.

There is also another variant called analytical ultracentrifugation (AUC) that spectroscopically (light absorption) monitors the sedimentation during the centrifugation process, from which many parameters on the morphology and spectroscopic information of the analyte can be derived. A fragmentation can be obtained as well[49,50].

3.2.2.4 Evaporation of Solvent

Evaporation of the solvent at reduced pressure, commonly with a rotary evaporator, is a technique from nanoparticle synthesis and especially useful for organic solvents[42]. It has, however, been applied for the concentration (factor 30) of environmentally more relevant, secondary PET nanoplastic suspensions (ca. 100 nm) in water, which were generated by laser ablation[51]. Since this technique does not remove dissolved matter and will be uneconomical for removing large volumes of water, it might be primarily

applicable to further concentrate suspensions from e.g. dialysis or cross-flow UF that could only be reduced to a certain volume.

3.2.3 Separation Techniques

3.2.3.1 Field-Flow Fractionation

Field-flow fractionation (FFF) is a separation technique that applies a perpendicular force on particles in flow. Depending on their diffusivity, which is determined by characteristics like density or shape, particles are retained in the flow channel for different durations, which causes a separation of the particles in the sample. FFF works without a stationary phase, precluding interactions with the plastic particle, however, interactions with the membrane of the flow channel are a common problem that has to be countered by a proper method optimization for each individual sample. There are different variants of FFF, using various separating fields, like thermal, electric, gravity (or centrifugal), or cross-flow, which cover the whole nanometer range (for AF4) and can extend to the low micrometer range (up to 100 µm)[52,53].

The most common variant of FFF is the AF4, which, like other flow techniques, is routinely coupled to online detectors[53,54]. Frequently applied are refractive index[51], UV-visible absorption[41] or fluorescence[32] detectors for particle presence in the fraction and multi angle light scattering (MALS)[32,41,51] as well as DLS[54] that offer size characterization. Additionally, a mass spectrometric technique has been reported, that combines Py-GC-MS analysis with AF4 allowing for the determination of the polymer type[41].

AF4 (s. Table 3.1) has been widely utilized for the analysis of ENPs in environmental samples[53]. It has also been shown to be of great potential for the separation of subµ- and nanoplastic samples: Gigault et al. published an AF4 method that is optimized for the fast separation of primary subµ- and nanoplastic PS beads in the range of 1 nm – 100 nm[55]. Correia et al. evaluated a protocol for the analysis of primary nanoplastic particles (PS 100 nm) in a fish tissue sample, that digested the matrix with Proteinase K (which was shown to prevent aggregation, as opposed to acid treatment, Section 3.2.1) and separated the sample with AF4-MALS-Fluorescence[32]. Mintenig et al. proposed AF4 and Py-GC-MS (Section 3.4.2) of samples that were preconcentrated by cross-flow UF for the analysis of plastic particles below 20 µm as part of a framework for MP, subµ- and nanoplastic and validated the setup with primary PS particles in the range from 50 nm – 1000 nm, suspended in drinking and surface water[41].

These methods have all been validated with primary subµ- and nanoplastic particles. In contrast, plastic particles in the environment are generated due to various stressors, which fragment the particle and usually oxidize the polymer[56], therefore, the surface can be expected to be rough and negatively charged[27]. In addition, methods that have been developed for ENPs, will need optimization for subµ- and nanoplastic particles due to their densities. These circumstances have to be accounted for in the method development of environmental subµ- and nanoplastic by optimizing the dispersion medium, flow rates and validating the detectors. The validation also needs to include a determination of the concentration ranges, in order to perform a quantification[57].

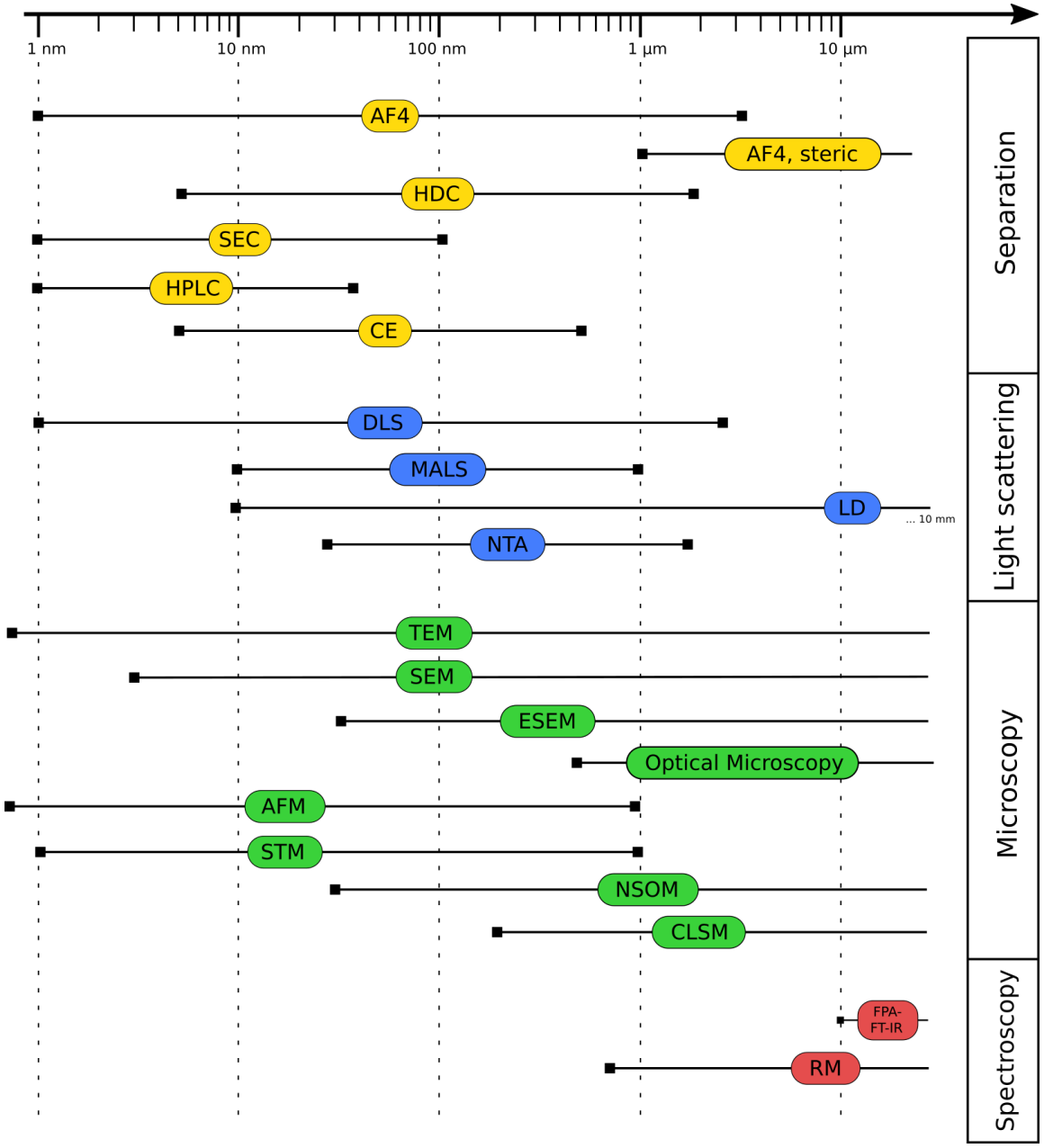

Fig. 3.2: Comparison of the particle size ranges for analysis with the different techniques that are discussed in this review.

When using AF4 for the separation of particles larger than around 1 µm, the so-called steric inversion occurs. Here particles are drawn to the membrane almost equally strong but due to their size, large particles experience stronger forces from the laminar flow causing them to elute faster than smaller particles. The point of inversion depends on different parameters like channel thickness, flow rate or cross-flow[53]. This brings the risk of co-elution of small and large particles due to the steric inversion, which would compromise the separation. Therefore, a separation, e.g. filtration, step at the point of inversion is suggested[41].

As with the other separation techniques below, FFF is coupled online to detectors, which should also provide quantitative information on the plastic particles. This is possible with mass-spectrometric detectors or UV, refractive index, or fluorescence detectors[58] by calibration with a standard[59]. However, problems with particle–membrane interaction and limited concentration ranges[60], as well as providing a representative calibration material for the quantification of secondary subµ- and nanoplastic will have to be addressed.

3.2.3.2 Chromatography

Chromatographic techniques (s. Table 3.1) use a stationary phase for the separation of analytes, which make its applicability for particulate samples difficult, since interactions with the stationary phase may occur and its pore size may not suffice. On the other hand, their wide-spread and easier application make them a noteworthy alternative to FFF, which requires lots of method optimization and user experience. Some techniques have been applied for ENP separation in environmental samples; among them are reverse phase high performance liquid chromatography (HPLC)[61], size exclusion chromatography (SEC)[62] and hydrodynamic chromatography (HDC)[63]. This indicates that they may be applicable to nanoplastic separation as well. However, in contrast to ENPs, subµ- and nanoplastic particles, which originate from fragmentation, can be expected to have rougher surfaces, which may increase their interaction with the stationary phase. Another point to consider, is the difference in density between ENPs and subµ- and nanoplastic, for which a stable suspension has to be ensured.

Many of the chromatographic methods, however, may only have an application for a specific analytical question, since the particle size range is much smaller (1 nm – 40 nm for HPLC[61] and 1 nm – 100 nm for SEC[62]) as compared to e.g. FFF[21] (Figure 3.2). Concerning these restrictions, HDC might be a chromatographic method that is applicable for subµ- and nanoplastic particles because its stationary phase is a non-porous material, packed into the column, in which the mobile phase flows through the interspaces. This brings a larger size range (5 nm – 1.2 µm[63]) and less interactions. In a study on gold ENPs (5 nm – 100 nm), HDC has shown better recoveries than AF4, although its separation resolution was smaller[64].

3.2.3.3 Electrophoresis

Electrophoresis (s. Table 3.1) employs the mobility of charged particles in an electric field to achieve a spatial separation. This review will focus only on capillary electrophoresis (CE) because it has the largest range of applicability as compared to e.g. gel electrophoresis[65,66]. CE has been applied on ENPs, indicating that it has the potential to be a promising alternative for the separation of subµ- and nanoplastic particles. This method will also have to be adapted to the nature of environmental subµ- and nanoplastic, especially its surface properties, which will depend on the influences that the particles have experienced.

In all the separation techniques of this chapter, the suspension has to be stabilized with surface functionalization agents. For CE they are also necessary to precisely control the surface charge[21]. These surfactants may, however, impede subsequent characterization of the nanoplastic particles.

3.3 Methods for the Characterization of Particle Size and Morphology

3.3.1 Particle Characterization by Light Scattering

There are multiple methods that apply the scattering of laser light on particles to obtain information on physical properties like size or PSD (Table 3.2). The most widely used, DLS measures particle sizes in the range from 1 nm to 3 µm based on the fluctuation of intensity of a laser beam that passes the suspension. This fluctuation is caused by the Brownian motion of the particles and can be associated to the hydrodynamic diameter (d_h) of the particles with an autocorrelation function[68]. Its easy application makes DLS a broadly used technique for particle size and PSD characterization, especially for primary nanoplastic, which is used for spiking and toxicological experiments.

It should, however, be kept in mind that DLS uses theoretical models that are based on spheres and that it works optimally with monodisperse suspensions. This is due to the fact that the signal intensity correlates with d^6 and therefore overestimates large particles. The technique is, thus, prone to errors due to contaminations that introduce large particles, which would mask the actual analyte. Such contaminations may be residues from the matrix, aggregates or dust[21,22]. Furthermore, gaining reliable information on polydisperse, non-spherical subµ- and nanoplastic dispersions, as would be present in the environment, is nonetheless possible[2,55]. When employing any of these light scattering detectors, especially for quantification, a preemptive method validation should contain a determination of the concentration range[69]. In addition, DLS does not provide any chemical information and cannot distinguish particles of similar form but different composition.

Commercial DLS instruments are usually coupled with the function to determine the zeta potential with electrophoretic light scattering (ELS). The principle of ELS is similar to DLS, in that it measures the fluctuation of laser intensity that is generated by particle movement in an electric field. This gives the electrophoretic velocity that in turn correlates to the zeta potential, which is the charge of the particle

Task	Technique	Range	Advantages	Disadvantages	References
Preconc.	Membrane filtration	> 10 nm	+ Easily available + Cheap	- Low flow rates with small pores - Small volumes	[1] / –
	UF	10 – 100 kDa ca. 5 – 50 nm	+ Large volumes + Little sample damage/aggregation + Little membrane clogging/fouling	- Interaction with membrane - Setup not plastic free	[2, 25, 41, 43] / –
	Dialysis	Similar to UF	+ Easily available + Cheap	- Low flow rates with small pores - Small volumes	– / [42]
	UC	Any	+ Simple + Washing of particles with centrifugation and redispersing	- Harsh conditions - No separation from particulate matrix - Difficult to obtain complete separation	– / [21, 42]
	AUC	1 nm – 1 mm	+ High resolution + Can provide many information + Multiple detectors	- Best for small particles (1 – 10 nm)	– / [49, 50, 67]
	Evaporation of solvent	Any	+ Cheap, easy	- Does not remove dissolved matter - Superheating	[51] / [42]
Separation	AF4	1 nm – 1 µm	+ No stationary phase + Sample focusing + Online Coupling	- Operation difficult - Interaction with membrane - Steric inversion	[32, 41, 55] / [53]
	HDC	5 nm – 1.2 µm	+ Less interaction with stationary phase + Coupled detectors	- Little used	– / [21]
	SEC	1 nm – 1 nm	+ Coupled detectors	- Stationary phase - Small range	– / [62]
	HPLC	1 nm – 40 nm	+ Coupled detectors	- Stationary phase - Small size range	– / [61]
	CE	5 nm – 500 nm	+ High separation resolution + Coupled detectors + Fast	- Charge required - Electrolyte/surface modification - Interaction with capillary/clogging - Might damage sample - Complex matrices difficult	– / [23, 65, 66]

Tab. 3.1: Methods for the preconcentration and separation (detectors are listed in Table 3.2) of subµ- and nanoplastic particles. References are divided whether they have been applied for subµ- and nanoplastic (left) and by documents from other fields (right).

shear surface. The zeta potential is a measure on the stability of a suspension, with values greater than ± 30 mV being considered stable against aggregation[22,68]. Since plastic particles in the environment will experience weathering in the environment[56], they will display oxidized surfaces[27] and with that changes in surface charge. Measuring the zeta potential can, therefore, be an important parameter to characterize the ageing of plastic particles.

Static light scattering (SLS), which is also called MALS, records scattered laser light at different angles to obtain information on the size of the particle, e.g. the radius of gyration dg. To provide precise size information, a monodisperse suspension is needed[21,68]. Therefore, MALS is commonly coupled online to AF4[32,41,51,55] to feed size-separated samples to the detector (see Section 3.2.3.1), which enables measurement of polydisperse, environmentally relevant, subµ- and nanoplastic particles[55].

Laser diffraction (LD) is another static laser scattering-based technique that is common in process analysis, which is capable of sizing (among others) solid particles in liquid media across a very large size range from 10 nm to 10 mm[68]. It would, therefore, be an interesting technique for characterizing both MP, subµ- and nanoplastic at the same time.

Nanoparticle tracking analysis (NTA) records scattered laser light with a microscope and a digital camera. Software processing tracks the motion, as recorded in the video, of the particles and correlates a hydrodynamic diameter due to its Brownian motion[21,26,70]. NTA suffers less perturbation from large particles in polydisperse samples[69], which makes it an alternative to DLS for the determination of PSD of subµ- and nanoplastic. This has already been shown for fragmented, i.e. secondary plastic[25–27]. Another consideration for the application of NTA for subµ- and nanoplastic could be to use its fluorescence mode in combination with particle staining, which would, however, have to be tested for interference with the preceding sample digestion.

3.3.2 Imaging

To obtain information on the morphology of a sample, microscopy is the most viable method because it offers direct access to its geometry and surface characteristics. There are many different operation modes of microscopes, from which three groups are most prominent in particle imaging: optical microscopy, EM and scanning probe microscopy (SPM). These types of microscopy utilize different sorts of interaction with the sample, which effect their resolution (Table 3.2).

3.3.2.1 Optical Microscopy

Optical microscopy is a ubiquitous tool in almost every laboratory and is an essential part of the single particle analysis of MP particles, i.e. micro-IR and RM. For the visualization of subµ- and nanoplastic, however, optical microscopes can only be applied for particles above the diffraction limit of 0.3 µm to 0.5 µm depending on the numerical aperture and the criterion for single point differentiation[71]. Some

techniques like fluorescence or RM (Section 3.4.1.1) utilize a confocal pinhole to block light from lateral parts of the focal point, thereby enabling a lateral and axial resolution close to the diffraction limit.

Fluorescence microscopy in combination with fluorescently marked particles is a common tool to analyze the behavior of (usually primary) subµ- and nanoplastic in organisms, e.g. to track the translocation of the particles in the tissue. Such an experiment has e.g. been performed with fluorescent PE MP in the Antarctic krill that breaks fluorescent reference particles down to secondary subµ-plastic particles with its mastication apparatus. The particles can be further translocated into different parts of the organism[72,73].

Even though fluorescence microscopes are diffraction limited, as well, it is possible to locate smaller particles as long as they emit sufficient fluorescence signal. This application is, however, limited to synthetic particles with fluorescent dyes. It could not be used for the analysis of environmental subµ- and nanoplastic because these particles do not usually contain fluorophores.

3.3.2.2 Electron Microscopy

In EM[74,75] the sample is scanned with an electron beam that is generated in an electron gun and focused with electron optics. The electrons display a wide variety of interactions with the sample that can be observed with different detectors and give specific and complementary information. Since the wavelength of the high-energy electrons is very short compared to the wavelength of visible light of optical microscopy, the resolution of EM is much higher, spanning the range from sub-nanometers to millimeters. Its high resolution makes EM a widely used technique that complements many studies with imaging information on nanometer-sized particles.

Scanning electron microscopy (SEM) uses lower acceleration voltages up to 30 kV, usually around 5 kV, which causes varied interactions with the surface of the sample and accordingly detection being (in an angle) above the sample. In most cases, imaging is performed by detecting lower energy secondary electrons whose emission from sample atoms has been caused by the electron beam and gives morphological information of the point of incidence. The electron beam can also eject an inner shell electron of a sample atom, whose replacement is accompanied with the emission of an element-specific X-ray photon that is registered on an energy dispersive spectroscopy (EDS) detector and gives information on the elemental composition of the irradiated part of the sample.

Transmission electron microscopy (TEM) detects the transmitting electron beam below the sample, which requires high electron acceleration voltages up to 300 kV and a very thin sample. This results in very high resolutions enabling the imaging of very small nanoparticles. Due to the transmission mode of operation, TEM provides information on the interior of the particles rather than the surface (for which SEM can be utilized). It, too, can be coupled with EDS or electron energy loss spectroscopy (EELS) for information on the elemental composition[21].

TEM and SEM are often applied to characterize size, shape and surface characteristics of subµ- and nanoplastic particles. Very commonly in studies that use primary nanoplastic that is pre-characterized

before being used to spike samples for method validation[32] or biota exposition experiments[76]. They have also been utilized to image secondary subµ- and nanoplastic, e.g. from fragmentation studies[25,26]. The strength of SEM to image surface topology has been used to analyze the heteroaggregation behavior of nanoplastic with natural organic and inorganic matter[28,77]. EM is sometimes applied to deduce a PSD[51,78] of a subµ- or nanoplastic sample, which, however, is prone to error, since the imaged section may not be representative for the whole sample and the number of measured particles may be too low.

In general, EM requires a sample preparation that makes the sample stable for high vacuum and precludes artefacts from charging due to the electron irradiation. Here, drying a sample dispersion on a suitable substrate, e.g. for TEM carbon coated Cu grids, is the common approach. This preparation, however, alters the sample and may induce aggregation of the particles or shrinkage of organic matter or bacteria. Furthermore, coating with a metal (Au, Pt, Ag) or carbon film is often applied in order to avoid a charging of the sample.

Environmental scanning electron microscopy (ESEM) is a variant of SEM that allows the analysis of environmental, wet samples in a low pressure (10 – 50 Torr) nitrogen atmosphere, thereby enabling the imaging of samples that would otherwise degrade in high vacuum. The detector of the ESEM mode is not based on direct secondary electron detection, but on the detection of an ion cascade caused by the interaction of the electron with the low-pressure atmosphere, therefore, non-conductive samples may be imaged without charge artefacts, even without prior metal coating.

Another method to image samples in their environmental condition, e.g. aggregation or the particle corona, is Cryo-EM. Here, a dispersion of the sample is very rapidly frozen with liquid nitrogen or liquid ethane, causing water in the sample to vitrify instead of crystallizing. Hence, water does not expand and preserve the sample integrity. This technique has been used to determine the agglomeration behavior of PS nanoplastic particles in the presence of NOM and different salts[77]. During the Cryo-SEM analysis and image acquisition, it is important to remind that the sample preparation may produce spherical droplets of vitreous ice with a diameter of few micrometers or below, which look similar to plastic particles. To preclude an observed particle being ice, a confirmation of their identity is very important e.g. by EDS or by heating and sublimating ice from the sample.

3.3.2.3 Scanning Probe Microscopy

A third group of microscopy that is not governed by the diffraction limitation of incident light is SPM[22]. With these, a sensor, in some cases a sharp tip, scans the surface of the sample and detects the interaction with it. For scanning tunneling microscopy (STM) this is the tunneling current between the conductive surface and the tip in close proximity, which is dependent on the distance, hence giving a topographic image[79]. Its application to nanoplastic may, therefore, be problematic, since the particles itself are not conductive. Atomic force microscopy (AFM) records the deflection of a cantilever carrying the tip, which is caused by electrostatic or van der Waals interactions, that generate a height profile of the sample[22,24]. AFM is able to analyze samples in liquid, e.g. the adsorption behavior of nanoplastic particles with the cell wall of green algae[80], however, characterization of the particle surface roughness

may be influenced by the tip geometry and needs to be accounted for by data processing models[81]. It can also be combined with IR[82–84] or Raman spectroscopy[85–87] to create chemical images of the samples (Section 3.4.1.1 and 3.4.1.2).

Another group of SPMs that are based on optical microscopy contain, on the one hand, the confocal lasers microscope (CLSM, alternatively LSCM), which is a confocal optical microscope that scans the sample with a resolution at the diffraction limit (down to about 200 nm), usually exciting and detecting fluorescence. CLSM is often used to investigate the translocation of fluorescently dyed nanoplastic particles in organisms[72,88–90]. And on the other hand, there is near-field scanning optical microscopy (NSOM, alternatively SNOM) that conducts laser light through a tip aperture. This aperture is smaller than the laser wavelength, which causes the light to evanesce in a strongly localized area in close proximity of the tip, hence producing sub-diffraction limit resolution[91]. Due to their resolution these techniques have the potential for subµ- and nanoplastic imaging.

These techniques offer high resolution but have the drawback of long and laborious measurements, which can only be performed for specific particles or sections of the sample, but not for a representative analysis. This makes SPMs, as well as the other types of microscopy, dependent on proper sample treatment and characterization to guarantee representativeness.

3.4 Chemical Identification

The chemical identification of the polymeric particle is of great importance for the analysis of subµ- and nanoplastic in environmental samples, because, on the one hand, it provides a confirmation of the analytical question i.e. the subµ- and nanoplastic presence in a system. On the other hand, it can provide an additional chemical characterization of the particle e.g. with information on additive presence and/or ageing (Table 3.3). In MP analysis, vibrational spectroscopy has usually been integrated with optical microscopy to provide imaging, which enables the analysis of individual particles. This gives a great amount of information on particle size, PSD, and geometry, as well as the spectroscopic identification. This methodology, however, becomes increasingly difficult with decreasing particle size (below 10 µm) due to (i) an increase in the amount of small particles and (ii) particle size detection limits of the method[3,14].

In subµ- and nanoplastic analysis, this calls for a combined approach of techniques that provide information on size and PSD (Section 3.3) and techniques that can give spectroscopic identification. This, in turn, eliminates the need for single particle analysis with the spectroscopic methods and only demands a bulk measurement (of e.g. a dried fraction), in case when the preceding sample treatment has generated a sufficiently pure (and monodisperse) sample fractions.

Micro-FT-IR and RM are being more and more automated and provide information on the amount of particles, their size, and PSD through their microscopy images, as well as chemical identity[15,92]. Their optical resolution is, however, limited by the wavelength of the light source, which restricts them to the micrometer range.

Task	Technique	Information	Range/Limits	Advantages	Disadvantages	References
Charact.	DLS	Size (d_h), PSD, aggregation behavior	1 nm – 3 µm c = 10^{-6}–10^{-1}	+ Fast, cheap + In situ + Non-invasive + Aggregation + Direct coupling	- Large particles - Polydispersity - Complex matrix - Non-spherical particles - Small volumes	[28, 29] / [68]
	ELS	Surface charge, stability	1 nm – 3 µm	+ Fast, cheap + Non-invasive + With DLS	- Electroosmotic effect - Sensitive to environment	[28] / [68]
	MALS	Size (d_g), PSD	10 nm – 1000 nm	+ Online coupling	- Requires clean samples	[41, 55] / [53, 54, 68]
	LD	Size	10 nm – 10 mm c = 10^{-5}–10^{-1}	+ Large size range + Easy, fast + Automated	- Only spherical model	– / [68]
	NTA	Size (d_h), PSD, number conc.	30 nm – 2 µm c = 10^{-6}–10^{-5}	+ Better with polydisperse samples + Complex media + Particle corona	- Complex in operation - Spherical model	[26, 27] / [69, 70]
Imaging	TEM	Size, shape, aggregation, imaging	< 1 nm	+ High resolution + Precise size information	- Quantification difficult - Sample preparation - Expensive	[5] / [21, 22, 24, 75]
	SEM	Size, shape, aggregation, imaging, surface morphology	ca. 3 nm	+ High resolution	- Quantification difficult - Sample preparation - Charging effects	[28] / [21, 22, 24, 74, 75]
	ESEM	Size, shape, imaging, surface morphology	ca. 30 nm	+ Wet samples + Environmental conditions + Non-conductive samples	- Reduced resolution	– / [21, 22, 24, 74, 75]
	EDS	Elemental composition	nm range	+ Complementary to EM	- Elemental information not sufficient	– / [21, 22, 24, 74, 75]
	Optical & Fluorescence Microscopy	Size, shape, morphology Particle Location	> 1 µm	+ Non-destructive + Cheap, easy to handle + Sub-diffraction variants	- Diffraction-limited - Environmental plastic is not fluorescent	[72, 73] / –
	AFM	Size, shape, topography, aggregation	ca. 0.1 nm	+ High resolution + AFM-IR + TERS + In liquid	- Slow - Small area - Artefacts due to particle movement	– / [22, 24]
	STM	Size, shape, topography, aggregation	ca. 1 nm	+ High resolution	- Conductive samples -Slow -Small area	– / [22, 24, 79]
	CLSM	Size, shape, location	> 0.2 µm	+ Fluorescence imaging	- Small area - Diffraction limit	[72, 88–90] / –
	NSOM	Size, shape	ca. 30 nm	+ Fluorescence	- Slow - Small area	– / [22, 24, 91]

Tab. 3.2: Techniques for the characterization and imaging of subµ- and nanoplastic particles. References are divided whether they have been applied for subµ- and nanoplastic (left) and by documents from other fields (right). Concentration ranges quoted from [68].

3.4.1 Spectroscopy

3.4.1.1 Infrared Spectroscopy

FT-IR[12,93] is the most common spectroscopic technique in MP analysis[94], in which the irradiation of a sample with infrared light excites vibrational transitions, whose absorbance gives a specific so-called fingerprint spectrum that provides identification of the sample. With polymers, it is even able to display ageing by observation of surface oxidation via characteristic bands (e.g. carbonyl). FT-IR is applied mainly in two different modes of operation: attenuated total reflection FT-IR (ATR-FT-IR) which is used for handpicked MP (> 500 µm)[10] and focal plane array (FPA) detector-based micro-FT-IR (FPA-FT-IR) which images MP particles on filters with a resolution of ca. 10 – 20 µm[10,12].

FT-IR can only be applied for the bulk analysis of subµ- and nanoplastic, since the size limit for FT-IR single particle analysis is in the range of 10 µm[3,10,12,95]. Such an analysis has already been done to confirm the identity of nanoplastic contained in facial scrubs as PE, by drying the filtered suspension and performing an ATR-FT-IR measurement on the powder[1]. This, however, requires a few mg of dried particles, in this study the suspension that was dried for the measurement amounted to around 10^{10} particles. Another method for measuring the subµ- and nanoplastic particles is by producing a KBr pellet containing the sample[76,96]. FT-IR, as well as, RM (see Section 3.4.1) is capable of identifying mixtures, which produce an overlay of the respective spectra of each individual substance. Nonetheless, deconvoluting a spectrum of a multitude of (possibly impure) polymers, which may be the case with an environmental bulk sample, poses a significant challenge in data processing. Here, a separation technique may provide alleviation, if the setup can achieve (partial) separation of the polymers, by e.g. density or material-dependent surface properties.

There exists a commercial set-up that combines FT-IR with AFM, in order to be able to record chemical images with a spatial resolution below the diffraction limit. Here IR absorption at the location of the tip causes thermal expansion, which induces an oscillation of the AFM cantilever tip. With that, spectral and spatial information in the range of 50 nm can be obtained[82–84]. AFM-IR can be an interesting method for the analysis of nanoplastic particles, mainly for the analysis of special samples and specific particles. Since the method images selected areas, a representative analysis of many particles could be hard to realize.

3.4.1.2 Raman Microspectroscopy

Besides FT-IR, there is RM[13–15], which employs the inelastic scattering of laser light that gives a vibrational fingerprint spectrum. This spectrum is complementary to the FT-IR spectrum and also enables the unambiguous identification of the plastic particles. Since the light source does not need to be infrared light, shorter wavelength lasers (e.g. 532 nm) can be utilized, which results in higher spatial resolution. RM is, therefore, applied for the analysis of MP particles down to 1 µm[10,14,97,98].

RM has the potential for single particle analysis of subµ-plastic, because, as mentioned in Section 3.3.2.1, Raman microscopes are confocal, giving them submicrometer resolution. Although this resolution enables the single particle analysis of subµ-plastics, it would take several days to identify a representative amount of particles. Therefore, bulk measurements after preceding particle separation and characterization would provide a reliable subµ- and nanoplastic analysis, which could easily be complemented with a bulk FT-IR analysis.

As with AFM-IR, Raman spectroscopy has also been coupled to AFM for nanoscale imaging with spectroscopic information at spatial resolutions of 10 nm[85–87]. In tip-enhanced Raman spectroscopy (TERS), the tips are coated with Ag or Au and are able to generate Raman signal enhancements due to localized surface plasmons and the lightning rod effect[87]. TERS has been used to investigate polymer-blend interactions in thin films[85], which suggests that it may be applied for environmental subµ- and nanoplastic analysis. This, however, remains to be seen, since the surface plasmon signal enhancement is strongly dependent on the distance from the sample and the probe tip. Hence organic matter on the surface of the environmental plastic particle may obstruct a Raman spectroscopic identification.

3.4.1.3 X-ray Photoelectron Spectroscopy

In X-ray photoelectron spectroscopy (XPS) the sample is irradiated with X-radiation that causes the emission of photoelectrons, which contain information on their binding energy, hence giving element-specific characteristic bands. XPS valence band analysis allows the assignment of the binding energies of different orbitals, which are influenced by their chemical structure (e.g. methylene vs. methyl groups)[99]. XPS spectra have been used to confirm the chemical composition of a primary subµ PS latex [96] and primary PE nanoplastic particles in cosmetics[1]. It has to be noted, though, that XPS alone may not be able to unambiguously identify the polymer type. However, it has the capability to observe changes in the surface oxidation of subµ- and nanoplastic particles via changes in the oxygen content of the sample[51,96]. Further, XPS has been utilized to investigate the changes in the extracellular polymeric substances of waste water treatment plant (WWTP) microorganisms, which were induced by nanoplastic particles[76].

3.4.2 Gas Chromatographic-Mass Spectrometric Methods

Besides spectroscopy, the mass spectrometric polymer identification is another common approach in MP analysis that gives information on the mass fraction of polymer rather than particle count. There are two different methods. The first is Py-GC-MS, in which the sample – usually a handpicked MP particle with a mass up to 350 µg[100] – is thermally degraded in an inert atmosphere with the result that the pyrolysis fragments of the polymer structure can be separated by gas chromatography and characterized by mass spectrometry. Hence, polymers are identified by typical pyrolysis products[16,17,101]. The second GC-MS-based approach, thermal extraction desorption gas chromatography mass spectrometry (TED-GC-MS) allows the analysis of plastic in environmental samples (sample mass up to 20 mg[18]) without removal of (in)organic matrix. It combines thermal extraction of thermogravimetric analysis

products onto a solid-phase adsorber, which comprises the main difference to Py-GC-MS. The pyrolysis fragments are subsequently thermally desorbed into gas chromatography mass spectrometry to enable the identification of the polymer[18,102]. Py-GC-MS has recently been used for the first observation of subµ- and nanoplastic (< 1.2 µm) in the environment, i.e. in the North Atlantic Subtropical Gyre. Comparison to a reference database and principle component analysis enabled the detection of PE, PS, polyethylene terephthalate, and polyvinylchloride in the subµ-plastic fraction[2]. Py-GC-MS has also been validated for the identification of subµ- and nanoplastic particles (PS, 50 nm – 1000 nm) in a protocol that combines cross-flow UF, AF4 and Py-GC-MS[41].

These techniques, however, suffer from limits of detection (LODs), which will be too high for subµ- and nanoplastic detection without preconcentration. Mintenig et al. reported a LOD of 4 mg/L for a PS nanoplastic suspension, which they could decrease by a factor of 200 to 20 µg/L by concentration with a cross-flow UF[41]. A preconcentration will be essential for the detection of subµ- and nanoplastic, because its mass in environmental samples can be expected to be very low (see Section 3.1). Since no data on subµ- and nanoplastic content in the environment is available, it is difficult to project the demands to LODs and preconcentration factors. However, in the one instance, where subµ- and nanoplastic has been detected in the North Atlantic Subtropical Gyre with Py-GC-MS, a preconcentration by a factor 100 sufficed to enable a detection of characteristic decomposition products[2].

Py-GC-MS and TED-GC-MS are faster than spectroscopic single particle analysis but cannot provide information on particle size, number or PSD, as well as morphology or aggregation, which will have to be obtained by other particle characterization techniques like AF4-MALS or DLS. This emphasizes the need to combine different methods to generate the specific information, which is demanded to answer the individual analytical question (see Section 3.5).

Technique	Information	Range	Advantages	Disadvantages	References
FPA-FT-IR	Vibrational spectrum, Pigments, Additives, Ageing	> 10 µm	+ Non-destructive + Automated	- Not applicable for single subµ- and nanoplastic - Strong interference from water	[1, 41] / [10, 12]
ATR-FT-IR		Bulk	+ Simple, Fast		
AFM-IR	Spectrum, imaging	> 50 nm	+ High resolution + Chemical imaging	- Slow - Small area	– / [82, 83]
RM	Fingerprint spectrum, Pigments, Additives	> 0.5 µm Bulk	+ Non-destructive + Easy sample preparation + Fast + No interference from water	- Fluorescence	– / [3, 14]
XPS	Binding energies of orbitals	Bulk	+ Surface characterization	- UHV - Laborious	[1, 51] / [99]
Py-CG-MS	Mass, Polymer type, Additives	Bulk LOD: ng – µg e.g. PS: LOD:4 mg/L	+ Little sample preparation	- LOD dependent on polymer type - Some polymers difficult - Dry sample needed - Preconcentration necessary	[2, 41] / [16, 17]
TED-GC-MS			+ Measurement with matrix + Fast + Higher sample masses		– / [18]

Tab. 3.3: Techniques for the chemical identification and characterization of subµ- and nanoplastic particles. References are divided whether they have been applied for subµ- and nanoplastic (left) and by documents from other fields (right).

3.5 Roadmap

When regarding MP analysis, there is no single protocol but a multitude that covers a complex field, requiring specific methods for each different type of sample. This is also true for subµ- and nanoplastic analysis. Therefore, the essential first step is to clearly define the analytical question. This contains the sampling scenario, like surface water, tap water, food, soil, or WWTP in-/effluent (Figure 3.3), which, in turn, determines the following steps, in particular, the sample treatment to provide that the sample can be analyzed by the different techniques. It should be noted that, initially, when a method is transferred to an environmental sample, a preceding validation will be necessary.

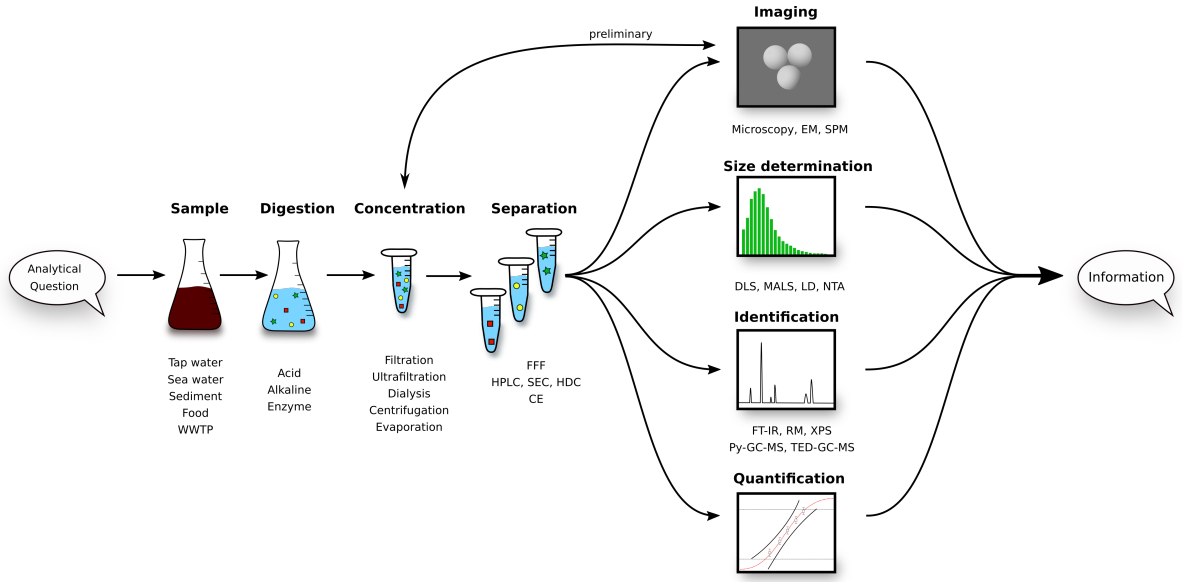

Fig. 3.3: Roadmap for the analytical process of subµ- and nanoplastic particles. Starting from the sample in its matrix, we present and discuss the single steps that will lead to a full subµ- and nanoplastic analysis.

The analytical question also defines the required information: Are detailed size parameters and geometry of importance or is a pure mass content sufficient information? Is chemical information on the polymer required? When a clear task has been set, the appropriate methods can be chosen.

If the sample contains too much organic matrix that would disrupt further analysis, a digestion of the matter is necessary. Acidic, alkaline, or enzymatic methods have been presented (Section 3.2.1). In case of samples without organic matrix, like drinking water, sample processing can be continued with the preconcentration step. Presumably, preconcentration is necessary for virtually all samples because – due to the small particle size – subµ- and nanoplastic content is always low when evaluated by mass. For this step, we discussed membrane filtration, UF, UC and mere removing of the solvent (Section 3.2.2). Here the desired information dictates the method of choice. If the PSD is to be studied, e.g. by DLS, sensitive UF should be utilized; if only SEM and spectroscopic identification are planned, filtration on a membrane filter could suffice; if a mass content is to be determined, a pellet from UC might be appropriate without further separation.

Following the concentration, a separation can isolate subµ- and nanoplastic from organic or inorganic

particles in other size fractions, for which we discussed field flow fractionation, chromatographic and electrophoretic methods (Section 3.2.3). If a sediment-free and digested sample is analyzed, so that only subµ- and nanoplastic particles should be left, the separation step could be omitted. In the present literature on subµ- and nanoplastic, AF4 has been the separation technique of choice because it has no stationary phase, its large size range and its online coupled detectors[32,41,51,55].

After the analyte has been isolated, a morphological characterization and chemical identification can be performed. For this, many different physicochemical parameters can be determined. Among these are size and PSD, shape, surface morphology, surface charge, degree of aggregation, surface functionalization, and chemical composition[22,23]. Which of them will be determined and with that, which methods will be applied depends on the research question. For data connected to particle size and PSD we discussed light scattering methods (Section 3.3.1) and for the imaging of the particles and their morphology, optical, electron and scanning probe microscopy (Section 3.3.2).

When applying methods for particle size and PSD characterization, the inherent differences between the spherical, monodisperse reference particles and environmental, secondary subµ- and nanoplastic have to be accounted for with a proper method validation. Environmental plastic is mostly generated by fragmentation, which causes the particles to have irregular shape and surface morphology, as well as a different surface charge as particle standards. However, the break-down of macroplastic to subµ- and nanoplastic will involve a substantially larger number of fragmentations, which should make the structural variety that we see in MP (e.g. fibers, sheets) less pronounced. Furthermore, these particles in the nanometer range will show increased Brownian motion and, therefore, be recognized by most methods by their hydrodynamic diameter rather than the actual shape. Therefore, the methods of Section 3.3 can, in many cases, be applied for the physical characterization of irregular subµ- and nanoplastic samples (e.g.[25–27]).

If the sample is polydisperse or suffers contaminations, laser scattering methods like DLS will lose accuracy. This emphasizes the need for a combined analysis with different techniques. Separation techniques like AF4, especially when coupled online, would alleviate the polydispersity and contamination problem by providing a monodisperse particle fractions at the moment of passage through the detector.

To characterize the morphology of the irregularly shaped particles, an imaging technique should complement the characterization. It should also be noted that, if possible, a preliminary imaging before deciding on a preconcentration and separation step could be well advised, because the morphology of secondary subµ- and nanoplastic can impact the efficiency of the individual methods (see Figure 3.3).

These methods for particle characterization and imaging, however, cannot provide information on polymer type. Finally, to obtain the chemical identification of the particle with respect to polymeric composition, single particle analysis or bulk measurements of a fraction can be performed, for which we presented spectroscopic and mass spectrometric methods (Section 3.4). Therein, depending on the analytical question, it is possible to obtain different information. Aside chemical identification of the polymer type, additives (e.g. stabilizer and pigments), as well as ageing can be determined. Most usually, though, a simple and fast distinction between polymer and natural particle is the core requirement of the

methods. Here, the thermoanalytical methods (Section 3.4.2) are currently the faster ones, considering that the microspectroscopic techniques perform single particle identification (on MP), which increases measurement time. When entering the realm of subµ- and nanoplastic, however, particle characterization can be performed by other, better suited, techniques (Section 3.3). This can make it sufficient to perform a spectroscopic bulk analysis on a plastic particle fraction, thereby reducing the measuring from thousands of spectra to a few, possibly making the time requirement equal to thermoanalytical methods. This directs the criteria for the choice of the method for chemical identification away from measurement time and towards the information, which the specific method can provide and its ability to be coupled to other techniques.

One such instance has been published by Mintenig et al. in which MP, subµ- and nanoplastic particles in aquatic samples can be detected and quantified. This framework connects the analysis of MP (by sieving/filtration and FT-IR) with the analysis of subµ- and nanoplastic, which is performed by preconcentrated with cross-flow UF and analyzed with AF4-MALS and Py-GC-MS[41]. The size limit for the change from FT-IR detection to AF4 and Py-GC-MS detection is 20 µm, which results the AF4 being in inversion mode down to ca. 1 µm, at which level another filtration is performed. This approach has the advantage of a fast FT-IR imaging, but requires two AF4 separations and Py-GC-MS identifications. Another protocol could be based on RM (Figure 3.3), which can perform MP analysis down to 1 µm, and, thus, would be more time consuming but could eliminate the AF4 separation in steric mode and also provide information on the single particle level for the entire MP range. This indicates that for the diverse analytical questions of subµ- and nanoplastic analysis, a versatile toolset will be of the essence.

3.6 Conclusion

Subµ- and nanoplastic pose new challenges to the methodology of environmental plastic analysis. In the chapters above, we discussed methods for the analysis of subµ- and nanoplastic, which have already been applied. In addition, from the field of environmental ENP analysis and from MP analysis, we discussed techniques, which have the potential to be transferred to plastic particles in the nanometer range. We emphasized the need to adapt the analytical protocol to the sample and the required information by selecting the appropriate techniques (Figure 3.2). This is important since subµ- and nanoplastic particles can be characterized by many different parameters, which influence their behavior, and it is unlikely to have one technique that gives a sufficient characterization.

Environmental analysis requires cost efficient and fast methods, which can handle a large number of samples in order to facilitate the evaluation of contamination and risk assessment. This emphasizes the need for optimized protocols that are tailored to quickly providing the required information on each sample, unless an academic interest warrants a full (and, therefore, time-consuming) characterization of a sample. It is, however, necessary to select and combine techniques that provide the minimal amount of data to answer the analytical question. This road to routine analysis will benefit from on-line coupling (e.g. AF4-UV-MALS, combined with a chemical identification) to enable reliability and high throughput.

For this, we presented various techniques that have the potential for subμ- and nanoplastic analysis and projected a roadmap for the whole analytical process.

Abbreviations

AF4	Asymmetric Flow Field-Flow Fractionation
AFM	Atomic Force Microscopy
ATR-FT-IR	Attenuated Total Reflection FT-IR
AUC	Analytical Ultracentrifugation
CE	Capillary Electrophoresis
CLSM	Confocal Laser Scanning Microscope
d_g	gyration diameter
d_h	hydrodynamic diameter
DLS	Dynamic Light Scattering
EDS	Energy Dispersive Spectroscopy
ELS	Electrophoretic Light Scattering
EM	Electron Microscopy
ENP	Engineered Nanoparticle
ESEM	Environmental Scanning Electron Microscopy
FFF	Field-Flow Fractionation
FPA-FT-IR	Focal Plane Array FT-IR
FT-IR	Fourier-Transform Infrared Spectroscopy
HDC	Hydrodynamic Chromatography
HPLC	High Performance Liquid Chromatography
LD	Laser Diffraction
LOD	Limit of Detection
MALS	Multi Angle Light Scattering
MP	Microplastic (1 µm – 5 mm)
Nanoplastic	1 – 100 nm
NOM	Natural Organic Matter
NSOM	Near-field Scanning Optical Microscopy
NTA	Nanoparticle Tracking Analysis
PE	Polyethylene
PS	Polystyrene
PSD	Particle Size Distribution
Py-GC-MS	Pyrolysis Gas Chromatography Mass Spectrometry
RM	Raman Microspectroscopy
SEC	Size Exclusion Chromatography
SEM	Scanning Electron Microscopy
SPM	Scanning Probe Microscopy
STM	Scanning Tunneling Microscopy
Subµ-plastic	Submicrometer-plastic (0.1 µm – 1 µm)
TED-GC-MS	Thermal Extraction Desorption Gas Chromatography Mass Spectrometry
TEM	Transmission Electron Microscopy

TERS	Tip-enhanced Raman Spectroscopy
UC	Ultracentrifugation
UF	Ultrafiltration
XPS	X-ray Photoelectron Spectroscopy

References

1. Hernandez, L. M.; Yousefi, N.; Tufenkji, N. Are There Nanoplastics in Your Personal Care Products? *Environmental Science & Technology Letters* **2017**, *4*, 280–285.
2. Ter Halle, A.; Jeanneau, L.; Martignac, M.; Jardé, E.; Pedrono, B.; Brach, L.; Gigault, J. Nanoplastic in the North Atlantic Subtropical Gyre. *Environmental Science & Technology* **2017**, *51*, 13689–13697.
3. Ivleva, N. P.; Wiesheu, A. C.; Niessner, R. Microplastic in Aquatic Ecosystems. *Angewandte Chemie, International Edition* **2017**, *56*, 1720–1739.
4. Commission, E. Commission recommendation of 18 October 2011 on the definition of nanomaterial (2011/696/EU). *Official Journal of the European Communities: Legis* **2011**, *L 275*, 38–40.
5. Gigault, J.; Halle, A. T.; Baudrimont, M.; Pascal, P.-Y.; Gauffre, F.; Phi, T.-L.; El Hadri, H.; Grassl, B.; Reynaud, S. Current opinion: What is a nanoplastic? *Environmental Pollution* **2018**, *235*, 1030–1034.
6. Hartmann, N. B.; Hüffer, T.; Thompson, R. C.; Hassellöv, M.; Verschoor, A.; Daugaard, A. E.; Rist, S.; Karlsson, T.; Brennholt, N.; Cole, M.; Herrling, M. P.; Hess, M. C.; Ivleva, N. P.; Lusher, A. L.; Wagner, M. Are We Speaking the Same Language? Recommendations for a Definition and Categorization Framework for Plastic Debris. *Environmental Science & Technology* **2019**, *53*, 1039–1047.
7. Costa, M. F.; Duarte, A. C. In *Characterization and analysis of microplastics*, Rocha-Santos, T. A. P., Duarte, A. C., Eds.; Comprehensive Analytical Chemistry, Vol. 75; Elsevier: Amsterdam, 2017, pp 25–47.
8. Imhof, H. K.; Schmid, J.; Niessner, R.; Ivleva, N. P.; Laforsch, C. A novel, highly efficient method for the separation and quantification of plastic particles in sediments of aquatic environments. *Limnology and Oceanography: Methods* **2012**, *10*, 524–537.
9. Hanvey, J. S.; Lewis, P. J.; Lavers, J. L.; Crosbie, N. D.; Pozo, K.; Clarke, B. O. A review of analytical techniques for quantifying microplastics in sediments. *Analytical Methods* **2017**, *9*, 1369–1383.
10. Huppertsberg, S.; Knepper, T. P. Instrumental analysis of microplastics-benefits and challenges. *Analytical and Bioanalytical Chemistry* **2018**, *410*, 6343–6352.

11. *Characterization and analysis of microplastics*; Rocha-Santos, T. A. P., Duarte, A. C., Eds.; Comprehensive Analytical Chemistry, Vol. / series editor: D. Barceló ; Volume 75; Elsevier: Amsterdam, 2017.

12. Löder, M. G. J.; Gerdts, G. In *Marine Anthropogenic Litter*, Bergmann, M., Gutow, L., Klages, M., Eds.; Springer International Publishing: Cham, 2015, pp 201–227.

13. Ribeiro-Claro, P.; Nolasco, M. M.; Araújo, C. In *Characterization and analysis of microplastics*, Rocha-Santos, T. A. P., Duarte, A. C., Eds.; Comprehensive Analytical Chemistry, Vol. 75; Elsevier: Amsterdam, 2017, pp 119–151.

14. Käppler, A.; Fischer, D.; Oberbeckmann, S.; Schernewski, G.; Labrenz, M.; Eichhorn, K.-J.; Voit, B. Analysis of environmental microplastics by vibrational microspectroscopy: FTIR, Raman or both? *Analytical and Bioanalytical Chemistry* **2016**, *408*, 8377–8391.

15. Araujo, C. F.; Nolasco, M. M.; Ribeiro, A. M. P.; Ribeiro-Claro, P. J. A. Identification of microplastics using Raman spectroscopy: Latest developments and future prospects. *Water Research* **2018**, *142*, 426–440.

16. Fischer, M.; Scholz-Böttcher, B. M. Simultaneous Trace Identification and Quantification of Common Types of Microplastics in Environmental Samples by Pyrolysis-Gas Chromatography-Mass Spectrometry. *Environmental Science & Technology* **2017**, *51*, 5052–5060.

17. Käppler, A.; Fischer, M.; Scholz-Böttcher, B. M.; Oberbeckmann, S.; Labrenz, M.; Fischer, D.; Eichhorn, K.-J.; Voit, B. Comparison of µ-ATR-FTIR spectroscopy and py-GCMS as identification tools for microplastic particles and fibers isolated from river sediments. *Analytical and Bioanalytical Chemistry* **2018**, *410*, 5313–5327.

18. Dümichen, E.; Eisentraut, P.; Bannick, C. G.; Barthel, A.-K.; Senz, R.; Braun, U. Fast identification of microplastics in complex environmental samples by a thermal degradation method. *Chemosphere* **2017**, *174*, 572–584.

19. Lenz, R.; Enders, K.; Nielsen, T. G. Microplastic exposure studies should be environmentally realistic. *Proceedings of the National Academy of Sciences of the United States of America* **2016**, *113*, E4121–2.

20. Hüffer, T.; Praetorius, A.; Wagner, S.; von der Kammer, F.; Hofmann, T. Microplastic Exposure Assessment in Aquatic Environments: Learning from Similarities and Differences to Engineered Nanoparticles. *Environmental Science & Technology* **2017**, *51*, 2499–2507.

21. Laborda, F.; Bolea, E.; Cepriá, G.; Gómez, M. T.; Jiménez, M. S.; Pérez-Arantegui, J.; Castillo, J. R. Detection, characterization and quantification of inorganic engineered nanomaterials: A review of techniques and methodological approaches for the analysis of complex samples. *Analytica Chimica Acta* **2016**, *904*, 10–32.

22. Lin, P.-C.; Lin, S.; Wang, P. C.; Sridhar, R. Techniques for physicochemical characterization of nanomaterials. *Biotechnology Advances* **2014**, *32*, 711–726.

23. Zänker, H.; Schierz, A. Engineered nanoparticles and their identification among natural nanoparticles. *Annual Review of Analytical Chemistry* **2012**, *5*, 107–132.

24. Tiede, K.; Boxall, A. B. A.; Tear, S. P.; Lewis, J.; David, H.; Hassellov, M. Detection and characterization of engineered nanoparticles in food and the environment. *Food Additives & Contaminants, Part A* **2008**, *25*, 795–821.

25. Gigault, J.; Pedrono, B.; Maxit, B.; Ter Halle, A. Marine plastic litter: The unanalyzed nano-fraction. *Environmental Science: Nano* **2016**, *3*, 346–350.

26. Lambert, S.; Wagner, M. Characterisation of nanoplastics during the degradation of polystyrene. *Chemosphere* **2016**, *145*, 265–268.

27. Lambert, S.; Wagner, M. Formation of microscopic particles during the degradation of different polymers. *Chemosphere* **2016**, *161*, 510–517.

28. Oriekhova, O.; Stoll, S. Heteroaggregation of nanoplastic particles in the presence of inorganic colloids and natural organic matter. *Environmental Science: Nano* **2018**, *5*, 792–799.

29. Chen, C.-S.; Le, C.; Chiu, M.-H.; Chin, W.-C. The impact of nanoplastics on marine dissolved organic matter assembly. *Science* **2018**, *634*, 316–320.

30. Rist, S.; Baun, A.; Hartmann, N. B. Ingestion of micro- and nanoplastics in Daphnia magna - Quantification of body burdens and assessment of feeding rates and reproduction. *Environmental Pollution* **2017**, *228*, 398–407.

31. Lu, Y.; Zhang, Y.; Deng, Y.; Jiang, W.; Zhao, Y.; Geng, J.; Ding, L.; Ren, H. Uptake and accumulation of polystyrene microplastics in zebrafish (danio rerio) and toxic effects in liver. *Environmental Science & Technology* **2016**, *50*, 4054–4060.

32. Correia, M.; Loeschner, K. Detection of nanoplastics in food by asymmetric flow field-flow fractionation coupled to multi-angle light scattering: Possibilities, challenges and analytical limitations. *Analytical and Bioanalytical Chemistry* **2018**, *410*, 5603–5615.

33. Ding, J.; Zhang, S.; Razanajatovo, R. M.; Zou, H.; Zhu, W. Accumulation, tissue distribution, and biochemical effects of polystyrene microplastics in the freshwater fish red tilapia (Oreochromis niloticus). *Environmental Pollution* **2018**, *238*, 1–9.

34. Zhu, B.-K.; Fang, Y.-M.; Zhu, D.; Christie, P.; Ke, X.; Zhu, Y.-G. Exposure to nanoplastics disturbs the gut microbiome in the soil oligochaete Enchytraeus crypticus. *Environmental Pollution* **2018**, *239*, 408–415.

35. Chen, Q.; Gundlach, M.; Yang, S.; Jiang, J.; Velki, M.; Yin, D.; Hollert, H. Quantitative investigation of the mechanisms of microplastics and nanoplastics toward zebrafish larvae locomotor activity. *Science of the Total Environment* **2017**, *584-585*, 1022–1031.

36. Jambeck, J. R.; Geyer, R.; Wilcox, C.; Siegler, T. R.; Perryman, M.; Andrady, A.; Narayan, R.; Law, K. L. Marine pollution. Plastic waste inputs from land into the ocean. *Science* **2015**, *347*, 768–771.

37. Oßmann, B. E.; Sarau, G.; Schmitt, S. W.; Holtmannspötter, H.; Christiansen, S. H.; Dicke, W. Development of an optimal filter substrate for the identification of small microplastic particles in food by micro-Raman spectroscopy. *Analytical and Bioanalytical Chemistry* **2017**, *409*, 4099–4109.

38. Käppler, A.; Windrich, F.; Löder, M. G. J.; Malanin, M.; Fischer, D.; Labrenz, M.; Eichhorn, K.-J.; Voit, B. Identification of microplastics by FTIR and Raman microscopy: A novel silicon filter substrate opens the important spectral range below 1300 cm(-1) for FTIR transmission measurements. *Analytical and Bioanalytical Chemistry* **2015**, *407*, 6791–6801.

39. Oßmann, B. E.; Sarau, G.; Holtmannspötter, H.; Pischetsrieder, M.; Christiansen, S. H.; Dicke, W. Small-sized microplastics and pigmented particles in bottled mineral water. *Water Research* **2018**, *141*, 307–316.

40. Pitt, J. A.; Kozal, J. S.; Jayasundara, N.; Massarsky, A.; Trevisan, R.; Geitner, N.; Wiesner, M.; Levin, E. D.; Di Giulio, R. T. Uptake, tissue distribution, and toxicity of polystyrene nanoparticles in developing zebrafish (Danio rerio). *Aquatic Toxicology* **2018**, *194*, 185–194.

41. Mintenig, S. M.; Bäuerlein, P. S.; Koelmans, A. A.; Dekker, S. C.; van Wezel, A. P. Closing the gap between small and smaller: Towards a framework to analyse nano- and microplastics in aqueous environmental samples. *Environmental Science: Nano* **2018**, *5*, 1640–1649.

42. Vauthier, C.; Bouchemal, K. Methods for the preparation and manufacture of polymeric nanoparticles. *Pharmaceutical Research* **2009**, *26*, 1025–1058.

43. Pansare, V. J.; Tien, D.; Thoniyot, P.; Prud'homme, R. K. Ultrafiltration of nanoparticle colloids. *Journal of Membrane Science* **2017**, *538*, 41–49.

44. Hassellöv, M.; Lyvén, B.; Haraldsson, C.; Sirinawin, W. Determination of continuous size and trace element distribution of colloidal material in natural water by on-line coupling of flow field-flow fractionation with ICPMS. *Analytical Chemistry* **1999**, *71*, 3497–3502.

45. Prestel, H.; Niessner, R.; Panne, U. Increasing the sensitivity of asymmetrical flow field-flow fractionation: Slot outlet technique. *Analytical Chemistry* **2006**, *78*, 6664–6669.

46. Sharp, D. G.; J. W. Beard Size and density of polystyrene particles measured by ultracentrifugation. *Journal of Biological Chemistry* **1950**, *185*, 247–253.

47. Li, P.; Kumar, A.; Ma, J.; Kuang, Y.; Luo, L.; Sun, X. Density gradient ultracentrifugation for colloidal nanostructures separation and investigation. *Science Bulletin* **2018**, *63*, 645–662.

48. Von der Kammer, F.; Ferguson, P. L.; Holden, P. A.; Masion, A.; Rogers, K. R.; Klaine, S. J.; Koelmans, A. A.; Horne, N.; Unrine, J. M. Analysis of engineered nanomaterials in complex matrices (environment and biota): General considerations and conceptual case studies. *Environmental Toxicology and Chemistry* **2012**, *31*, 32–49.

49. Planken, K. L.; Cölfen, H. Analytical ultracentrifugation of colloids. *Nanoscale* **2010**, *2*, 1849–1869.

50. Mächtle, W.; Börger, L., *Analytical ultracentrifugation of polymers and nanoparticles*, 1. Aufl.; Springer laboratory; Springer-Verlag: s.l., 2006.

51. Magrì, D.; Sánchez-Moreno, P.; Caputo, G.; Gatto, F.; Veronesi, M.; Bardi, G.; Catelani, T.; Guarnieri, D.; Athanassiou, A.; Pompa, P. P.; Fragouli, D. Laser Ablation as a Versatile Tool To Mimic Polyethylene Terephthalate Nanoplastic Pollutants: Characterization and Toxicology Assessment. *ACS Nano* **2018**, *12*, 7690–7700.

52. Giddings, J. Field-flow fractionation: Analysis of macromolecular, colloidal, and particulate materials. *Science* **1993**, *260*, 1456–1465.

53. Baalousha, M.; Stolpe, B.; Lead, J. R. Flow field-flow fractionation for the analysis and characterization of natural colloids and manufactured nanoparticles in environmental systems: A critical review. *Journal of Chromatography A* **2011**, *1218*, 4078–4103.

54. Wagner, M.; Holzschuh, S.; Traeger, A.; Fahr, A.; Schubert, U. S. Asymmetric Flow Field-Flow Fractionation in the Field of Nanomedicine. *Analytical Chemistry* **2014**, *86*, 5201–5210.

55. Gigault, J.; El Hadri, H.; Reynaud, S.; Deniau, E.; Grassl, B. Asymmetrical flow field flow fractionation methods to characterize submicron particles: Application to carbon-based aggregates and nanoplastics. *Analytical and Bioanalytical Chemistry* **2017**, *409*, 6761–6769.

56. Klein, S.; Dimzon, I. K.; Eubeler, J.; Knepper, T. P. In *Freshwater Microplastics : Emerging Environmental Contaminants?*, Wagner, M., Lambert, S., Eds.; Springer International Publishing: Cham, 2018, pp 51–67.

57. Bednar, A. J.; Poda, A. R.; Mitrano, D. M.; Kennedy, A. J.; Gray, E. P.; Ranville, J. F.; Hayes, C. A.; Crocker, F. H.; Steevens, J. A. Comparison of on-line detectors for field flow fractionation analysis of nanomaterials. *Talanta* **2013**, *104*, 140–148.

58. Gigault, J.; Zhang, W.; Lespes, G.; Charleux, B.; Grassl, B. Asymmetrical flow field-flow fractionation analysis of water suspensions of polymer nanofibers synthesized via RAFT-mediated emulsion polymerization. *Analytica Chimica Acta* **2014**, *819*, 116–121.

59. Engel, A.; Plöger, M.; Mulac, D.; Langer, K. Asymmetric flow field-flow fractionation (AF4) for the quantification of nanoparticle release from tablets during dissolution testing. *International Journal of Pharmaceutics* **2014**, *461*, 137–144.

60. Wahlund, K.-G. Flow field-flow fractionation: Critical overview. *Journal of Chromatography A* **2013**, *1287*, 97–112.

61. Soto-Alvaredo, J.; Montes-Bayón, M.; Bettmer, J. Speciation of silver nanoparticles and silver(I) by reversed-phase liquid chromatography coupled to ICPMS. *Analytical Chemistry* **2013**, *85*, 1316–1321.

62. Zhou, X.-X.; Liu, R.; Liu, J.-F. Rapid chromatographic separation of dissoluble Ag(I) and silver-containing nanoparticles of 1-100 nanometer in antibacterial products and environmental waters. *Environmental Science & Technology* **2014**, *48*, 14516–14524.

63. Tiede, K.; Boxall, A. B. A.; Tiede, D.; Tear, S. P.; David, H.; Lewis, J. A robust size-characterisation methodology for studying nanoparticle behaviour in 'real' environmental samples, using hydrodynamic chromatography coupled to ICP-MS. *Journal of Analytical Atomic Spectrometry* **2009**, *24*, 964.

64. Gray, E. P.; Bruton, T. A.; Higgins, C. P.; Halden, R. U.; Westerhoff, P.; Ranville, J. F. Analysis of gold nanoparticle mixtures: A comparison of hydrodynamic chromatography (HDC) and asymmetrical flow field-flow fractionation (AF4) coupled to ICP-MS. *Journal of Analytical Atomic Spectrometry* **2012**, *27*, 1532.

65. Adam, V.; Vaculovicova, M. Capillary electrophoresis and nanomaterials - Part I: Capillary electrophoresis of nanomaterials. *Electrophoresis* **2017**, *38*, 2389–2404.

66. Rodriguez, M. A.; Armstrong, D. W. Separation and analysis of colloidal/nano-particles including microorganisms by capillary electrophoresis: A fundamental review. *Journal of Chromatography B* **2004**, *800*, 7–25.

67. Diaz, L.; Peyrot, C.; Wilkinson, K. J. Characterization of polymeric nanomaterials using analytical ultracentrifugation. *Environmental Science & Technology* **2015**, *49*, 7302–7309.

68. Xu, R. Light scattering: A review of particle characterization applications. *Particuology* **2015**, *18*, 11–21.

69. Filipe, V.; Hawe, A.; Jiskoot, W. Critical evaluation of Nanoparticle Tracking Analysis (NTA) by NanoSight for the measurement of nanoparticles and protein aggregates. *Pharmaceutical Research* **2010**, *27*, 796–810.

70. Gallego-Urrea, J. A.; Tuoriniemi, J.; Pallander, T.; Hassellöv, M. Measurements of nanoparticle number concentrations and size distributions in contrasting aquatic environments using nanoparticle tracking analysis. *Environmental Chemistry* **2010**, *7*, 67.

71. Zoubir, A., *Raman imaging: Techniques and applications*; Springer Series in Optical Sciences, Vol. 168; Springer: Berlin, Heidelberg, 2012.

72. Dawson, A. L.; Kawaguchi, S.; King, C. K.; Townsend, K. A.; King, R.; Huston, W. M.; Bengtson Nash, S. M. Turning microplastics into nanoplastics through digestive fragmentation by Antarctic krill. *Nature Communications* **2018**, *9*, 1001.

73. Dawson, A.; Huston, W.; Kawaguchi, S.; King, C.; Cropp, R.; Wild, S.; Eisenmann, P.; Townsend, K.; Bengtson Nash, S. Uptake and depuration kinetics influence microplastic bioaccumulation and toxicity in Antarctic Krill (Euphausia superba). *Environmental Science & Technology* **2018**, *52*, 3195–3201.

74. Zhou, W.; Wang, Z. L., *Scanning microscopy for nanotechnology: Techniques and applications*; Springer: New York, NY, 2007.

75. Michler, G. H., *Electron microscopy of polymers*; Springer Laboratory; Springer: Berlin and Heidelberg, 2008.

76. Feng, L.-J.; Wang, J.-J.; Liu, S.-C.; Sun, X.-D.; Yuan, X.-Z.; Wang, S.-G. Role of extracellular polymeric substances in the acute inhibition of activated sludge by polystyrene nanoparticles. *Environmental Pollution* **2018**, *238*, 859–865.

77. Cai, L.; Hu, L.; Shi, H.; Ye, J.; Zhang, Y.; Kim, H. Effects of inorganic ions and natural organic matter on the aggregation of nanoplastics. *Chemosphere* **2018**, *197*, 142–151.

78. Liu, J.; Ma, Y.; Zhu, D.; Xia, T.; Qi, Y.; Yao, Y.; Guo, X.; Ji, R.; Chen, W. Polystyrene nanoplastics-enhanced contaminant transport: Role of irreversible adsorption in glassy polymeric domain. *Environmental Science & Technology* **2018**, *52*, 2677–2685.

79. Bonnell, D. A., *Scanning probe microscopy and spectroscopy: Theory, techniques, and applications*, 2. ed.; Wiley-VCH: New York, NY, 2001.

80. Nolte, T. M.; Hartmann, N. B.; Kleijn, J. M.; Garnæs, J.; van de Meent, D.; Jan Hendriks, A.; Baun, A. The toxicity of plastic nanoparticles to green algae as influenced by surface modification, medium hardness and cellular adsorption. *Aquatic Toxicology* **2017**, *183*, 11–20.

81. Chen, Y.; Huang, W. Numerical simulation of the geometrical factors affecting surface roughness measurements by AFM. *Measurement Science and Technology* **2004**, *15*, 2005–2010.

82. Dazzi, A.; Saunier, J.; Kjoller, K.; Yagoubi, N. Resonance enhanced AFM-IR: A new powerful way to characterize blooming on polymers used in medical devices. *International Journal of Pharmaceutics* **2015**, *484*, 109–114.

83. Dazzi, A.; Prater, C. B.; Hu, Q.; Chase, D. B.; Rabolt, J. F.; Marcott, C. AFM-IR: Combining atomic force microscopy and infrared spectroscopy for nanoscale chemical characterization. *Applied Spectroscopy* **2012**, *66*, 1365–1384.

84. Dazzi, A.; Prater, C. B. AFM-IR: Technology and Applications in Nanoscale Infrared Spectroscopy and Chemical Imaging. *Chemical Reviews* **2017**, *117*, 5146–5173.

85. Yeo, B.-S.; Amstad, E.; Schmid, T.; Stadler, J.; Zenobi, R. Nanoscale Probing of a Polymer-Blend Thin Film with Tip-Enhanced Raman Spectroscopy. *Small* **2009**, *5*, 952–960.

86. Schmid, T.; Opilik, L.; Blum, C.; Zenobi, R. Nanoscale chemical imaging using tip-enhanced Raman spectroscopy: A critical review. *Angewandte Chemie, International Edition* **2013**, *52*, 5940–5954.

87. Kumar, N.; Mignuzzi, S.; Su, W.; Roy, D. Tip-enhanced Raman spectroscopy: Principles and applications. *EPJ Techniques and Instrumentation* **2015**, *2*, 1538.

88. Cui, R.; Kim, S. W.; An, Y.-J. Polystyrene nanoplastics inhibit reproduction and induce abnormal embryonic development in the freshwater crustacean Daphnia galeata. *Scientific Reports* **2017**, *7*, 12095.

89. González-Fernández, C.; Tallec, K.; Le Goïc, N.; Lambert, C.; Soudant, P.; Huvet, A.; Suquet, M.; Berchel, M.; Paul-Pont, I. Cellular responses of Pacific oyster (Crassostrea gigas) gametes exposed in vitro to polystyrene nanoparticles. *Chemosphere* **2018**, *208*, 764–772.

90. Chae, Y.; Kim, D.; Kim, S. W.; An, Y.-J. Trophic transfer and individual impact of nano-sized polystyrene in a four-species freshwater food chain. *Scientific Reports* **2018**, *8*, 284.

91. Heinzelmann, H.; Pohl, D. W. Scanning near-field optical microscopy. *Applied Physics A Solids and Surfaces* **1994**, *59*, 89–101.

92. Primpke, S.; Lorenz, C.; Rascher-Friesenhausen, R.; Gerdts, G. An automated approach for microplastics analysis using focal plane array (FPA) FTIR microscopy and image analysis. *Analytical Methods* **2017**, *9*, 1499–1511.

93. Renner, G.; Schmidt, T. C.; Schram, J. In *Characterization and analysis of microplastics*, Rocha-Santos, T. A. P., Duarte, A. C., Eds.; Comprehensive Analytical Chemistry, Vol. 75; Elsevier: Amsterdam, 2017, pp 67–118.

94. Renner, G.; Schmidt, T. C.; Schram, J. Analytical methodologies for monitoring micro(nano)plastics: Which are fit for purpose? *Current Opinion in Environmental Science & Health* **2018**, *1*, 55–61.

95. Simon, M.; van Alst, N.; Vollertsen, J. Quantification of microplastic mass and removal rates at wastewater treatment plants applying Focal Plane Array (FPA)-based Fourier Transform Infrared (FT-IR) imaging. *Water Research* **2018**, *142*, 1–9.

96. Lu, S.; Zhu, K.; Song, W.; Song, G.; Chen, D.; Hayat, T.; Alharbi, N. S.; Chen, C.; Sun, Y. Impact of water chemistry on surface charge and aggregation of polystyrene microspheres suspensions. *Science of the Total Environment* **2018**, *630*, 951–959.

97. Imhof, H. K.; Laforsch, C.; Wiesheu, A. C.; Schmid, J.; Anger, P. M.; Niessner, R.; Ivleva, N. P. Pigments and plastic in limnetic ecosystems: A qualitative and quantitative study on microparticles of different size classes. *Water Research* **2016**, *98*, 64–74.

98. Schymanski, D.; Goldbeck, C.; Humpf, H.-U.; Fürst, P. Analysis of microplastics in water by micro-Raman spectroscopy: Release of plastic particles from different packaging into mineral water. *Water Research* **2018**, *129*, 154–162.

99. Foerch, R.; Beamson, G.; Briggs, D. XPS valence band analysis of plasma-treated polymers. *Surface and Interface Analysis* **1991**, *17*, 842–846.

100. Fries, E.; Dekiff, J. H.; Willmeyer, J.; Nuelle, M.-T.; Ebert, M.; Remy, D. Identification of polymer types and additives in marine microplastic particles using pyrolysis-GC/MS and scanning electron microscopy. *Environmental Science. Processes & Impacts* **2013**, *15*, 1949–1956.

101. Kusch, P. In *Characterization and analysis of microplastics*, Rocha-Santos, T. A. P., Duarte, A. C., Eds.; Comprehensive Analytical Chemistry, Vol. 75; Elsevier: Amsterdam, 2017, pp 169–207.

102. Dümichen, E.; Barthel, A.-K.; Braun, U.; Bannick, C. G.; Brand, K.; Jekel, M.; Senz, R. Analysis of polyethylene microplastics in environmental samples, using a thermal decomposition method. *Water Research* **2015**, *85*, 451–457.

Chapter 4

Raman Microspectroscopy and Scanning Electron Microscopy for Primary and Secondary Nanoplastic

4.1 Introduction

One approach to close the methodological gap for nanoplastic (Section 1.2.2) is to start with established techniques for MP particle analysis and optimize measurement approaches with the objective of pushing analysis to lower size limits (Section 1.2.4). Since RM incorporates an optical microscope, its size range is determined by the numerical aperture and the wavelength. From that follows a limit for the resolution at ca. 250 nm. This could allow the analysis of subµ-plastic particles, however the morphological characterization would be insufficient this close to the diffraction limit. Thus, in this thesis RM was combined with scanning electron microscopy (SEM) to provide high-resolution imaging of the investigated particles. To this end, a suitable substrate and sample preparation was developed and, subsequently the applicability on primary and secondary nanoplastic was shown.

4.2 Coupling of RM and SEM

4.2.1 Theoretical Resolution

The feasible limit of single particle analysis is determined by the Airy disc of the laser and the governing criterion for the distinction of two separate points, as discussed in Chapter 2. Briefly, the size of the Airy disc is $d_{\mathrm{Laser}} = \frac{1.22\lambda}{N.A.}$, with the wavelength λ and the numerical aperture $N.A.$. For the present study, a green laser of $\lambda = 532\,\mathrm{nm}$ and a 100 $\times$ magnification objective with a numerical aperture of $N.A. = 0.9$ has been used. Thus, the laser spot size equates to $d_{\mathrm{Laser}} = 0.72\,\mu\mathrm{m}$ and with the different criteria the resolution will result in $r_{\mathrm{Rayleigh}} = 0.31\,\mu\mathrm{m}$, $r_{80\,\%} = 0.25\,\mu\mathrm{m}$ and $r_{\mathrm{Sparrow}} = 0.20\,\mu\mathrm{m}$, respectively[1]. Furthermore, as the definition of the Airy disc implies, this resolution could, theoretically, be improved by

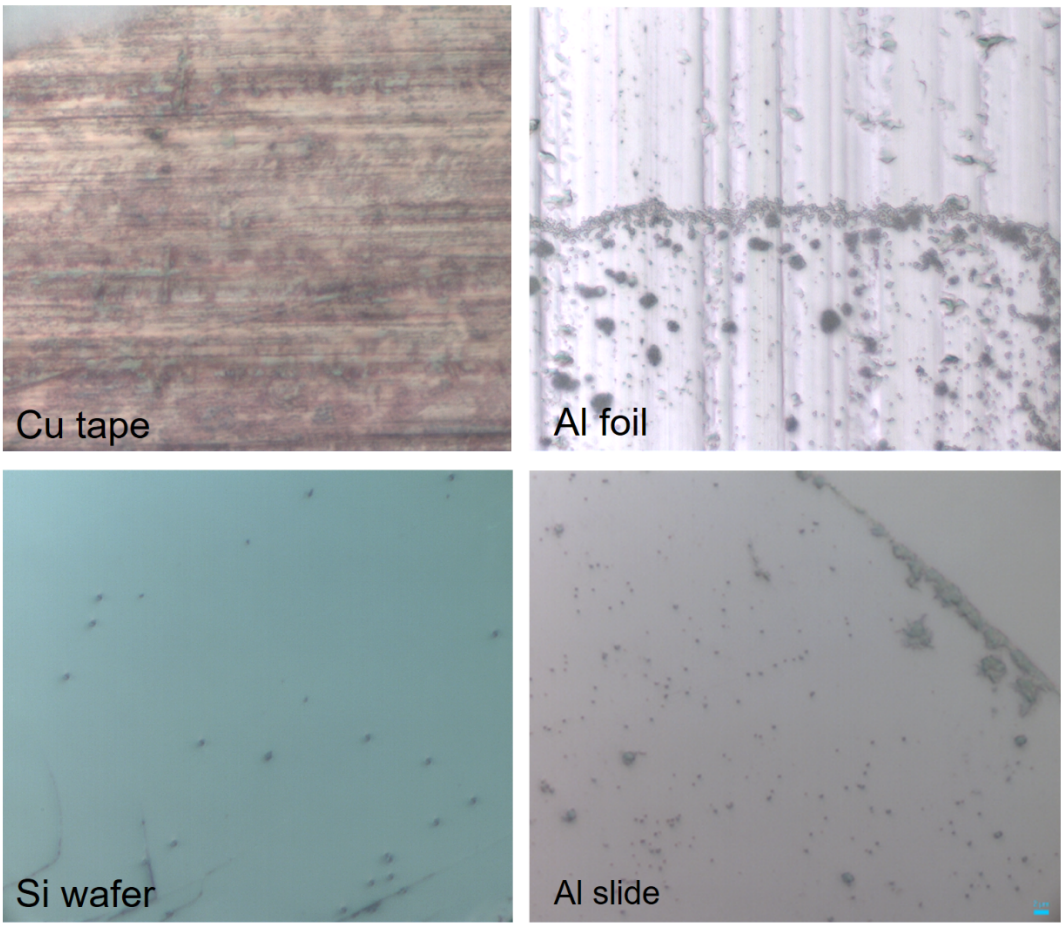

Fig. 4.1: Substrates that were tested for the coupling of RM and SEM. Cu tape showed an insufficiently smooth surface and background Raman signal. Al foil had no background but was still too rough. Si is perfectly smoot but has an obstructive spectrum. Hence, Al coated slides were the optimal choice for the nanoplastic analysis.

increasing the numerical aperture (e.g. with an oil immersion objective, which is, however, impractical for dried particles on a substrate) or using a shorter wavelength (i.e. ultra-violet) laser.

From these values, it seems reasonable to project 0.25 µm as lower particle size, which should be possible to analyze in RM single particle analysis. As the following characterization will show, this theoretical limit can be achieved. It needs, however, to be kept in mind that the theoretical definition of resolution remains an optimal case. The application of real nanoplastic single particle analysis, may, of course, see detrimental effects due to sample treatment or the fragmented nature of the particles. As the nanoplastic particles will be smaller than the laser spot, the RM analysis needs to be done on separately placed particles. If two nanoplastic particles lay next to each other, it will be impossible to target the individual particle. Consequently, if the light of the laser spot interacts with adjacent particles, the resulting chemical identification can become ambiguous.

4.2.2 Sample Preparation

Implementing a combined analysis with RM and SEM of subµ-plastic particles requires an adequately smooth surface due to the small particle size, which is in the size range of visible light. Further, the sample carrier should be electrically conducting to provide an electron sink for visualization by SEM. For this application, we have evaluated copper tape, aluminum foil, aluminum coated glass slides and silicon wafers (Figure 4.1). Copper tape proved to be too rough and inappropriate for the visualization of 500 nm particles and it produced a fluorescence background, which impeded RM. To reduce the obstructing fluorescence, an aluminum substrate was used, but a standard aluminum foil is too uneven for subµ-plastic particles. For greater smoothness, we tested a silicon wafer, which gave an optimal surface for subµ-particles. However it is Raman active and produces strong peaks that overlap with the comparably low intensity signals of the small plastic particles (Figure 4.2). Eventually, an aluminium-coated object slide has proved optimal, because it combined smoothness comparable to silicon wafers, electrical conductivity allowing SEM imaging, and lack of Raman background. This is in agreement with the other studies: Sarau et al. used Al-coated polycarbonate filters[2], Sobhani et al. prepared their samples for RM measurement on glass slides and for SEM analysis on gold-coated silicon wafers[3], and Hernandez et al. used silicon wafers for SEM analysis[4].

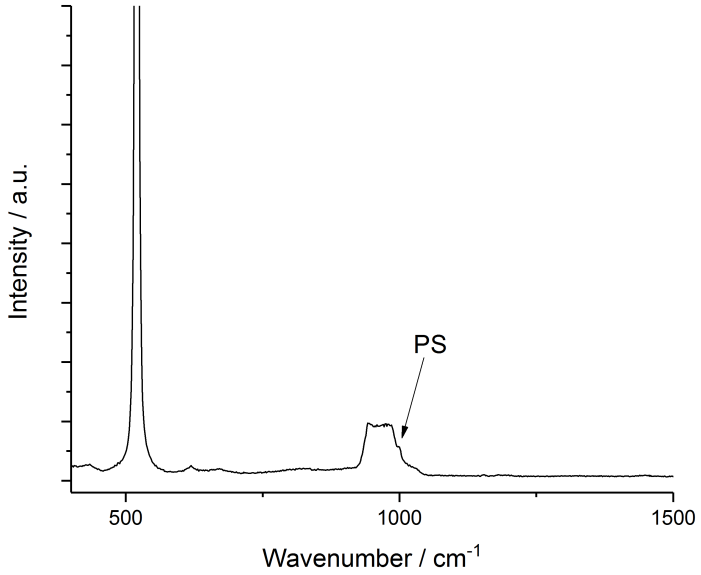

Fig. 4.2: The Si wafer has an own spectrum, which is much more intense than the signal of the nanometer sized particles and, thus, interferes with the signal of e.g. polystyrene.

For RM and SEM analysis, 1 µL of the particle suspension was dropped on the respective substrates and was left to dry. This treatment showed to be sufficient for both RM and SEM. For the latter analysis type, it might be necessary to coat the sample with metal or to switch to low vacuum mode if the plastic particles are too large and exhibit charging effects. Nanoplastic, however, experienced no detrimental effects in SEM visualization. Although, in some cases the electron irradiation in the SEM prevented RM analysis so that the otherwise stable particles only showed amorphous carbon signals in the spectrum. Thus, RM analysis has to be performed before the SEM imaging. Caution has also to be advised

on finding the same area of interest for SEM analysis, where the RM inspection has been performed before. Although high-end instruments that correlate RM and SEM[2] (see Chapter 2) are available, in this study, the samples were transferred between the instruments manually. Thus, the position needs to be located by reference to characteristic „landmarks“ in the dried sample spot, or, alternatively, to special non-symmetric markings in the substrate. Here, to facilitate this, images of different magnification were documented so that the location can easily be found. This is exemplified in Figure 4.3.

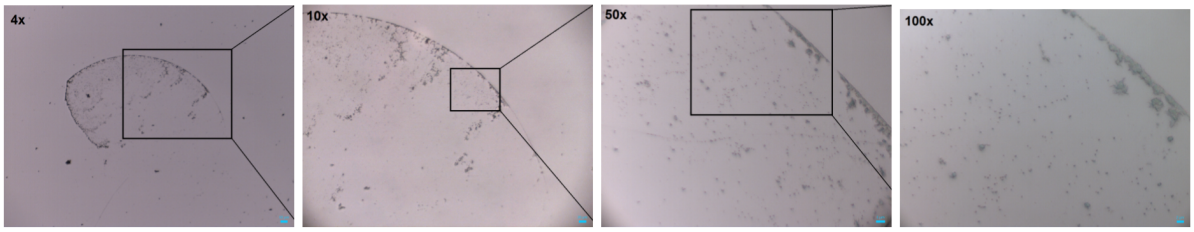

Fig. 4.3: Documenting images of different magnification helps in orienting and finding the region of interest when transferring the sample from RM to SEM.

4.2.3 RM-SEM

The coupling of RM and SEM was demonstrated on two systems. First, well-characterized PS Latices were used to establish the coupling and perform size characterization. Second, fragmented PS particles were used to show the applicability for nanoplastic samples.

4.2.3.1 500 nm Polystyrene Particles

First, RM-SEM has been performed on 500 nm polystyrene particles (PS500), the data of which can be seen in Figure 4.4. These particles can easily be recognized and targeted with the optical microscope due to their uniform, spherical form and the smoothness of the Al-coated slide. Individual spectra confirm the polymer identity and demonstrate the ability of the technique to analyze unknown environmental samples. The chemical identification is illustrated here with a 2D Raman map displaying the precision of the applied DuoScan stage, which measures with 0.05 µm steps. In Figure 4.4 this is depicted in a height profile, plotting the intensity of the 1000 cm^{-1} band. Here, the diameter of the 500 nm spheres appears much larger ($\sim$ 2 µm), which is caused by the fact that the laser spot has a diameter of $\sim$ 0.7 µm and, therefore, increases the effective range of interaction. From this sample, it can be further seen that directly adjacent particles cannot be distinguished by the Raman map, which is the case for the three adjacent particles. However, the other two close particles can indeed be distinguished by the Raman intensity profile. Finally, the optical and Raman information are complemented by the SEM image wherein the morphology of the particles is clearly visible and sizes can be acquired.

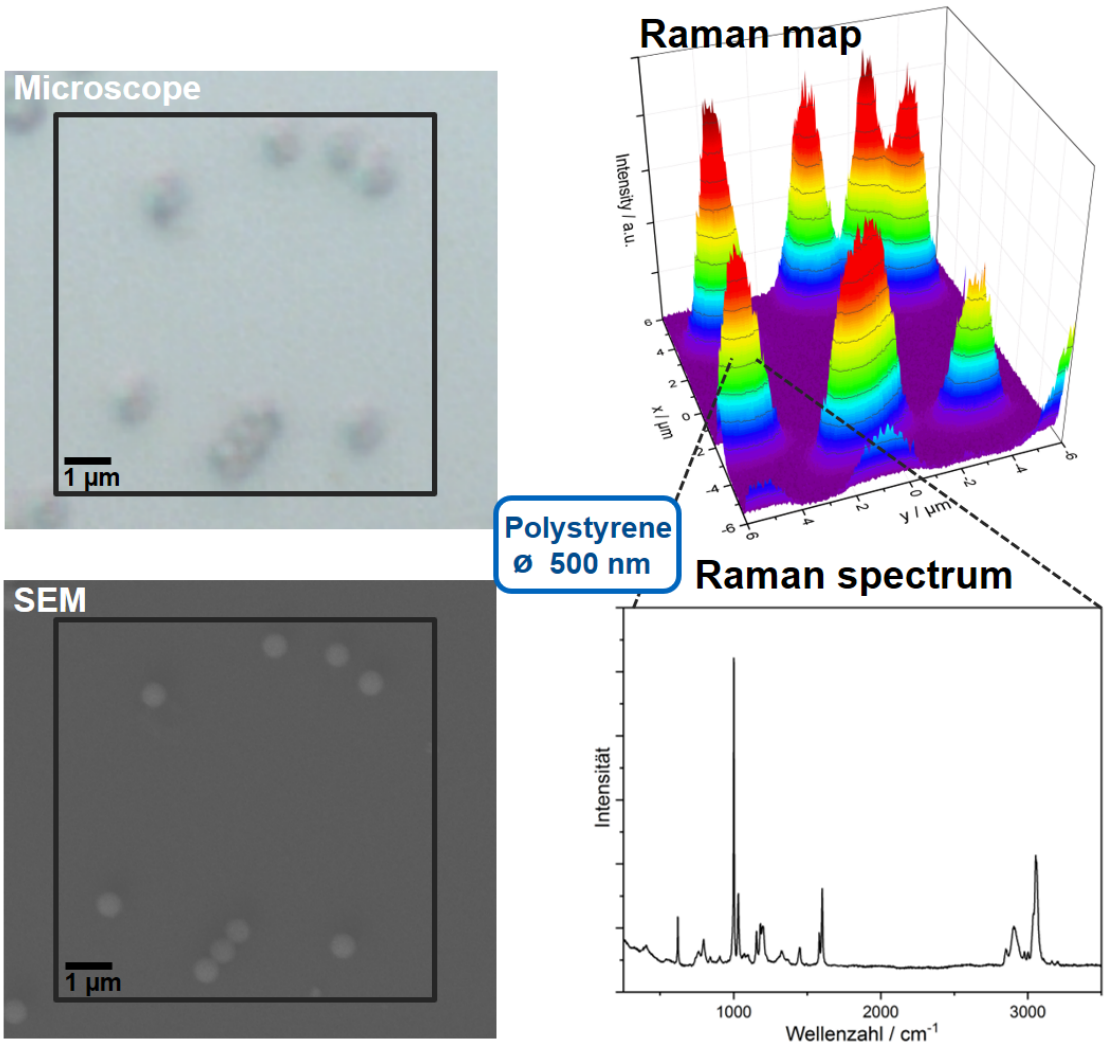

Fig. 4.4: RM-SEM of 500 nm PS particles. The microscope image shows the particles and permits targeting for single particle analysis and the SEM image augments the high-resolution morphology of the particles. The 3D Raman map of the 1000 cm^{-1} band illustrates that, on this sample, each point with a 0.05 µm step size can be investigated by Raman spectroscopy, giving precise chemical information.

4.2.3.2 250 nm Polystyrene Particles

In a next step, PS particles with a diameter of 250 nm (their labelled size was 226 nm, although the SEM sizing showed them to be closer to 250 nm, thus, this denomination was chosen) were tested with RM-SEM. The respective data can be seen in Figure 4.5. Here, again the particles can be seen, however barely, since they are at the theoretical size limitation, due to the smoothness of the Al-coated object slide. The correlated SEM image complements the morphology of the particles. RM enables the spectral identification of each particle, however the precise targeting could only be achieved manually. To illustrate the resolution a line scan was performed over two close particles. This choice was due to the instability of the particles against the thermal stress of the prolonged irradiation during a 2D map acquisition (which took 18h in the case of Figure 4.4). This line scan shows the resolution of the two

particles roughly according to the Rayleigh criterion and, furthermore, demonstrates the possibility of RM-SEM to visualize and chemically identify particles of 250 nm.

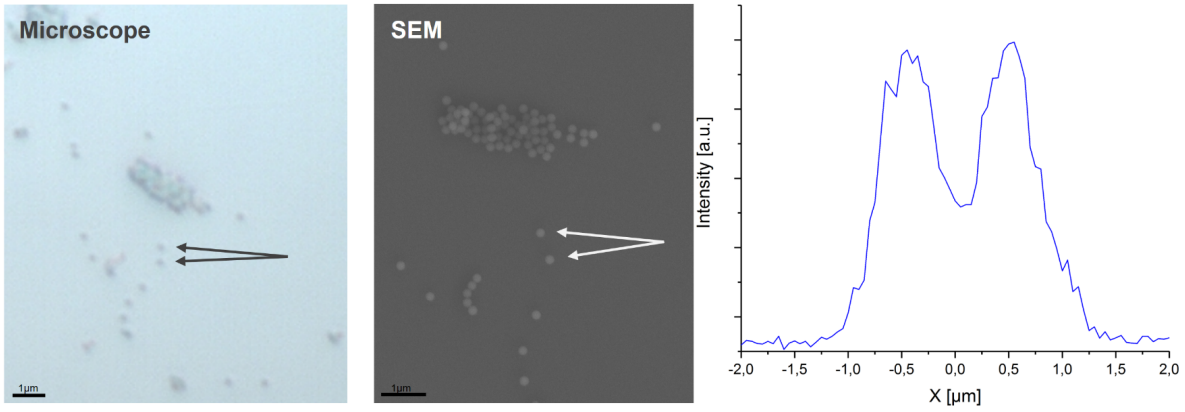

Fig. 4.5: RM-SEM of 250 nm PS particles. The microscope image shows the particles and permits targeting for single particle analysis and the SEM image augments the high-resolution morphology of the particles. The Raman line scan at the 1000 cm^{-1} band illustrates the resolution of two distinct particles at the theoretical limit and Raman spectroscopy, giving precise chemical information.

4.2.3.3 100 nm Polystyrene Particles

Using this RM-SEM setup, the next limit was attempted by analyzing 100 nm PS particles, however here is was no longer possible to see the particles with the optical microscope, hence targeting for RM identification could not be performed. This allows to delineate the limit of practical single particle analysis at 250 nm, which is in accordance with the theoretical considerations (Section 4.2.1).

4.2.3.4 Fragmented Polystyrene Particles

Subsequent to the size characterization with PS latices, secondary nanoplastic, i.e. fragmented particles were analyzed by RM-SEM. These were produced in accordance with the method of von der Esch et al.[5] by ultrasonication followed by filtration through a 1 µm filter membrane to separate larger particles. Figure 4.6 depicts the data of such an analysis. Here the optical microscope image can show the particle location only roughly, which is sufficient for the targeting of individual particles (a – e). In the SEM image these particles can be characterized by their morphology and size, which was in the range of 387 nm – 770 nm. This is an agreement with the sizes of the primary nanoplastic, considering that irregular particles delineate from the homogeneous shape of the spheres. Therefore, the lower limit of 250 nm seems to be challenging to be achieved. However, the spectra permit the chemical identification of secondary nanoplastic, as well as the primary, and the Raman map, principally, shows the spatial distribution of the particles. However, in this sample the particles were too closely adjacent to each other to be distinguished.

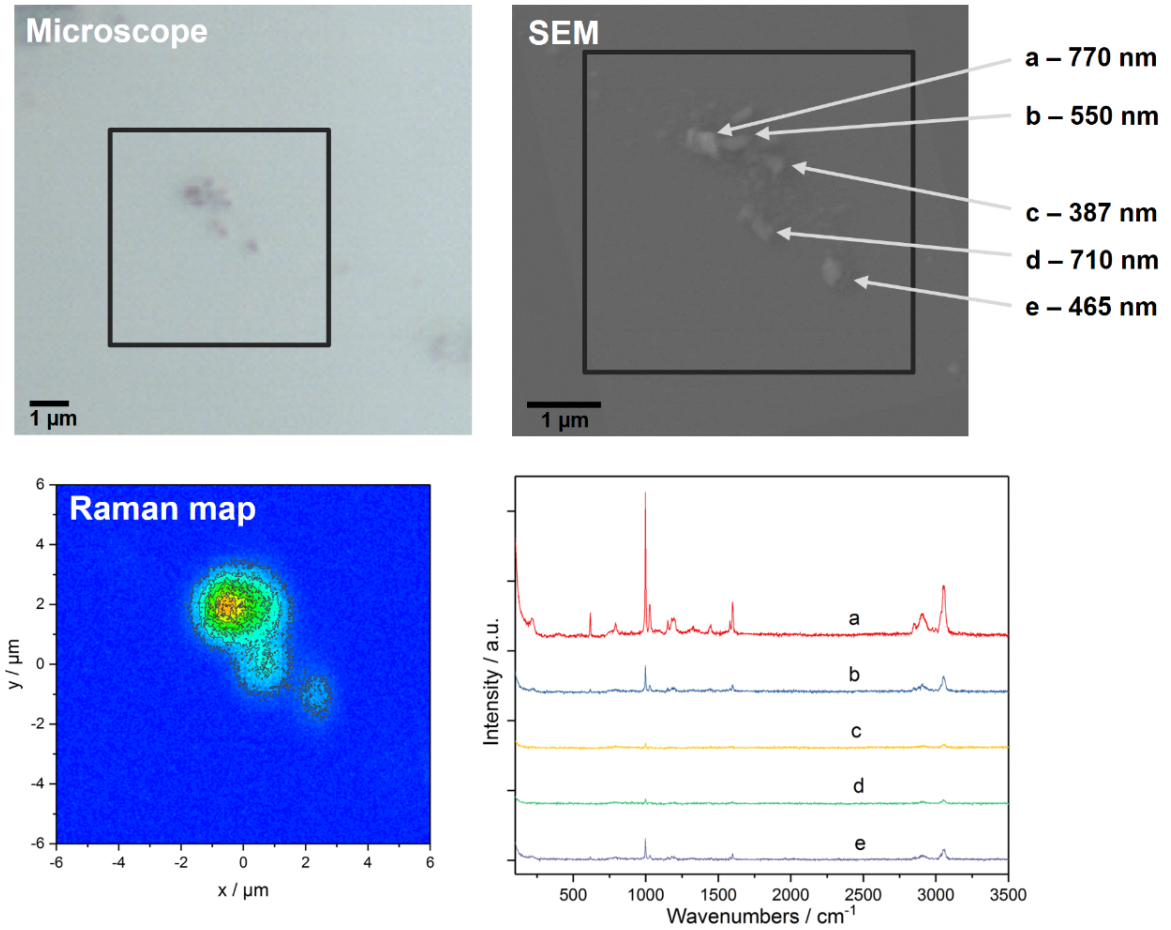

Fig. 4.6: RM-SEM of fragmented PS particles. The microscope image shows the particle cluster and permits targeting for single particle analysis and the SEM image augments the high-resolution morphology and sizes of the particles a — e. The 2D Raman map of the 1000 cm^{-1} band illustrates that, on this sample, each point with a 0.05 µm step size can be investigated by Raman spectroscopy, it the particles lay separately on the Al-coated slide. The individual spectra of the particles a – e show their respective chemical identity.

4.3 Discussion

In this work, a practical measurement approach for the analysis of subµ-plastic particles by RM and SEM has been explored. To this end, Aluminium coated object slides were found to be optimal substrates and a suitable sample preparation was performed, which enabled the investigation of the same particles of the sample. At first, primary nanoplastic (500 nm, 250 nm, 100 nm) was used to find the lowest particle size, which could be targeted. This was 250 nm, which is in agreement with the theoretical limit. Subsequently, secondary nanoplastic, which had been produced by fragmentation through ultrasonic treatment[5], was analyzed chemically and morphologically. Thus, it could be shown that the present coupling of RM and SEM is able to perform particle identification by Raman spectroscopy and to provide visual characterization by SEM.

Parallel to this work, Sobhani et al. published the application of Raman imaging for primary nanoplastic down to 100 nm[3]. Subsequent studies of this group extended the Raman imaging to particles smaller than

the diffraction limit by correlating the Raman emission intensity profile to the original particle size[6] They also improved the signal-to-noise ratio by analyzing multiple images of the same particle[7]. Furthermore, Valsesia et al. analyzed nanoplastic, which was first extracted by enzymatic digestion/filtering from mussel tissue and that was collected on a nano-structured surface comprising a microcavity array (capillary forces) by RM[8]. This can have the potential to accelerate the analysis, if the cavities are in precisely defined positions.

Thses results and the present thesis both document the applicability of RM for nanoplastic. Sobhani et al. used Raman imaging, which enabled the detection of smaller particles, depending on the small size of the pixels for the chemical image. The present approach aimed at a particle-by-particle analysis and, thus, relied on the optical targeting of the particles, which could not be performed on 100 nm particles. Nonetheless, both approaches seem to be limited to the analysis of only few selected particles, due to the relatively long measurement times.

Using the same approach as projected for this thesis, several reports on correlated SEM and RM analysis have appeared recently demonstrating the identification and visualization of different primary MP (especially aggregates)[2], nanoplastic (PS 200 nm) in different solvents (distilled water, sea salt, human amniotic fluid)[9], and irregular and heterogeneous (i.e. polymeric and inorganic) nanoplastic (> 360 nm)[10]. Those studies, however, used integrated systems that had the RM directly in the sample chamber of the SEM. Our work shows the applicability with two separate systems. This will be important for laboratories and applications where such an integrated system is not available or economically feasible.

In addition to the classical RM-based approaches, which might be hindered by low signal intensities due to the small mass of the nanoplastic particles, some studies used surface-enhanced Raman scattering (SERS) to enable nanoplastic analysis. Here, the use of Ag nanoparticles has been shown for chemical imaging of PS nanoplastic as small as 50 nm[11] or to identify primary PS, PE, PP nanoplastic (100 nm, 500 nm and 10 µm; concentrations down to 40 mg/L) in pure and sea water by using a handheld Raman spectrometer[12]. Secondly, nanostructured surfaces were used to analyze primary nanoplastic and collected atmospheric particles (< 2.5 µm; down to 450 nm)[13].

4.4 Conclusion

The method presented here, together with the recent advances towards RM analysis of nanoplastic, highlight the great interest in new Raman-based techniques for this new analyte. This interest is based on the theoretical capability of RM for the subµ size range, as well as the established processes for RM-based chemical identification in MP analysis. Thus, it remains important to establish RM in this size range and to push the limit further down and towards the application on particulate matrix (e.g. inorganic particles). Furthermore, the question of quantification needs to be addressed, which means that decisions need to be made on how many particles need to be selected and analyzed for the measurement to be representative. Hence, an optimized automated analysis process is required or

the transition to bulk analysis needs to be evaluated. Nonetheless, the applicability of RM-SEM for subµ-plastic particles has proved to be promising for the investigation of the nanoplastic size range. It also offers the possibility to provide valuable information on specific analytical questions which focus on single-particle analysis.

4.5 Materials and Methods

4.5.1 Particles and Chemicals

Spherical PS particles with 100 nm, 250 nm, 500 nm, 1.4 µm, and 10 µm suspended in ethanol, were provided by BS-Partikel GmbH, Germany, PMMA 500 nm was purchased from microParticles GmbH, Germany, and SiO_2 500 nm from NanoComposix, San Diego, CA, USA. Novachem (Postnova Analytics GmbH, Germany) was used as surfactant. Suspensions were prepared with ultrapure water (MilliQ Integral 5, Merck Millipore, Germany, resistance 18.2 MΩ). Fragmented particles were produced in accordance to a procedure by von der Esch et al[5] by cutting down PS objects (spatulas, Carl Roth GmbH & Co KG, Germany) and putting them in an aqueous solution in an ultrasonic bath for 15 h. Then, the suspension was filtrated over a 1 µm polycarbonate filter to separate the nanoplastic particle-containing suspension.

4.5.2 Substrates

The copper tape and silicon wafers were purchased from Plano GmbH, Germany. Aluminium foil was purchased from Carl Roth GmbH & Co KG, Germany, and the Al-coated object slides were purchased from Dynasil EMF, Ithaca, NY, USA.

4.5.3 Raman Microspectroscope

Raman measurements for the RM-SEM coupling (Section 4.2) were performed on an LabRAM HR Raman microscope (Horiba Scientific, France), which was equipped with the DuoScan module for precise mapping of the sample. It moves the laser spot by piezo-electrically controlled mirrors instead of sample stage movement. This allows step sizes down to 0.05 µm. The Raman maps acquired in this way had sizes of 12 µm $\times$ 12 µm with 0.05 µm steps, equating to 58081 pixels with acquisition times of 1 s and 1 accumulation. Of the PS particle spectra, the 1000 cm^{-1} band was plotted.

4.5.4 Scanning Electron Microscope

SEM imaging was performed on a Zeiss Sigma VP FE-SEM (Carl Zeiss Microscopy GmbH, Germany), which was equipped with an EDS Quantax XFlash 6l60 Detector (Bruker Nano GmbH, Germany). Images were taken with a SE detector at acceleration voltages of 3.0 – 5.0 kV.

References

1. Zoubir, A., *Raman imaging: Techniques and applications*; Springer Series in Optical Sciences, Vol. 168; Springer: Berlin, Heidelberg, 2012.
2. Sarau, G.; Kling, L.; Oßmann, B. E.; Unger, A.-K.; Vogler, F.; Christiansen, S. H. Correlative Microscopy and Spectroscopy Workflow for Microplastics. *Applied Spectroscopy* **2020**, *74*, 1155–1160.
3. Sobhani, Z.; Zhang, X.; Gibson, C.; Naidu, R.; Megharaj, M.; Fang, C. Identification and visualisation of microplastics/nanoplastics by Raman imaging (i): Down to 100 nm. *Water Research* **2020**, *174*, 115658.
4. Hernandez, L. M.; Yousefi, N.; Tufenkji, N. Are There Nanoplastics in Your Personal Care Products? *Environmental Science & Technology Letters* **2017**, *4*, 280–285.
5. Von der Esch, E.; Lanzinger, M.; Kohles, A. J.; Schwaferts, C.; Weisser, J.; Hofmann, T.; Glas, K.; Elsner, M.; Ivleva, N. P. Simple Generation of Suspensible Secondary Microplastic Reference Particles via Ultrasound Treatment. *Frontiers in Chemistry* **2020**, *8*, 169.
6. Fang, C.; Sobhani, Z.; Zhang, X.; Gibson, C. T.; Tang, Y.; Naidu, R. Identification and visualisation of microplastics/ nanoplastics by Raman imaging (ii): Smaller than the diffraction limit of laser? *Water Research* **2020**, *183*, 116046.
7. Fang, C.; Sobhani, Z.; Zhang, X.; McCourt, L.; Routley, B.; Gibson, C. T.; Naidu, R. Identification and visualisation of microplastics / nanoplastics by Raman imaging (iii): algorithm to cross-check multi-images. *Water Research* **2021**, *194*, 116913.
8. Valsesia, A.; Quarato, M.; Ponti, J.; Fumagalli, F.; Gilliland, D.; Colpo, P. Combining microcavity size selection with Raman microscopy for the characterization of Nanoplastics in complex matrices. *Scientific Reports* **2021**, *11*, 1–12.
9. Schmidt, R.; Nachtnebel, M.; Dienstleder, M.; Mertschnigg, S.; Schroettner, H.; Zankel, A.; Poteser, M.; Hutter, H.-P.; Eppel, W.; Fitzek, H. Correlative SEM-Raman microscopy to reveal nanoplastics in complex environments. *Micron* **2021**, *144*, 103034.
10. Zhang, W.; Dong, Z.; Zhu, L.; Hou, Y.; Qiu, Y. Direct Observation of the Release of Nanoplastics from Commercially Recycled Plastics with Correlative Raman Imaging and Scanning Electron Microscopy. *ACS Nano* **2020**, *14*, 7920–7926.

11. Zhou, X.-X.; He, S.; Gao, Y.; Chi, H.-Y.; Wang, D.-J.; Li, Z.-C.; Yan, B. Quantitative Analysis of Polystyrene and Poly(methyl methacrylate) Nanoplastics in Tissues of Aquatic Animals. *Environmental Science & Technology* **2021**, *55*, 3032–3040.

12. Lv, L.; He, L.; Jiang, S.; Chen, J.; Zhou, C.; Qu, J.; Lu, Y.; Hong, P.; Sun, S.; Li, C. In situ surface-enhanced Raman spectroscopy for detecting microplastics and nanoplastics in aquatic environments. *Science of The Total Environment* **2020**, *728*, 138449.

13. Xu, G.; Cheng, H.; Jones, R.; Feng, Y.; Gong, K.; Li, K.; Fang, X.; Tahir, M. A.; Valev, V. K.; Zhang, L. Surface-Enhanced Raman Spectroscopy Facilitates the Detection of Microplastics <1 µm in the Environment. *Environmental Science & Technology* **2020**, *54*, 15594–15603.

Chapter 5

Which Particles to Select, and if Yes, how Many? Subsampling Methods for Raman Microspectroscopic Analysis of Very Small Microplastic

Reference

Christian Schwaferts, Patrick Schwaferts, Elisabeth von der Esch, Martin Elsner and Natalia P. Ivleva, *Analytical and Bioanalytical Chemistry* **2021**, 413, 3625–3641, https://doi.org/10.1007/s00216-021-03326-3, https://link.springer.com/article/10.1007/s00216-021-03326-3.

Permission statement

Open Access: This article is licensed under a Creative Commons Attribution 4.0 International License, which permits use, sharing, adaptation, distribution and reproduction in any medium or format, as long as you give appropriate credit to the original author(s) and the source, provide a link to the Creative Commons licence, and indicate if changes were made. The images or other third party material in this article are included in the article's Creative Commons licence, unless indicated otherwise in a credit line to the material. If material is not included in the article's Creative Commons licence and your intended use is not permitted by statutory regulation or exceeds the permitted use, you will need to obtain permission directly from the copyright holder. To view a copy of this licence, visit http://creativecommons.org/licenses/by/4.0/.

Abstract

Micro- and nanoplastic contamination is becoming a growing concern for environmental protection and food safety. Therefore, analytical techniques need to produce reliable quantification to ensure proper risk assessment. Raman microspectroscopy (RM) offers identification of single particles, but to ensure that the results are reliable, a certain number of particles has to be analyzed. For larger MP, all particles on the Raman filter can be detected, errors can be quantified, and the minimal sample size can be calculated easily by random sampling. In contrast, very small particles might not all be detected, demanding a window-based analysis of the filter. A bootstrap method is presented to provide an error quantification with confidence intervals from the available window data. In this context, different window selection schemes are evaluated and there is a clear recommendation to employ random (rather than

systematically placed) window locations with many small rather than few larger windows. Ultimately, these results are united in a proposed RM measurement algorithm that computes confidence intervals *on-the-fly* during the analysis and, by checking whether given precision requirements are already met, automatically stops if an appropriate number of particles are identified, thus, improving efficiency.

5.1 Introduction

The ubiquitous plastic contamination in the environment, especially Microplastic (MP, 1 µm – 1 mm) and, more recently, Nanoplastic (< 1 µm) is of great concern and has spawned many efforts to assess the highly diverse aspects of this topic, ranging from its quantity in environmental systems[1] or food (e.g., drinking water[2]) to its toxicity[3]. All of these investigations, however, depend on harmonized analytical methods[4] for which thorough validation is essential. Thus, there are many advances for the several established techniques for MP analysis, which comprise sampling, sample processing, chemical identification, quantification & data processing/reporting[5,6]. Most of them fall in two main groups: thermoanalytical and spectroscopic methods. The former are based on the analysis of the thermal decomposition products of the polymer by gas-chromatography-mass-spectrometry (GC-MS). Two realizations thereof are pyrolysis-GC-MS[7–10] and theromoextraxtion-desorption-GC-MS[11,12], which give the mass content of different polymers but cannot provide information on the number, size distribution, and morphology of the (plastic) particles. Spectroscopic techniques, on the other hand, comprise mainly Fourier-Transform-Infrared spectroscopy[13,14] and Raman microspectroscopy (RM)[15–17]. Here, the particles are identified by characteristic vibrational “fingerprint” spectra. This paper focusses on RM, which has been established for the analysis of MP due to the specific data (size distribution, shape, morphology), which are provided by the analysis of individual particles down to 1 µm (and even below)[15].

RM analysis of MP is very time consuming and, until recently, has been also very labour intensive, since the particles had to be measured manually[18]. Hence, substantial advances in its automation have been made, so that there are now several open source[19–21] and commercial[19,22,23] softwares. Currently they are applicable down to the low µm range and are dependent of the maximum image resolution of the RM that was used (von der Esch et al.: 10 µm[19], Brandt et al.: 2-3 µm[21], Ossmann et al.: 1 µm[22]). These automated programs follow the workflow of acquiring an optical image of the filter, particle recognition, RM measurement at resulting coordinates, database matching and result output, where some can control the RM directly[21–23] and others output the coordinates that have to be passed to the RM control software[19,20]. There are some applications of Raman imaging, i.e. spectral imaging of entire areas[24], however, the particle-by-particle approach seems to be preferable[19,21]. This progress has effected an increase in measured particle numbers in more recent studies (up to several thousand)[16,25]. Furthermore, the automatic particle recognition removes the operator bias when deciding on which particle to measure and also provides the ratio of MP/non-MP which is an important quantity as opposed to absolute MP number[16].

Parallel to the advances of automated MP quantification, the lower µm range has been targeted. Since the particle number increases exponentially[26], it will become nearly impossible to analyze all particles below a certain size. Thus a subset of the complete sample has to be selected, which in itself is another sampling. This subsampling – as any sampling – has to satisfy the requirements for correct sampling as laid out by the Theory of Sampling (TOS), demanding that each particle has the same probability to be selected and is not altered[27–29], and thus, enables a bias-free quality control.

The automated routines make it possible to acquire a microscope image of the whole filter and detect all particles (assuming perfect image recognition), thereby the whole sample can be subjected to a random sampling. This equalizes the probability of a particle being selected and makes the spatial structure of the particles on the filter irrelevant. Ergo, this random sampling is a correct sampling and can be modelled statistically (urn model without replacement) to provide an error quantification (via confidence intervals (CI)) and to calculate a minimal sample size such that a certain precision requirement is met[16] (see box in Figure 5.1 and the appendix in Section 5.6.1.).

For MP, the random sampling is well applicable down to 10 µm[19]. However, for very small MP and especially nanoplastic[30–33], the complete filter cannot be imaged in a practical manner and the total particle number is not accessible, thus, another subsampling method has to be found. Of course, this problem is not restricted to MP analysis or a specific size range, it is rather universal and relevant whenever particles (points) have to be selected from a two-dimensional surface.

For very small MP (ca. < 10 µm) and even subµ-plastic we expect that random sampling may not be feasible due to the following technical concerns.

The measurement time and the computational resources to process the resulting amount of data[34,35] will increase substantially, due to the fact that smaller particles demand the use of higher magnification objectives (such as 50×). For the optical imaging of the complete filter, this leads to a very high number of images that have to be stitched together (our RM would need around 12100 images for a filter with 22 mm diameter, not including image overlap for stitching). It might even be impossible to generate such large images with some commercial RM software, such that some workaround has to be found.

The automated particle measurement critically depends on the RM's ability to target the particles at their calculated locations. This may become difficult for decreasing particle size, as the deviations by the microscope stage become more and more detrimental. There are multiple parameters that characterize the quality of the microscope stage, which are normed by ISO[36]. From these, there are three, that will inhibit the particle identification: accuracy, repeatability and drift. Accuracy describes the discrepancy of the target and the actual position after motion. Repeatability is the accuracy when sequentially positioning. Drift describes the slow temporal component of the position stability. It is usually attributed to temperature fluctuations.

In this application, repeatability[37] is the most pertinent source for deviations, where the positioning system has to be fit to accurately target particles with diameters down to $\sim$ 1 µm. For MP samples with up to 10000 measurement points, this deviation can accumulate to a substantial amount (several µm). Position accuracy and drift over a measurement duration of 2–3 days may, too, be in the same

Sample size and confidence interval in random sampling (urn model without replacement):
From all N particles on the filter a subset with S particles is selected randomly (each particle has the same probability to be selected) and identified with RM, yielding S_p plastic particles. The ratio $r = \frac{N_p}{N}$ of plastic particles N_p on the filter can be estimated from the corresponding ratio in the subset: $\hat{r} = S_p/S$. This estimate $\hat{r}$ might be erroneous, which can be accounted for by a confidence interval.
For a given error probability α one is willing to accept, a $(1-\alpha)$ confidence interval (CI) is an interval of values around the estimate $\hat{r}$ which covers the true value r with probability $(1-\alpha)$:

$$CI(\hat{r}) = [\hat{r} \pm e] = [\hat{r} \pm z \cdot sd(\hat{r})] \ , \tag{5.1.1}$$

where $e = z \cdot sd(\hat{r})$ denotes the absolute error margin and can be calculated with the $(1-\frac{\alpha}{2})$-quantile z of the normal distribution (frequently used values are $z_{0.95} = 1.64$ for $\alpha = 0.10$ and $z_{0.975} = 1.96$ for $\alpha = 0.05$). When reporting the number of plastic particles on the filter $\hat{N}_p = N \cdot \hat{r}$, the CI can be transformed into $CI\left(\hat{N}_p\right) = N \cdot CI(\hat{r})$. The (estimated) standard deviation of the ratio estimate is:

$$sd(\hat{r}) = \sqrt{\frac{\hat{r} \cdot (1-\hat{r})}{S} \cdot \frac{N-S}{N-1}} \ . \tag{5.1.2}$$

By knowing N, assuming a plausible ratio r, and specifying requirements on α and e (only an error probability of α should be accepted that the ratio estimate $\hat{r}$ deviates more than e from the true ratio r) the minimal number S of particles to identify with RM can be obtained by

$$S \geq \frac{r \cdot (1-r)}{\frac{e^2}{z^2} + \frac{r \cdot (1-r)}{N}} \ . \tag{5.1.3}$$

Frequently, the requirement on e is instead expressed by a relative error e_{rel}, which needs to be transferred to the absolute error margin $e = r \cdot e_{rel}$ beforehand.
A comprehensive, step-by-step formalization of this calculation is given in the appendix in Section 5.6.1.

Fig. 5.1: Box containing a summary of sample size and confidence interval calculation in random sampling on a completely imaged filter (urn model without replacement).

order of magnitude as the particles of concern in this study. Aside the precision of the microscope stage, mosaicking mismatch may also introduce a deviation, since the image stitching is dependent on the availability and recognition of common features in the margins of the single images[34]. The sum of these influences on the deviation is neglible for larger particles (> 10 µm), but prohibits the targeting of very small particles for RM identification, when the images are all taken at once and only then the spectra are acquired.

The acceptable overall positioning error d_{err} depends on the particle diameter d and the laser spot size $d_{laser} = \frac{1.22 \cdot \lambda}{N.A.}$, where λ is the wavelength of the laser and $N.A.$ is the numerical aperture of the objective. Its upper bound is $d_{err} < \frac{1}{2}(d + \frac{1.22 \cdot \lambda}{N.A.})$, which implies that the laser barely touches the particle. As example, a particle with $d = 1\mu m$, measured with a green laser of $\lambda = 532nm$ and a 50$\times$ objective with $N.A. = 0.7$ equates to $d_{err} = 0.96\mu m$.

With sub-nanometer applications of e.g. scanning probe microscopy in mind, it is obvious that the quality of high-end positioning systems exceeds the requirement for this problem in some aspects. However, for high-throughput and cost efficient analysis, such high-end technical instrumentation may not be economically feasible.

In this work, we consider the case in which the complete filter cannot be imaged (e.g. in the context of very small MP) and present a window subsampling strategy. Window sampling schemes, although common in MP analysis[22,38–41], have the risk of sampling particles incorrectly (cf. TOS) and, furthermore, lack the information on the total particle number, such that corresponding confidence intervals are not analytically accessible. To solve this problem, we describe a bootstrap method to estimate confidence intervals in window sampling schemes and outline that the preferable window scheme uses random window locations. This allows to correctly subsample on the filter and to provide error quantifications via estimated confidence intervals. In the future, this approach can be implemented in the RM measurement process to adjust the sample size with the acquired data *on-the-fly*.

5.2 Window Selection Schemes

If complete optical imaging of the filter is not feasible (Section 5.1), RM analysis needs to be restricted to a set of selected windows on the filter. Indeed, this approach is used by many MP laboratories in different varieties (instead of random sampling of all particles). Some studies choose a number of windows (with differing area ratios of the filter) at fixed, arbitrary positions (although referred to as "random", no randomization was reported and positions seem to be fixed)[22,38,39]. There are other window placements that follow a specific arrangement, such as a cross with five[40] and with 19 windows[42]. Other approaches use a spiral[41] or a stratified random window placement[43]. These patterns aim to incorporate potential information about the spatial structure into the window pattern. Thaysen et al.[43] demonstrated the importance of taking the spatial structure of the particles on the filter into account. The resulting information was used to derive a stratified sampling in rings to account for the radial pattern of the particles. However, it is extremely difficult to assess the spatial structure in its entirety, since each statistical analysis only highlights one aspect of the spatial structure.

Systematic window placement, especially with very few windows, as our example will show, is a critical source of bias (Figure 5.3a). Thus, we evaluate these two options: A random window scheme, in which each segment of the filter has equal probability of being investigated, and a systematic scheme with similar distances to the next windows, such that the whole filter is covered by the uniform systematic pattern. We, further, investigate the effect of the window size by comparing windows with a size of 1 and 4 fields of view (FOV), as it might be technically difficult to perform RM on an exceedingly large amount of windows. These will be referred to as *1-FOV sampling* and *4-FOV sampling*, respectively. FOV denotes the size of the microscope image at the respective magnification, which is dependent on the individual microscope (e.g. the RM at the authors lab gives images, i.e. 1-FOV, of 222 µm $\times$ 139 µm at 50 $\times$ magnification). Consequently, *4-FOV* is a 2$\times$2 rectangle of microscope images (444 µm $\times$ 278 µm). Adapting the terminology of Minkkinen et al.[44], we denote random vs. systematic windows as *sampling modus* and many small (*1-FOV*) vs. few large windows (*4-FOV*) as *sampling type*. Elaborations within this section serve mainly as illustration for the two-dimensional sampling case depicted here and as basis for further elaborations in the subsequent sections. For the general treatment of sampling see[27–29].

5.2.1 Estimation of the Number of Plastic Particles

5.2.1.1 Formalization

Formally, the number N_p of plastic particles of the filter is of interest and can be calculated by considering the number N of all particles on the filter and the ratio r of plastic particles on the filter: $N_p = N \cdot r$. Both N and r are unknown and need to be estimated from the window data consisting of k windows in total with W particles, of which W_p are plastic particles. It is assumed that all particles in the windows will be subjected to RM identification (such that W corresponds to the previously used S, see Figure 5.1), as the number of particles per window is expected to be very low (around 1.6 in the illustrating simulation described below, with 20 000 particles, multiplied by the ratio of window area to filter area). The ratio estimate $\hat{r} = W_p/W$ (compare Box in Figure 5.1) is obtained directly from the window data and the number of particles on the filter can be extrapolated by considering the area $a(F)$ of the filter in relation to the area $a(W)$ of the set of windows:

$$\hat{N} = W \cdot \frac{a(F)}{a(W)} \,. \tag{5.2.1}$$

Together, the number N_p of plastic particles on the filter can be estimated as

$$\hat{N}_p = \hat{N} \cdot \hat{r} = W \cdot \frac{a(F)}{a(W)} \cdot \frac{W_p}{W} = W_p \cdot \frac{a(F)}{a(W)} \,. \tag{5.2.2}$$

5.2.1.2 Window Edge Issues

There are some issues if particles overlap with the window edges and are cut off. In this case they will give a false particle size and a distortion in the particles number. Consider Figure 5.2, in which many particles overlap the inner window border. Since some are cut off, the 8 recognized particles would truly belong in a slightly larger (outer) window with a larger area, resulting in a lower final estimate for N_p according to equation (5.2.2). It is even conceivable that a particle is counted twice, if it laps into two closely put windows.

However, a solution to these issues can be achieved by restricting the window-based RM measurement to particles smaller than a certain limit (e.g. 10 µm) and cutting off the radius (i.e. 5 µm) of this limit diameter of each window border (similar to overlap regions in image stitching[34]). Only particles that have their center within this smaller window are of interest. The number of all particles that have their centers within this smaller window, but are completely contained within the larger window (e.g. 3 in the example in Figure 5.2) and the area of the smaller window in equation (5.2.2) will give an unbiased final estimate.

With regard to our target size range, the window size of an image with 50× magnification is 222 µm × 139 µm, the smaller window would be 212 µm × 129 µm which is still large compared to the size of the particles and should not lead to other serious issues. Should the analysis target larger particles, a larger

window would need to be applied (*4-FOV* sampling), since edge issues are smaller with larger windows. In that, edge issues need not be a reason to resign from *1-FOV* sampling when measuring very small microplastic particles.

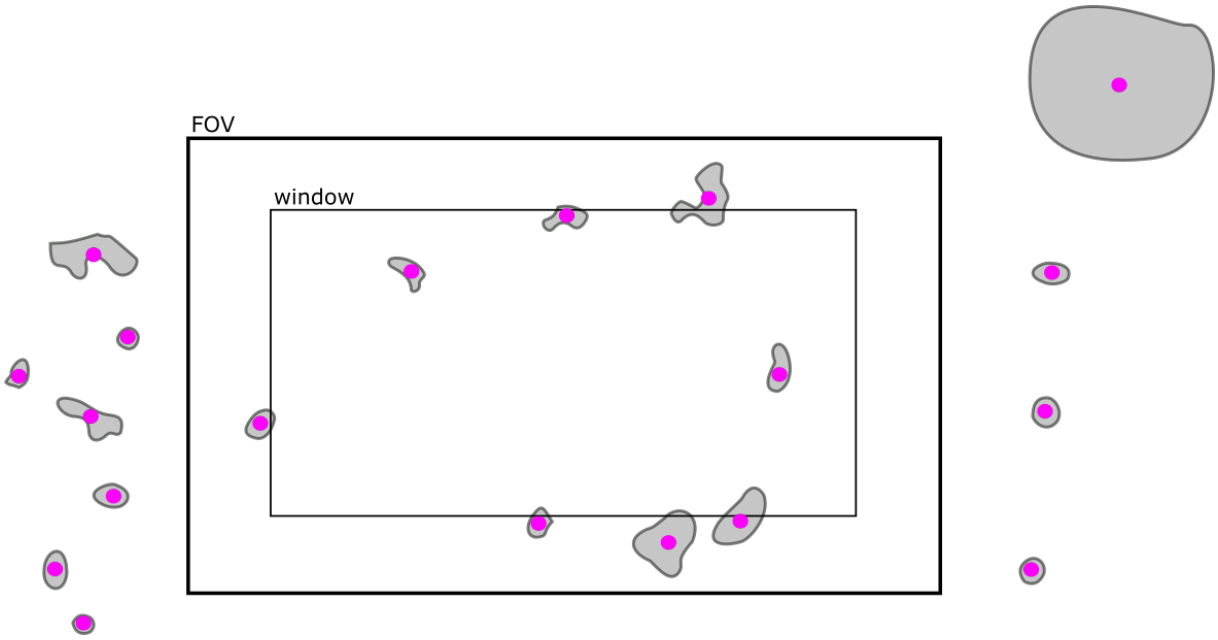

Fig. 5.2: Schematic filter section to illustrate window edge issues: To avoid bias in particle number due to cut off particles, one should only use an inner window of the whole FOV, in which only particles that have their center (magenta) within the inner window, but are contained completely within the outer window (FOV), are counted. So, instead of 8 particles with too low diameter only three particles with correct diameter would be counted.

5.2.1.3 Bias and Standard Deviation

The final estimate $\hat{N}_p$ is a random variable and might be erroneous. Potential errors might be systematic or statistical (random), which can be described by the bias

$$bias\left(\hat{N}_p\right) = E\left(\hat{N}_p\right) - N_p \tag{5.2.3}$$

and the standard deviation $sd\left(\hat{N}_p\right)$, respectively. The bias of $\hat{N}_p$ is the deviation of its expected value $E\left(\hat{N}_p\right)$ from the true value N_p, and should ideally be zero. In that case the estimate $\hat{N}_p$ is unbiased, and if not there is a systematic error that can hardly be controlled in real applications. In fact, the confidence calculation as outlined in Figure 5.1 assumes that the estimate $\hat{N}_p$ is unbiased, which is the case if random sampling is used.

By assessing both systematic and statistical error for different window sampling schemes, the quality of these schemes can be assessed. However, bias and standard deviation of the final estimate $\hat{N}_p$ depend on the spatial influences on the particles on the filter, which are hardly ever fully known, such that explicit formulas cannot be provided. Consequently, obtaining confidence intervals and performing sample size calculations require computational statistical methods.

5.2.2 Simulation Details

To illustrate and elaborate on the questions about sampling modus and type in the next sections, we generated artificial filters, which aimed to resemble a typical preprocessed sample. Since these elaborations target the subsampling on the filter, the other critical aspects of the MP analysis by RM, i.e. particle recognition, or Raman identification, are assumed to be ideal. Method development on these aspects of the analysis is critical to ensure that these assumptions are met and potential error is avoided. A total of $N = 20000$ circular particles, having diameters from 1 µm to 200 µm that follow the power law distribution as reported by Kooi et al.[26], were randomly placed on a circular surface with 22 mm diameter (similar to an Au-coated polycarbonate filter, as used in our laboratory), such that no particles overlap with each other. Out of these particles $r = 0.2$ (20 %) were labeled as plastic, resulting in $N_p = 4000$ plastic particles. This particle number has been chosen with regard to typical filters in the authors' lab, onto which an appropriate aliquot has to be filtrated such that the filter is not overloaded.

Different influences on the spatial structure of the particles on the filter can be classified as internal and external. Internal influences are interactions between the particles themselves irrespective of their locations on the filter, such as clustering (particles attract each other) or regularity (particles repulse each other), and external influences affect particle (or cluster) locations in general irrespective of potential particle interactions, e.g. particles might tend towards the margin or the center of the filter (for a more comprehensive view on spatial structures see Supplementary Information Section 5.6.2). Naturally, particles on the filter express regularity as they cannot be in the same place. This is called a *hard core* and signifies an area, in which other particles cannot be located. For the illustration of the external influences, two types of spatial probability distributions were applied in the simulation: a uniform, resulting in a *regular* reference filter without external influence (Supplementary Information Figure S.5.2, left), and a *Gaussian* distribution, resulting in a filter with external influence that collects the particles in the center[45] (Supplementary Information Figure S.5.2, right), similar to the filters by Thaysen et al.[43]. In this manner, 5000 filters have been generated. Window sizes were 222 µm $\times$ 139 µm as obtained with the 50$\times$ magnification of our *alpha 300R* Raman microspectroscope (Witec GmbH, Germany) (and 444 µm $\times$ 278 µm for evaluating *4-FOV* sampling, see Section 5.2.4) and windows were not allowed to overlap with each other.

For each window sampling scheme of interest, the final estimate $\hat{N}_p$ was calculated within each of the 5000 simulated filters. All of them (together) allow to estimate its bias $bias\left(\hat{N}_p\right)$ and standard deviation $sd\left(\hat{N}_p\right)$ as well as to illustrate effects of external influences on the minimal required sample size W, and, thus, the required minimal number k of windows. Technical information about the simulation is provided within the supplementary material (Section 5.6.3).

5.2.3 Sampling Modus – Random vs. Systematic Windows

The impact of the sampling modus (random windows vs. systematic windows) on the bias and the standard deviation of the final estimate depends on the number of windows and the actual spatial

structure of the particles. Random window locations were allowed such that windows might exceed the margin of the filter, as long as at least some part of the window was still contained within the filter. This ensures that each part of the filter has the same probability to be contained within a window. In contrast, if (random) windows were restricted to be completely within the filter, the outer parts of the filter are underrepresented within the windows, leading to an estimation bias (exemplified and elaborated on in the Supplementary Information in Section 5.6.4). For systematic windows, a sunflower seed pattern was used, such that the k (systematic) windows fill the complete filter with similar distances to their neighbors, trying to cover the area of the filter as uniformly as possible.

Both types of artificial filters (regular & Gaussian) were analyzed using random windows and systematic windows, respectively, for varying numbers of windows k. Figure 5.3a depicts the expected value $E\left(\hat{N}_p\right)$, which, if unbiased, should equal to $N_p = 4000$, and Figure 5.3b depicts the standard deviation $sd\left(\hat{N}_p\right)$.

Regarding the bias, Figure 5.3a shows that the estimate $\hat{N}_p$ is unbiased (the true value is $N_p = 4000$) in three cases: both of the regular filters and the random windows on the Gaussian filter. The strong oscillation of those lines for small k reflects only the simulation variance and will diminish with increasing number of filters analyzed (not just 5000). Only systematic windows on the Gaussian filters lead to a biased estimate. This underestimation is caused by the centralized external influence, which is not adequately represented by the systematic windows. To illustrate this point, imagine a square positioning of 9 windows on the filter. Of these, one lies on the center and 8 lie toward the border. For our centralized, Gaussian particle pattern, this would result in only one window covering a large amount of particles but 8 covering very few, causing an underestimation of the particle number. Similarly, if a spatial structure was present that accumulates particles on the border (as could occur during filtration due to adhesion on the glasswares), this misrepresentation would cause an overestimation of the result.

In general, the strength of this bias depends on the match between the spatial structure of the particles and the pattern of systematic windows used. Within our simulation, this match (Gaussian, centralized structure and sunflower seed arrangement) gets better with increasing number k of windows, even nullifying the bias for a certain value of k (somewhere between 500 and 1000 windows). This, however, need not be the case in general, and considerable thought should be given to the pattern of window locations, if systematic windows are used. Without any prior information about the spatial structure of the particles, it is difficult to justify the choice of systematic window pattern. In the application of RM analysis of MP, it might however be conceivable to use the spatial information that is gained from the complete filter optical image (for larger MP particles) for the generation of a systematic window scheme for the small size range. Of course, this incorporates the assumption that the small particles behave the same as the large particles. To check this assumption, one might employ an overlap of the size ranges (e.g. complete filter: 10 µm – 500 µm and window sampling: 1 µm – 50 µm) and compare the results.

It might seem peculiar, that even for Gaussian filters random windows will yield an unbiased estimate. This is because, with random window locations every part of the filter has the same probability to be covered by a window. No matter what the spatial structure looks like and which external influences

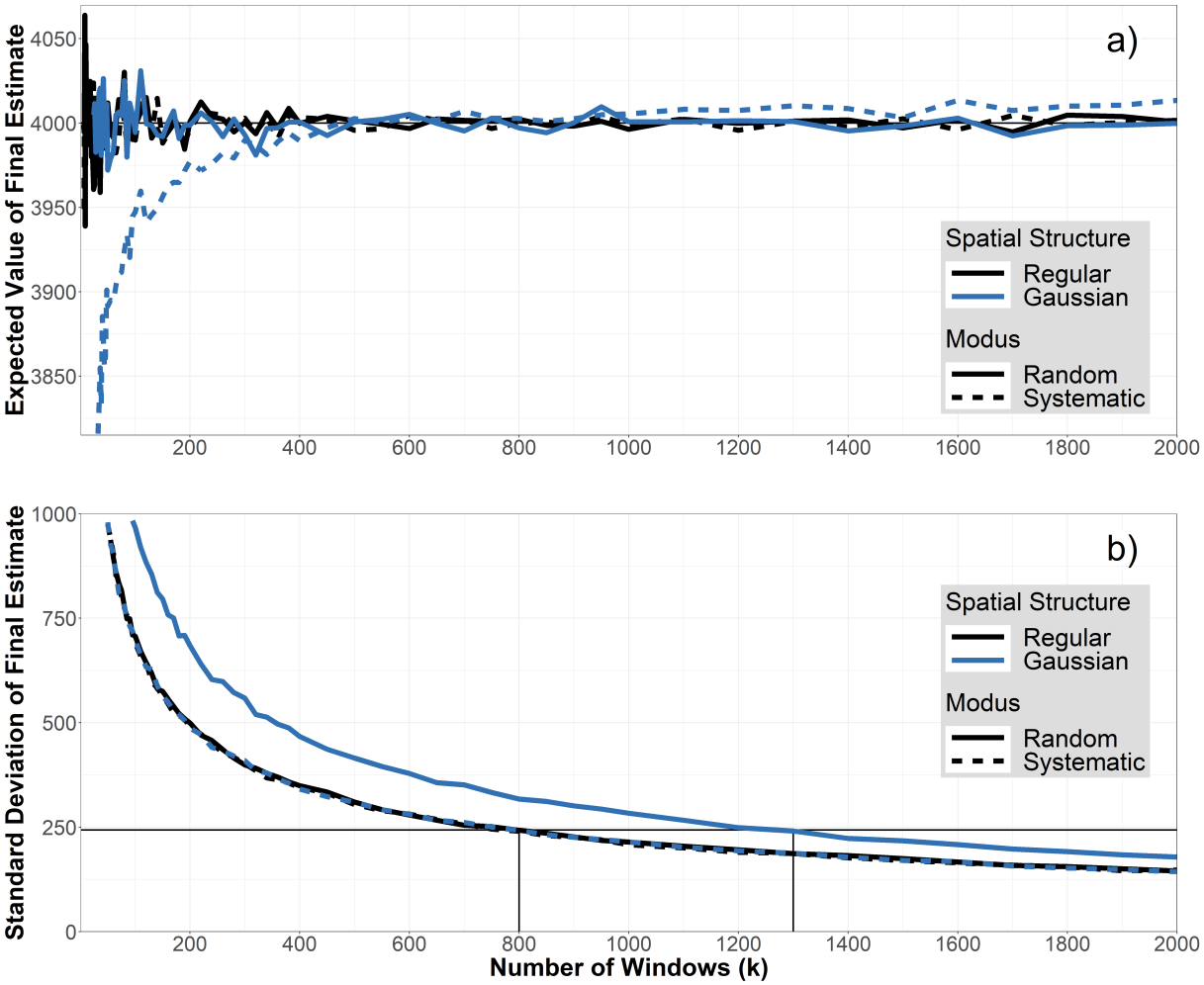

Fig. 5.3: Sampling Modus. Artificial filters with regular (black line) and Gaussian (blue line) spatial structure have been analyzed with a random (solid line) and systematic (dotted line) window scheme. Thus, the black and solid line represents random windows on the regular filter. a) Bias plot: k vs. $E(\hat{N}_p)$. Only systematic windows on the Gaussian filters have a bias (deviation from the true value $N_p = 4000$ (horizontal black line)). b) Plot of standard deviation: k vs. $sd(\hat{N}_p)$. Random windows on the Gaussian filter have increased standard deviation. The horizontal black line at $sd(\hat{N}_p) = 243.2$ corresponds to the precision requirement $e_{rel} = 0.1$ and $\alpha = 0.1$. These are met for $k = 800$ and $k = 1300$ windows for regular and Gaussian filters, respectively.

are present, each characteristic of the spatial structure will be observed with equal probability and no spatial characteristic is systematically missed. This also extends to the case, where plastic particles and non-plastic particles have different characteristics, i.e. if the ratio r is not spatially uniform on the filter.

The unbiasedness of random windows, however, comes with an increase in the standard deviation of the estimate. Figure 5.3b shows that – as expected – the standard deviation decreases with increasing number k of windows. This decrease is, again, comparable in three cases: both regular filters and the systematic windows on the Gaussian filter. Only for random windows on the Gaussian filters, the standard deviation is higher, because the procedure of selecting window locations at random introduces additional randomness on the final estimate. The increase in standard deviation for random windows becomes apparent when using the plot to derive a minimal sample size according to predefined precision requirements for the Gaussian filters, as shown in Figure 5.3b. Here, precision requirements were specified as $e_{rel} = 0.1$ and $\alpha = 0.1$. For $N = 20000$ and $r = 0.2$ this demands the absolute error margin to be smaller than $e = N \cdot r \cdot e_{rel} = 400$ and, thus, the standard deviation to be smaller than $sd(\hat{N}_p) = e/z = 243.2$ (with $z = 1.64$, compare box in Figure 5.1). In order to obtain this standard deviation (y-value) with the Gaussian filters, random windows require $k = 1300$ windows, containing $W = 2065$ particles to identify in total, and systematic windows requires $k = 800$ windows, containing $W = 1295$ particles to identify in total.

Considering systematic windows on the Gaussian filters, it can also be seen that the standard deviation is not affected by the potential bias (see Figure 5.3a), emphasizing that both quantities (bias and standard deviation) behave independently and a bias in the data cannot be detected by data processing, as it was laid out in Section 5.2.1.3.

In summary, two characteristics for the sampling modus were observed in this simulation analysis: In the presence of external influences, random windows have an increased standard deviation and systematic windows might yield biased estimates. Although the former increases the probability to obtain a more unrepresentative window sample (due to the increased randomness), this issue can be tackled by increasing the number k of windows, however, the latter might introduce a systematic error of unknown size that impairs the representativity of the window sample, which is not controllable in real RM analyses. In that, systematic windows should only be used if their pattern matches well with the spatial structure of the particles. However, as the spatial structures are expected to differ depending on sample origins (marine or limnic waters, drinking waters, processed biota, etc.) and different laboratories with different filtration setups/procedures, such a match needs to be evaluated for each new study. Besides, in contrast to random windows, systematic windows do not allow for an easy way to increase the number of windows adaptively during the analysis, such that a match of the pattern with the spatial structure of the particles can be guaranteed for all numbers of windows.

5.2.4 Sampling Type – Smaller vs. Larger Windows

The impact of the sampling type (*1-FOV* sampling vs. *4-FOV* sampling) on the bias and the standard deviation of the final estimate depends on the number of windows, the actual spatial structure of the

particles, and the sampling modus.

As described above (Section 5.2.2), window sizes were 222 µm $\times$ 139 µm as obtained with 50$\times$ magnification for *1-FOV* sampling, and 444 µm $\times$ 278 µm for *4-FOV* sampling, in order to realistically implement using four smaller windows with 50$\times$ magnification to obtain one larger window. For comparing both sampling types, the number of windows k denotes the number of small windows needed to obtain all larger windows in *4-FOV* sampling. As there is no external influence within the regular filters, every window - no matter how its location was determined - has the same distribution of particles or plastic particles. In that, there is no difference between *1-FOV* and *4-FOV* sampling on regular filters, such that results (Figure 5.4) focus on the Gaussian filters only. Those were analyzed using both sampling modi (random vs. systematic) and both sampling types (*1-FOV* vs. *4-FOV* sampling) for an increasing number k of windows. Again, the figures depict the expected value $E\left(\hat{N}_p\right)$ (Figure 5.4a) and the standard deviation $sd\left(\hat{N}_p\right)$ (Figure 5.4b). Lines for *1-FOV* sampling (dark blue) are the same as in Figs. 5.3a and 5.3b.

Figure 5.4a shows that the bias (deviation from the true value of $N_p = 4000$) inherent to systematic windows (compare Section 5.2.3) is larger for *4-FOV* sampling than for *1-FOV* sampling. This is because, *1-FOV* sampling is able to capture the external influence better than *4-FOV* sampling, as more different locations of the filter can be observed. This allows a more comprehensive picture of the different characteristics of external influences, leading to the lower bias in *1-FOV* sampling. Random sampling is still unbiased, independent of the sampling type.

Analogously, Figure 5.4b shows that the increase in standard deviation inherent to random windows (compare Section 5.2.3) is even higher if *4-FOV* sampling is used compared to *1-FOV* sampling. Again, this can be explained because *4-FOV* sampling uses fewer window locations than *1-FOV* sampling, impeding a comprehensive picture of the different characteristics of the external influences.

In summary, *4-FOV* sampling amplifies the problems inherent to random or systematic windows, respectively, in comparison to *1-FOV* sampling, and its effect depends on the strength of the external influences. Therefore, *1-FOV* sampling (i.e. maximizing the number of different window locations) is to be preferred. However, window sizes need also consider the particle size range of interest (compare Section 5.2.1.2) as well as processing times, which might be longer for a larger number of smaller windows. Yet, when employing *4-FOV* sampling to reduce processing time, technical limitations for image stitching have to be taken into account (Section 5.1), and the overall number of particles to identify with RM might be larger than with *1-FOV* sampling, due to the increase in variance, which increases the measurement time.

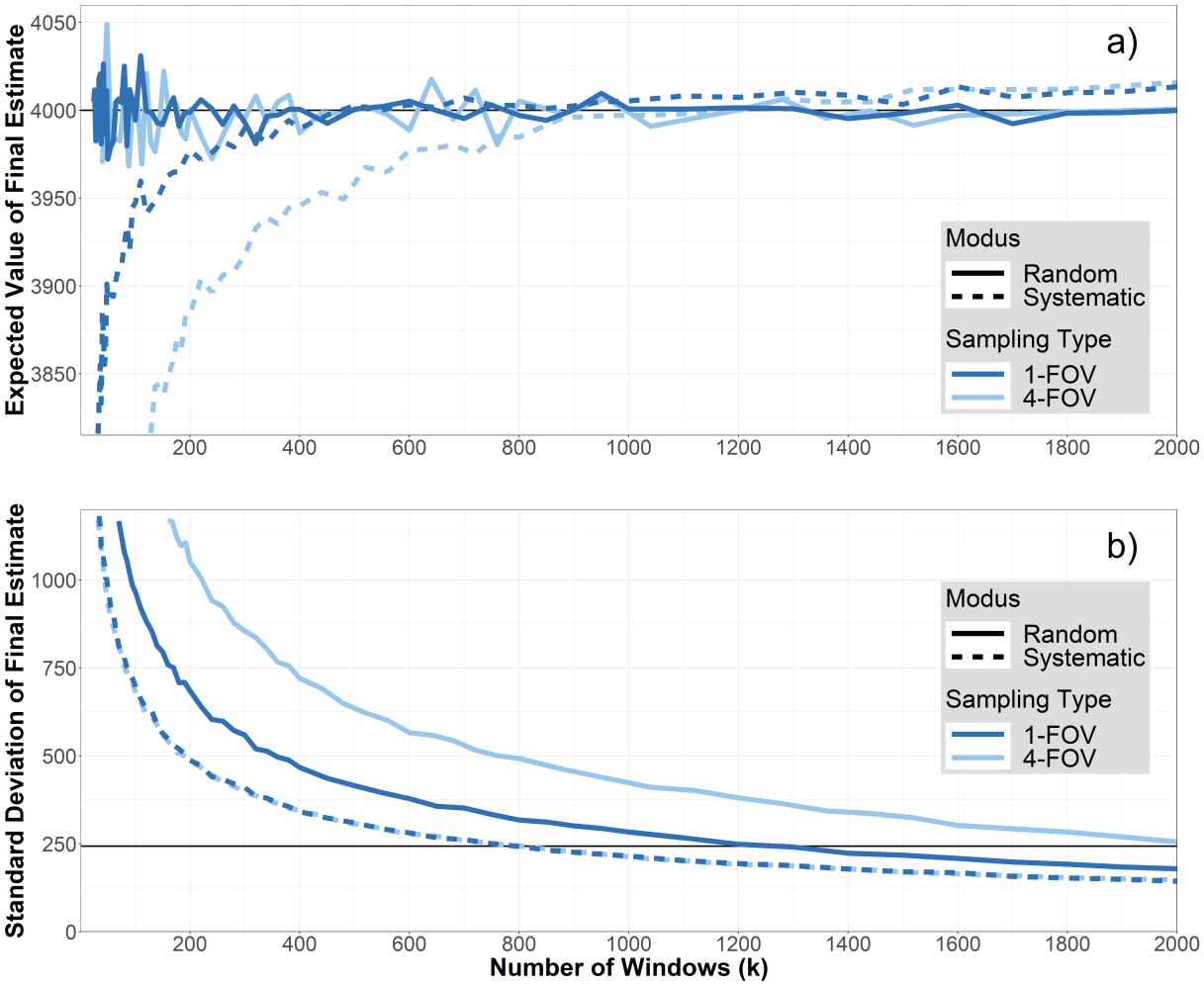

Fig. 5.4: Sampling Type. Artificial filters with Gaussian spatial structure have been analyzed with a random and systematic window scheme for both *1-FOV* (dark blue) and *4-FOV* sampling (light blue). The solid line denotes random windows, the dotted line denotes systematic windows. For *4-FOV* sampling, k denotes the number of smaller windows needed to obtain the large windows. a) Bias plot: k vs. $E(\hat{N}_p)$. For systematic windows the bias is more pronounced with *4-FOV* sampling than with *1-FOV* sampling. b) Plot of standard deviation: k vs. $sd(\hat{N}_p)$. The standard deviation of random windows is higher for *4-FOV* sampling than for *1-FOV* sampling. Analogue to Figure 5.3, the black line at $sd(\hat{N}_p) = 243.2$ corresponds to the precision requirements $e_{rel} = 0.1$ and $\alpha = 0.1$.

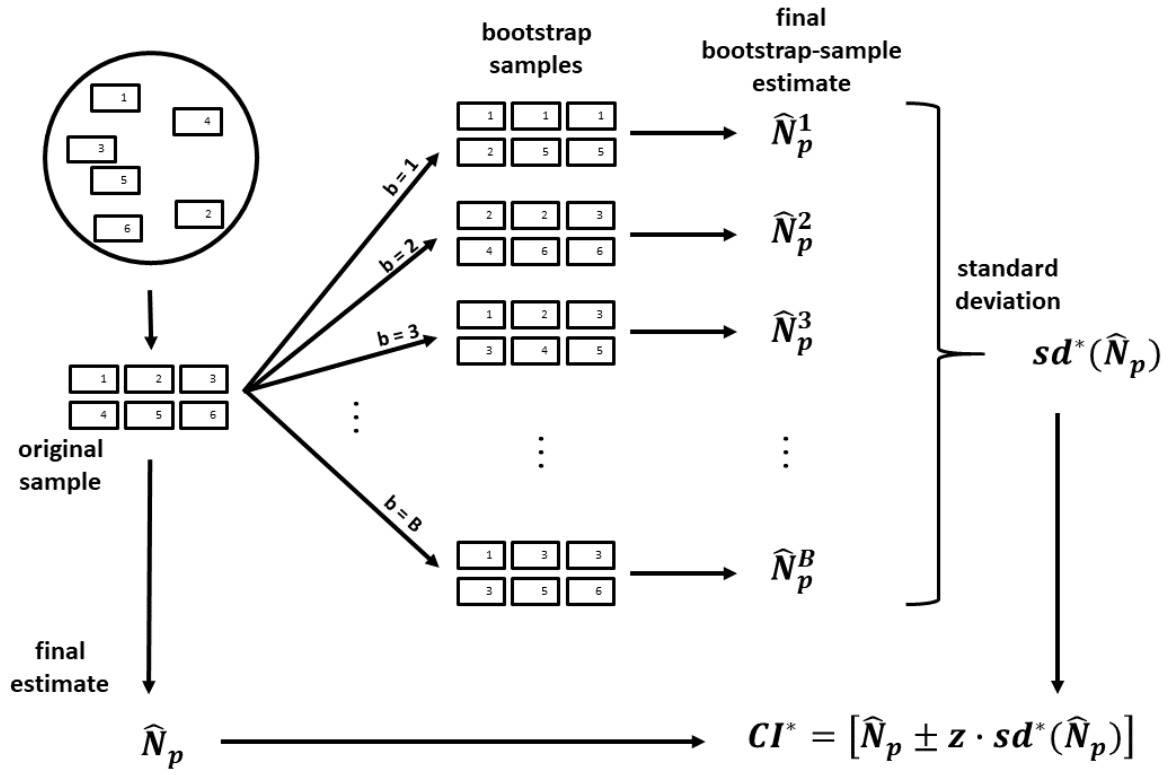

Fig. 5.5: Scheme of Bootstrap Analysis. From one original window data of the filter (left), B samples of the same size are drawn with replacement, each providing a *final bootstrap-sample estimate* for the number of plastic particles $\hat{N}_p^b$, $b = 1, ..., B$ (middle). These are used to calculate a bootstrap standard deviation $sd^*(N_p)$ (right), which – together with the final estimate $\hat{N}_p$ (bottom left) – can be used to estimate a confidence interval CI^* (bottom right).

5.3 Confidence Interval via Bootstrap

5.3.1 Theory

If a certain number of windows on the filter were observed, their particles identified, and the final estimate calculated (equation (5.2.2)), the standard deviation of the final estimate is of interest to calculate a confidence interval. As this depends on the spatial structure of the particles, which is typically not fully known (due to influences of e.g. the filtration setup, characteristics of the sample or sample treatment), it cannot be obtained analytically (i.e. exactly with a formula). However, bootstrap methods offer a way to estimate this standard deviation and thus the confidence interval.

In bootstrap methods (see Figure 5.5) new window samples are drawn from the original window sample with replacement (such that in a new sample some original windows might occur more often and other original windows might not occur at all). In a new bootstrap sample, the final estimate might also be calculated (equation (5.2.2)), thereafter referred to as *final bootstrap-sample estimate*.

Such a bootstrap sample might be drawn many times (e.g. $B = 5000$ times) from the original sample, leading to many *final bootstrap-sample estimates*. The standard deviation of these many *final bootstrap-*

sample estimates might then be used as proxy (i.e. a bootstrap-estimate) for the standard deviation of the final estimate, in order to calculate a (bootstrap-based) confidence interval.

Formally, denote the b-th ($b = 1, \ldots, B$) *final bootstrap-sample estimate* as $\hat{N}_p^b$. Their mean and standard deviation are (with * indicating the reference to the bootstrap samples)

$$\overline{N_p^*} = \frac{1}{B} \sum_{b=1}^{B} \hat{N}_p^b \tag{5.3.1}$$

and

$$sd^*\left(\hat{N}_p\right) = \sqrt{\frac{1}{B} \sum_{b=1}^{B} \left(\hat{N}_p^b - \overline{N_p^*}\right)^2}, \tag{5.3.2}$$

respectively. The latter can be used as proxy for the standard deviation $sd\left(\hat{N}_p\right) = sd^*\left(\hat{N}_p\right)$ of the final estimate, leading to the bootstrap-based confidence interval

$$CI^*\left(\hat{N}_p\right) = \left[\hat{N}_p \pm z \cdot sd^*\left(\hat{N}_p\right)\right] . \tag{5.3.3}$$

In every bootstrap method, the representativity of the original (window) sample for the population (filter) is of fundamental importance. Assume e.g. a Gaussian filter and that all windows are located near the margin of the filter, such that there is hardly any particle in any window. Of course, this window data does not represent the filter well and any bootstrap method might not yield useful results. If the original window sample is less representative for the complete filter, then the bootstrap confidence interval might be longer or shorter than the true confidence interval. While longer confidence intervals provide a conservative error quantification (i.e. the true error probability is smaller than required), smaller confidence intervals provide liberal error quantifications (i.e. the true error probability is larger than required). Typically, the latter is considered far worse than the former, as there is no guarantee that the required limit on the error probability can be kept. As outlined above (Section 5.2.3), systematic windows might suffer from a bias, impairing the representativity of the window sample in an uncontrollable manner, and random windows express greater variation in the window samples (increasing the likelihood of randomly getting less representative window data), which, however, can be controlled by increasing the number k of windows.

5.3.2 Assessment

A simulation analysis was done to assess the performance of the bootstrap-based confidence interval estimation w.r.t. potential impairments due to a lack of representativity and the additional error introduced by bootstrap estimation. Three conditions were evaluated: random windows for both types of filters (regular and Gaussian) and systematic windows for Gaussian filters (the fourth condition was omitted to save computational resources). Within each condition, for each of the 5000 simulated filters, a varying number k of windows were selected. Each of those window data (original sample) were used to estimate

a bootstrap-based confidence interval as outlined above, using a given error probability $\alpha = 0.10$. So, for each value of k and each condition, 5000 bootstrap-based confidence intervals were obtained (each with $B = 5000$ bootstrap samples), and Figure 5.6 shows the 90%-bands of the corresponding absolute error margins (these bands include 90% of these error margin values and exclude the 5% lowest and 5% largest values). Figure 5.6 also plots the expected absolute error margin obtained with the simulation of Section 5.2.3 (compare Figure 5.3b; values of the absolute error margin relate to those of the standard deviation by $e = z \cdot sd\left(\hat{N}_p\right)$). This band illustrates the extra variation that is introduced by using a bootstrap method, which - as expected - decreases with increasing number k of windows (the band narrows down).

Bootstrap based confidence intervals tend to be longer than the true confidence interval that was obtained with the previous simulation (the band deviates upwards from the line), especially for increasing number k of windows. In that, these bootstrap-based confidence intervals tend to be conservative, such that the true error probability might be smaller than the previously specified maximal error probability α. Within the Gaussian filters, obtaining a liberal confidence interval becomes unlikely for larger, but reasonable (compare Supplementary Information Section 5.6.5), numbers of windows $k > 1300$ (the lower limits of the 90%-bands surpass the blue line). Although corresponding numbers of particles to identify might be larger with these bootstrap intervals, their conservativeness is a very advantageous property, as it reduces the risk of not being able to meet the requirement on the error probability α, which is inherent to a bootstrap method if the original sample is less representative. An analysis of the true error probability of the bootstrap confidence intervals shows that the given error probability α could be kept for reasonable numbers k of windows (see Figure S.5.4 in the Supplementary Information).

The 90%-bands for random and systematic windows are quite similar. This illustrates an important characteristic of bootstrap methods: New bootstrap window-samples are treated as a *random* window-sample of the filter, even if the original window locations were selected according to a systematic window scheme. Although systematic windows yield a smaller standard deviation than random windows (compare Section 5.2.3), this is not the case for the bootstrap-estimated standard deviation. In that, when using bootstrap methods to estimate confidence intervals, systematic windows are expected to have no benefit as the standard deviation caused by random windows now compares to systematic windows, and only their downside of generating a potential bias remains.

In summary, bootstrap methods allow to estimate a confidence interval and, thus, to assess the error within the final estimate (which is not possible with formulas), at the cost of introducing an additional source of error. This error, however, seems to shift results in a conservative direction, such that the true error rate might be lower than implied by the results. As a consequence, this might increase the number of particles to identify, but tackle potential representativity issues inherent to bootstrap methods.

Most importantly, a bootstrap confidence interval is only an estimate of the actual (analytically inaccessible) confidence interval and might also be erroneous. It should also be noted that bootstrap methods are not free of critique (for a first overview about bootstrap in general, see[46]). However, in the present case, they might offer a way to check whether the required error margin is roughly reached.

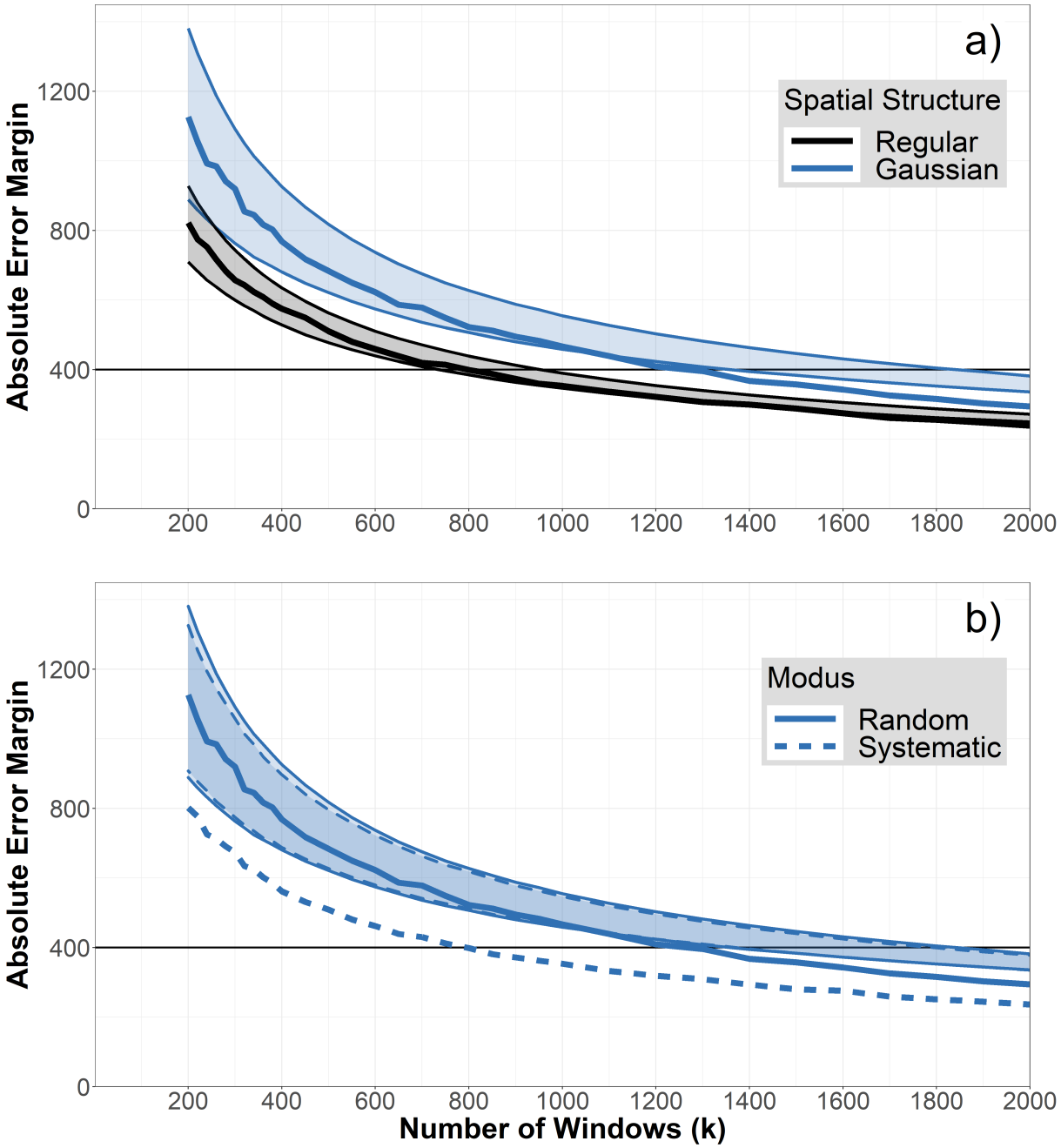

Fig. 5.6: Bootstrap Confidence Intervals. Plots depict lengths of the confidence intervals (absolute error margin e) for varying numbers k of windows. While the thick lines depict the "true" length of the confidence intervals as obtained by the simulation (see Section 5.2.3 and Figure 5.3b), the bands depict estimates of the absolute error margins obtained by the bootstrap methods: For each condition and each number k of windows, 5000 bootstrap confidence intervals were estimated and the bands include 90% of the corresponding error margin values, excluding the 5% lowest and 5% largest values. These 90%-bands illustrate the additional variation introduced via bootstrap. a) For both Gaussian (blue) and regular (black) filters, bootstrap confidence intervals tend to be longer, i.e. more conservative, than the "true" confidence interval, especially for larger number k of windows (the band deviates upwards from the line). b) Bootstrap confidence intervals tend to be similar for random (solid lines) and systematic (dashed lines) windows (both bands are similar), although the "true" confidence interval with systematic windows is shorter than with random windows (see Section 5.2.3 and Figure 5.3b), illustrating that bootstrap samples are treated as *random* representation of the filter, even if the original windows were placed systematically.

5.4 *On-The-Fly* Raman Microspectroscopy for Very Small Microplastic

Traditional sample size calculations (if the complete filter is known, see Box in Figure 5.1) require specifications of the number N of particles on the filter and the ratio r of plastic particles. The latter is not known prior to the analysis and the former is unknown if window methods are employed. Therefore, those sample size calculations require initial guesses for these values. If those deviate from the true values, then the number of identified particles is too low or too high. Thus, we want to outline an *on-the-fly* algorithm that solves this issue and provides an optimal number of windows. Here, the RM data is analyzed during the measurement by computing a bootstrap confidence interval and assessing whether given precision requirements are already met. If so, the measurement would stop. This avoids having an eventually insufficient sample size or measuring more particles than actually needed.

5.4.1 Procedure

Aside the precision requirements α and e, an initial number k_{ini} of windows should be chosen as starting point for the first bootstrap confidence interval calculation. This is necessary, as mathematical peculiarities might erroneously lead to stop the procedure prematurely, if only few windows were used. In our simulation setup, the average number of particles per window was around 1.6, such that using 100 windows (for *1-FOV* or *4-FOV*) initially might be a reasonable choice. With regard to Section 5.2.4, the window size should be chosen as small as possible. This number is influenced by N and r, thus, the sample size calculation of the large particles (random sampling Box in Figure 5.1) can inform this choice, as this is an optimistic "best case" of the window sampling and displays a lower limit of particles to identify.

After identifying the particles in the k_{ini} windows, if the precision requirements were not met, the number of windows should be increased by an increment k^+ of windows. In theory, it is possible to choose $k^+ = 1$, but performing too many bootstrap estimations yields the risk of erroneously reaching the stopping criterion (because of the additional randomness inherent to bootstrap methods), especially when approaching the stopping criterion. For the examples in this paper, $k^+ = 50$ was used. Examples are depicted in Figure 5.7.

The total number B of bootstrap samples to estimate a confidence interval should be sufficiently large. Within our simulation, we used $B = 5000$, which is comparatively small, to reduce simulation times. In a real application, values as $B = 10000$ or even higher should be easily manageable.

With these specifications, the *on-the-fly* procedure is as follows:

1. As initialization, select k_{ini} window locations randomly (allowing windows to exceed the filter borders, compare Section 5.2.3).

2. Detect (consider window edge issues, Supplementary Information Section 5.2.1.2) and analyze all particles within the (newly) chosen windows with RM.

3. Using the complete data set, estimate the number $\hat{N}_p$ of microplastic particles on the filter using formula (5.2.2).

4. Estimate the standard deviation $sd^*\left(\hat{N}_p\right)$ of this estimate via bootstrap:

   a) For $b = 1, ..., B$:

      - Draw a bootstrap sample by drawing k windows from the original sample (consisting of the original k windows) with replacement.

      - Calculate the *final bootstrap-sample estimate* N_p^b within this bootstrap sample using formula (5.2.2).

   b) Use all B *final bootstrap-sample estimates* to calculate their standard deviation $sd^*\left(\hat{N}_p\right)$ (equation (5.3.2)).

5. For the given significance level α, calculate the bootstrap confidence interval (equation (5.3.3)) and determine the (absolute or relative) error margin.

6. If this (absolute or relative) error margin is larger than the desired (absolute or relative) error margin, select another k^+ windows randomly and return to step 2, else stop the RM analysis.

Within the application of the *on-the-fly* procedure, random windows were used. In theory, it is possible to use systematic windows as well, however, it might be difficult to find a pattern of windows that allows to increase the number of windows sequentially, such that the structure of the systematic windows stays the same. Further, even if such a pattern was found and employed, the benefit in reducing the standard deviation (see Section 5.2.3 and Figure 5.3b) is mitigated by using bootstrap methods for estimating confidence intervals (see Section 5.3.2). Nevertheless, a potential and uncontrollable bias might be introduced by systematic windows, compared to random windows, that might impair the representativity of the window samples in an unknown manner and cannot be controlled by (subsequently) increasing the number of windows. Moreover, it is conceivable that the ratio of MP r also exhibits a spatial structure, whose influence is easily circumvented by the random window sampling.

Sample size considerations depend on N and r, and when using window based sampling or bootstrap estimation methods this number will be even higher, compared to the random sampling. Our simulation-based illustration uses $N = 20000$ and $r = 0.20$, however, values in real applications cover a very wide range. If the plastic ratios r is smaller or the particle number N is larger, the sample size may be exceedingly large, such that it may not be possible to identify this amount of particles in reasonable time. In this case, the *on-the-fly* procedure should have a predefined stopping point. Then, of course, it would not meet the precision requirements and it should be considered if some other, less strict precision requirements are agreeable. Furthermore, the experimentator can opt to perform an enrichment step (e.g. density separation) to increase the ratio of MP r or, ultimately, decide on a different technique (e.g. thermoanalytical), which of course will trade off the in-depth information of RM for measurement speed (see Section 5.1).

5.4.2 Examples and Assessment

Figure 5.7 shows three different runs of the *on-the-fly* procedure on the Gaussian filters using $k_{ini} = 100$, $k^+ = 50$, and $B = 5000$. For each iteration, the estimate (point) and its bootstrap-estimated confidence interval (with $\alpha = 0.10$) are depicted in relation to the true value $N_p = 4000$ (black horizontal line). The last confidence interval that was estimated (in blue) is characterized by a relative error lower than the prespecified requirement of $e_{rel} = 0.10$, leading to stop the procedure. Figure 5.7a depicts a case, in which the final result (estimate plus confidence interval) does not cover the true value, representing an error which might be caused randomly by an unrepresentative window placement. Figure 5.7b shows an example, where $\hat{N}_p$ falls too low but recovers and yields a correct result and Figure 5.7c depicts a run that arrives at the true value directly.

In order to assess the performance of the *on-the-fly* procedure, all 5000 filters (of each type) were analyzed (with differing increment sizes to reduce computation time: $k^+ = 50$ for $k < 1000$ and $k^+ = 100$ for $k > 1000$). For a significance level of $\alpha = 0.10$, the first k with a confidence interval with $e_{rel} < 0.10$ was used as result.

The resulting number of windows for regular filters ranged from 650 to 1100 with a mean of 872 $\pm$ 108 and for Gaussian filters from 1300 to 2100 with a mean of 1665 $\pm$ 69 (respective distributions are depicted in the Supplementary Information Figure S.5.5). This tends to be higher than the minimal number of windows as obtained by the simulation (800 and 1300, respectively, see Section 5.2.3), which might result from the tendency of the bootstrap estimation to extend confidence intervals in this setup (see Section 5.2.3).

Of all *on-the-fly* runs on regular and Gaussian filters, only 8.58 % and 5.2 % yielded confidence intervals that do not cover the true value $N_p = 4000$, respectively, indicating the conservativeness of bootstrap-based *on-the-fly* results, as an error probability of $\alpha = 0.1$ was allowed in this simulation. In that, the higher window number of bootstrap is counterbalanced by the profit of reducing the true error probability.

In summary, the *on-the-fly* procedure with the bootstrap-based confidence interval provides an algorithmic implementation of error quantification and sample size considerations into window-based RM analyses. By its nature, this adaptive procedure tackles typical specification issues inherent to classic sample size calculations (Box in Figure 5.1), however, still tending towards conservative results, which, in turn, counteracts potential representativity issues of bootstrap methods. Here, the question about sampling modus is clearly answered: Random windows should be employed, as the only benefit of systematic windows (lower standard deviation) seems to get lost by using bootstrap methods.

5.5 Conclusion

Microplastic assessment demands reliable quantification from the analytical techniques, among which RM is able to cover very small particles. Providing quality control to its data has previously been enabled

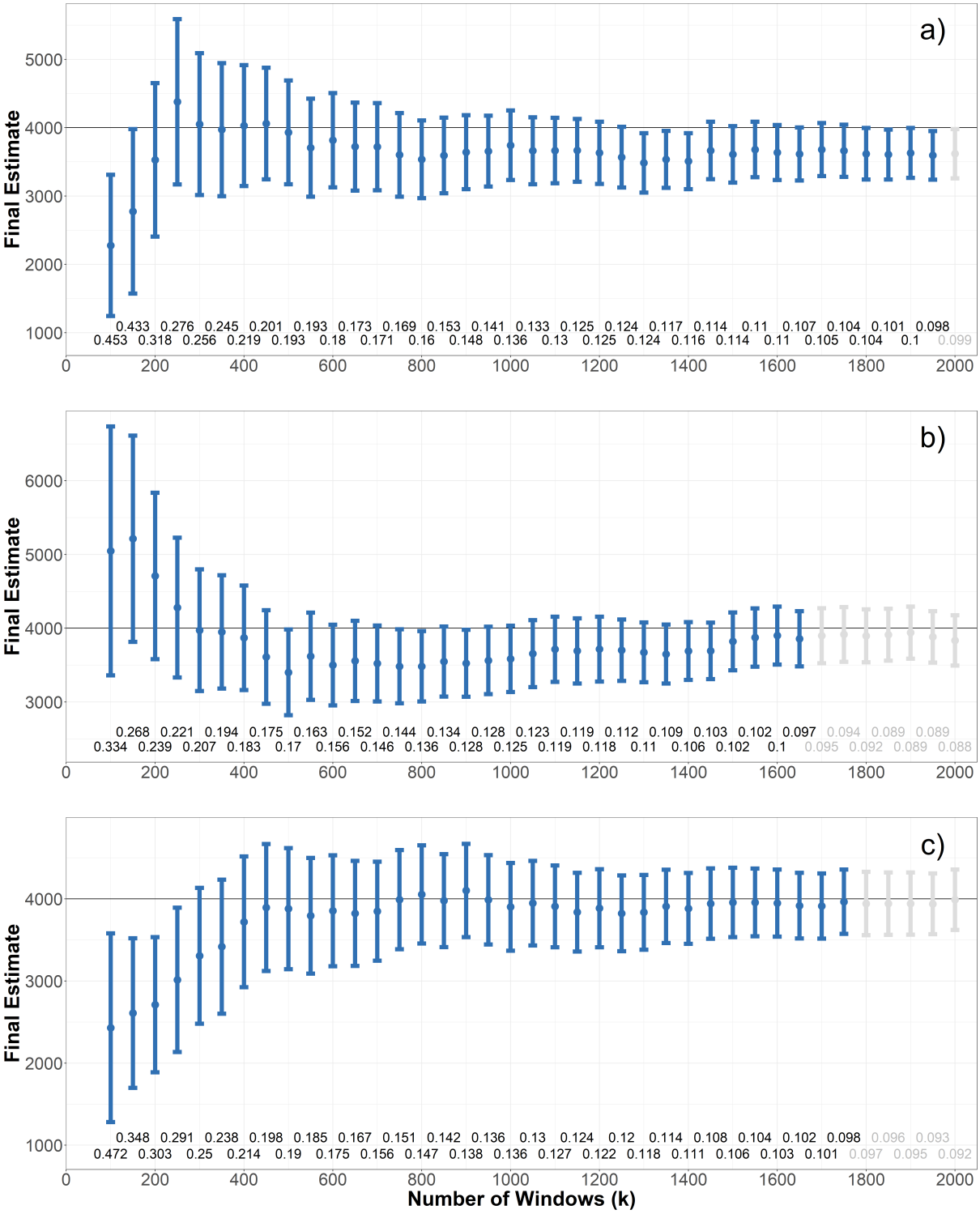

Fig. 5.7: *On-The-Fly* Procedure: Exemplary Runs. For each number k of windows, with $k_{ini} = 100$ and $k^+ = 50$, the point represents the final estimate with the vertical bar depicting the bootstrap confidence interval (with $B = 5000$, and $\alpha = 0.10$). The procedure is stopped after the relative error margin (numbers below each confidence interval) fell below $e_{rel} = 0.1$, after which the subsequent confidence interval would not be available in a real application but is depicted here for illustrative purposes (greyed out). The black line depicts the true value $N_p = 4000$. a) The *on-the-fly* procedure misses the true value of N_p (due to the statistical error). b) and c) The algorithm yields a correct result.

for particles > 10 µm, where random sampling can be applied[19]. Since the smaller particles are more difficult to analyze, a new window-based selection scheme is proposed, for which - as for random sampling - confidence intervals can be obtained. This approach is illustrated on two kinds of spatial structures on the filter: a random distribution with the only stipulation that particles cannot lie within each other, and a Gaussian structure where the particles tend towards the center of the filter. Comparing random and systematic window placement, it is demonstrated that systematic windows are prone to bias, random windows, however, pay for the unbiasedness with increased variance (i.e. standard deviation) and, in turn, number of particles to identify. Further, the importance of using as many small windows as possible rather than few large windows is shown, since the latter amplifies the bias of systematic windows and the variance of random windows, respectively. To achieve a confidence interval for the estimate of the plastic particle number, a bootstrap method was used. Here, the representativity of the sample taken is essential, and random windows are clearly to be preferred. Moreover, due to the random resampling in the bootstrap method, the variance benefit of systematic windows compared to the random windows is lost, nullifying its advantage for this application. Finally, these results were unified in the projection of an *on-the-fly* RM measurement protocol, in which increments of particles are selected, identified and the result instantly subjected to a bootstrap calculation. Its resulting confidence interval then informs the decision to either stop or continue the measurement. This iterative approach solves the problem that an initial sample size calculation requires information on the particle number and MP content, which are only available after the analysis. Therefore, an automated RM analysis could generate MP quantification within a required precision for particles in this very low size range, while also being efficient with measurement time by stopping after the required precision has been reached.

Acknowledgements

The authors gratefully acknowledge financial support from the Federal Ministry of Education and Research, Germany (BMBF) for the project *SubµTrack* (grant number: 02WPL1443A) and *HOTMIC* (grant number: 03F0851B). In addition, we want to thank Philipp Anger for the inspiring discussions on this topic.

Conflict of interest

The authors declare that they have no conflict of interest.

Data availability

The datasets and the respective R code generated and analyzed during the current study are available online under https://doi.org/10.14459/2021mp1596628.

5.6 Supplementary Information

5.6.1 Random Sampling on the Complete Filter

If every particle is known, then the spatial structure is irrelevant, only the set of particles is relevant. By using random sampling, the error can be controlled and minimized[16]. Thus, random sampling has to be preferred, whenever the possibility. The following section will lay out the formal theory of the confidence interval and sample size calculation for the random sampling. A brief summary has been given in the Box in Figure 5.1. In the statistical treatment of this problem, a perfect technical implementation of Raman measurement and particle detection shall be assumed – although it still is a current topic, on which diligent work is being performed.

5.6.1.1 Formalizing the Estimation

Denote the number of particles and of plastic particles on the filter as N and N_p, respectively. Accordingly, the ratio of plastic particles over all particles on the filter is

$$r = \frac{N_p}{N} \,. \tag{5.6.1}$$

Only the total number N of particles on the filter is available, but the number N_p of plastic particles on the filter is of interest, which can be calculated by

$$N_p = N \cdot r \,. \tag{5.6.2}$$

The ratio r is unknown and usually it is not possible to identify the type of every particle on the filter. Therefore, a subset of all particles on the filter should be selected for RM. Denote the number of particles and plastic particles within this subset as S and S_p, respectively. Both of these quantities are known after RM analysis and the ratio of plastic particles over all particles within this subset can be calculated:

$$r_S = \frac{S_p}{S} \,. \tag{5.6.3}$$

This ratio r_S can then be used as an estimate for the ratio r on the filter. In that, we denote the estimate as (an estimate will always be indicated with a hat $\hat{}$ within this section)

$$\hat{r} = r_S \,. \tag{5.6.4}$$

By selecting the subset randomly, this estimate $\hat{r}$ is a random variable, and by plugging in this estimate into equation (5.6.2), also the quantity of interest becomes a random variable:

$$\hat{N_p} = N \cdot \hat{r} = N \cdot r_S \,. \tag{5.6.5}$$

5.6.1.2 Confidence Interval - Theory

Naturally, this estimate $\hat{N}_p$ might be erroneous and its error can be quantified by considering its standard deviation $sd\left(\hat{N}_p\right)$, which in turn can be derived from the standard deviation $sd(\hat{r})$ of the (random) ratio estimate:

$$sd\left(\hat{N}_p\right) = N \cdot sd(\hat{r}) \ . \tag{5.6.6}$$

In that, it suffices to assess the standard deviation of the ratio estimate $\hat{r}$ in order to then quantify the error of the final estimate $\hat{N}_p$.

This standard deviation depends on N, N_p, S, and on the selection scheme of the subset (i.e. which kind of randomness).

The obvious question to ask here is which sampling scheme is the best (i.e. resulting in the lowest standard deviation). Universally agreed on[27,29] and already elaborated on in the field of microplastic[16], this selection should be “completely random”, in a sense that each particle on the filter should have the same probability to be selected for RM identification.

By using this random sampling, the selection of particles for RM can be represented by a classical urn model without replacement and the formula for the standard deviation is:

$$sd(\hat{r}) = \sqrt{\frac{r \cdot (1-r)}{S} \cdot \frac{N-S}{N-1}} \, . \tag{5.6.7}$$

So, after selecting the subset, doing the RM analysis and calculating the ratio estimate $\hat{r}$ (equation (5.6.4)), the standard deviation $sd(\hat{r})$ can be used to determine a confidence interval around the ratio estimate $\hat{r}$. This confidence interval specifies a range of the most plausible values for the ratio estimate $\hat{r}$ and therefore accounts for the estimation uncertainty (in contrast to the point estimate $\hat{r}$ alone).

A confidence interval always refers to a given confidence level $(1-\alpha)$ (where α is the error probability or significance level), such that the probability of the interval covering the true value r is $(1-\alpha)$. Although typical choices are 80%, 90%, 95%, or 99%, the confidence level should be specified according to the actual requirements of the applied context.

The estimate $\hat{r}$ (random variable) is approximately normally distributed (central limit theorem), such that the confidence interval of $\hat{r}$ can be calculated as

$$CI(\hat{r}) = \left[\hat{r} - z_{1-\frac{\alpha}{2}} \cdot sd(\hat{r}) \, , \hat{r} + z_{1-\frac{\alpha}{2}} \cdot sd(\hat{r})\right] \ , \tag{5.6.8}$$

where $z_{1-\frac{\alpha}{2}}$ is the $(1-\frac{\alpha}{2})$-quantile of the normal distribution (referring to the given confidence level $(1-\alpha)$). Frequently used values are $z_{0.90} = 1.28$, $z_{0.95} = 1.64$, $z_{0.975} = 1.96$, and $z_{0.995} = 2.58$ for the four α-values mentioned above.

This $(1-\alpha)$ confidence interval of the ratio estimate $\hat{r}$ can then be used to calculate the $(1-\alpha)$ confidence interval of the final estimate (of the number of plastic particles on the filter)

$$CI\left(\hat{N}_p\right) = N \cdot CI(\hat{r}) \ . \tag{5.6.9}$$

This confidence interval is then interpreted as being the range of values for $\hat{N}_p$ that covers the true value N_p with probability $(1-\alpha)$, which means that if this procedure of random sampling would be repeated infinitely and confidence intervals would be calculated analogously, then only α of these confidence intervals do not contain the true value N_p.

5.6.1.3 Confidence Interval - Estimation

Unfortunately, these confidence intervals cannot be calculated as the true ratio r in the formula for $sd(\hat{r})$ (equation (5.6.7)) is unknown. Instead, the confidence intervals can only be estimated by using the estimate $\hat{r}$. In that, the estimated standard deviation is

$$\hat{sd}(\hat{r}) = \sqrt{\frac{r_S \cdot (1-r_S)}{S} \cdot \frac{N-S}{N-1}} \tag{5.6.10}$$

and the estimated confidence interval of $\hat{r}$ becomes

$$\hat{CI}(\hat{r}) = \left[\hat{r} - z_{1-\frac{\alpha}{2}} \cdot \hat{sd}(\hat{r}) \, , \hat{r} + z_{1-\frac{\alpha}{2}} \cdot \hat{sd}(\hat{r})\right] \ , \tag{5.6.11}$$

leading to the estimated confidence interval of the final estimate

$$\hat{CI}\left(\hat{N}_p\right) = N \cdot \hat{CI}(\hat{r}) \ . \tag{5.6.12}$$

Instead of reporting solely the point estimate $\hat{N}_p$, this estimated confidence interval $\hat{CI}\left(\hat{N}_p\right)$ should be provided in every microplastic analysis.

5.6.1.4 Sample Size Calculation

In addition, these considerations about confidence intervals can be used to calculate the required size S of the subset, such that a confidence interval of a given length can be obtained.

As can be seen in equation (5.6.8), the confidence interval $\hat{CI}(\hat{r})$ of the ratio estimate $\hat{r}$ is a symmetric interval around the point estimate $\hat{r}$ with “radius”

$$e = z_{1-\frac{\alpha}{2}} \cdot \hat{sd}(\hat{r}) \ , \tag{5.6.13}$$

which is frequently denoted by e and referred to as absolute error margin.

In contrast, the relative error margin e_{rel} relates the absolute error margin e to the ratio estimate $\hat{r}$:

$$e_{rel} = \frac{e}{\hat{r}}\,. \tag{5.6.14}$$

For example, assume two different confidence intervals around the point estimates $\hat{r} = 0.5$ and $\hat{r} = 0.1$, respectively, both with a relative error of $e_{rel} = 0.1$. In that, the absolute error margins are $e = e_{rel} \cdot \hat{r} = 0.05$ and $e = e_{rel} \cdot \hat{r} = 0.01$, yielding the confidence intervals $[0.45, 0.55]$ and $[0.09, 0.11]$, respectively.

In order to calculate the required number S of particles that should be subjected to RM identification, one needs the following quantities: N, r, $(1-\alpha)$, and e. The first is known, the second is unknown (and no estimate $\hat{r}$ is available prior to the RM identification analysis), and the remaining two should be specified according to the "precision requirements" of the analysis, in a sense that one should state the error probability α, one is willing to accept, that the ratio estimate $\hat{r}$ deviates more than e (absolute error margin) from the true ratio value r. The usual handling of the unknown ratio r is to assume a plausible value and use this assumed ratio.

The required minimum size S can then be calculated as[16]:

$$S \geq \frac{r \cdot (1-r)}{\frac{e^2}{(z_{1-\frac{\alpha}{2}})^2} + \frac{r \cdot (1-r)}{N}} \tag{5.6.15}$$

Of course, the assumed ratio r used in this calculation prior to the RM identification process might differ from the estimate $\hat{r}$ (i.e. r_S) that is obtained after RM identification. This might explain that the estimated confidence interval (equation (5.6.11)), which is calculated with the ratio estimate $\hat{r}$, might not keep the previously specified "precision requirements" (α and e), which are based on the assumed ratio r.

Nevertheless, it is highly recommended to perform an own sample size calculation prior to RM analysis, as each RM analysis has its own characteristics and requirements. This can be done easily with the following steps:

- Determine the total number N of particles on the filter that might be subjected to RM identification.
- Assume a plausible value for the ratio r of plastic particles among all particles on the filter. If it is too difficult to decide on one single value, try different plausible values. Applying a smaller r increases the sample size but increases the chances that the precision requirements are met.
- State the "precision requirements" (α and e): Only an error probability of α should be accepted that the ratio estimate $\hat{r}$ deviates more than e from the true ratio r. Frequently, the precision requirement is expressed by a relative error e_{rel}, which needs to be transferred to the absolute margin of error $e = r \cdot e_{rel}$.
- Determine the $z_{1-\frac{\alpha}{2}}$-quantile for the desired maximal error probability α.
- Calculate the minimum sample size S using equation (5.1.3).

Of course, all S particles that should be subjected to RM identification have to be selected randomly from all N particles, else the error calculations as outlined above do not hold.

As illustration, table S.5.1 contains results of the sample size calculation for a specific set of precision requirements, i.e. $\alpha = 0.1$ and $e_{rel} = 0.1$. Note that for decreasing r and increasing N the sample size increases, respectively.

Tab. S.5.1: Exemplary values of S for different precision requirements. Columns are N and rows are r.

$\alpha = 0.1$										
$e_{rel} = 0.1$	1000	2000	5000	10000	20000	50000	100000	200000	500000	1000000
0.5000	213	239	257	264	267	270	270	271	271	271
0.4000	289	338	376	391	398	403	405	406	406	406
0.3000	387	480	561	594	612	624	628	630	631	631
0.2000	520	703	890	977	1027	1060	1071	1077	1080	1082
0.1000	709	1099	1638	1959	2171	2322	2378	2406	2424	2430
0.0500	838	1440	2535	3396	4090	4662	4890	5012	5089	5115
0.0050	982	1929	4576	8434	14583	25925	34998	42421	48607	51090
0.0005	999	1993	4955	9819	19287	45769	84396	146008	259809	351003

5.6.2 Spatial Structure of Particle Locations

In many MP laboratories, window sampling is necessary and especially when approaching very small MP it will be mandatory. Here, the influence of the spatial structure of the particles can no longer be evaded by random sampling. This section will discuss the fundamental concepts of spatial structures (especially different types of influences), as laid out in the field of spatial statistics[45].

In principle, there is a so called random point process that can generate spatial structures, which are said to be realizations of this point process. In that, we assume that our observed spatial structure on the filter (e.g. in Figure S.5.2) belongs to a certain, but unknown point process. In the case of MP filtration, the point process would be characterized by the properties of the particles (e.g. propensity for clustering) and the filtration setup (e.g. vacuum pump, fluid dynamic) and the spatial structure would be the actual arrangement of the particles on this one specific filter. Hypothetically, filtering the particle suspension (water sample) again, would give another spatial structure, which is another realization of the same point process.

In spatial statistics different point processes are discerned[45]. The stereotypical and idealized point process is characterized by *complete spatial randomness* (CSR), such that the location of every point (i.e. particle) is uniformly distributed in the area of interest (i.e. on the filter), which means that every location on the filter has the same probability to be selected as location for a particle (see Figure S.5.1a). With CSR different points might be arbitrarily close to each other.

In general, there are two different types of influences on the spatial structure that deviate it from CSR.

- First, there might be an interaction between the points (particles) themselves (irrespective of their locations on the filter). In that, two different interactions might be distinguished:

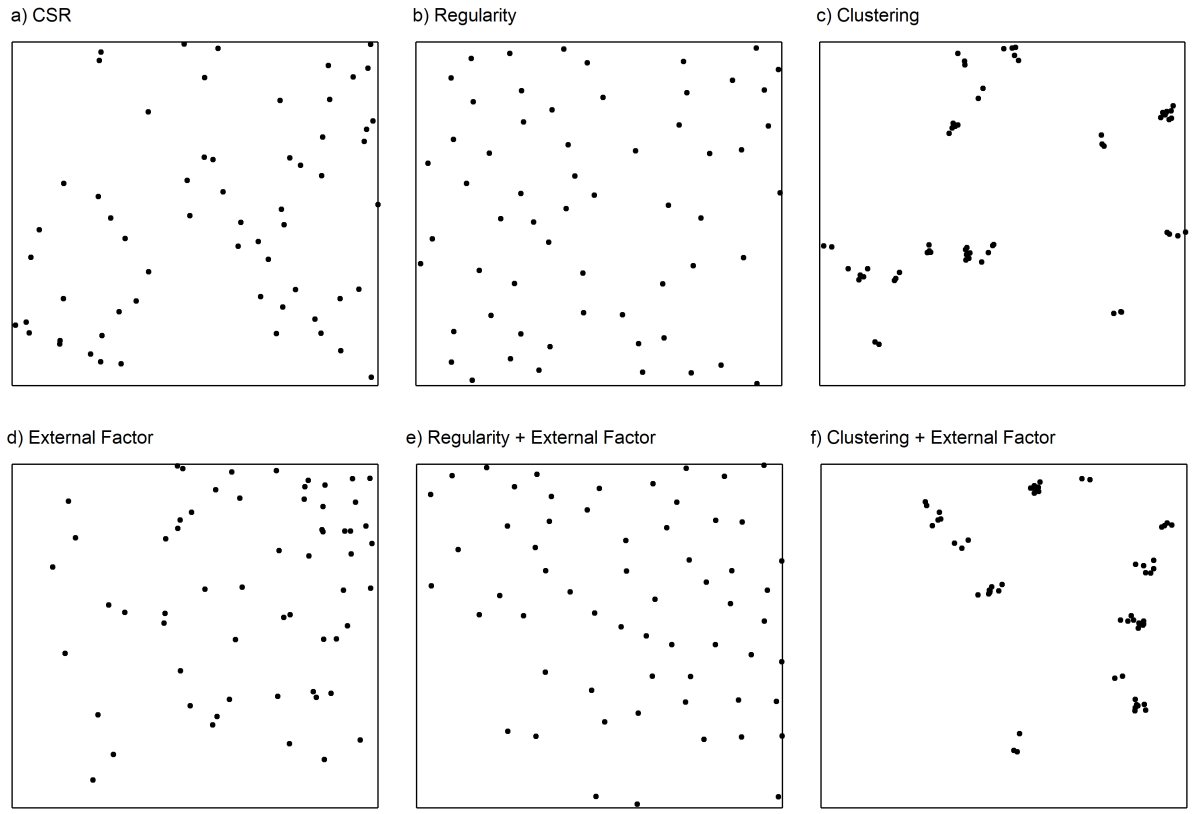

Fig. S.5.1: Influences on Spatial Structures. a) Complete Spatial Randomness: the particle locations have a uniform probability distribution. b) Regularity: particles repulse each other, so that they are less likely to appear close to each other. c) Clustering: particles attract each other, so that they are more likely to appear close to each other. d) External influence: an influence that directs particles to certain locations (here upper right). e) Regular particle distribution with external influence. f) Clustering particles with external influence.

  - *Regularity.* In a regular point process, the points repulse each other, such that it is unlikely or impossible for points to be close to other points (Figure S.5.1b). Points or particles are said to have a *hard core*, if it is impossible for other particles to be located within its core (i.e. near surrounding).

  - *Clustering.* When particles attract each other, clusters of particles occur. Cluster locations, however, might still be uniformly distributed on the filter (Figure S.5.1c) or influenced by external influences (Figure S.5.1f).

- Second, point locations might be influenced by external influences (irrespective of the interactions between the points), e.g. points (or cluster locations) might tend towards the margin or the center of the area of interest (see Figure S.5.1d–f).

Having these different types of influences on spatial structures in mind, it appears obvious that spatial structures might be quite complex and their characterization cannot be summarized in one single quantity. In fact, the field of spatial statistics offers a range of different functions, each one only being able to describe a single aspect of a spatial structure[45]. In that, comprehensively describing or even modeling spatial structures is a very difficult task. “Practically”, Pitard even “conclude[s] that the sampling of

two-dimensional lots (...) is an unsolvable problem" [29, p. 589].

Interactions between particles influence only the standard deviation of the final estimate, with regularity reducing it and clustering increasing it. Consider the following:

- If particles express regularity (which they do as they have a hard core), it is less likely that in one single window there would be extremely many or extremely few particles compared to when particles would not express regularity. In that, the standard deviation of the number of particles in this window (and therefore also the standard deviation of the final estimate) is lower with regularity compared to without regularity.

- If particles cluster (with random cluster locations), it is more likely that in a single window there would be extremely many (if the window is on a cluster) or extremely few particles (of the window is not on a cluster) compared to when particles do not cluster. Thus, the standard deviation of the number of particles in this window (and therefore the standard deviation of the final estimate) is higher with clustering than without.

A bias would arise if characteristics of the spatial structure would be systematically missed within the observed windows. This is not the case with regularity or clustering per se, as particle locations or cluster locations would still follow a random pattern. Only with an external influence (that affects the locations of particles or cluster, e.g. a vacuum pump vortex) a bias might arise in dependence of the window selection scheme, as illustrated in the paper in Section 5.2).

Furthermore, concerning the use of the term "homo-/heterogeneity", it seems that those terms are used with strongly differing meanings. In analytical chemistry they can refer to the spatial structure of particles, but also to chemical composition. Spatial statistics uses the term homogeneity in a sense of CSR (Figure S.5.1a) where particle locations have a uniform probability distribution[45]. It, however, appeared to the authors that in analytical chemical texts a "homogeneous" spatial structure typically refers to a regular point process as in Figure S.5.1b. This discrepancy might result from the observation that the distances between the points in the regular spatial structure are relatively similar, thus "homogeneous". Due to this multitude of meanings, we urge for studies to clearly and explicitly denominate the concept of "homo-/heterogeneity" that is employed and we want to emphasize that care has to be taken with those terms in interdisciplinary communication.

5.6.3 Simulation Details

Exemplary realizations of the artificial filters (regular and Gaussian) are depicted in Figure S.5.2. Simulations and analyses were performed in **R** (version $4.0.0$) and the code is accessible in an online repository at https://doi.org/10.14459/2021mp1596628. Used packages were boot (version $1.3.24$), spatstat (version $1.63.3$), ggplot2 (version $3.3.0$), ggforce (version $0.3.1$), and stringr (version $1.4.0$).

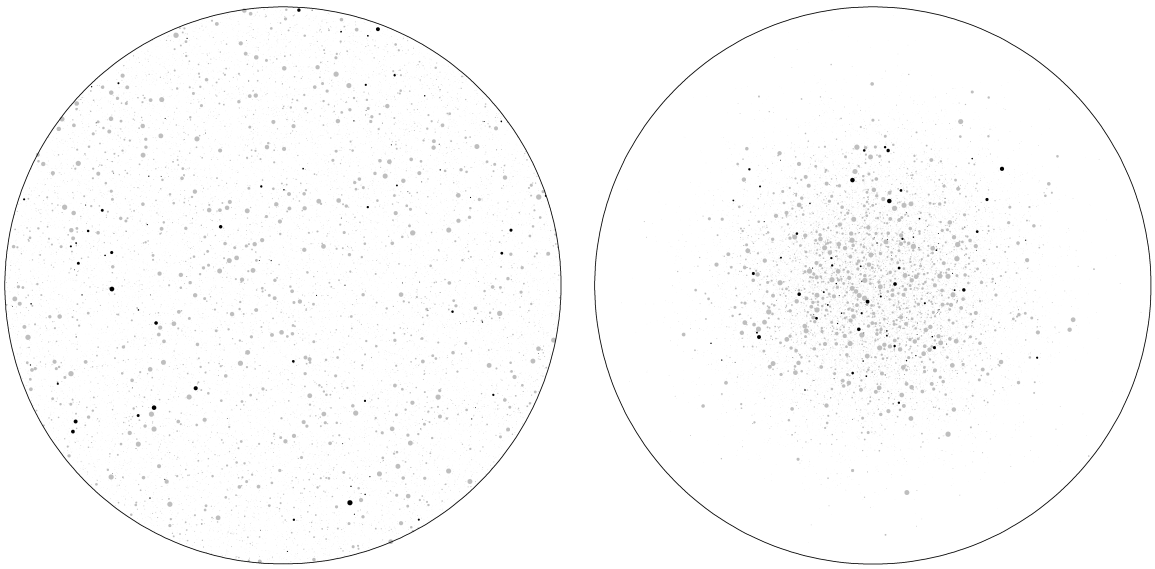

Fig. S.5.2: Example Filters in Simulation. Left: regular filter with particles with hard-core property a uniform probability distribution. Right: Gaussian filter with a Gaussian-like external influence that directs particles to the center. Each filter contains $N = 20000$ particles of which $r = 0.20$ are plastic particles (black). Particle sizes range from 1 µm to 20 µm and follow a power law as reported by Kooi et al.[26].

5.6.4 Filter Edge Issues

With the random window scheme it is important that the windows are allowed to overlap the border of the filter. Otherwise, there would be parts of the outer filter that are not properly represented within the windows. This effects an underrepresentation of the border, which can lead to a bias in the final estimate. This is exemplified in Figure S.5.3, where windows did not overlap and, in the presence of an external influence (Gaussian filter), the true value $N_p = 4000$ was overestimated by $\sim$ 80 particles.

5.6.5 Conservativeness in Bootstrap Estimates

By its definition, the $(1 - \alpha)$-confidence interval should cover the true value N_p with probability $(1 - \alpha)$, i.e. out of all confidence intervals (using the same setup, but different filters with the same external influences), only a ratio of α should be allowed to miss the true value N_p. Figure S.5.4 depicts for different numbers k of windows the ratio of all 5000 bootstrap confidence intervals that do not cover the true value. It shows that for a low number k of windows the bootstrap confidence intervals do not keep the given limit of $\alpha = 0.10$ (black horizontal line), but are conservative for a larger number k of windows.

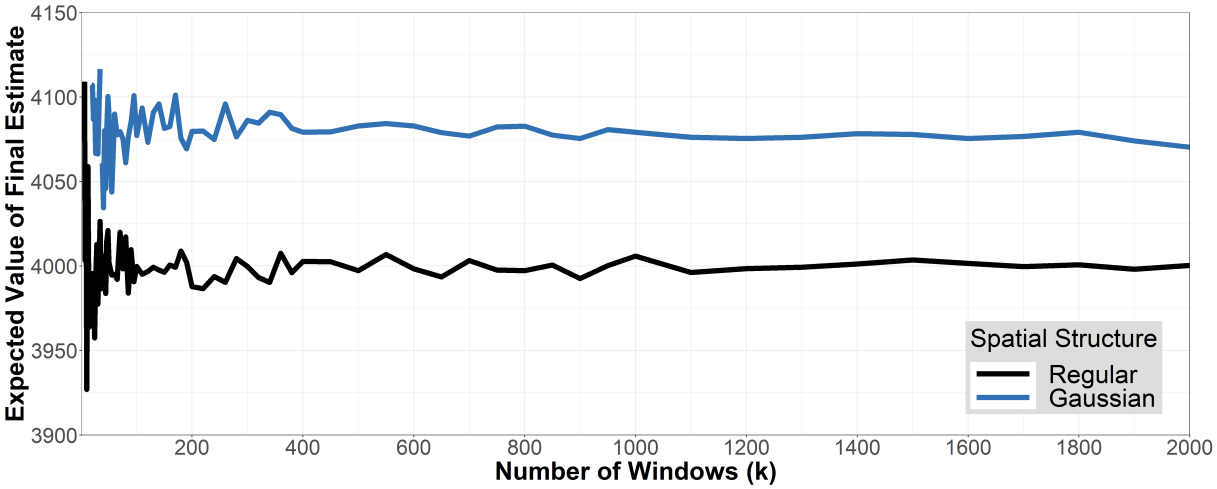

Fig. S.5.3: Filter Edge Issues. Random windows not overlapping the filter border causes an underrepresentation of this part of the filter in the windows. On the two cases of this paper, i.e. regular and Gaussian filters, this effects a bias for the Gaussian filter (blue) that overestimates the true value $N_p = 4000$.

5.6.6 Distribution of Window Number in *on-the-fly*

Within the simulation, actual window numbers after termination of the *on-the-fly* procedure with $e_{rel} = 0.1$ and $\alpha = 0.1$ are depicted in Figure S.5.5 for both regular and Gaussian filters.

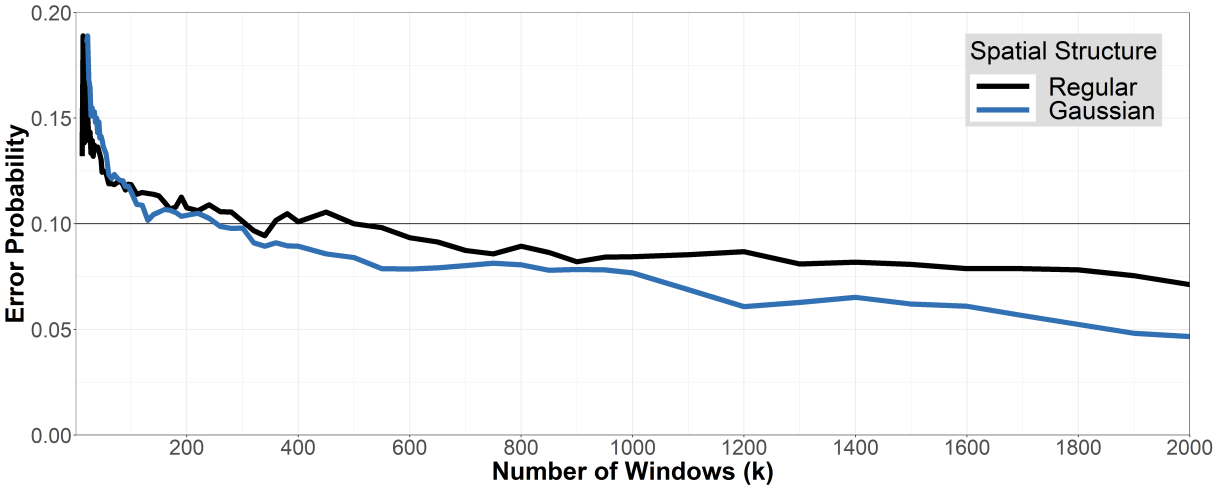

Fig. S.5.4: Conservativeness of Bootstrap Confidence Intervals. The plot depicts the ratio of all 5000 bootstrap confidence interval (with $\alpha = 0.1$) that do not cover the true value of $N_p = 4000$, which estimates the actual error probability α, for both regular and Gaussian filters. For typical numbers of windows (in the *on-the-fly* procedure on Gaussian filters: $1300 - 2100$, see Figure S.5.5) bootstrap confidence intervals are conservative, as their actual error probability is below the nominated $\alpha = 0.1$.

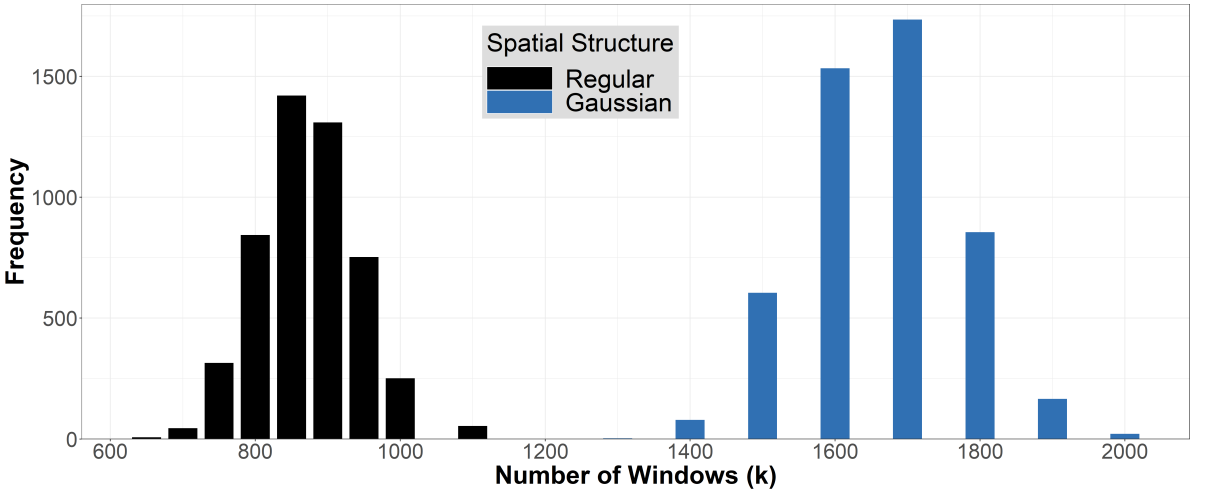

Fig. S.5.5: *On-The-Fly* Procedure: Actual Sample Sizes. Of the 5000 simulated filter, the stopping points k range from 650 to 1100 with $m \pm sd = 1665 \pm 69$ for regular filters and from 1300 to 2100 with $m \pm sd = 872 \pm 108$ for Gaussian filters. Window numbers were investigated in increments of 50 for $k \leq 1000$ and 100 for $k \geq 1000$.

References

1. Triebskorn, R.; Braunbeck, T.; Grummt, T.; Hanslik, L.; Huppertsberg, S.; Jekel, M.; Knepper, T. P.; Krais, S.; Müller, Y. K.; Pittroff, M.; Ruhl, A. S.; Schmieg, H.; Schür, C.; Strobel, C.; Wagner, M.; Zumbülte, N.; Köhler, H.-R. Relevance of nano- and microplastics for freshwater ecosystems: A critical review. *Trends in Analytical Chemistry* **2019**, *110*, 375–392.
2. Koelmans, A. A.; Mohamed Nor, N. H.; Hermsen, E.; Kooi, M.; Mintenig, S. M.; De France, J. Microplastics in freshwaters and drinking water: Critical review and assessment of data quality. *Water Research* **2019**, *155*, 410–422.
3. Chae, Y.; An, Y.-J. Effects of micro- and nanoplastics on aquatic ecosystems: Current research trends and perspectives. *Marine Pollution Bulletin* **2017**, *124*, Special Issue: Hong Kong Conference 2016, 624–632.
4. Hartmann, N. B.; Hüffer, T.; Thompson, R. C.; Hassellöv, M.; Verschoor, A.; Daugaard, A. E.; Rist, S.; Karlsson, T.; Brennholt, N.; Cole, M.; Herrling, M. P.; Hess, M. C.; Ivleva, N. P.; Lusher, A. L.; Wagner, M. Are We Speaking the Same Language? Recommendations for a Definition and Categorization Framework for Plastic Debris. *Environmental Science & Technology* **2019**, *53*, 1039–1047.
5. Primpke, S.; Christiansen, S. H.; Cowger, W.; Frond, H. D.; Deshpande, A.; Fischer, M.; Holland, E. B.; Meyns, M.; O'Donnell, B. A.; Ossmann, B. E.; Pittroff, M.; Sarau, G.; Scholz-Böttcher, B. M.; Wiggin, K. J. Critical Assessment of Analytical Methods for the Harmonized and Cost-Efficient Analysis of Microplastics. *Applied Spectroscopy* **2020**, *74*, 1012–1047.
6. Schwaferts, C.; Niessner, R.; Elsner, M.; Ivleva, N. P. Methods for the analysis of submicrometer- and nanoplastic particles in the environment. *Trends in Analytical Chemistry* **2019**, 52–65.
7. Fischer, M.; Scholz-Böttcher, B. M. Microplastics analysis in environmental samples – recent pyrolysis-gas chromatography-mass spectrometry method improvements to increase the reliability of mass-related data. *Analytical Methods* **2019**, *11*, 2489–2497.
8. Hermabessiere, L.; Himber, C.; Boricaud, B.; Kazour, M.; Amara, R.; Cassone, A.-L.; Laurentie, M.; Paul-Pont, I.; Soudant, P.; Dehaut, A., et al. Optimization, performance, and application of a pyrolysis-GC/MS method for the identification of microplastics. *Analytical and Bioanalytical Chemistry* **2018**, *410*, 6663–6676.
9. Materić, D.; Kasper-Giebl, A.; Kau, D.; Anten, M.; Greilinger, M.; Ludewig, E.; van Sebille, E.; Röckmann, T.; Holzinger, R. Micro- and Nanoplastics in Alpine Snow: A New Method for Chemical Identification and (Semi)Quantification in the Nanogram Range. *Environmental Science & Technology* **2020**, *54*, 2353–2359.
10. Mintenig, S. M.; Bäuerlein, P. S.; Koelmans, A. A.; Dekker, S. C.; van Wezel, A. P. Closing the gap between small and smaller: Towards a framework to analyse nano- and microplastics in aqueous environmental samples. *Environmental Science: Nano* **2018**, *5*, 1640–1649.

11. Dümichen, E.; Eisentraut, P.; Bannick, C. G.; Barthel, A.-K.; Senz, R.; Braun, U. Fast identification of microplastics in complex environmental samples by a thermal degradation method. *Chemosphere* **2017**, *174*, 572–584.
12. Duemichen, E.; Eisentraut, P.; Celina, M.; Braun, U. Automated thermal extraction-desorption gas chromatography mass spectrometry: A multifunctional tool for comprehensive characterization of polymers and their degradation products. *Journal of Chromatography A* **2019**, *1592*, 133–142.
13. Löder, M. G. J.; Gerdts, G. In *Marine Anthropogenic Litter*, Bergmann, M., Gutow, L., Klages, M., Eds.; Springer International Publishing: Cham, 2015, pp 201–227.
14. Renner, G.; Sauerbier, P.; Schmidt, T. C.; Schram, J. Robust Automatic Identification of Microplastics in Environmental Samples Using FTIR Microscopy. *Analytical Chemistry* **2019**, *91*, 9656–9664.
15. Ivleva, N. P.; Wiesheu, A. C.; Niessner, R. Microplastic in Aquatic Ecosystems. *Angewandte Chemie, International Edition* **2017**, *56*, 1720–1739.
16. Anger, P. M.; von der Esch, E.; Baumann, T.; Elsner, M.; Niessner, R.; Ivleva, N. P. Raman microspectroscopy as a tool for microplastic particle analysis. *Trends in Analytical Chemistry* **2018**, *109*, 214–226.
17. Araujo, C. F.; Nolasco, M. M.; Ribeiro, A. M. P.; Ribeiro-Claro, P. J. A. Identification of microplastics using Raman spectroscopy: Latest developments and future prospects. *Water Research* **2018**, *142*, 426–440.
18. Imhof, H. K.; Ivleva, N. P.; Schmid, J.; Niessner, R.; Laforsch, C. Contamination of beach sediments of a subalpine lake with microplastic particles. *Current Biology* **2013**, *23*, R867–R868.
19. Von der Esch, E.; Kohles, A. J.; Anger, P. M.; Hoppe, R.; Niessner, R.; Elsner, M.; Ivleva, N. P. TUM-ParticleTyper: A detection and quantification tool for automated analysis of (Microplastic) particles and fibers. *PLOS ONE* **2020**, *15*, e0234766.
20. Anger, P. M.; Prechtl, L.; Elsner, M.; Niessner, R.; Ivleva, N. P. Implementation of an open source algorithm for particle recognition and morphological characterisation for microplastic analysis by means of Raman microspectroscopy. *Analytical Methods* **2019**, *11*, 3483–3489.
21. Brandt, J.; Bittrich, L.; Fischer, F.; Kanaki, E.; Tagg, A.; Lenz, R.; Labrenz, M.; Brandes, E.; Fischer, D.; Eichhorn, K.-J. High-Throughput Analyses of Microplastic Samples Using Fourier Transform Infrared and Raman Spectrometry. *Applied Spectroscopy* **2020**, *74*, 1185–1197.
22. Oßmann, B. E.; Sarau, G.; Holtmannspötter, H.; Pischetsrieder, M.; Christiansen, S. H.; Dicke, W. Small-sized microplastics and pigmented particles in bottled mineral water. *Water Research* **2018**, *141*, 307–316.
23. Schymanski, D.; Goldbeck, C.; Humpf, H.-U.; Fürst, P. Analysis of microplastics in water by micro-Raman spectroscopy: Release of plastic particles from different packaging into mineral water. *Water Research* **2018**, *129*, 154–162.

24. Xu, J.-L.; Thomas, K. V.; Luo, Z.; Gowen, A. A. FTIR and Raman imaging for microplastics analysis: State of the art, challenges and prospects. *Trends in Analytical Chemistry* **2019**, *119*, 115629.

25. Schymanski, D.; Oßmann, B. E.; Benismail, N.; Boukerma, K.; Dallmann, G.; von der Esch, E.; Fischer, D.; Fischer, F.; Gilliland, D.; Glas, K.; Hofmann, T.; Käppler, A.; Lacorte, S.; Marco, J.; Rakwe, M. E.; Weisser, J.; Witzig, C.; Zumbülte, N.; Ivleva, N. P. Analysis of microplastics in drinking water and other clean water samples: Minimum requirements and best practice guidelines. *Water Research* **2021**, *submitted*.

26. Kooi, M.; Koelmans, A. A. Simplifying Microplastic via Continuous Probability Distributions for Size, Shape, and Density. *Environmental Science & Technology Letters* **2019**, *6*, 551–557.

27. Gy, P. Sampling of discrete materials – a new introduction to the theory of sampling: I. Qualitative approach. *Chemometrics and Intelligent Laboratory Systems* **2004**, *74*, 7–24.

28. Gy, P. Sampling of discrete materials: II. Quantitative approach – sampling of zero-dimensional objects. *Chemometrics and Intelligent Laboratory Systems* **2004**, *74*, 25–38.

29. Pitard, F. F., *Theory of Sampling and Sampling Practice*; CRC Press: 2019.

30. Sobhani, Z.; Zhang, X.; Gibson, C.; Naidu, R.; Megharaj, M.; Fang, C. Identification and visualisation of microplastics/nanoplastics by Raman imaging (i): Down to 100 nm. *Water Research* **2020**, *174*, 115658.

31. Fang, C.; Sobhani, Z.; Zhang, X.; Gibson, C. T.; Tang, Y.; Naidu, R. Identification and visualisation of microplastics/ nanoplastics by Raman imaging (ii): Smaller than the diffraction limit of laser? *Water Research* **2020**, *183*, 116046.

32. Sarau, G.; Kling, L.; Oßmann, B. E.; Unger, A.-K.; Vogler, F.; Christiansen, S. H. Correlative Microscopy and Spectroscopy Workflow for Microplastics. *Applied Spectroscopy* **2020**, *74*, 1155–1160.

33. Zhang, W.; Dong, Z.; Zhu, L.; Hou, Y.; Qiu, Y. Direct Observation of the Release of Nanoplastics from Commercially Recycled Plastics with Correlative Raman Imaging and Scanning Electron Microscopy. *ACS Nano* **2020**, *14*, 7920–7926.

34. Chalfoun, J.; Majurski, M.; Blattner, T.; Bhadriraju, K.; Keyrouz, W.; Bajcsy, P.; Brady, M. Mist: accurate and scalable microscopy image stitching tool with stage modeling and error minimization. *Scientific Reports* **2017**, *7*, 1–10.

35. Lünsdorf, N. K.; Kalies, J.; Ahlers, P.; Dunkl, I.; von Eynatten, H. Semi-Automated Heavy-Mineral Analysis by Raman Spectroscopy. *Minerals* **2019**, *9*, 385.

36. ISO, *ISO 230-2; Test code for machine tools - Part 2: Determination of accuracy and repeatability of positioning of numerically controlled axes*; Beuth Verlag, Berlin: 2014.

37. Hng, K. I.; Dormann, D. ConfocalCheck - A Software Tool for the Automated Monitoring of Confocal Microscope Performance. *PLOS ONE* **2013**, *8*, e79879.

38. Imhof, H. K.; Laforsch, C.; Wiesheu, A. C.; Schmid, J.; Anger, P. M.; Niessner, R.; Ivleva, N. P. Pigments and plastic in limnetic ecosystems: A qualitative and quantitative study on microparticles of different size classes. *Water Research* **2016**, *98*, 64–74.

39. Fortin, S.; Song, B.; Burbage, C. Quantifying and identifying microplastics in the effluent of advanced wastewater treatment systems using Raman microspectroscopy. *Marine Pollution Bulletin* **2019**, *149*, 110579.

40. Cabernard, L.; Roscher, L.; Lorenz, C.; Gerdts, G.; Primpke, S. Comparison of Raman and Fourier Transform Infrared Spectroscopy for the Quantification of Microplastics in the Aquatic Environment. *Environmental Science & Technology* **2018**, *52*, 13279–13288.

41. Huppertsberg, S.; Knepper, T. Validation of an FT-IR microscopy method for the determination of microplastic particles in surface waters. *MethodsX* **2020**, *7*, 100874.

42. Tong, H.; Jiang, Q.; Hu, X.; Zhong, X. Occurrence and identification of microplastics in tap water from China. *Chemosphere* **2020**, *252*, 126493.

43. Thaysen, C.; Munno, K.; Hermabessiere, L.; Rochman, C. M. Towards Raman Automation for Microplastics: Developing Strategies for Particle Adhesion and Filter Subsampling. *Applied Spectroscopy* **2020**, *74*, 976–988.

44. Minkkinen, P. O.; Esbensen, K. H. Grab vs. composite sampling of particulate materials with significant spatial heterogeneity—A simulation study of “correct sampling errors”. *Analytica Chimica Acta* **2009**, *653*, 59–70.

45. Illian, J.; Penttinen, A.; Stoyan, H.; Stoyan, D., *Statistical analysis and modelling of spatial point patterns*; John Wiley & Sons: 2008; Vol. 70.

46. Tibshirani, R. J.; Efron, B. An introduction to the bootstrap. *Monographs on Statistics and Applied Probability* **1993**, *57*, 1–436.

Chapter 6

Nanoplastic Analysis by Online Coupling of Raman Microscopy and Field-Flow Fractionation Enabled by Optical Tweezers

Reprinted with permission from:
Christian Schwaferts, Vanessa Sogne, Roland Welz, Florian Meier, Thorsten Klein, Reinhard Niessner, Martin Elsner and Natalia P. Ivleva, *Analytical Chemisty* **2020**, 92, 5813–5820, https://doi.org/10.1021/acs.analchem.9b05336, https://pubs.acs.org/doi/10.1021/acs.analchem.9b05336.
Copyright 2020 American Chemical Society.

Permission statement

Authors may reuse all or part of the Submitted, Accepted or Published Work in a thesis or dissertation that the author writes and is required to submit to satisfy the criteria of degree-granting institutions. Such reuse is permitted subject to the ACS' „Ethical Guidelines to Publication of Chemical Research" (http://pubs.acs.org/page/policy/ethics/index.html).

Abstract

Nanoplastic pollution is of emerging environmental concern, but current analytical approaches are facing limitations in this size range. However, the coupling of nanoparticle separation with chemical characterization bears potential to close this gap. Here, we realize the hyphenation of particle separation / characterization (field-flow fractionation (FFF), UV and multi angle light scattering (MALS)) with subsequent chemical identification by online Raman microspectroscopy (RM). The problem of low Raman scattering was overcome by trapping particles with 2D optical tweezers. This setup enabled RM to identify particles of different materials (polymers and inorganic) in the size range from 200 nm to 5 µm, with concentrations in the order of 1 mg/L (10^9 particles L^{-1}). The hyphenation was realized for asymmetric flow FFF (AF4) and centrifugal FFF (CF3), which separate particles based on different properties. This technique shows potential for application in nanoplastic analysis, as well as many other fields of nanomaterials.

6.1 Introduction

Nanoplastic particles are formed by fragmentation of ubiquitous plastic waste contaminations (secondary nanoplastic) or are produced for specific applications (primary nanoplastic)[1,2]. It can, therefore, be expected in the aquatic[3,4] and terrestrial environment[5] and may have detrimental effects on biota[6,7]. Analytical data, however, are still very scarce[8], and approaches are challenged by various problems. Specifically, aquatic nanoplastic will occur very diluted[9] and, just as microplastic (MP)[10,11], it will have to be analyzed in highly differing matrices[12–14] and alongside with natural colloids. Especially the chemical identification of plastic is a challenge, since a mere elemental analysis cannot confirm the presence of carbon-based synthetic polymers in an organic matrix. To overcome this problem, MP identification relies on vibrational spectroscopy (IR spectroscopy and Raman microspectroscopy (RM)) or thermoanalytical methods coupled with mass spectrometry[10,15,16]. However, these methods are not easily adapted to nanoplastic, because particle sizes fall below optical resolution, and small mass-per-particle ratios make it difficult to gather sufficient sample for thermoanalytics / mass spectrometry[17].

Field-Flow Fractionation (FFF) belongs to the flow-based separation techniques, where separation takes place in a small, ribbon-like channel under laminar flow conditions in absence of a stationary phase[18]. In FFF, separation is generally induced by counteraction of dissolved or suspended sample constituents with an external force field that acts perpendicular to the laminar channel flow (Figure S.6.1). Based on the nature of the applied force field, FFF can be divided into different sub-techniques of which Asymmetrical Flow Field-Flow Fractionation (AF4) and Centrifugal Field-Flow Fractionation (CF3) are among the most prominent representatives[19]. In AF4, separation is induced by a second flow (cross-flow), which pushes the sample constituents towards the lower, semipermeable channel wall (accumulation wall) and forces them to align in different channel heights depending on their different diffusion coefficients and thus hydrodynamic sizes (Figure S.6.2). In CF3, rotating the channel creates a centrifugal field, which forces the sample constituents to align depending on their different buoyant masses and densities (Figure S.6.3). Since the laminar channel flow exhibits a parabolic flow profile with the highest flow velocities towards the center of the channel, this alignment leads to a common elution order from smaller to larger hydrodynamic size (AF4) or mass and density (CF3), respectively, with a typical application range from 1 nm – 10 µm (AF4) and 10 nm – 20 µm (CF3, density-dependent)[20].

FFF is a prime technique for nanoplastic because it is able to separate particles in the whole nm-range[9,17,21,22] and can deliver physical information, like particle sizes through routinely used detectors (UV, multi angle light scattering (MALS)) even without visual recognition. Chemical characterization may be conducted based on elemental analysis, e.g. by inductively coupled plasma-mass spectrometry (ICP-MS)[23,24]. However, this approach does not suffice if the chemical structure is of interest, such as in the case of polymer particles, metal oxides or other nanominerals. Specifically, while ICP-MS[25] as well as an organic carbon detector (OCD)[26] were used as elemental carbon detectors for particles, they could not provide information about the nature of the measured carbon. For nanoplastic, FFF has been demonstrated to be well-suited because it can be applied to polydisperse samples[21], separate nanoplastic from digested biota samples[13] and has been combined with pyrolysis-gas chromatography-

mass spectrometry (Py-GC-MS) for polymer identification and its quantification by mass[9]. The sensitivity of this approach, however, is dependent on the polymer type and limited to the materials that have been validated. Furthermore, until now, the coupling has only been realized offline, meaning that fractions from the FFF effluent were collected and processed by Py-GC-MS at a later stage. This approach disregards the great advantage of FFF-online coupling and the possibility for automation. Raman spectroscopy, on the other hand, is in principle well-suited for an online detection of nanoplastic in an aqueous flow due to its spectroscopic insensitivity to water (as opposed to IR spectroscopy). It is also able to unambiguously identify any plastic particles via characteristic fingerprint spectra, which makes Raman spectroscopy, in combination with optical microscopy (i.e. Raman microspectroscopy, RM) a commonly used technique for analysis of MP[10,27]. Since the particle sizes of nanoplastic fall below the optical resolution and due to their great numbers, the traditional single-particle approach of RM may not be feasible for nanoplastic particles[17]. Here, the hyphenation of RM to FFF could, therefore, close a blind spot – the size characterization would be performed by FFF-MALS, rather than the diffraction-limited optical microscope and chemical identification would subsequently be achieved by RM. This would offer a fast and automatable analysis for nanoplastic that delivers size information and chemical characterization at the same time.

Numerous designs exist for Raman flow-cells, which have been reviewed elsewhere[28,29]. All of them aim to overcome a main problem with Raman flow cells, viz. the low signal intensity due to low Raman scattering efficiencies. To solve this, enhancement effects like surface-enhanced Raman scattering[30–32] or resonance Raman scattering[33,34] have been exploited. On the other hand, instrumental approaches, like liquid wave cores to maximize the light-sample interaction[35–37] or high laser powers[38], have been tested. Those approaches, however, require more elaborate flow-cell setups and limit analysis to specific molecules for which the enhancement effects are viable. Raman-based flow-cells with no further enhancement are, thus, limited to more concentrated samples (> 0.25 g/L)[39–41]. This is also true for microfluidic lab-on-a-chip applications, which use RM for concentrated samples, e.g. in reaction monitoring[42–44], or have to, again, employ similar enhancement effects as the hyphenation interfaces, like SERS[29] or resonance Raman[45]. The abovementioned setups are, additionally, conceived for dissolved molecules. There is only one report of a Raman flow cell for MP particles for the on-line analysis of tap water, which is restricted to large MP (> 100 µm)[46] due to the low Raman efficiency. These limitations currently preclude the analysis of nanoplastic in the prospected low concentrations. Thus, viable approaches for the hyphenation of Raman spectroscopy to separation techniques for the online detection of nanoplastic particles are still lacking.

To overcome the sensitivity problem, which results from the very short interaction of the particle with the Raman light source, in this study we employ an optical trap to retain the particles for sufficient spectra collection. Different types of trapping are a common tool in microfluidics[47], where optical tweezers, are readily used for the manipulation of particles and microorganisms[48]. When a laser-based particle trapping is combined with Raman spectroscopy, it is called Raman Tweezers (RT). This technique has been used for the analysis of single cells, cell sorting as well as studies on nanoparticles (see[49] and references therein). Although the applicability of RT for micro- and nanoplastic has been demonstrated for individual particles in suspension[49], a hyphenation to flow techniques has not yet been demonstrated.

Here, we present a solution for the sensitivity problem of Raman flow-cells. This allows, for the first time, the online coupling of particle separation techniques, like field-flow fractionation (FFF), to RM with a 2D optical trapping-based particle retention. In addition, the separated particles can be subjected to online chemical and physical analysis as provided by the series of coupled detectors (FFF-UV-MALS-RM). This setup is shown to be suitable for the analysis of primary and secondary nanoplastic particles.

6.2 Experimental Section

6.2.1 Particles and Chemicals

Spherical PS particles with 100 nm, 2000 nm, 350 nm and, 600 nm for this study were obtained from Duke Standards, Thermo Fisher Scientific. PS 500 nm and 1.4 µm, suspended in ethanol, were provided by BS-Partikel GmbH, Germany, PS 5 µm was purchased from Interfacial Dynamics Corporation IDC (white surface latex), PMMA 500 nm was purchased from microParticles GmbH, Germany, and SiO_2 500 nm from NanoComposix, San Diego, CA, USA. As surfactant, Novachem (Postnova Analytics GmbH, Germany) and SDS (Carl Roth GmbH, Germany) was used. Eluents were prepared with ultrapure water (MilliQ Integral 5, Merck Millipore, Germany, resistance 18.2 MΩ). Particle number concentrations were calculated with the volume of spheres and densities of 1.05 g/mL, 1.18 g/mL and 2.65 g/mL for PS, PMMA and SiO_2, respectively.

6.2.2 Flow Cell Design

The RM flow cell was produced on a metal block with a gold-coated surface that would provide the area for the trapped particles. The flow channel with a length of 1.3 cm and a width of 1.5 mm was confined by a polymeric spacer with a height of 350 µm and topped with a glass cover slip. Flow in- and outlet was conducted through the bottom metal block (Figure 6.1). For this rectangular channel geometry, the Reynolds number was calculated using the hydraulic diameter, $d_h = \frac{4A}{U} = \frac{2ab}{(a+b)}$, with A, the channel cross-section's area and U, its circumference, to accommodate for the rectangular geometry of the flow channel. Thus, the Reynold's number, Re, was given by $Re = \frac{(v_m \cdot d_h)}{(\eta\rho^{-1})}$ with v_m, the flow rate averaged over the cross-section and $\eta\rho^{-1}$, the kinematic viscosity. In our setup, the parameters are a = 1.5 mm, b = 350 µm, d_h = 0.57 mm, η_w = 0.89 mPa · s, ρ_w = 997 kgm^{-3} (pure water) and v_m = 6.36 mms^{-1} derived from 0.2 mL/min. This calculates to Re = 4.1, indicating that the flow is laminar (turbulence would occur at $Re \geq 2300$, which corresponds to a flow velocity of v_m = 3602 mms^{-1} = 113.5 mL/min), which is needed to preserve the separation of the particles and to ensure lower flow velocities at the cell bottom. This value is in the expected range for microfluidic devices[50].

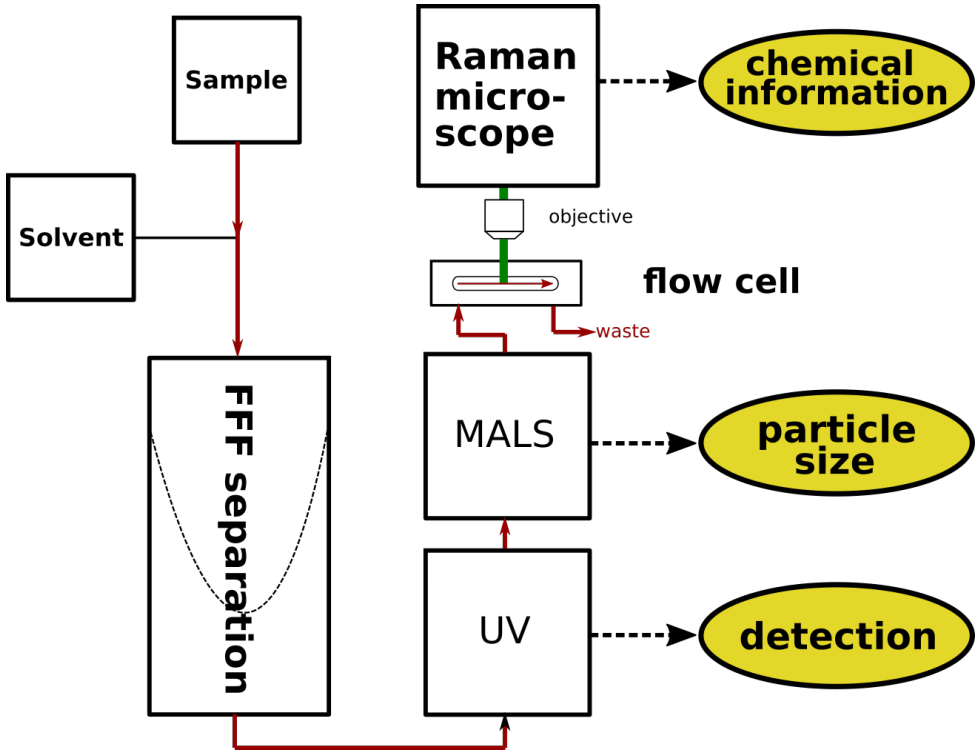

Fig. 6.1: Schematic of the hyphenated devices. The sample is injected into the solvent stream, which passes the FFF separation channel, where the particles are separated. Then the fractions pass a UV detector to indicate their presence in the stream, followed by the MALS detector, which gives the particle sizes. Finally, the particles pass the optical trapping-based flow cell, where a Raman spectrum is acquired. Particle flow is indicated by red arrows.

6.2.3 Instruments

Raman measurements were performed on an alpha300 access confocal Raman microscope (Witec GmbH, Germany), equipped with a 532 nm diode laser and water immersion objectives (20×, 40×, 60×, 100×; LumPlanFL series; Olympus, Japan). For all measurements a 600 lines/mm grating was used, the laser power was measured through an open microscope channel with a PM160T handheld power meter (ThorLabs Inc., USA). Data acquisition was done in time series of 10 s spectrum integration, each, at 20 mW (unless stated otherwise) over the whole time of particle injection and separation. Spectra were baseline-corrected with a rolling ball algorithm (150 pixel). The AF4 (AF2000 MT, Postnova Analytics GmbH, Germany), operated with a 350 µm spacer, a 10 kDa regenerated cellulose membrane, and the CF3, (CF2000, Postnova Analytics GmbH, Germany) were equipped with a UV (254 nm, Postnova PN3211 UV) and a MALS detector (Postnova PN3621 MALS). The AF4 flows were: injection with 0.2 mL/min at a cross-flow of 2 mL/min for 7 min and the cross-flow profile for the elution was (i) exponential decay from 2 mL/min to 0.01 mL/min with an exponent of 0.1 for 30 min, (ii) linear decrease from 0.01 mL/min to 0 mL/min for 20 min and (iii) constant flow with 0 mL/min cross-flow for 5 min. The channel outlet flow was set to 0.2 mL/min and the slot-outlet was 0.3 mL/min. The eluent was ultrapure water containing 0.0125 % of the surfactant NovaChem. Samples were injected with a 100 µL injection loop and measurements were performed in triplicate. For the validation of the RM flow cell, the suspensions were injected using the same instrument, however, the separation channel was omitted;

hence, the suspension only passed the detectors.

6.3 Results and Discussion

6.3.1 Design of the Optical Trapping Raman Flow Cell

Optical forces result from the interaction of light with particles, wherein the electrical field gradient of a highly focused light source induces a dipole in the particle, which causes a force directing it to the center of the beam (depending on the refractive index). There are several models for the calculation of the optical forces. Those that provide simple correlations are either based on approximating Rayleigh scattering for particles with $d \ll \lambda$ or ray optics for $d \gg \lambda$. In the intermediate range with $d \cong \lambda$ the model requires a more detailed description of the electrical field of the laser beam to calculate the scattering interactions sufficiently well[49].

Optical trapping[51] requires a microscope objective of high numerical aperture (N.A.), which, for RT, is already provided by the Raman microscope. Therefore, in order to enable access for the RM, the flow cell comprises an optically transparent top, as well as a rectangular cross section and a gold-coated cell bottom to reduce heating (through enhanced reflection and thermal dissipation) and to improve the visualization of the particles (see Materials and Methods). In this setup the microscope optics of the RM accomplishes both: (1) focusing the laser for particle trapping and (2) collecting Raman-scattered photons that provide the characteristic vibrational spectra to inform about particle identity. It was observed that the 20× and 100× magnification objective produces less Raman signal than the 40× and 60× (Figure S.6.4). This is due to the weaker trapping efficiency of lower magnifications and the smaller focal volume of high magnification objectives, which retain less particles that consequently produce less Raman signal. Therefore, the 40× water immersion objective with a N.A. = 0.6 was chosen due to reduced signal loss by refraction on the air-glass surface, representing a compromise between trapping (only 2D trapping will occur) and Raman signal intensity.

In this flow cell, a cluster of particles will be retained in the focal point due to an equilibrium of various forces (Figure 6.2). Microscopic investigation shows that for 1.4 µm and 5 µm particles, there are 5 and 1 particles in the focal volume, respectively. Thus the focal volume sphere/ellipsoid can be derived geometrically to be roughly 3-4 µm in diameter. The optical scattering force ($F_{scatter}$) in the direction of light transition pushes the particles towards the cell bottom, creating the 2D trap. This restriction to the cell bottom has been confirmed by varying the z-axis position of the focal point, which stopped the ability to acquire a Raman signal when diverging the focus by more than $\sim$ 3 µm from the surface (Figure S.6.5). The second force that is generated by the focused laser is the optical gradient force (F_{grad}) that is directed towards the point of highest light intensity, i.e. the center of the focal point. This force is opposed by the shear force (F_{flow}) due to the laminar flow, which pulls the particles out of the laser focus. The laminar flow produces a parabolic flow profile, which has smallest forces at the cell bottom, thus, facilitating particle retention at the surface. The impact of the shear force was observed when varying the flow rates, where higher flow rates reduced the Raman signal (Figure S.6.6). This

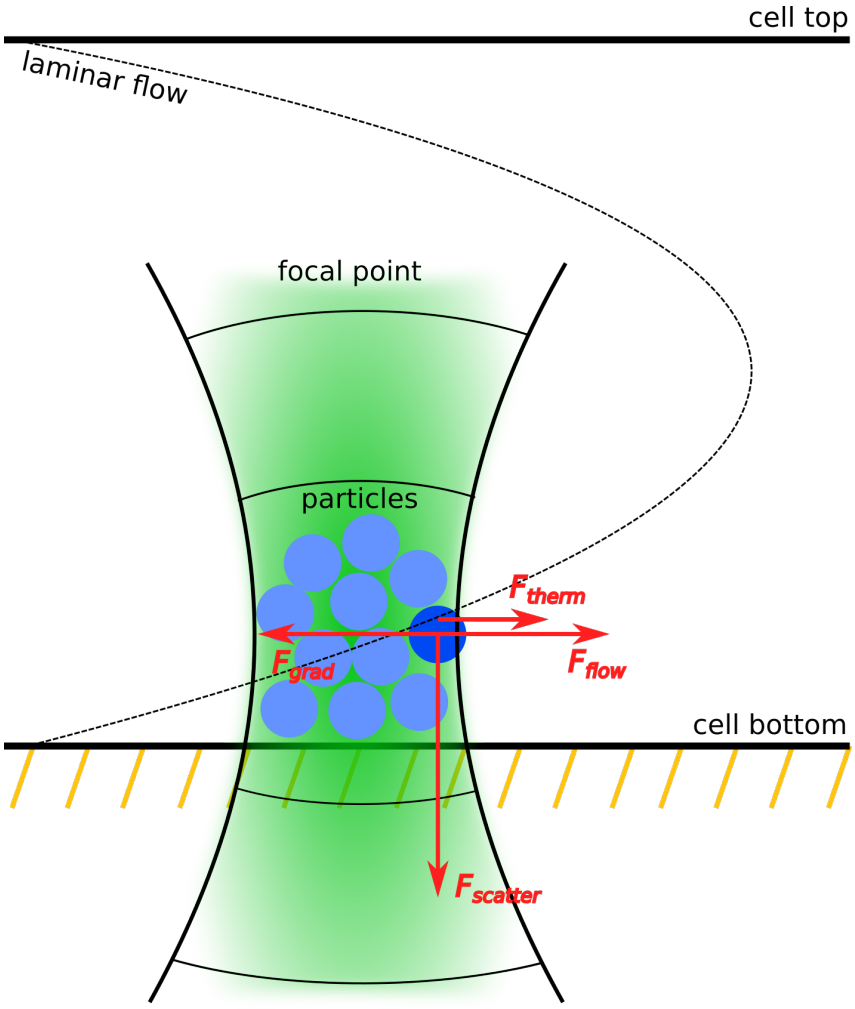

Fig. 6.2: Model of the optical trap in the subsequent flow cell. The focal point at the cell bottom generates a 2D trap that accumulates particles (the representation of the focal volume is enlarged). The forces are (i) optical scattering ($F_{scatter}$), that pushes the particles to the cell bottom, (ii) optical gradient force (F_{grad}) that is directed towards the maximum intensity of the laser, i.e. the center, (iii) shear forces (F_{flow}) that drag the particles away from the laser, (iv) thermal effects (F_{therm}) that add additional destabilization, i.e. outward of the 2D trap. To illustrate, the forces are centered on a particle (dark blue) on the outer part of the focal point. The sum of all forces directs the particle back to the center of the focal point.

correlation is in agreement with the model, according to which higher shear forces have to be met with higher optical gradient forces to stabilize the trap. Those are, however, limited to the very center of the trap thereby reducing the available particles for Raman analysis and, consequently, the signal.

Another destabilizing effect can be observed at higher laser powers, which causes a local heating due to remaining absorption and heating of the solvent in close proximity, and, consequently, a thermophoretic force (F_{therm}) out of the heated spot[52,53]. This is evident when observing the critical flow velocities, i.e. the flow rates for which no Raman signal could be observed anymore because the particles were all pulled out of the focus (Figure 6.3). This experiment shows that greater flow velocities could be realized when the laser power was increased (up to 10 mW), reflecting the effect of the increased trapping force. For higher laser powers, however, a decrease was observed, which was attributed to a thermophoretic effect that moved the particles out of the focal volume. If the optical gradient force is strong enough, the

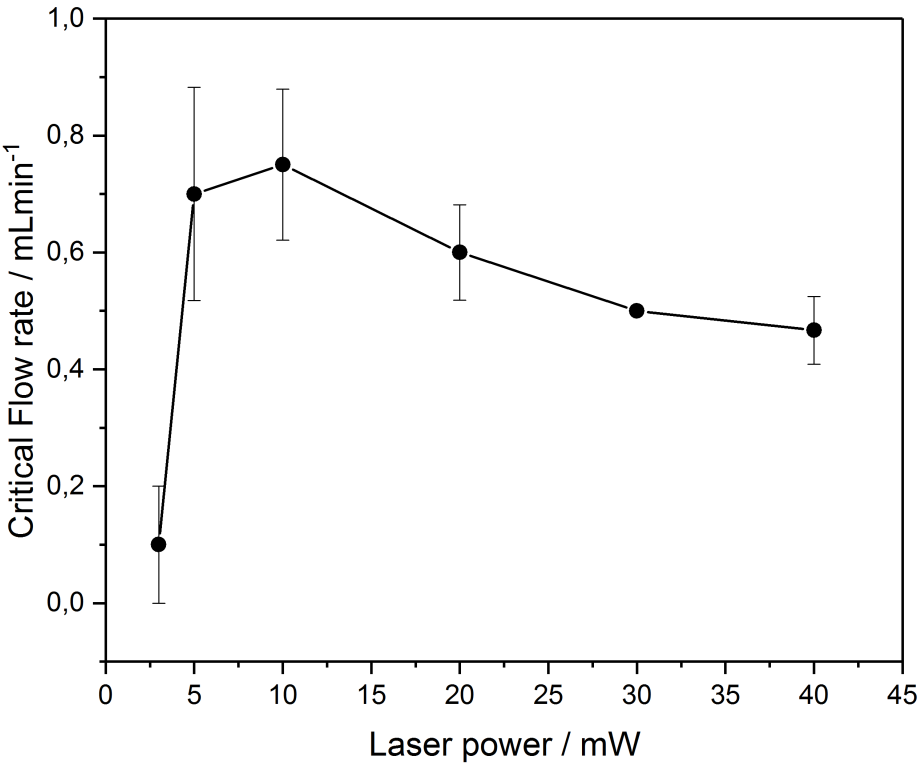

Fig. 6.3: Dependency of critical velocity of polystyrene 600 nm particles (10 mg/L) on the laser power. Increased laser power, i.e. trapping force, enabled higher flow rates before all particles were eliminated by shear forces from the trap. On the other hand, for even higher laser power an increasing thermal effect drove the particles out of the trap.

sum of all forces directs the particles to the center of the focal point, which creates a stable optical trap (Figure 6.2).

6.3.2 Validation of the Flow Cell

Before using the flow cell to couple RM to FFF, the cell was validated with direct injections using spherical particles. A laser power of 20 mW was found to be optimal for Raman spectra acquisition and, hence, was chosen for the experiments. Raman data were acquired continuously over the whole injection time. A series of vibrational spectra with 10 s integration time, each, was stored to give a time profile (as can be seen in Figure 6.4 where a time series of spectra is plotted).

First, the working range with respect to the particle size was investigated for polystyrene (PS) particles with diameters of 200 nm, 350 nm, 500 nm, 600 nm, 1.4 µm and 5 µm. The 5 µm particles experienced greatest shear forces due to their size and higher mass, so that an increased trapping power (30 mW) was needed. The 100 nm particles, on the other hand, did not produce a Raman signal, most likely due to the more pronounced particle mobility, which makes trapping very challenging[49]. This was also shown in an experiment, where a mixture of PS 100 nm and poly(methyl methacrylate) (PMMA) 500 nm was injected in the flow cell and the spectra only indicated PMMA (Figure S.6.7). Ergo, good applicability was obtained for particles between 200 nm – 5 µm, which lies in the upper working range of FFF. And

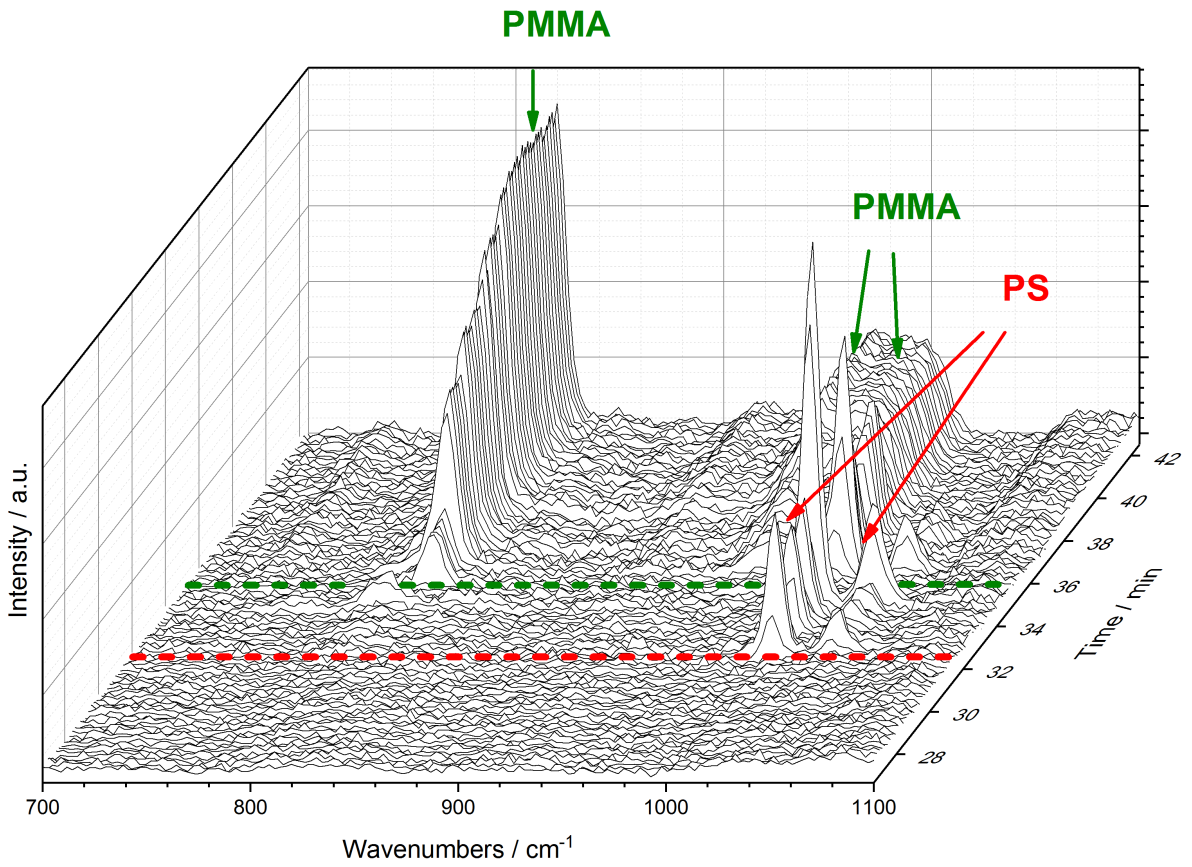

Fig. 6.4: 3D plot of an AF4 separation of PS 350 nm (red) and PMMA 500 nm (green) particles. It shows a section that illustrates the different Raman bands for each polymer. The particles that have been separated by AF4 elute after each other (t = 32 min & t = 36 min) as seen here by the Raman signals.

further, three 500 nm particle systems of different materials, i.e. PS, PMMA, SiO_2 (Table 6.1) were tested, thus, enabling the analysis of organic and inorganic particles. Each particle type was identified by its characteristic spectrum and a prominent band was chosen for the temporal plots (1000 cm^{-1}, 812 cm^{-1} and 488 cm^{-1} for PS, PMMA and SiO_2 (Figure S.6.16), respectively).

Subsequently, the sensitivity of the setup was investigated. It has to be noted, however, that the Raman intensity mainly depends on the focal volume and is subject to fluctuations, which is caused by particle material properties (refractive index, crystallinity), ageing or coating that can affect the trapping and will be difficult to control in environmental samples. Hence, no linear correlation of signal intensity and particle concentration can be assumed. Quantification solely via the Raman flow cell will be challenging, thus, the quantification will have to be performed by the other detectors, such as e.g. UV or MALS. Therefore, the sensitivity is given in terms of the minimal particle concentration of suspensions that can be injected in the flow cell and will give a detectable Raman signal. This means that at lower concentrations, particles can no longer be efficiently accumulated in the laser for sufficient signal acquisition. Here, a better particle collection would further improve sensitivity.

These minimal particle concentrations are listed in Table 6.1. It is apparent that, for most particles, the

Particle	Minimal concentration	Particle number
PS 200 nm	200 mg/L	$4.5 \cdot 10^{13}$ L^{-1}
PS 350 nm	100 µg/L	$4.2 \cdot 10^{9}$ L^{-1}
PS 500 nm	1 mg/L	$1.5 \cdot 10^{10}$ L^{-1}
PS 600 nm	10 µg/L	$8.4 \cdot 10^{7}$ L^{-1}
PMMA 500 nm	500 µg/L	$6.5 \cdot 10^{9}$ L^{-1}
SiO_2 500 nm	1 mg/L	$5.8 \cdot 10^{9}$ L^{-1}

Tab. 6.1: Minimal particle concentration for the evaluated particle systems.

suspension mass contents are below 1 mg/L (10^9 L^{-1}) with the lowest value being 10 µg/L for PS 600 nm ($8.4 \cdot 10^7$ L^{-1}). When approaching the size limit of 200 nm particles, the required particle concentration drastically increases. Similar to the Raman intensities, these limits show a fluctuation that is likely connected to the slight changes in surface properties due to different surfactants in the commercial particles from different suppliers.

The observed sensitivity lies around 1 mg/L, which is comparable with other techniques for nanoplastic analysis. Mintenig et al. report a LOD of 4 mg/L for their offline coupling of AF4 and Py-GC-MS[9]. Gagné et al. employed the hypsochromic shift of Nile red fluorescence to detect nanoplastic with a LOD of 0.1 mg/L and 0.3 mg/L[54], and Lin et al. demonstrated the applicability of MALDI-TOF-MS for nanoplastic with a sensitivity of 25 mg/L[55]. Real samples will, however, be more diluted, as observed by TerHalle et al. who found the marine colloidal fraction to be below the detection limit of their DLS instrument of 20 µg/L, which necessitated a preconcentration[8]. Thus, most current techniques will require a preconcentration such as cross-flow ultrafiltration, as described by Mintenig et al.[9].

6.3.3 Periodic Controlled Release of Trapped Particles

In the next step, i.e. the online coupling of the RM flow cell to FFF, initial experiments showed that the effectivity of trapping varied strongly with different particle systems, i.e. PS particles were only shortly retained, whereas PMMA and SiO_2 particles could be trapped for at least 20 minutes. (Figure 6.5 and Figures S.6.8 – S.6.12). However, a situation in which particles were trapped for a very long time would compromise the separation of the FFF. Therefore, we implemented a periodic interruption of the laser beam at regular intervals (30 s) so that the particles were released in a controlled manner and new particles could accumulate in the next time window. This approach allowed us to collect particles for detection while maintaining the required temporal resolution. Figure 6.5 shows the effect of laser interruption for PMMA 500 nm particles that passed the AF4. Instead of being trapped for more than 20 minutes, the particles were detected by a Raman signal that followed the actual elution peak profile. This resulted in a „comb-like“ time profile (Figure 6.5, bottom) because after each interruption it took several seconds to fill the focal volume again.

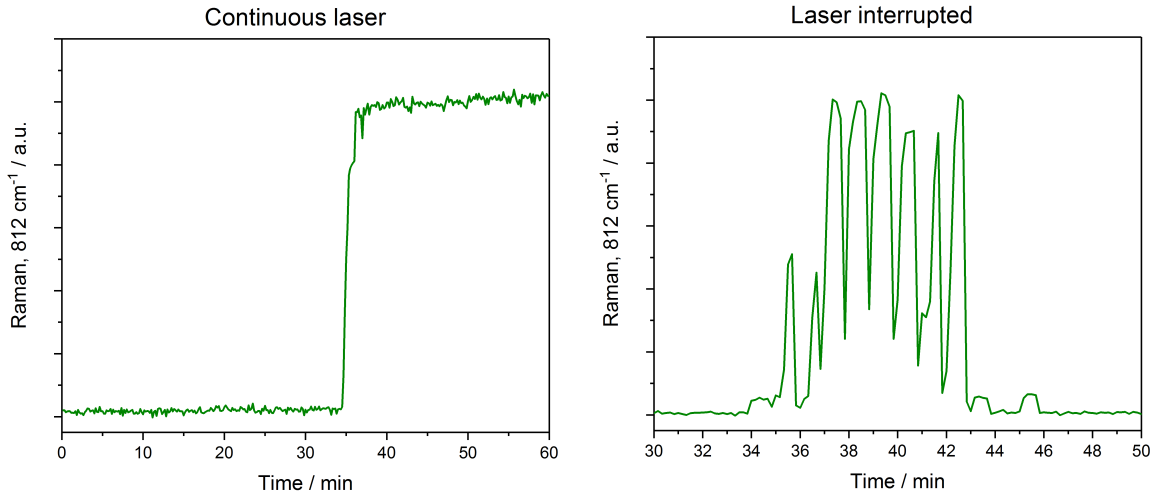

Fig. 6.5: AF4-Raman data of PMMA 500 nm particles. The lower panel has been zoomed to 30 min – 50 min. The upper panel shows the outcome of a constant laser irradiation that causes the particles to reside indefinitely in the focal volume and to produce constant signal. The lower panel shows the signal when the laser was interrupted at regular intervals (30 s), thereby preserving the temporal elution profile.

6.3.4 Hyphenation of RM and AF4

When proceeding with the online coupling of the RM flow cell as a „chemical“ detector to an FFF-UV-MALS system, two variants of FFF (AF4 and CF3) were chosen. In a first step, the hyphenation was realized with AF4. After tests with monodisperse particles (Figures S.6.13 – S.6.16), a separation of a mixture of PS 350 nm and PMMA 500 nm (25 mg/L and 100 mg/L, respectively, to account for the different Raman cross-sections) was performed to demonstrate the identification capabilities of the RM flow cell for the AF4 fractions. The three detectors of AF4-UV-MALS-RM produce complementary information that is plotted in one graph, as represented in Figure 6.6. In this plot, the separation of PS 350 nm and PMMA 500 nm particles is displayed by the UV signal that indicates the particle separation as a main peak, representing PS 350 nm with a shoulder of the PMMA 500 nm particles. But the MALS signal, which is converted into the geometric diameter (see supporting information) shows the two distinct fractions by their different sizes. Additionally, the Raman signal that identifies the two polymers by characteristic wavenumbers (PS: 1000 cm^{-1}, PMMA: 812 cm^{-1}) matches the elution of first PS followed by PMMA (Figure 6.6).

For another mixture of PS 500 nm and PMMA 500 nm, it was shown that even with particles of almost equal size, it is possible to provide an identification of the components with the Raman spectrum of the combined particle systems, even when the other detectors cannot distinguish between the two (Figure S.6.17). In the experiments with this mixture, a competition of the particles for the limited space in the trapping volume can be seen in the Raman intensities, when either the PS band or the PMMA bands were of high intensity and caused a decrease of the other (Figure S.6.18).

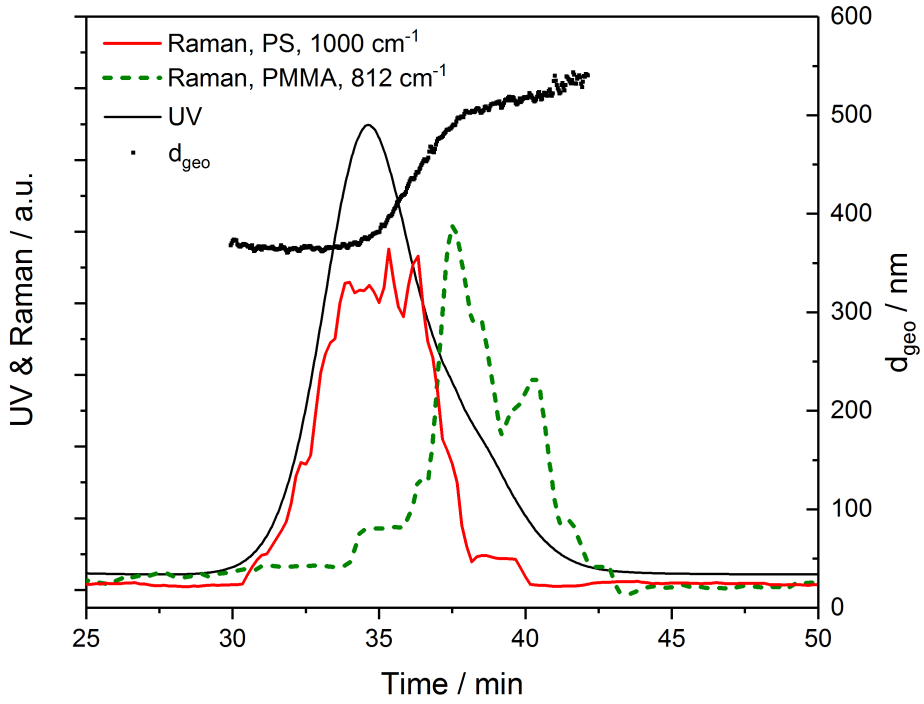

Fig. 6.6: AF4-UV-MALS-RM data. The mix of PS 350 nm and PMMA 500 nm particles is separated by AF4. The two fractions appear as a peak with a shoulder in the UV signal (black line, left axis). The geometric diameter (black dots, right axis) gives size information and shows the successful separation. The Raman intensity of the 812 cm^{-1} band for PMMA (dotted green line, left axis) and the 1000 cm^{-1} band for PS (red line, left axis) identify the polymer for each fraction. The laser was interrupted at 30 s intervals, UV and Raman intensities were normalized, the Raman plot was adjusted for time shift and smoothed (10 point average) for visibility, for original data see Figure S.6.11.

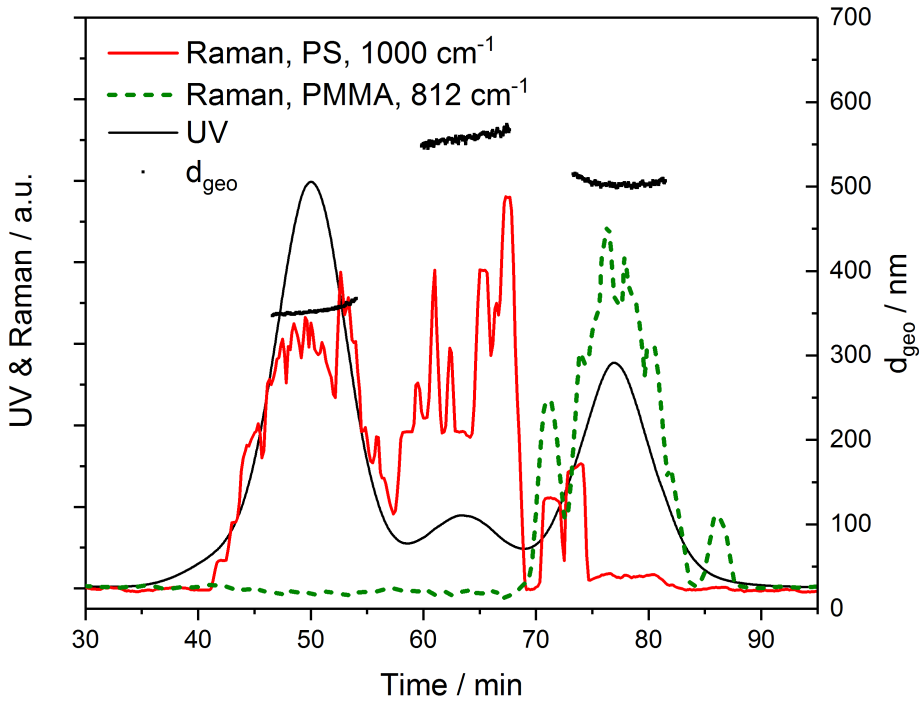

Fig. 6.7: CF3-UV-MALS-RM data. The mix of PS 350 nm, PS 500 nm and PMMA 500 nm particles is separated by CF3. The three separated fractions are illustrated by UV signal (black line, left axis). The geometric diameter (black dots, right axis) gives size information of the individual particles. The Raman intensity of the 812 cm^{-1} band for PMMA (dotted green line, left axis) and the 1000 cm^{-1} band for PS (red line, left axis) identify the polymer for each fraction. The laser was interrupted at 30 s intervals, UV intensities were normalized, for Raman, peak areas were plotted, normalized, adjusted for time shift and smoothed (10 point average) for visibility (for original data see Figure S.6.19).

6.3.5 Centrifugal Field-Flow Fractionation

The close proximity of the two fractions of the mix PS 350 nm and PMMA 500 nm is in accordance with literature, which states a decreased resolution for particles larger than 200 nm in AF4[21]. Even though our results show that co-eluting fractions can still be identified by the hyphenation to RM, a FFF variant that has a better resolution in the validated size range of the flow cell could be preferable. In a next step, we therefore tested coupling of CF3 instead of AF4 (for a more detailed comparison of the two techniques for particle analysis see Ref.[56]) to RM. The resulting separation and characterization of a mixture of PS 350 nm, PS 500 nm and PMMA 500 nm (25 mg/L, 25 mg/L and 100 mg/L, respectively) with CF3-UV-MALS-RM is plotted in Figure 6.7. Here, the UV signal shows three clearly separated fractions to which the MALS detector provides size information. These are, in order of elution: PS 350 nm, PS 500 nm (which are slightly larger than labelled) and finally PMMA 500 nm. The latter two are separated due to their different densities (PS: 1.05 g/mL, PMMA: 1.18 g/mL) that have a stronger effect in the gravity-based separation field of the CF3[20], even though the PS particles are slightly larger. Furthermore, in conjunction with the UV and MALS data, the RM detector provides spectra that can identify the fractions. The time profile of two characteristic bands is also plotted in Figure 6.7.

This impact of density makes CF3-UV-MALS-RM especially suited for nanoplastic analysis because it does not only facilitate the separation of polymers from sediments, but may also serve to fractionate

different polymer types. Furthermore, the CF3 has a larger size range (10 nm – 20 µm)[20] than the AF4 and may, thus, better serve to cover the gap of established techniques for MP analysis (i.e. FT-IR or Raman microspectroscopy), viz. very small MP and nanoplastic analysis[9,17].

6.4 Conclusion

To satisfy the emerging demand for nanoplastic analysis, we developed an optical trap-based flow cell for the hyphenation of FFF with RM, wherein the particles were focused and retained sufficiently long to enable spectrum acquisition. With this setup, we are able to analyze particles of different material (polymer and inorganic) in the size range of 200 nm and 5 µm and a minimal concentration around 1 mg/L (10^9 L^{-1}). For the coupling to FFF we implemented a periodic particle release, to conserve the separation information. The hyphenation has been realized, first, with AF4 for single, monodisperse particles and for mixtures to demonstrate the advantages of the Raman detector. The approach was able to provide spectral information on each fraction even when it was not possible to achieve a full separation of the particles. Subsequently, CF3 was hyphenated to RM to illustrate the applicability of the RM flow cell to multiple variants of particle separation techniques. As CF3 allows for the separation of particles not only by size but also by densities, fractionation of polymers with higher resolution could be achieved and combined with chemical RM analysis.

To proceed with the presented online coupling, for environmental or food samples, however, it has to be regarded that nanoplastic particles can be expected to be polydisperse and irregularly shaped and to occur most likely in aggregates[12,57]. This is reflected by the various methods brought forward to produce such environmentally relevant particles[23,24,58,59]. The capability of RT to optically trap micro and nanoplastic particles of different shapes has recently been demonstrated[49], indicating that the RM flow cell can also be applied to irregularly shaped particles that represent real samples, like PET fragments from drinking water bottles, as our preliminary results, indeed, suggest. Thus, FFF UV MALS RM offers a great potential to cover a methodological gap and enables online particle identification and, more specifically, in the environmental field of plastic particle contamination that ranges from very small MP to nanoplastic. With the goal to enable a systematic contamination assessment, it will be necessary to validate the application range of the technique to preprocessed samples and demonstrate its applicability for real-world samples. This will include a – in many cases vital – preconcentration step to provide a sufficiently high particle number. Also, improvements in terms of analyzable particles (opaque, metallic), the size range, the dependence of the optical trapping of the particle, and automation should enable a broad application in a wide variety of scientific fields that transcend environmental plastic analysis. This new hyphenation can be of interest for nanomaterial characterization in general because it can provide the structural insight that Raman (i.e. vibrational) spectroscopy supports.

6.5 Supporting Information

6.5.1 Working Principles of FFF, AF4 and CF3

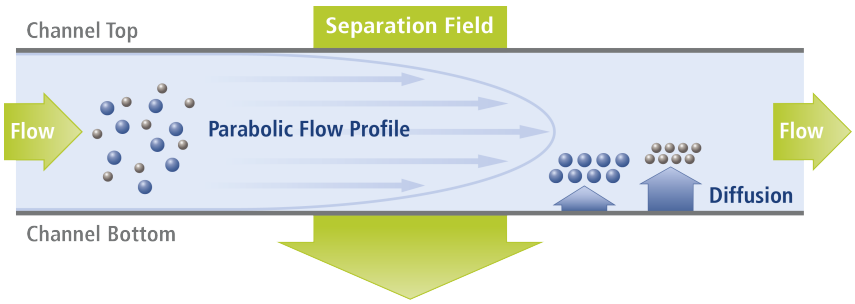

Fig. S.6.1: Working principle of FFF. Particle suspension passes a ribbon-like channel in laminar flow. Simultaneously, a perpendicular separation field (e.g. cross-flow or centrifugal force) is applied that causes the particles to be retained at the channel bottom, where they experience less flow velocity. According to their properties they are more or less well retained at the bottom and, thus, elute faster or slower.

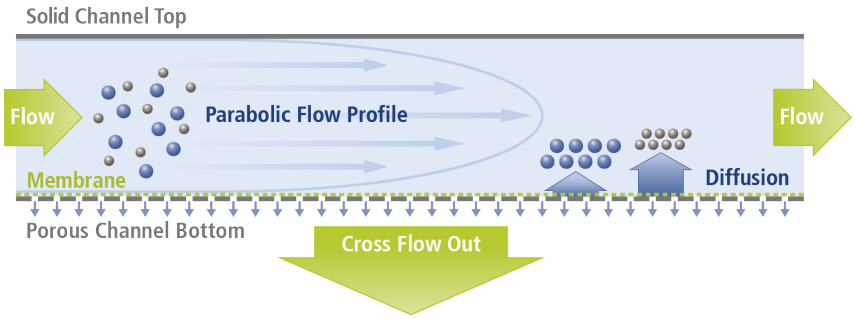

Fig. S.6.2: Working principle of Asymmetrical Flow Field-Flow Fractionation. The perpendicular force is generated via a cross-flow that is generated by a second pump below a porous membrane on the channel bottom. Thus, the separation is determined by hydrodynamic diffusivity.

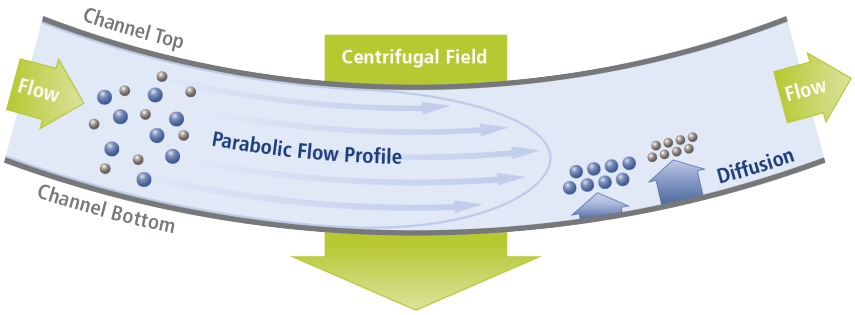

Fig. S.6.3: Working principle of Centrifugal Field-Flow Fractionation: The perpendicular force is generated by a centrifuge, in which the flow channel is placed. The separation depends on mass and particle density.

6.5.2 Comparison of Objectives

A light source with a Gaussian intensity profile (TEM_{00}) and water immersion objectives were aimed to be used as readily available equipment. However, they turned out to have numerical apertures that do not suffice for stable 3D trapping and can only provide a 2D trap at the bottom of the flow cell. A comparison of 20×, 40×, 60× and 100× magnification water immersion objectives was performed to find an optimal setup for Raman signal acquisition and particle trapping.

This was done by investigating the intensity of the PS band at 1000 cm^{-1} for 1.4 µm and 350 nm PS particles. Where a maximal Raman signal yield was obtained for the 40× objective. This is reasoned to result from the fact that higher magnification objectives have higher N.A. and, therefore, provide stronger trapping. For even higher magnification, however, the focal volume decreases, hence, reducing the number of particles to produce Raman signal.

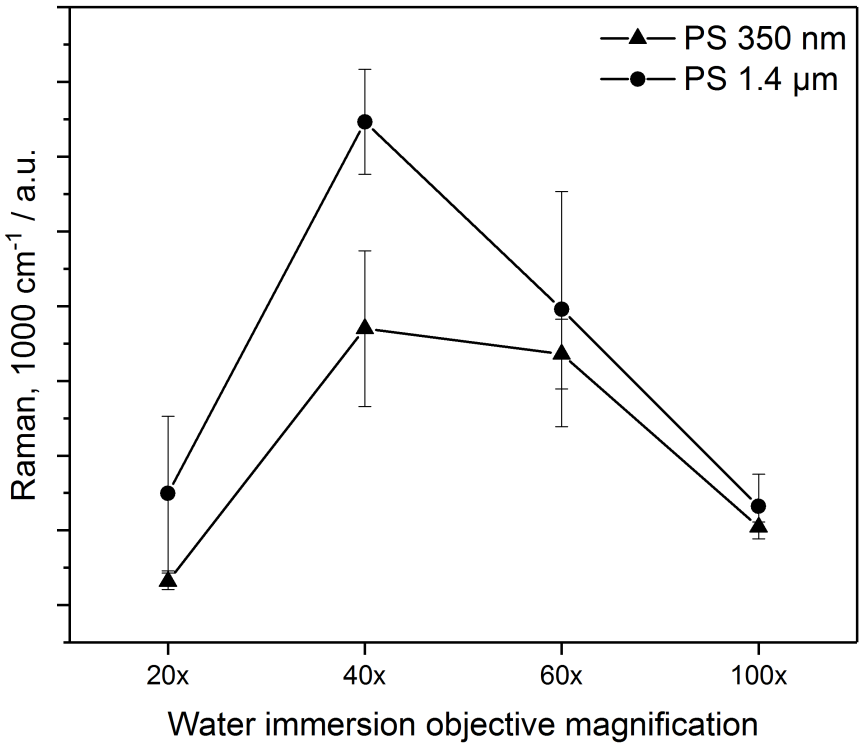

Fig. S.6.4: Relative intensities of the 1000 cm^{-1} band of polystyrene for two particle systems: 350 nm (1000 mg/L) and 1.4 µm (100 mg/L), showing the 40× water immersion objective to yield the highest Raman intensities.

6.5.3 Distance to Surface

The particles are trapped 2 dimensionally, strictly bound to the surface. This was observed, when varying the height position of the focal point, wherein for distances larger than ca. 3 µm, the Raman signal drops to 0.

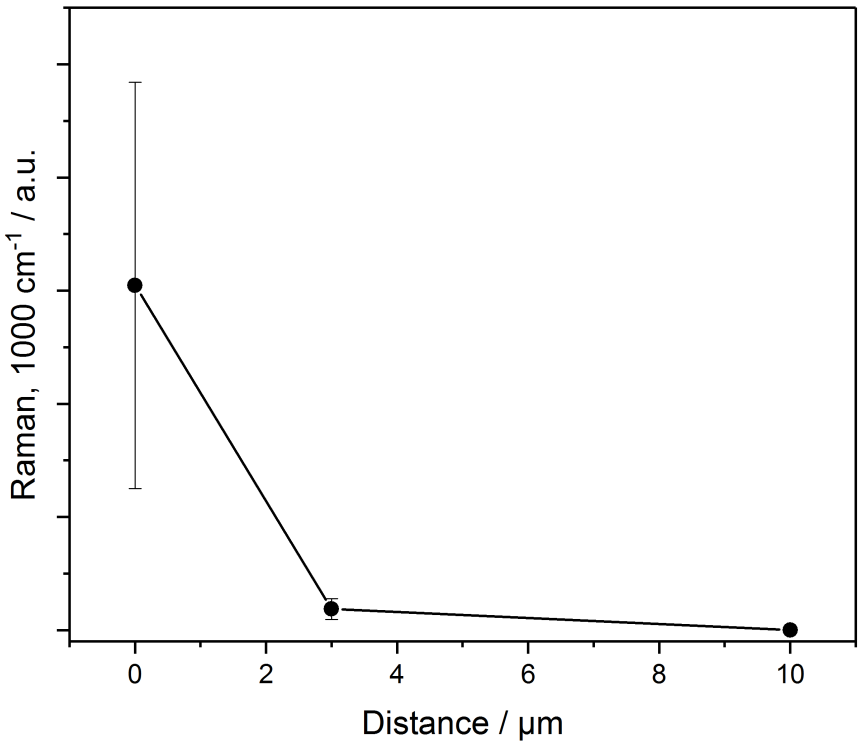

Fig. S.6.5: Measurements of PS 1.4 µm, 100 mg/L, 20x WI objective in different distances to the surface of the cell bottom show that the signal quickly drops to 0.

6.5.4 Dependency on Flow Rate

The optical trapping force is in an equilibrium with the shear forces of the flow that pull the particles out of the confocal volume. Ergo, higher flow rates mean less particles which generate less Raman signal. This can be seen in an experiment where particles (PS 600 nm, 10 mg/L) are injected with different flow rates.

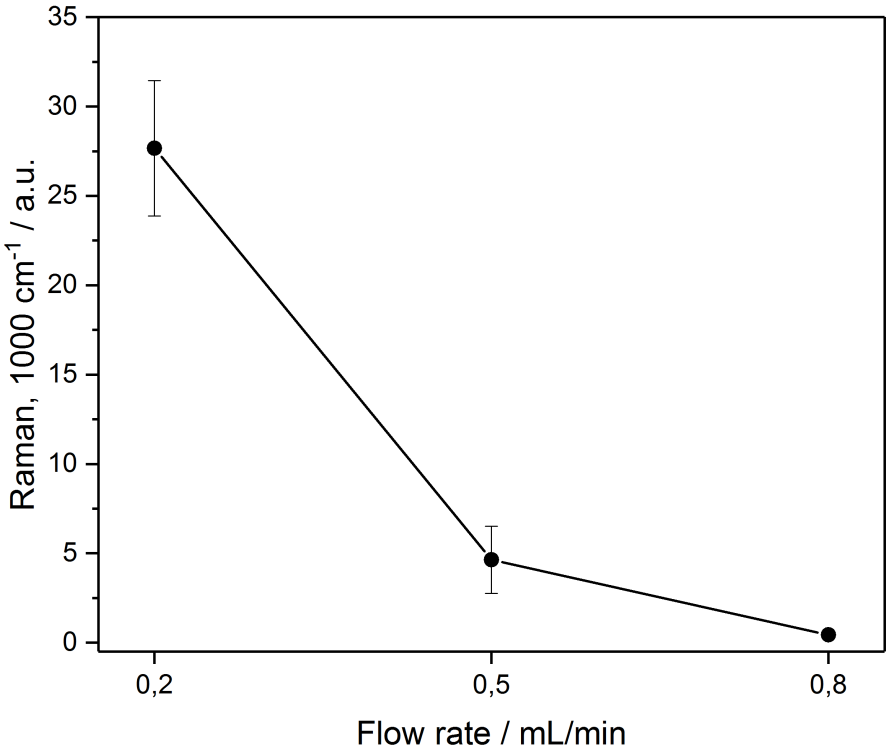

Fig. S.6.6: Variation of flow rates for the particle system PS 600 nm, 10 mg/L, 20 mW shows a decrease in intensity for the 1000 cm^{-1} band.

6.5.5 Particle Size Limit

We performed the experiment with the mix PS100/PMMA500 to show that no PS signal appears, indicating that 100 nm particles can, in principle, not be measured.

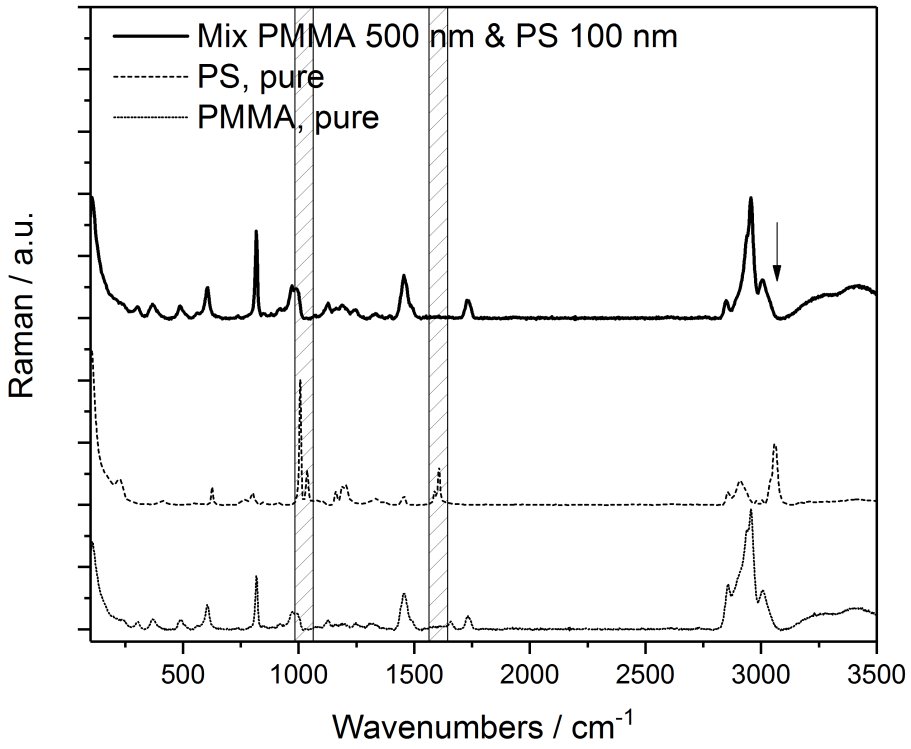

Fig. S.6.7: Spectra of a mix of PS 100 nm and PMMA 500 nm (50 mg/L each) illustrate that only PMMA can be measured.

6.5.6 Periodic Controlled Particle Release

To retain the particle separation, a periodic interruption of the laser has been implemented

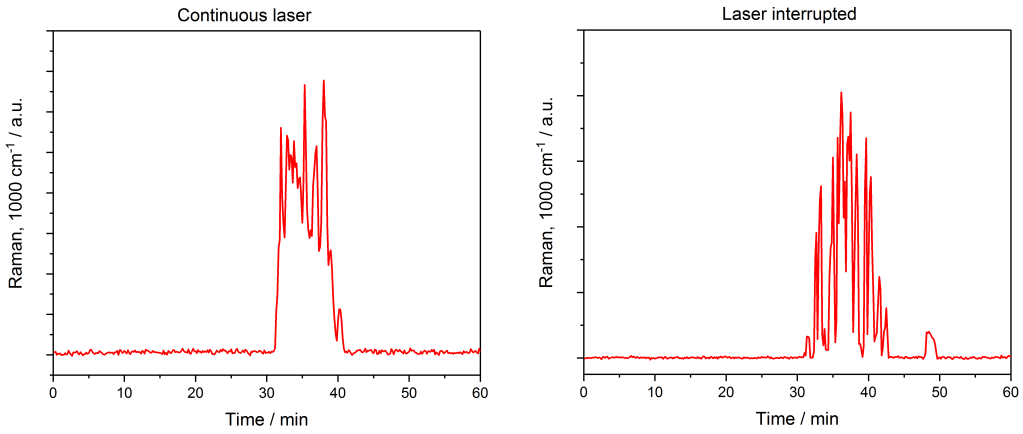

Fig. S.6.8: AF4-Raman data of PS 350 nm without (left) and with (right) interruption of the laser.

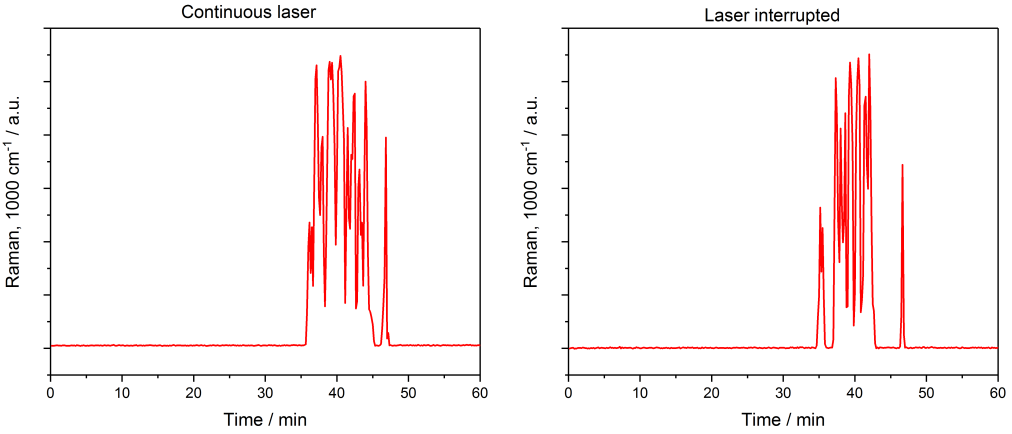

Fig. S.6.9: AF4-Raman data of PS 500 nm without (left) and with (right) interruption of the laser.

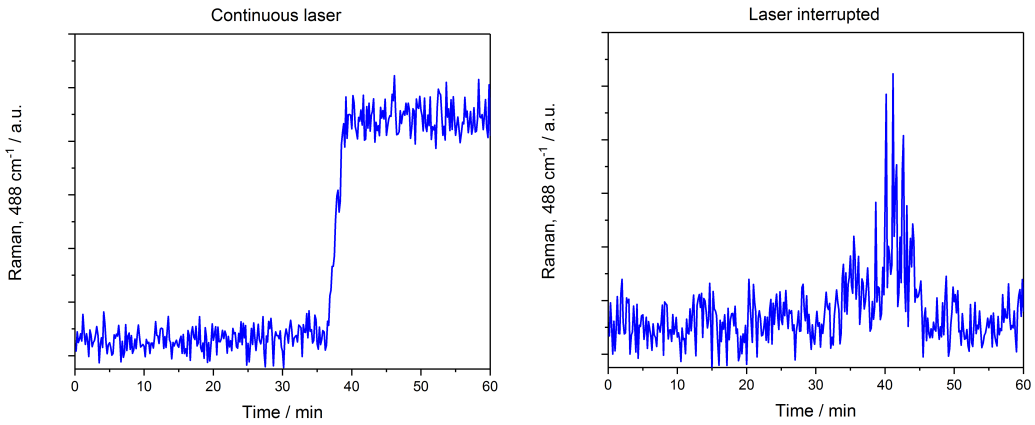

Fig. S.6.10: AF4-Raman data of SiO_2 500 nm without (left) and with (right) interruption of the laser.

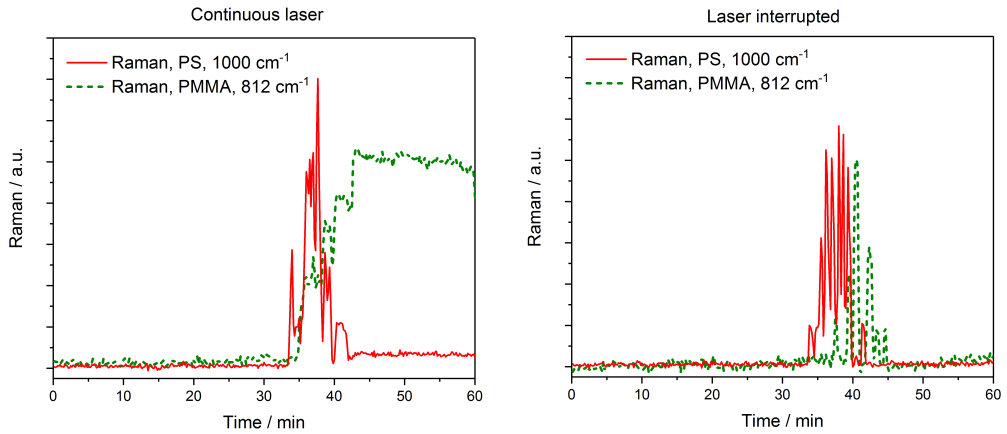

Fig. S.6.11: AF4-Raman data of the mix of PS 350 nm and PMMA 500 nm without (left) and with (right) interruption of the laser.

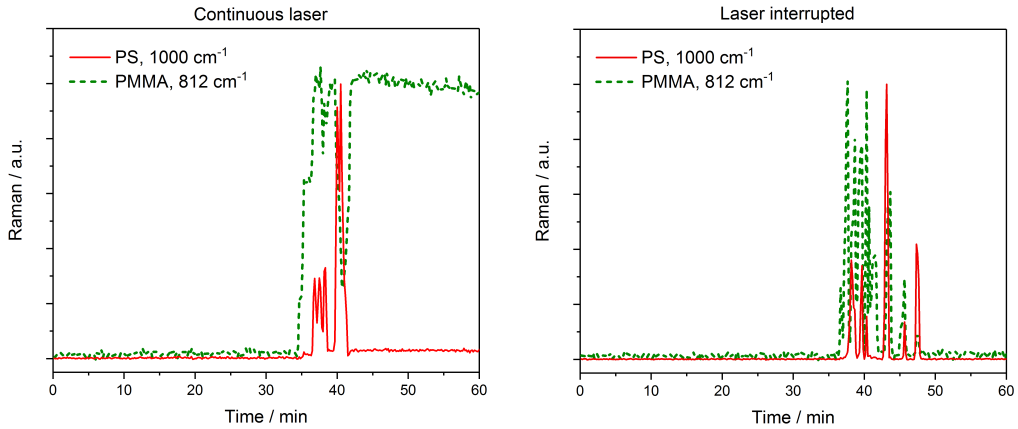

Fig. S.6.12: AF4-Raman data of the mix of PS 500 nm and PMMA 500 nm without (left) and with (right) interruption of the laser.

6.5.7 Calculation of Geometric Diameter from MALS Signal

The MALS signal is processed with 20 (of 21) active angles and a sphere algorithm to obtain the gyration diameter which is multiplied by 2/0.775 to give the geometric diameters of the latices.

This formula derives as follows: Assuming a homogeneous sphere of a geometrical radius r_{geo} and a density of ρ, which center of mass is at its geometrical center and its volume is $\frac{4}{3} \cdot \pi \cdot r_{geo}^3$, the correlation between gyration size r and geometrical size r_{geo} can be simplified to the following equation:

$$\int_0^a r^4 dr = \frac{4\pi}{5} \cdot r_{geo}^5$$

Solving this integral leads to

$$r^2 = \frac{3}{5} \cdot r_{geo}^2$$

and thus

$$r = \sqrt{\frac{3}{5}} \cdot r_{geo} = 0.775 \cdot r_{geo}$$

For more in-depth information on the mathematical correlation between gyration size and geometrical size also for other particle shapes, the interested reader is referred to M. Kerker, *Scattering of Light and other electromagnetic radiation*. 1969, Academic Press Inc. New York, ISBN: 978-0-12-404550-7[60].

6.5.8 AF4 Validation with Monodisperse Particles

Before separating mixtures, the coupling was investigated with four monodisperse particle systems of different size and material, i.e. polymeric and inorganic, namely PS 350 nm, PS 500 nm, PMMA 500 nm and SiO_2 500 nm. As shown in the Figures S.6.13 – S.6.16, the AF4 fractionation produced one elution peak in each case that could be characterized online with the UV, MALS and the Raman detector.

The UV signals are Gauss-like, which indicates the elution of a monodisperse fraction. It is possible to obtain the elution times from the UV signal. They can be obtained from all detectors, with a systematic offset in elution times that is attributable to the fact that the detectors are passed in sequence.

PS 350 nm	29 min
PS 500 nm	32 min
PMMA 500 nm	31 min
SiO_2 500 nm	34.5 min

Tab. S.6.1: AF4 elution times of four monodisperse particles.

The values for the elution times fit the expected results from an AF4 fractionation, where the smallest PS 350 nm particles elute first, followed by the larger polymeric 500 nm particles. This difference can be attributed to the fact that the PS 500 nm particles are larger than nominated with a d_{geo} around 580 nm (Figure S.6.14) and, therefore, elute slightly later. The SiO_2 500 nm particles have the longest elution time, which is attributable to their higher density, which is about twice as high as the density of the polymers.

The MALS detector confirms the diameters of the particles, which is (more or less) constant over the elution of the fraction confirming the monodispersity. It can be seen that the PS 500 nm particles are slightly larger than labelled and the SiO_2 500 nm particles are rather poly- than monodisperse.

The RM flow cell produces full spectra over the whole AF4 elution (60 min), from which particles can be identified and characteristic bands are selected and plotted over time. Signal intensity of SiO_2 is much weaker, due to its lower Raman cross-section and also less reproducible. These intensities match the elution peaks of the UV detector and identify the material of the particles. SiO_2 and PMMA show the ability to be trapped relatively long, as opposed to PS.

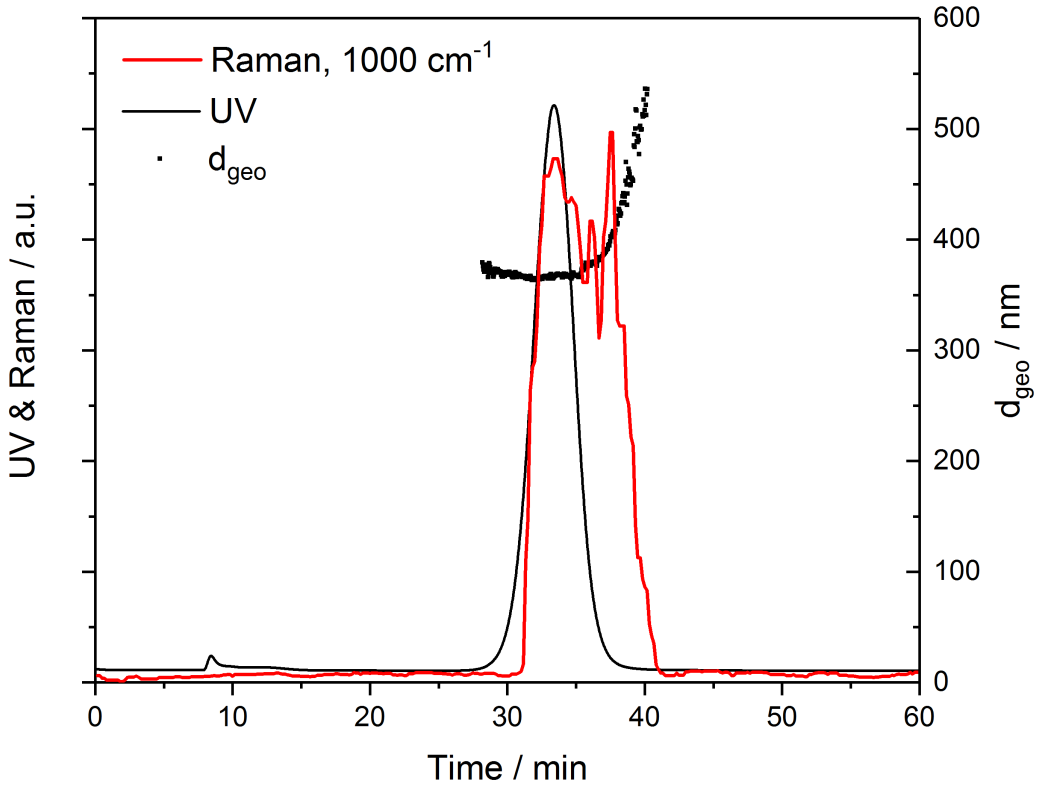

Fig. S.6.13: AF4-UV-MALS-Raman data of PS 350 nm. Raman intensity of 1000 cm^{-1} band, laser not interrupted. UV and Raman intensities have been normalized. Raman plot has been smoothed for visibility.

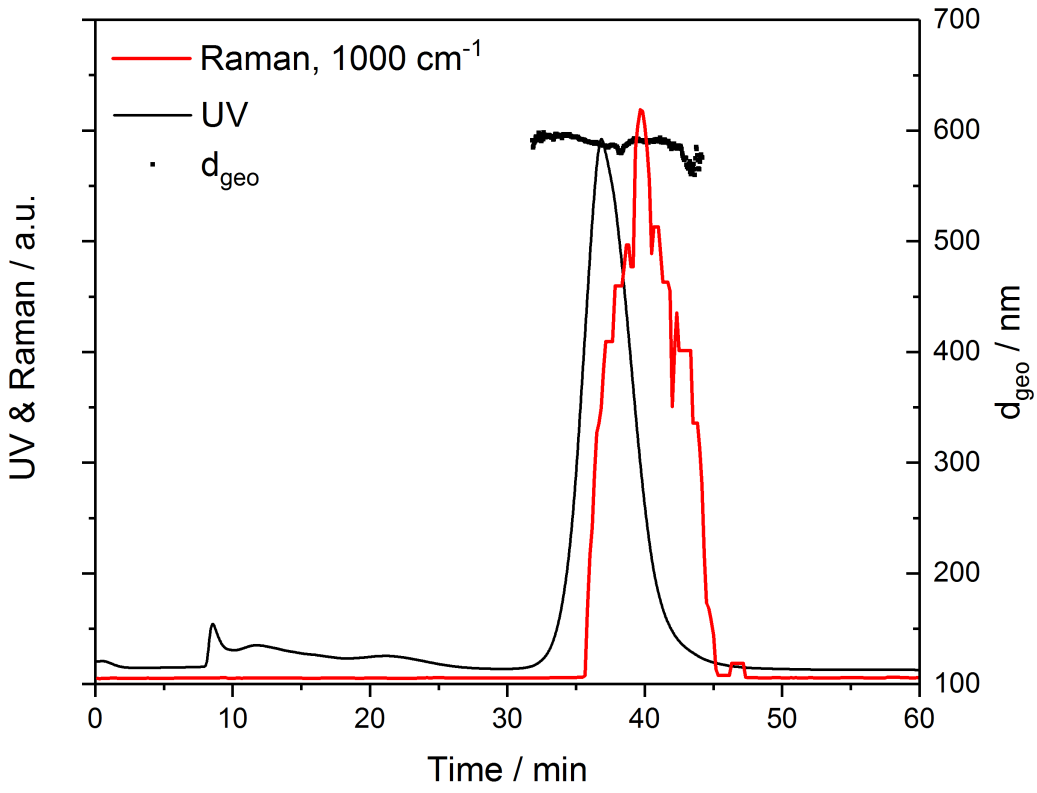

Fig. S.6.14: AF4-UV-MALS-Raman data of PS 500 nm. Raman intensity of 1000 cm^{-1} band, laser not interrupted. UV and Raman intensities have been normalized. Raman plot has been smoothed for visibility.

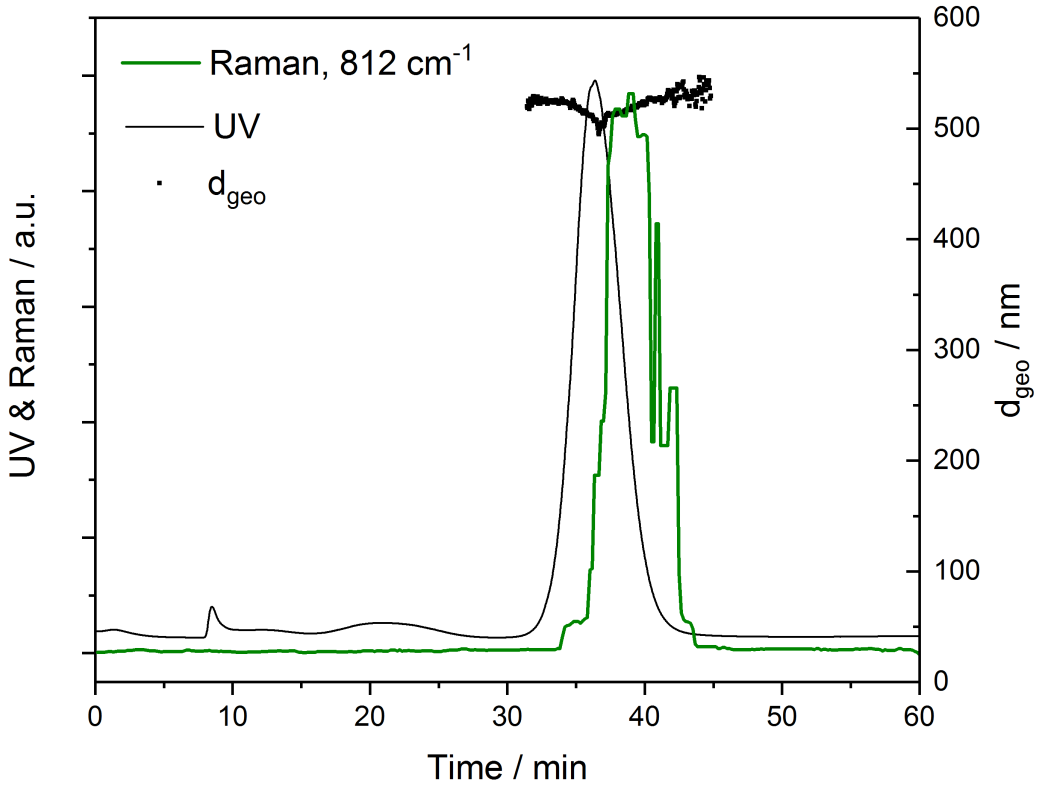

Fig. S.6.15: AF4-UV-MALS-Raman data of PMMA 500 nm. Raman intensity of 812 cm^{-1} band, laser interrupted. UV and Raman intensities have been normalized. Raman plot has been smoothed for visibility.

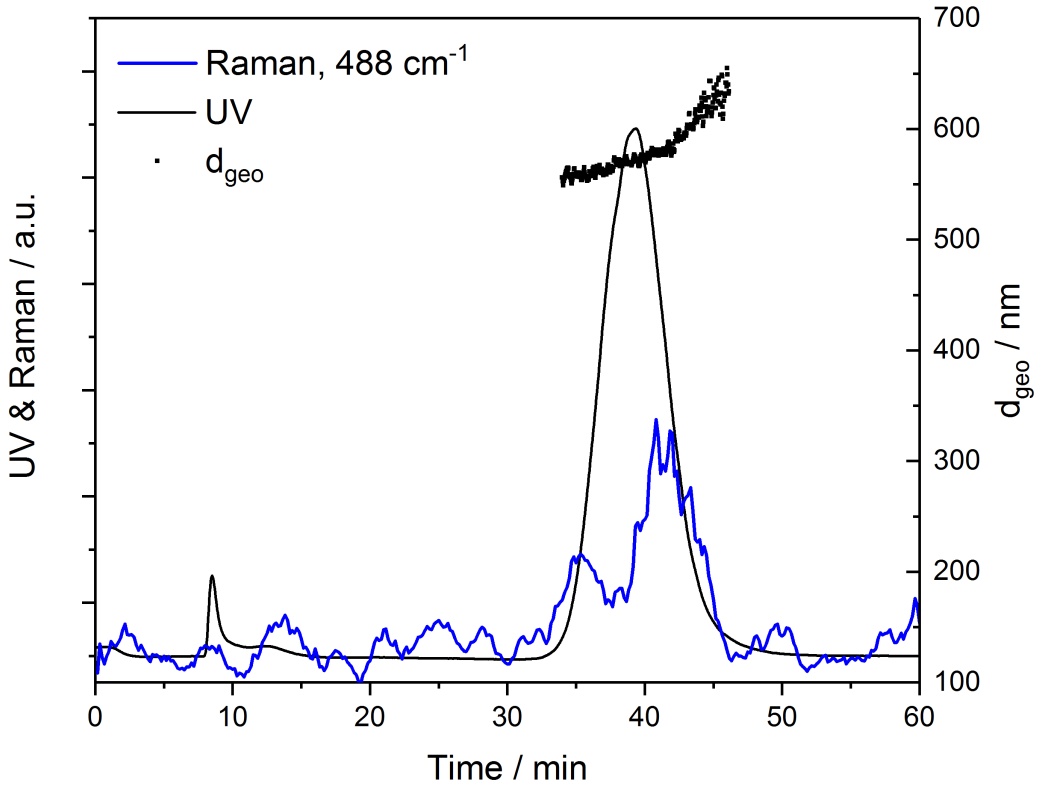

Fig. S.6.16: AF4-UV-MALS-Raman data of SiO_2 500 nm. Raman intensity of 488 cm^{-1} band, laser interrupted. Raman plot has been smoothed for visibility.

6.5.9 AF4-UV-MALS-RM of PS 500 nm and PMMA 500 nm

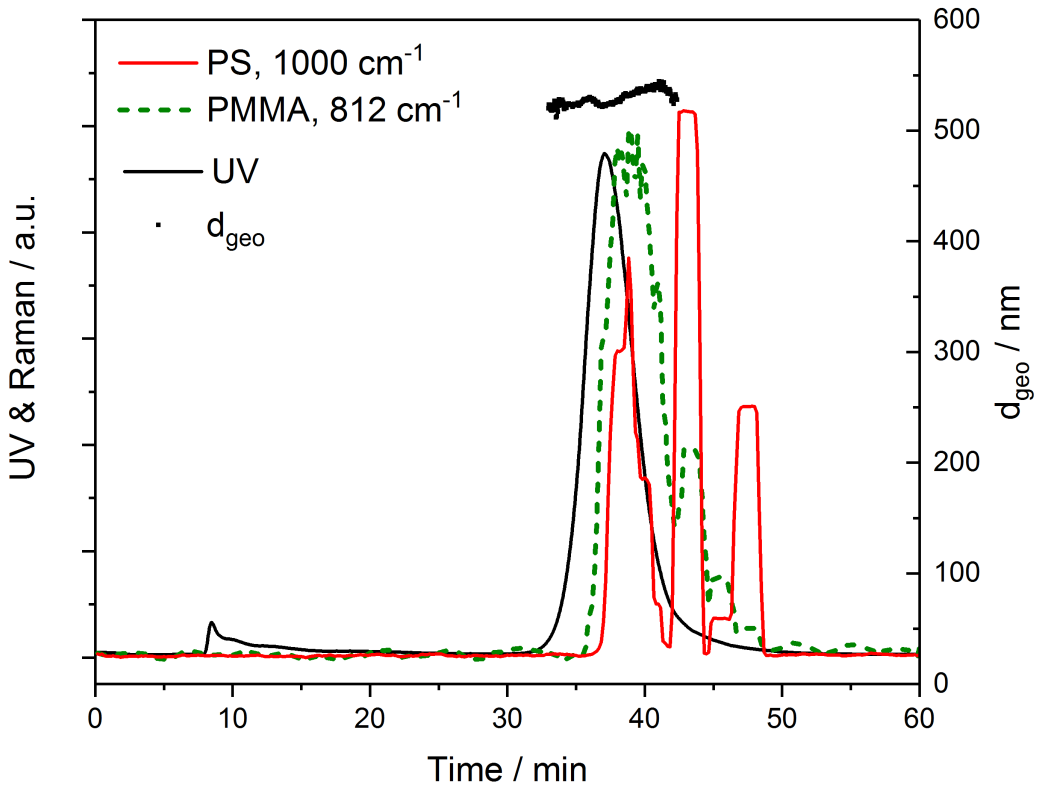

Fig. S.6.17: AF4-UV-MALS-Raman data of the mix of PS 500 nm and PMMA 500 nm (5 mg/L and 50 mg/L, respectively). Raman intensity of the 812 cm^{-1} band for PMMA and the 1000 cm^{-1} band for PS, laser interrupted. UV and Raman intensities have been normalized. Raman plot has been smoothed (10 point average) for visibility.

6.5.10 Capacity of the Focal Volume

The AF4-RM data from the monodisperse PMMA 500 nm particles (Figure 6.5) show that there is a maximum signal intensity, which corresponds to a completely filled focal volume. This is further illustrated within the data from the mixture of PS 500 nm and PMMA 500 nm, where a competition for the spots in the focal volume can be seen. At t = 41 min the signal of PS shows a spike, while PMMA shows a short dip.

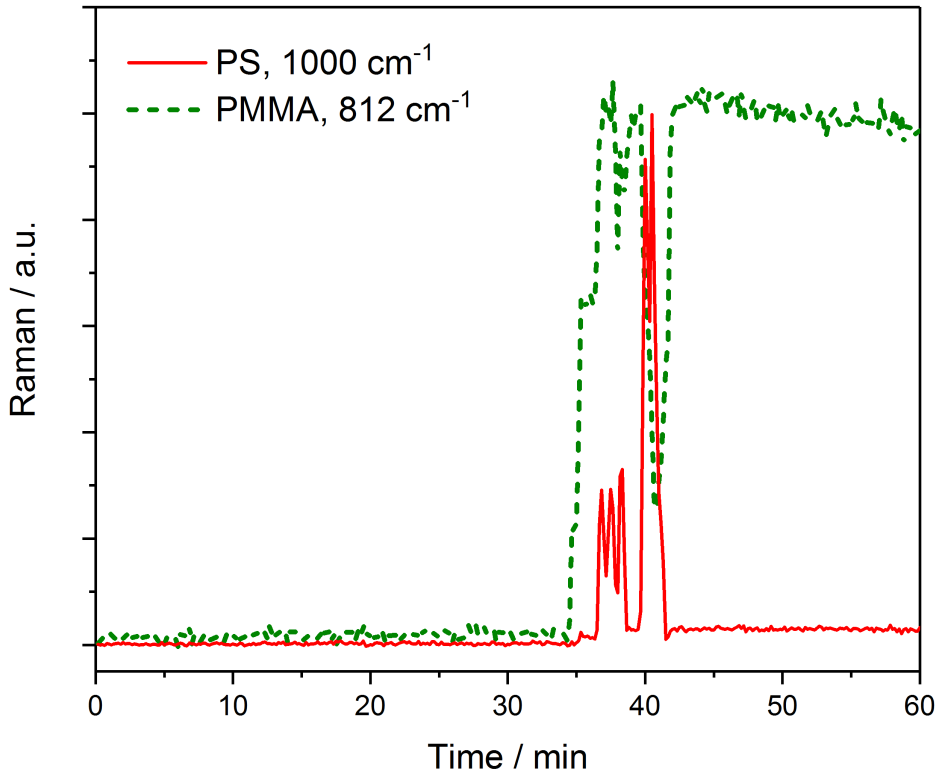

Fig. S.6.18: Raman intensities of the AF4 elution of PMMA 500 nm and PS 500 nm.

6.5.11 CF3-UV-MALS-RM of PS 350 nm, PS 500 nm and PMMA 500 nm

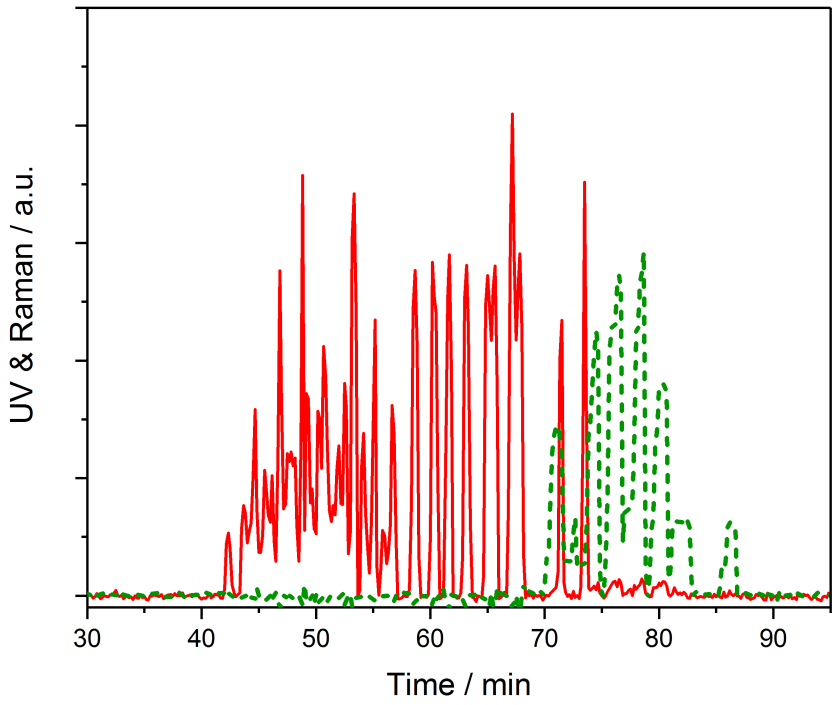

Fig. S.6.19: Original, unsmoothed CF3-Raman data including the comb-like structure. Red: PS at 1000 cm^{-1}; Green: PMMA at 812 cm^{-1}

References

1. Gigault, J.; Pedrono, B.; Maxit, B.; Ter Halle, A. Marine plastic litter: The unanalyzed nano-fraction. *Environmental Science: Nano* **2016**, *3*, 346–350.
2. Lambert, S.; Wagner, M. Formation of microscopic particles during the degradation of different polymers. *Chemosphere* **2016**, *161*, 510–517.
3. Mattsson, K.; Hansson, L.-A.; Cedervall, T. Nano-plastics in the aquatic environment. *Environmental Science. Processes & Impacts* **2015**, *17*, 1712–1721.
4. Alimi, O. S.; Farner Budarz, J.; Hernandez, L. M.; Tufenkji, N. Microplastics and Nanoplastics in Aquatic Environments: Aggregation, Deposition, and Enhanced Contaminant Transport. *Environmental Science & Technology* **2018**, *52*, 1704–1724.
5. Ng, E.-L.; Huerta Lwanga, E.; Eldridge, S. M.; Johnston, P.; Hu, H.-W.; Geissen, V.; Chen, D. An overview of microplastic and nanoplastic pollution in agroecosystems. *The Science of the Total Environment* **2018**, *627*, 1377–1388.
6. Chae, Y.; An, Y.-J. Effects of micro- and nanoplastics on aquatic ecosystems: Current research trends and perspectives. *Marine Pollution Bulletin* **2017**, *124*, Special Issue: Hong Kong Conference 2016, 624–632.
7. Besseling, E.; Redondo-Hasselerharm, P.; Foekema, E. M.; Koelmans, A. A. Quantifying ecological risks of aquatic micro- and nanoplastic. *Critical Reviews in Environmental Science and Technology* **2018**, *49*, 32–80.
8. Ter Halle, A.; Jeanneau, L.; Martignac, M.; Jardé, E.; Pedrono, B.; Brach, L.; Gigault, J. Nanoplastic in the North Atlantic Subtropical Gyre. *Environmental Science & Technology* **2017**, *51*, 13689–13697.
9. Mintenig, S. M.; Bäuerlein, P. S.; Koelmans, A. A.; Dekker, S. C.; van Wezel, A. P. Closing the gap between small and smaller: Towards a framework to analyse nano- and microplastics in aqueous environmental samples. *Environmental Science: Nano* **2018**, *5*, 1640–1649.
10. Ivleva, N. P.; Wiesheu, A. C.; Niessner, R. Microplastic in Aquatic Ecosystems. *Angewandte Chemie, International Edition* **2017**, *56*, 1720–1739.
11. Hartmann, N. B.; Hüffer, T.; Thompson, R. C.; Hassellöv, M.; Verschoor, A.; Daugaard, A. E.; Rist, S.; Karlsson, T.; Brennholt, N.; Cole, M.; Herrling, M. P.; Hess, M. C.; Ivleva, N. P.; Lusher, A. L.; Wagner, M. Are We Speaking the Same Language? Recommendations for a Definition and Categorization Framework for Plastic Debris. *Environmental Science & Technology* **2019**, *53*, 1039–1047.
12. Hüffer, T.; Praetorius, A.; Wagner, S.; von der Kammer, F.; Hofmann, T. Microplastic Exposure Assessment in Aquatic Environments: Learning from Similarities and Differences to Engineered Nanoparticles. *Environmental Science & Technology* **2017**, *51*, 2499–2507.

13. Correia, M.; Loeschner, K. Detection of nanoplastics in food by asymmetric flow field-flow fractionation coupled to multi-angle light scattering: Possibilities, challenges and analytical limitations. *Analytical and Bioanalytical Chemistry* **2018**, *410*, 5603–5615.

14. Rist, S.; Baun, A.; Hartmann, N. B. Ingestion of micro- and nanoplastics in Daphnia magna - Quantification of body burdens and assessment of feeding rates and reproduction. *Environmental Pollution* **2017**, *228*, 398–407.

15. Huppertsberg, S.; Knepper, T. P. Instrumental analysis of microplastics-benefits and challenges. *Analytical and Bioanalytical Chemistry* **2018**, *410*, 6343–6352.

16. Renner, G.; Schmidt, T. C.; Schram, J. Analytical methodologies for monitoring micro(nano)plastics: Which are fit for purpose? *Current Opinion in Environmental Science & Health* **2018**, *1*, 55–61.

17. Schwaferts, C.; Niessner, R.; Elsner, M.; Ivleva, N. P. Methods for the analysis of submicrometer- and nanoplastic particles in the environment. *Trends in Analytical Chemistry* **2019**, 52–65.

18. Schimpf, M. E.; Caldwell, K.; Giddings, J. C., *Field-flow fractionation handbook*; Wiley-Interscience: New York and Chichester, 2000.

19. International Organization for Standardization, *Nanotechnologies — Analysis of nano-objects using asymmetrical-flow and centrifugal field-flow fractionation*; ISO/TS 21362:2018.

20. Contado, C. Field flow fractionation techniques to explore the “nano-world”. *Analytical and Bioanalytical Chemistry* **2017**, *409*, 2501–2518.

21. Gigault, J.; El Hadri, H.; Reynaud, S.; Deniau, E.; Grassl, B. Asymmetrical flow field flow fractionation methods to characterize submicron particles: Application to carbon-based aggregates and nanoplastics. *Analytical and Bioanalytical Chemistry* **2017**, *409*, 6761–6769.

22. Nguyen, B.; Claveau-Mallet, D.; Hernandez, L. M.; Xu, E. G.; Farner, J. M.; Tufenkji, N. Separation and Analysis of Microplastics and Nanoplastics in Complex Environmental Samples. *Accounts of Chemical Research* **2019**, *52*, 858–866.

23. Davranche, M.; Veclin, C.; Pierson-Wickmann, A.-C.; El Hadri, H.; Grassl, B.; Rowenczyk, L.; Dia, A.; Ter Halle, A.; Blancho, F.; Reynaud, S.; Gigault, J. Are nanoplastics able to bind significant amount of metals? The lead example. *Environmental Pollution* **2019**, *249*, 940–948.

24. Mitrano, D. M.; Beltzung, A.; Frehland, S.; Schmiedgruber, M.; Cingolani, A.; Schmidt, F. Synthesis of metal-doped nanoplastics and their utility to investigate fate and behaviour in complex environmental systems. *Nature Nanotechnology* **2019**, *14*, 362–368.

25. Nischwitz, V.; Gottselig, N.; Missong, A.; Meyn, T.; Klumpp, E. Field flow fractionation online with ICP-MS as novel approach for the quantification of fine particulate carbon in stream water samples and soil extracts. *Journal of Analytical Atomic Spectrometry* **2016**, *31*, 1858–1868.

26. Missong, A.; Holzmann, S.; Bol, R.; Nischwitz, V.; Puhlmann, H.; V Wilpert, K.; Siemens, J.; Klumpp, E. Leaching of natural colloids from forest topsoils and their relevance for phosphorus mobility. *The Science of the Total Environment* **2018**, *634*, 305–315.

27. Anger, P. M.; von der Esch, E.; Baumann, T.; Elsner, M.; Niessner, R.; Ivleva, N. P. Raman microspectroscopy as a tool for microplastic particle analysis. *Trends in Analytical Chemistry* **2018**, *109*, 214–226.

28. Dijkstra, R. J.; Ariese, F.; Gooijer, C.; Brinkman, U. A. Raman spectroscopy as a detection method for liquid-separation techniques. *Trends in Analytical Chemistry* **2005**, *24*, 304–323.

29. Jahn, I. J.; Žukovskaja, O.; Zheng, X.-S.; Weber, K.; Bocklitz, T. W.; Cialla-May, D.; Popp, J. Surface-enhanced Raman spectroscopy and microfluidic platforms: Challenges, solutions and potential applications. *The Analyst* **2017**, *142*, 1022–1047.

30. Cowcher, D. P.; Jarvis, R.; Goodacre, R. Quantitative online liquid chromatography-surface-enhanced Raman scattering of purine bases. *Analytical Chemistry* **2014**, *86*, 9977–9984.

31. Nguyen, A.; Schultz, Z. D. Quantitative online sheath-flow surface enhanced Raman spectroscopy detection for liquid chromatography. *The Analyst* **2016**, *141*, 3630–3635.

32. Wang, W.; Xu, M.; Guo, Q.; Yuan, Y.; Gu, R.; Yao, J. Rapid separation and on-line detection by coupling high performance liquid chromatography with surface-enhanced Raman spectroscopy. *RSC Advances* **2015**, *5*, 47640–47646.

33. Dijkstra, R. J.; Martha, C. T.; Ariese, F.; Brinkman, U. A. T.; Gooijer, C. On-Line Identification Method in Column Liquid Chromatography: UV Resonance Raman Spectroscopy. *Analytical Chemistry* **2001**, *73*, 4977–4982.

34. Dijkstra, R. J.; Efremov, E. V.; Ariese, F.; Brinkman, U. A. T.; Gooijer, C. Capillary electrophoresis coupled on-line with ultraviolet resonance Raman spectroscopy. *Analytical Chemistry* **2003**, *75*, 5697–5702.

35. Dijkstra, R. J.; Bader, A. N.; Hoornweg, G. P.; Brinkman, U. A. T.; Gooijer, C. On-Line Coupling of Column Liquid Chromatography and Raman Spectroscopy Using a Liquid Core Waveguide. *Analytical Chemistry* **1999**, *71*, 4575–4579.

36. Marquardt, B. J.; Vahey, P. G.; Synovec, R. E.; Burgess, L. W. A Raman Waveguide Detector for Liquid Chromatography. *Analytical Chemistry* **1999**, *71*, 4808–4814.

37. Fischer, B., *Entwicklung eines Raman-Detektors zur Integration in eine HT-HPLC/irMS-Kopplung*; Dissertation: 2015.

38. Steinert, R.; Bettermann, H.; Kleinermanns, K. Identification of Xylene Isomers in High-Pressure Liquid Chromatography Eluates by Raman Spectroscopy. *Applied Spectroscopy* **2016**, *51*, 1644–1647.

39. Cooper, S. D.; Robson, M. M.; Batchelder, D. N.; Bartle, K. D. Development of a universal Raman detector for microchromatography. *Chromatographia* **1997**, *44*, 257–262.

40. Hong, T. D. N.; Jouan, M.; Quy Dao, N.; Bouraly, M.; Mantisi, F. Coupling of high-performance liquid chromatography with Raman spectrometry. *Journal of Chromatography A* **1996**, *743*, 323–327.

41. Nelson, G. L.; Lines, A. M.; Casella, A. J.; Bello, J. M.; Bryan, S. A. Development and testing of a novel micro-Raman probe and application of calibration method for the quantitative analysis of microfluidic nitric acid streams. *The Analyst* **2018**, *143*, 1188–1196.

42. Leung, S.-A.; Winkle, R. F.; Wootton, R. C. R.; deMello, A. J. A method for rapid reaction optimisation in continuous-flow microfluidic reactors using online Raman spectroscopic detection. *The Analyst* **2005**, *130*, 46–51.

43. Fletcher, P. D. I.; Haswell, S. J.; Zhang, X. Monitoring of chemical reactions within microreactors using an inverted Raman microscopic spectrometer. *Electrophoresis* **2003**, *24*, 3239–3245.

44. Widjaja, E.; Teh, S. Y.; Garland, M. Characterizing diffusion and transport in microfluidics channels: A combined Raman microscopy and band-target entropy minimization study. *Applied Spectroscopy* **2012**, *66*, 1226–1232.

45. Matthiae, M.; Zhu, X.; Marie, R.; Kristensen, A. In-line whole blood fractionation for Raman analysis of blood plasma. *The Analyst* **2019**, *144*, 602–610.

46. Kniggendorf, A.-K.; Wetzel, C.; Roth, B. Microplastics Detection in Streaming Tap Water with Raman Spectroscopy. *Sensors* **2019**, *19*, 1839.

47. Chrimes, A. F.; Khoshmanesh, K.; Stoddart, P. R.; Mitchell, A.; Kalantar-Zadeh, K. Microfluidics and Raman microscopy: Current applications and future challenges. *Chemical Society Reviews* **2013**, *42*, 5880–5906.

48. Paiè, P.; Zandrini, T.; Vázquez, R. M.; Osellame, R.; Bragheri, F. Particle Manipulation by Optical Forces in Microfluidic Devices. *Micromachines* **2018**, *9*, 200.

49. Gillibert, R.; Balakrishnan, G.; Deshoules, Q.; Tardivel, M.; Magazzù, A.; Donato, M. G.; Maragò, O. M.; La Lamy de Chapelle, M.; Colas, F.; Lagarde, F.; Gucciardi, P. G. Raman Tweezers for Small Microplastics and Nanoplastics Identification in Seawater. *Environmental Science & Technology* **2019**, *53*, 9003–9013.

50. Baroud, C. N.; Okkels, F.; Ménétrier, L.; Tabeling, P. Reaction-diffusion dynamics: Confrontation between theory and experiment in a microfluidic reactor. *Physical Review. E, Statistical, Nonlinear, and Soft Matter Physics* **2003**, *67*, 060104.

51. Neuman, K. C.; Block, S. M. Optical trapping. *The Review of Scientific Instruments* **2004**, *75*, 2787–2809.

52. Schermer, R. T.; Olson, C. C.; Coleman, J. P.; Bucholtz, F. Laser-induced thermophoresis of individual particles in a viscous liquid. *Optics Express* **2011**, *19*, 10571–10586.

53. Michaelides, E. E. Brownian movement and thermophoresis of nanoparticles in liquids. *International Journal of Heat and Mass Transfer* **2015**, *81*, 179–187.

54. Gagné, F.; Auclair, J.; Quinn, B. Detection of polystyrene nanoplastics in biological samples based on the solvatochromic properties of Nile red: application in Hydra attenuata exposed to nanoplastics. *Environmental Science and Pollution Research* **2019**, *26*, 33524–33531.

55. Lin, Y.; Huang, X.; Liu, Q.; Lin, Z.; Jiang, G. Thermal fragmentation enhanced identification and quantification of polystyrene micro/nanoplastics in complex media. *Talanta* **2020**, *208*, 120478.

56. Sogne, V.; Meier, F.; Klein, T.; Contado, C. Investigation of zinc oxide particles in cosmetic products by means of centrifugal and asymmetrical flow field-flow fractionation. *Journal of Chromatography A* **2017**, *1515*, 196–208.

57. Gigault, J.; Halle, A. T.; Baudrimont, M.; Pascal, P.-Y.; Gauffre, F.; Phi, T.-L.; El Hadri, H.; Grassl, B.; Reynaud, S. Current opinion: What is a nanoplastic? *Environmental Pollution* **2018**, *235*, 1030–1034.

58. Balakrishnan, G.; Déniel, M.; Nicolai, T.; Chassenieux, C.; Lagarde, F. Towards more realistic reference microplastics and nanoplastics: preparation of polyethylene micro/nanoparticles with a biosurfactant. *Environmental Science: Nano* **2019**, *6*, 315–324.

59. Magrì, D.; Sánchez-Moreno, P.; Caputo, G.; Gatto, F.; Veronesi, M.; Bardi, G.; Catelani, T.; Guarnieri, D.; Athanassiou, A.; Pompa, P. P.; Fragouli, D. Laser Ablation as a Versatile Tool To Mimic Polyethylene Terephthalate Nanoplastic Pollutants: Characterization and Toxicology Assessment. *ACS Nano* **2018**, *12*, 7690–7700.

60. Kerker, M., *Scattering of light and other electromagnetic radiation*; Physical chemistry, Vol. 8; Elsevier Science: New York, 2016.

Chapter 7

Discussion and Conclusion of the Thesis

The objective of this thesis has been to enable nanoplastic analysis by closing the methodological gap between microplastic (MP) techniques on the one hand, which have been lacking suffiently low size limits of detection, and nanoparticle techniques on the other hand, which have (mostly) not been able to chemically identify the polymeric nature of the particles (Section 1.2.2). To overcome these limitations, advances were made in the application of Raman microspectroscopy (RM), which was combined with scanning electron microscopy (SEM), field-flow fractionation (FFF), and chemometrics for the identification, physical characterization, and quantification of micro- and nanoplastic particles.

To this end, three topics were pursued in this thesis. First, RM in combination with SEM was evaluated for the use on primary and secondary nanoplastic particles. The lower limit of the application range was established to be at the theoretical limit of ca. 250 nm. Secondly, a chemometric algorithm based on window sampling and bootstrap was developed to enable a robust quantification. It enables the selection of particles to be analyzed on the Raman filter so that very small MP and potentially nanoplastic can be analyzed by automated RM. Finally, the online-coupling of FFF to RM (FFF-Raman) was implemented by a flow-cell based on an optical trap, which provides the size analysis by FFF-UV-MALS (multi-angle light scattering) and the chemical identification by RM. In this overarching discussion, the works of the thesis will be contextualized and put in relation to the advances in the research of nanoplastic analysis.

7.1 Progress in the Field of Nanoplastic

The nanoplastic issue was a newly emerging topic, which posed (and still poses) special challenges to the analytical methods (Section 1.2.2). The following paragraphs will briefly display the recent advances in this field and relate them to the works presented in this thesis as illustrated in Figure 7.1. For a comprehensive overview of the current state of nanoplastic analysis, the reader is referred to recent reviews[1,2].

Initially, proper methodologies and knowledge were very scarce (see State of the Art, Section 1.2.3). Thus, a critical review of the current state of the art, including a selection of possible techniques that can be transferred from related fields, has been brought forward in this thesis (Chapter 3). It concluded with a

projected roadmap (Figure 3.3, Section 3.5) for the future developments toward nanoplastic identification and quantification. In essence, the earliest papers hypothesized on the presence and properties of nanoplastic[3,4], demonstrated that plastic debris fragmentation indeed generates nanoplastic[5–7], and provided the first detections of primary and secondary nanoplastic[8,9] (Figure 7.1a). The methods applied in those studies were adapted from engineered nanoparticle and MP research, respectively.

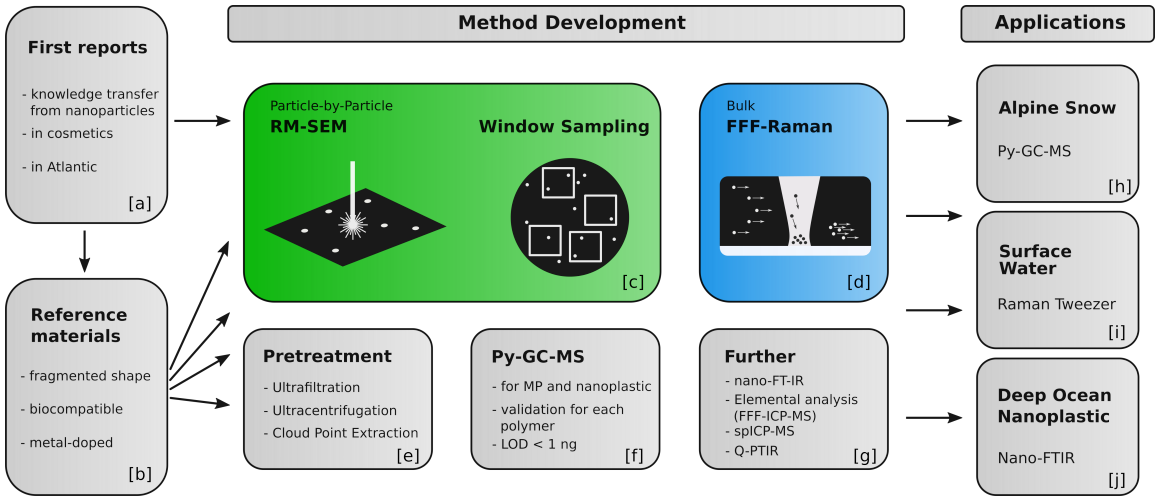

Fig. 7.1: Progress in nanoplastic analysis. General overview illustrating the recent developments in nanoplastic analysis. Moving forward from the initial reports, a great effort on the production of suitable reference materials has been made. This accelerated and enabled the method development, which has seen progress on a multitude of techniques. This thesis is focused on RM-based innovations on the particle-by-particle approach (green) and the online-coupling of FFF and RM (blue). These new methods enable the assessment of relevant environmental systems.

In the following years, there has been substantial progress in the field of nanoplastic, which can be put in distinct phases. Here, topics like (i) the development of reference materials, (ii) new method development, and (iii) applications of the new methods can (in general terms) be distinguished. Exempt from this are toxicological studies, which were mainly performed with standardized polystyrene (PS) latex beads, which are commercially available, and are not the focus of this, instrumentation-oriented, thesis and discussion.

The first step towards new method developments for nanoplastic analysis was the production of suitable reference materials to adequately emulate the environmental contamination (i.e. polydisperse, and irregular[10]). These also need to be free of toxic additives, surfactants, or biocides, which could strongly affect the studies in which they are employed[11]. Thus, there are many publications[a] which have sought to solve this demand either by fragmenting larger plastic pieces[12–17] (top-down), or by specifically

[a] Top down particle generation can be performed by various impacts. Of note are an ultrasonic treatment for the generation of suspendable, polydisperse secondary MP and nanoplastic, of different materials[12], or mechanical fragmentation by blade grinding[13], in some cases combined with ball milling[14]. Other studies used cryo-milling[15,16]. Furthermore, the use of laser ablation of polyethylene terephthalate (PET) has been used to form $\sim$ 100 nm polydisperse particles with oxidized surfaces[17]. Those protocols usually produce a broad range of sizes, hence, the resulting suspensions are filtered for the nanoplastic, and can, in principle, be used for many different polymer types. Bottom-up methods synthesize the particles specifically, which could limit the use to certain polymers, depending on their chemical properties. Here, polyethylene particles (200 nm – 800 nm) were created by precipitation from toluene[18] and PET particles ($\sim$ 200 nm) by precipitation from trifluoroacetic acid (TFA)[19]. Further emulsion polymerization of polypropylene (80 nm – 350 nm)[20] or copolymerization of PS-Polyacrylate ($\sim$ 400 nm)[21] were reported. Some of those protocols were designed to omit hazardous surfactants[18,20,21].

synthesizing the particles[18–21] (bottom-up). This research impacted subsequent method development, as it enables the optimization and validation with more realistic nanoplastic particles (Figure 7.1b).

Alongside of the development of reference materials, the methodology for nanoplastic analysis has seen great progress. Equal to MP analysis, the main goal was to enable the chemical identification to distinguish plastic from natural particles. For nanoplastic, this is even more important, since nanoscale particles can only be identified by suitable techniques; the issues with visual identification (Section 1.1.3) of MP do not occur.

The sample treatment (Figure 7.1e) of nanoplastic faces new challenges compared to MP (Section 1.1.3), since the colloidal particles have an increased tendency to agglomerate with natural organic matter and leach additives. Thus, new methods need to be suited to preserve the properties of the complex nanoplastic analyte. The critical review in this thesis (Chapter 3) discusses those differences and suitable methods. One of the most important steps is the preconcentration of the particles, as the particle content (especially by mass) may be very small. Here, ultrafiltration[9,22], rotavap treatment[17], or lyophilization[13] can be employed. Recently, also cloud point extraction (CPE)[23–25] has been tested for nanoplastic with an enrichment factor of 500 and a subsequent chemical identification[b] by pyrolysis-gas-chromatography-mass-spectrometry (Py-GC-MS)[23,24] or single particle ICP-MS(spICP-MS)[25]. Ultracentrifugation has been used for the preconcentration of nanoplastic as well[27].

In terms of chemical identification, RM is well established for the analysis of MP (Section 1.1.3) due to its ability to provide an unambiguous identification on single particles[1]. And, based on its theoretical size limit in the subµ range, an application for nanoplastic seemed possible as well (Section 1.2.4). The results of this thesis contributed to the method development of RM for nanoplastic in two conceptually different aspects: On the one hand, improvements on the particle-by-particle analysis (Figure 7.1c) were made, in which single particles are analyzed individually. Here, the lowest size limits for RM in combination with SEM was investigated (Chapter 4). To complement this qualitative approach, a chemometric method was devised for the optimized particle selection in RM for very small MP and nanoplastic in order to enable a reliable quantification (Chapter 5). On the other hand, Raman analysis of nanoplastic particles in bulk (Figure 7.1d) was pursued, in which a greater amount of particles is identified, which loses the single particle information, but gains greatly improved measurement times. Thus, the bulk approach needs to be combined with other techniques that provide this physical characterization, which was done with FFF in this thesis (Chapter 6). These advances will be discussed below in their respective paragraphs (Section 7.2 and 7.3).

A further branch of techniques for chemical identification of plastic particles is the thermoanalytical mass-spectrometry (MS) of characteristic pyrolytic fragments. It is an established technique for MP (Chapter 1), which also shows the potential to be transferred to the topic of nanoplastic, provided sufficient preconcentration is performed (Section 1.2.3). In recent years, this approach has seen further

[b] Zhou et al. showed the use of Py-GC-MS on nanoplastic extracted by CPE[23]. Recently, this group also showed the analysis of nanoplastic by Py-GC-MS (LODs: 0.03 µg/g for PS and 0.09 µg/g for PMMA) after alkaline digestion of matrix (aquatic animals) and particle precipitation by bovine serum albumin (BSA) corona formation followed by increasing the salinity[26]. Similarly, Li et al.[24] showed Py-GC-MS analysis of nanoplastic obtained by CPE (LOD: 0.05 – 1.9 µg/L). Further, CPE was used with subsequent spICP-MS analysis[25].

progress with improved limits of detection (LOD) (< 1 ng for PS (1 µm))[28]. Py-GC-MS analyzes plastic particles in bulk as well. Thus, it could be used complementary to the FFF-Raman flow-cell and could provide cross-validation in their respective method developments, especially since the offline-coupling of Py-GC-MS and asymmetric-flow FFF (AF4) has already been shown[22]. Besides the thermoanalytical methods, developments with other MS techniques, such as spICP-MS[c] (sp-ICP-MS) or matrix-assisted laser desorption/ionization time-of-flight mass spectrometry[d] (MALDI-TOF-MS) were also explored (Figure 7.1f).

Recently, new approaches aside RM and Py-GC-MS have been tested and discussed for the analysis of nanoplastic as well (Figure 7.1g). Many of these incorporate the visualization of the particle, which is an important information on this morphologically diverse analyte (Chapter 3). These microspectroscopic techniques have the appeal of providing both the shape and chemical characterization. Of note are dark-field hyperspectral microscopy[33,34], fluorescence lifetime microscopy (FLIM)[35], optical photothermal Infrared and simultaneous Raman spectroscopy (O-PTIR)[36,37], and AFM-IR (nano-FTIR)[38–40]. Furthermore, metal-doped (e.g. Pd[41]) nanoplastic particles have been developed to track the transport and distribution in specific systems (recently for the assessment of uptake and effects on *Gammarus pulex*[42]). Similarly, tracking and quantification has also been achieved with radioisotope-labelled (C-14) particles[43,44] or positron emission tomography (Zr-89)[45] (Figure 7.1b). An advantage of the techniques with doped particles is that they can be analyzed with established elemental identification techniques such as ICP-MS[41]. Such labels, however, will not occur in environmental nanoplastic.

The advancement of analytical methods for nanoplastic allows the next step, i.e. investigation of environmental samples (Figure 7.1h-j). To this end, some studies have recently been published extending the initial knowledge of 2017 (Figure 7.1a). One study found nanoplastic in alpine snow using Py-GC-MS[28]. Their results show the presence of PET, PVC, and polycarbonate in the MP range but only PET in the nanoplastic range (filtration < 0.2 µm), which is in agreement with the findings of the earlier reports on marine systems[9]. Furthermore, Raman tweezers (RT) were used to identify very small MP (> 2.5 µm) in marine surface waters[46] and AFM-IR was used to detect PET nanoplastic particles down to 20 nm in deep ocean waters (5000 m)[40]. These efforts are the starting point for the necessary assessments of the various systems (e.g. marine and limnic waters, food, or organisms), which have been shown to contain MP. New knowledge on the plastic particle contamination will extend the known size range to comprise the nanoplastic range, as well.

[c] Bolea-Fernandez et al. demonstrated the application of sp-ICP-MS for spherical polystyrene microspheres of 1 and 2.5 µm[29] and Jimenez et al. showed its applicability for nanoplastic (PS with negatively charged carboxylate groups of up to 1 µm), which was labelled with small Au nanoparticles (17±3 nm), at low concentrations (LOQ 8.4×10^5 L^{-1}, lowest size detectable: 135 nm)[30]. Further, spICP-MS was used to identify in-situ Au-NP labelled nanoplastic (50 nm – 1200 nm, LOD: 4.6×10^8 L^{-1}), which was concentrated by CPE[25].

[d] MALDI-TOF-MS was used to identify and quantify MP and nanoplastic demonstrating its simple and quick applicability[31]. Also, nanostructured laser desorption/ionization time-of-flight mass spectrometry (NALDI-TOF-MS) with in-laboratory built nanostructures (zinc oxide, titanium oxide and cobalt) was evaluated for the analysis of micro/nanoplastic in water and snow matrices, without sample pre-treatment (LOD: ∼ 5 pg in ambient snow)[32].

7.2 Particle-by-Particle Raman Microspectroscopy

The particle-by-particle approach in the analysis by RM has to provide both qualitative and quantitative information – which is true for most of the analytical chemical discipline. The works of the thesis address both of these aspects. For the qualitative part, i.e. the identification, one of the main challenges is to push down the lower size limit to achieve nanoplastic analysis. For the quantification, the issue is a matter of analyzing sufficient particles in a feasible way, which will establish the reliability of the results.

Thus, with regard to the qualitative analysis, the RM identification of MP particles was limited to particle sizes in the range of 1 – 10 µm[47]. Hence, the challenge was to push this size limit down to the nanometer range. A solution was pursued in this thesis using RM, which has a theoretical size limit at ca. 0.25 µm (Section 4.2.1). Furthermore, as the optical microscopic visualization of the particles close to the diffraction limit lacks the resolution required for a proper morphological characterization, the RM analysis is combined with SEM (RM-SEM). This provides both spectroscopic information and high-resolution visualization. Thus, one key achievement of this thesis is the development of a suitable RM-SEM method and the demonstration of its applicability to primary (down to 250 nm) and secondary nanoplastic (Chapter 4).

Subsequent to this development, there were more recent efforts by other groups, who pushed the size limit even further down (< 100 nm)[48–50]. This was achieved by using Raman imaging, however at the cost of longer measurement times compared to the single particle approach. Nonetheless, this provides new methods in the analysts' toolkit for different investigations. Furthermore, the RM-SEM method described was advanced in recent papers on the analysis of nanoplastic by correlated RM and SEM[51–53] using integrated, commercial systems. This could enable higher sample throughput. The method of this thesis, however, can be used when such an instrument is not available or economically not feasible (Section 4.3). Third, surface-enhanced Raman scattering (SERS) was shown to be applicable for MP and nanoplastic[26,54,55]. This development holds potential for future developments, as the enhanced signals can permit faster spectrum acquisition, hence, substantially accelerate the measurements (see Figure 7.2).

With regard to the quantitative aspects of subµ-plastic analysis, the particle-by-particle approach will face the problem of very high particle numbers, as the distribution of particle number by particle size was seen to be exponential[56]. Hence, a proper subsampling for the very small MP and subµ-plastic, which are to be analyzed by RM, needs to be performed. In general, proper subsampling has become relevant with the advancing automatization of the RM particle analysis and first considerations on the issues of random sampling for larger MP particles were published by Anger and von der Esch et al.[57] in 2018 (Figure 7.2). This topic is also addressed and properly formalized in the present work (Section 5.6.1).

For larger particles above a threshold of ca. 10 µm[58,59], it is feasible to acquire an optical microscope image of the whole filter and detect all the particles on it by image recognition. With that, an automated Raman identification of selected particles can be performed[58–62]. When all particles are detected, a random sampling of these particles can be performed, which ensures an equal probability for each

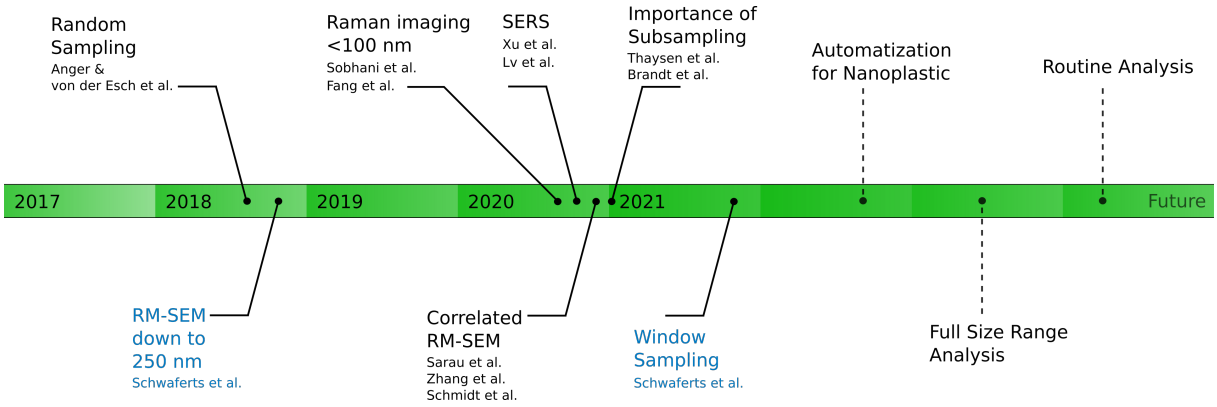

Fig. 7.2: Timeline depicting the progress and outlook of RM-based analysis of MP and nanoplastic. The development moves from automation and random sampling for large MP to smaller particle sizes, new approaches (RM-SEM, SERS), and window sampling. The outlook aims for the technical implementation of window sampling for nanoplastic, the closure of the knowledge gap with regard to the full plastic particle size range, and routine analysis.

particle to be selected. This, in turn, makes the results independent of the spatial structure of the particles on the filter and, thus, representative of the sample. For random sampling it is easy to calculate the confidence interval (CI) and derive a minimal subsample size to satisfy a given precision requirement (urn model without replacement)[57].

However, for smaller particles, it is no longer feasible to image the whole filter, because the precision of the microscope stage of common RMs is in the same order of magnitude (or larger) as the size of the investigated particles (Section 5.1). Consequently, random sampling is no longer available, since the total particle number is now unknown. Hence, a window sampling strategy in combination with a bootstrap method is presented in this thesis (Chapter 5) to enable particle selection and a CI estimation for error quantification. Errors of systematic window sampling and random window sampling are compared and a preference for the use of random windows, especially in view of the subsequent use of the bootstrap method, can be derived. Ultimately, both window sampling and the bootstrap method are included in a proposed *on-the-fly* measurement algorithm (Section 5.4), which instantly and automatically calculates the CI of small increments of particles by bootstrap and decides whether the measurement process can be stopped. Otherwise, the next increment would be analyzed.

This *on-the-fly* algorithm is a key achievement of the results presented in Chapter 5, as it offers a solution for the particle-by-particle analysis of such small particles and, furthermore, removes the requirement for the preemptive knowledge of the MP ratio, making the analysis less prone to error. In addition, the measurement times could be reduced, as the analysis would stop at an optimal point instead of identifying a fixed number of particles. Finally, the projected subsampling is discussed in general terms and, thus, can be of interest for any subsampling, in which particles have to be selected from a 2D surface.

Preceding the development of the *on-the-fly* algorithm, there were reports that also propose subsampling strategies. Thaysen et al.[e] demonstrated the importance of taking the spatial structure of the particles

[e] Thaysen et al. investigated the particle distribution on the filter by light microscopy of artificial samples. They calculated the coefficient of variation between windows (with an arbitrary 10 % threshold) and used a distance-to-center plot identifying that

on the filter into account and recommended a stratified sampling in rings to account for the radial pattern of the particle distribution[63]. However, it is very difficult to give a complete or, most often, even adequate description of the spatial pattern. The spatial pattern will vary for each laboratory and sample type as well. This becomes apparent in comparing their results to the spatial structures observed by Brandt et al.[65], which differed substantially. Contrary to this approach, the subsampling in this thesis has the advantage that it is based on randomness, which entirely avoids the dependency on preemptive knowledge of the spatial structure.

Brandt et al.[65] evaluated common subsampling strategies in microscopy-based MP identification (i.e. µFT-IR & RM)[f] and reported an exponential decrease of the error with increasing fraction of particles or area, respectively. It was further seen that none of the subsampling methods outperformed the others, except for edge scenarios, e.g. low particle numbers. Additionally, the results show that the sampling errors are > 50 % if less than 5 % of the filter is measured. This is an important result, since early studies were often restricted to areas far below that percentage[66,67]. Mintenig et al. performed an investigation[g] on the impact of sample size in the case of a river water study, which is in agreement with this requirement for sufficient sample size[68]. From these reports, two things should be concluded: (i) Previous studies with small sample sizes should be critically assessed, as performed e.g. by Koelmans et al.[69], if they are used for any conclusions. And if the uncertainty is too large, the results of these studies should be treated with caution. (ii) Future studies should include a solid quality assurance protocol to produce reliable data.

The window sampling method of this thesis improves these studies, as the *on-the-fly* algorithm is aimed at finding an optimal particle subset for the individual sample. Furthermore, is it based on precision parameters (margin of error, error probability), which can be predefined to suit the quality control of the respective study. This makes it more general than the recommendations of the abovementioned studies, which were only applied on samples with MP ratios and particle numbers in a certain range.

These new RM-based methods close critical methodological gaps of subµ- and nanoplastic analyses. To advance the technique and bring the scientific field forward to establishing analytical routines, there are still some open challenges. Among these are the application on different (in)organic matrices and

the particles had a „starburst“ pattern, i.e. the particles tended to the center[63]. It has to be noted that this kind of plot disregards any non-radial influences on the pattern, since only the distance to the center is taken into account. Furthermore, there are much more such methods, which all provide different aspects of the spatial structure[64].

[f] Brandt et al. subjected a dataset of 27 fully analyzed MP samples from previous studies to the different subsampling strategies (i.e. random particle sampling, stratified random particle sampling, a cross and a spiral of windows, random windows over the whole filter, and random sampling over a quarter filter) with varying fractions of particle number/area. By comparing the extrapolated MP number to the MP number of the full analysis, an error was quantified. From the analyzed samples, it was concluded that with a maximal error of 20 %, 50 % of the total particle number or 7000 particles need to be analyzed, which is in agreement with von der Esch et al.[58]. A similar threshold for window sampling was given, in which the maximal error of 20 % is achieved by analyzing 50 % of the area of the filter. Further, a decreasing error with increasing MP content is observed, which is as expected by the theoretical error description, which was laid out by Anger and von der Esch et al.[57] and further elaborated on in Chapter 5. From that, the need to increase the MP ratio, e.g. by an enrichment step, like density separation, is highlighted.

[g] Mintenig et al.[68] compared the reliability of reducing the investigated filter area of the µ-FT-IR analysis. The subsampling was deemed acceptable by the criterion of the coefficient of variation being ≤ 1. It was concluded that at least 50 % of the filter area needs to be analyzed in order to accurately identify the particles of the sample by particle number and polymer type. This percentage can be reduced, if the MP number on the filter was very large. Further, the MP type analysis of very common polymers (PE, PP, natural rubber) can be achieved by lower subsections of at least 5 % of the filter. Conversely, very rare polymers need higher percentages (75 %).

different systems, including biota. Further, the many possibilities of SEM imaging (such as energy dispersive spectroscopy, EDS) should be explored with regard to their use in RM-SEM on nanoplastic. An improved automation that incorporates the smaller particle fractions should also be one of the central future goals (Figure 7.2).

Thus, the subsequent work for the automation of RM for very small MP and nanoplastic is the technical implementation of the projected *on-the-fly* algorithm. This would require an improved control software expanding the functionality of the *TUM-ParticleTyper*[58], which would have a more frequent communication with the RM. To perform this implementation, some technical answers are necessary. On the one hand, the image recognition for the very small particles using higher-magnification objectives needs to be validated. Further, the targeting and proper chemical identification of the smaller particles, especially in the z-axis, needs to be validated as well. On the other hand, application tests are needed to obtain information on the time consumption by the individual steps of the *on-the-fly* algorithm, like interfacing, data processing, microscope stage movement, or the bootstrap calculations. In addition, the optimal size range correlating to specific microscope objectives needs to be found and, possibly, a cross-check of the accuracy with particle detection/identification by random sampling in an overlap size range should give insight in the quality of the analysis in the new, small size range. Finally, the lower bounds for the applicability need to be tested, since the image recognition can, in principle, process any image (e.g. the *TUM-ParticleTyper* could detect particles on SEM images).

With this technical improvement, it will be possible to enlarge the size range of future plastic particle research studying micro- and nanoplastic. This, of course, would need a reevaluation of the various systems that are relevant for the MP issue. Nonetheless, a major knowledge gap can be envisioned to be closed and answers to the presence and fate of the smallest size fraction of plastic particles can be obtained. This is especially critical as the assessment of toxicological effects is not yet conclusive, but is speculated to bear bigger risks with smaller particle sizes (Section 1.2.1). Down the road, this knowledge and the developed techniques will enable a suitable routine analysis, surveillance, and prevention of the plastic particle contamination issue.

7.3 Bulk Raman Spectroscopy coupled to Field-Flow Fractionation

The particle-by-particle approach based on RM was shown in Chapters 4 and 5 and the section above, providing chemical identification and quantification with a great degree of information on individual particles. This will, however, in most cases be accompanied by long measurement times. Thus, a complementary approach, as portrayed in the roadmap (Figure 7.1), is devised in this thesis. There, the particles are separated first by FFF and, subsequently, are chemically identified with Raman spectroscopy in bulk. This bulk approach shows promise, as the physical characterization can be performed by established techniques. To this end, FFF, and especially AF4, is most promising, as it is a versatile method for the analysis of nanoparticles[2,70,71]. Indeed, a first proof-of-principle study has shown that AF4 is well suited for the separation and size characterization of secondary nanoplastic[72] (Figure 7.3).

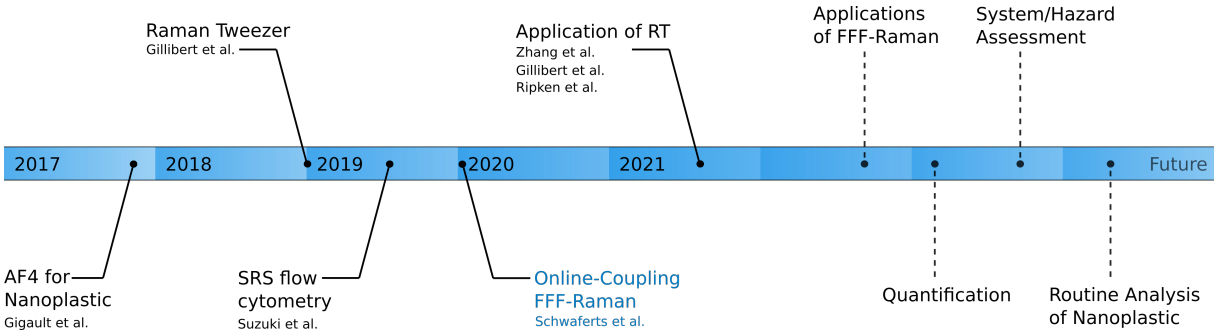

Fig. 7.3: Timeline depicting the progress and outlook of flow- and suspension-based Raman spectroscopy of nanoplastic in the environment. With proof-of-principle studies for AF4 and RT for nanoplastic in place, FFF-Raman was the next step in method development. Subsequently, first applications of RT were reported. In the future, applications of FFF-Raman, its validation for quantification, and routine analysis, could be expected.

However, there was a methodological gap concerning the chemical identification of the nanoplastic particles. The available detectors for FFF only provided elemental analysis (e.g. ICP-MS) that cannot identify the polymer type of plastic particles (Section 6.1). The presented study has solved this problem, utilizing Raman spectroscopy, as it is well suited for the application in aqueous samples. This is due to its insensitivity to water, which is based on the low absorption of water in the visible spectrum and its low Raman cross-section[73]. In this thesis, a flow-cell for the online-coupling to FFF was developed. However, when constructing Raman flow-cells, one needs to solve problems with low signal intensities due to low ratios of sample to eluent and short interaction times with the laser. Over the last 40 years, many designs for RM flow-cells have been developed for dissolved analytes, which essentially either employ high laser powers or a Raman enhancement effect (see Chapter 6).

In recent years, several groups presented new Raman flow-cell designs for the analysis of micro- and nanoplastic in the bulk approach (Figure 7.3). Kniggendorf et al. have developed a flow-cell, which enables Raman spectroscopy of MP in tap water with (relatively) high flow rates (1 L/h)[74]. This cell does not rely on a particle focussing and simply uses high laser powers. Thus, it is limited to large MP particles > 100 µm, which are analyzed individually nonetheless. In some other studies, flow cytometry was combined with Raman spectroscopy and acoustic focussing[75,76] for the identification of cells and particles (ca. 10 µm)[h]. In these applications, however, the size range is still limited to micrometer sized particles.

Furthermore, RTs, i.e. optical trapping and Raman spectroscopy, were used for the analysis of suspended plastic particles. Here, the targeted subµ size range was achieved. The first identification of suspended plastic particles in the nanometer range (down to 50 nm) using RT[i] was performed by Gillibert et al.[77].

[h] Zhang et al. described a stimulated Raman scattering (SRS) flow cell for flow cytometry[75]. This approach was later extended by Suzuki et al. to SRS microscopy enabling a label-free chemical imaging. In this flow-cell, acoustic focussing is used to position the particles[76]. This SRS flow-cytometry was validated with polymer particles (PS, PMMA, 10 µm; size limit > 1 µm) and applied to the distinction of adipose cell-differentiation states[75]. Additionally, microalgal and cancer cells were analyzed[76].

[i] GIllibert et al. employed an inverted microscope and a Raman spectrometer setup, equipped either with a 633 nm or a 785 nm laser to identify plastic particles in the range of 50 nm – 20 µm, with different shapes (beads, fragments, and fibers) and different ageing. This application to particle sizes as low as 50 nm is enabled by the use of a 100 × oil immersion objective with with N.A. = 1.3[77].

This technique, however, works on single particles and is, thus, limited to low numbers of analyzed particles.

By that, two important proof-of-principles were presented: The use of AF4 on nanoplastic[72] was demonstrated, as well as the optical trapping to manipulate and identify nanoplastic[77]. Hence, the logical next advance is to combine the two in an optical trapping-based flow-cell to solve the sensitivity problems of Raman flow-cells for particulate analytes.

This development is a key achievement of this thesis, in which the online-coupling of FFF (AF4 and CF3) to RM, enabled by an optical tweezer-based flow cell. The approach was developed and its applicability was shown for nanoplastic in the size range of 200 nm to 5 µm (Chapter 6). With FFF-Raman, a new method for the bulk analysis of nanoplastic is therefore available, which can also provide size information on the separated particles (Figure 7.3). In the past, this combined information required the time-intensive individual analysis of a very large number of individual particles in the particle-by-particle approach. Other bulk methods (e.g. Py-GC-MS) could only give the total mass without size information. This opens the possibility to characterize nanoplastic with a great amount of detail in a high-throughput manner.

Hence, new perspectives for the analysis of nanoplastic particles have opened up (Figure 7.3). As suitable methods for the detection of nanoplastic particles are now available, initial studies on the presence of nanoplastic are an immediate goal. In fact, in 2021, RT was applied for environmental studies, which aimed to detect MP (1 µm – 20 µm) in crabs and fish[78] and for marine surface waters[46] (> 2.5 µm)[j]. These studies were, however, still performed on single MP in the low µm-range. Consequently, analyzing particles < 1 µm is of great interest, since reports on the detection of nanoplastic are still very rare. Knowledge is currently limited to nanoplastic in cosmetics[8], the Atlantic ocean[9], deep ocean waters[40], and Alpine snow[28,80]. Here, the online-coupling of FFF-Raman has the potential to fill this need, as it can better provide size information and possibly quantification of nanoplastic particles. By the method development and validation performed in this thesis, FFF-Raman is ready for first applications on such systems to demonstrate its ability to detect nanoplastic in real samples.

Furthermore, a development and validation of FFF-Raman towards reliable quantification needs to be followed, as it constitutes an important aspect of the required information on contamination assessment[k]. This would also include the development of a preconcentration method[l] to account for the often very low particle contents in large volumes of sample (Chapter 3). By this advance, FFF-Raman can play a major part in the assessment of the various systems that are relevant in MP research, for which information

[j] Gillibert et al. also gave a proof-of-principle for the analysis of tire wear (> 600 nm) by RT[79].

[k] The MALS detector (at 90° angle) has been used for the quantification of poly(DL-lactide-co-glycolide) (PLGA) subµ-particles[81], SiO_2 nanoparticles[82], or Influenza A virusses[83]. The UV detector was used on Au nanoparticles[84] or liposomes[85]. However, it is difficult to use the UV detector for quantification of particulate matter, since the signal is not only affected by absorption, but also by the turbidity and light scattering. Hence, only well characterized and monodisperse particles can be calibrated for quantification. This is similar for the MALS signal (90°), where the reports were restrained to monodisperse samples. Analyzing polydisperse and irregular secondary nanoplastic particles will be difficult, since the light scattering at certain angles is dependent on the size and shape of the particles. Further, staining with marker substances (Rhodamine phosphatidylethanolamine or Sudan Red) has shown to facilitate quantification of liposomes with UV[85], as well as MP on filters for RM[86].

[l] For example by ultrafiltration[9,22], in-channel-focussing[87] or the slot-outlet technique[88] of the AF4, cloud point extraction, which has been performed on ENPs[89,90] and nanoplastic[23,24], or solid-phase extraction[91].

on nanoplastic occurrence is equally important. Among those are marine[92], limnic[93], and terrestrial[94] systems, as well as drinking water[69,95] and the ingestion by wildlife[96]. These assessments would enable regulatory steps for this contaminant and FFF-Raman could be part of the routine analysis for monitoring nanoplastic.

Finally, FFF-Raman has the potential to be used in a broader set of particle analytes than just nanoplastic. For instance, organic and inorganic environmental colloids[97] could be analyzed, since RM can give insight into functional groups and is also capable of identifying minerals and polymorphs. Moreover, as the demonstrated size range is in the same order as microorganisms[98,99], those cells could be of interest for further studies, e.g. in the context of biomedical applications[100,101].

References

1. Ivleva, N. P. Chemical Analysis of Microplastics and Nanoplastics: Challenges, Advanced Methods, and Perspectives. *Chemical Reviews* **2021**, *121*, 11886–11936.
2. Nguyen, B.; Claveau-Mallet, D.; Hernandez, L. M.; Xu, E. G.; Farner, J. M.; Tufenkji, N. Separation and Analysis of Microplastics and Nanoplastics in Complex Environmental Samples. *Accounts of Chemical Research* **2019**, *52*, 858–866.
3. Koelmans, A. A.; Besseling, E.; Shim, W. J. In *Marine Anthropogene Litter*; Springer: 2015, pp 325–340.
4. Hüffer, T.; Praetorius, A.; Wagner, S.; von der Kammer, F.; Hofmann, T. Microplastic Exposure Assessment in Aquatic Environments: Learning from Similarities and Differences to Engineered Nanoparticles. *Environmental Science & Technology* **2017**, *51*, 2499–2507.
5. Gigault, J.; Pedrono, B.; Maxit, B.; Ter Halle, A. Marine plastic litter: The unanalyzed nano-fraction. *Environmental Science: Nano* **2016**, *3*, 346–350.
6. Lambert, S.; Wagner, M. Characterisation of nanoplastics during the degradation of polystyrene. *Chemosphere* **2016**, *145*, 265–268.
7. Lambert, S.; Wagner, M. Formation of microscopic particles during the degradation of different polymers. *Chemosphere* **2016**, *161*, 510–517.
8. Hernandez, L. M.; Yousefi, N.; Tufenkji, N. Are There Nanoplastics in Your Personal Care Products? *Environmental Science & Technology Letters* **2017**, *4*, 280–285.
9. Ter Halle, A.; Jeanneau, L.; Martignac, M.; Jardé, E.; Pedrono, B.; Brach, L.; Gigault, J. Nanoplastic in the North Atlantic Subtropical Gyre. *Environmental Science & Technology* **2017**, *51*, 13689–13697.
10. Gigault, J.; Halle, A. T.; Baudrimont, M.; Pascal, P.-Y.; Gauffre, F.; Phi, T.-L.; El Hadri, H.; Grassl, B.; Reynaud, S. Current opinion: What is a nanoplastic? *Environmental Pollution* **2018**, *235*, 1030–1034.

11. Pikuda, O.; Xu, E. G.; Berk, D.; Tufenkji, N. Toxicity Assessments of Micro- and Nanoplastics Can Be Confounded by Preservatives in Commercial Formulations. *Environmental Science & Technology Letters* **2019**, *6*, 21–25.

12. Von der Esch, E.; Lanzinger, M.; Kohles, A. J.; Schwaferts, C.; Weisser, J.; Hofmann, T.; Glas, K.; Elsner, M.; Ivleva, N. P. Simple Generation of Suspensible Secondary Microplastic Reference Particles via Ultrasound Treatment. *Frontiers in Chemistry* **2020**, *8*, 169.

13. Ekvall, M. T.; Lundqvist, M.; Kelpsiene, E.; Šileikis, E.; Gunnarsson, S. B.; Cedervall, T. Nanoplastics formed during the mechanical breakdown of daily-use polystyrene products. *Nanoscale Advances* **2019**, *1*, 1055–1061.

14. El Hadri, H.; Gigault, J.; Maxit, B.; Grassl, B.; Reynaud, S. Nanoplastic from mechanically degraded primary and secondary microplastics for environmental assessments. *NanoImpact* **2020**, *17*, 100206.

15. Eitzen, L.; Paul, S.; Braun, U.; Altmann, K.; Jekel, M.; Ruhl, A. S. The challenge in preparing particle suspensions for aquatic microplastic research. *Environmental Research* **2019**, *168*, 490–495.

16. Astner, A.; Hayes, D.; O'Neill, H.; Evans, B.; Pingali, S.; Urban, V.; Young, T. Mechanical formation of micro- and nano-plastic materials for environmental studies in agricultural ecosystems. *Science of The Total Environment* **2019**, *685*, 1097–1106.

17. Magrì, D.; Sánchez-Moreno, P.; Caputo, G.; Gatto, F.; Veronesi, M.; Bardi, G.; Catelani, T.; Guarnieri, D.; Athanassiou, A.; Pompa, P. P.; Fragouli, D. Laser Ablation as a Versatile Tool To Mimic Polyethylene Terephthalate Nanoplastic Pollutants: Characterization and Toxicology Assessment. *ACS Nano* **2018**, *12*, 7690–7700.

18. Balakrishnan, G.; Déniel, M.; Nicolai, T.; Chassenieux, C.; Lagarde, F. Towards more realistic reference microplastics and nanoplastics: preparation of polyethylene micro/nanoparticles with a biosurfactant. *Environmental Science: Nano* **2019**, *6*, 315–324.

19. Rodríguez-Hernández, A. G.; Muñoz-Tabares, J. A.; Aguilar-Guzmán, J. C.; Vazquez-Duhalt, R. A novel and simple method for polyethylene terephthalate (PET) nanoparticle production. *Environmental Science: Nano* **2019**, *6*, 2031–2036.

20. Cassano, D.; La Spina, R.; Ponti, J.; Bianchi, I.; Gilliland, D. Inorganic Species-Doped Polypropylene Nanoparticles for Multifunctional Detection. *ACS Applied Nano Materials* **0000**, *0*, null.

21. Pessoni, L.; Veclin, C.; El Hadri, H.; Cugnet, C.; Davranche, M.; Pierson-Wickmann, A.-C.; Gigault, J.; Grassl, B.; Reynaud, S. Soap- and metal-free polystyrene latex particles as a nanoplastic model. *Environmental Science: Nano* **2019**, *6*, 2253–2258.

22. Mintenig, S. M.; Bäuerlein, P. S.; Koelmans, A. A.; Dekker, S. C.; van Wezel, A. P. Closing the gap between small and smaller: Towards a framework to analyse nano- and microplastics in aqueous environmental samples. *Environmental Science: Nano* **2018**, *5*, 1640–1649.

23. Zhou, X.-x.; Hao, L.-t.; Wang, H.-y.-z.; Li, Y.-j.; Liu, J.-f. Cloud-Point Extraction Combined with Thermal Degradation for Nanoplastic Analysis Using Pyrolysis Gas Chromatography–Mass Spectrometry. *Analytical Chemistry* **2019**, *91*, 1785–1790.

24. Li, Q.-c.; Lai, Y.-j.; Yu, S.-j.; Li, P.; Zhou, X.-x.; Dong, L.-j.; Liu, X.; Yao, Z.-w.; Liu, J.-f. Sequential Isolation of Microplastics and Nanoplastics in Environmental Waters by Membrane Filtration, Followed by Cloud-Point Extraction. *Analytical Chemistry* **2021**, *93*, 4559–4566.

25. Lai, Y.; Dong, L.; Li, Q.; Li, P.; Hao, Z.; Yu, S.; Liu, J. Counting Nanoplastics in Environmental Waters by Single Particle Inductively Coupled Plasma Mass Spectroscopy after Cloud-Point Extraction and In Situ Labeling of Gold Nanoparticles. *Environmental Science & Technology* **2021**, *55*, 4783–4791.

26. Zhou, X.-X.; He, S.; Gao, Y.; Chi, H.-Y.; Wang, D.-J.; Li, Z.-C.; Yan, B. Quantitative Analysis of Polystyrene and Poly(methyl methacrylate) Nanoplastics in Tissues of Aquatic Animals. *Environmental Science & Technology* **2021**, *55*, 3032–3040.

27. Cai, H.; Chen, M.; Du, F.; Matthews, S.; Shi, H. Separation and enrichment of nanoplastics in environmental water samples via ultracentrifugation. *Water Research* **2021**, *203*, 117509.

28. Materić, D.; Kasper-Giebl, A.; Kau, D.; Anten, M.; Greilinger, M.; Ludewig, E.; van Sebille, E.; Röckmann, T.; Holzinger, R. Micro- and Nanoplastics in Alpine Snow: A New Method for Chemical Identification and (Semi)Quantification in the Nanogram Range. *Environmental Science & Technology* **2020**, *54*, 2353–2359.

29. Bolea-Fernandez, E.; Rua-Ibarz, A.; Velimirovic, M.; Tirez, K.; Vanhaecke, F. Detection of microplastics using inductively coupled plasma-mass spectrometry (ICP-MS) operated in single-event mode. *Journal of Analytical Atomic Spectrometry* **2020**, *35*, 455–460.

30. Jiménez-Lamana, J.; Marigliano, L.; Allouche, J.; Grassl, B.; Szpunar, J.; Reynaud, S. A Novel Strategy for the Detection and Quantification of Nanoplastics by Single Particle Inductively Coupled Plasma Mass Spectrometry (ICP-MS). *Analytical Chemistry* **2020**, *92*, 11664–11672.

31. Lin, Y.; Huang, X.; Liu, Q.; Lin, Z.; Jiang, G. Thermal fragmentation enhanced identification and quantification of polystyrene micro/nanoplastics in complex media. *Talanta* **2020**, *208*, 120478.

32. Wang, Z.; Saadé, N. K.; Ariya, P. A. Advances in Ultra-Trace Analytical Capability for Micro/Nanoplastics and Water-Soluble Polymers in the Environment: Fresh Falling Urban Snow. *Environmental Pollution* **2021**, *276*, 116698.

33. Fakhrullin, R.; Nigamatzyanova, L.; Fakhrullina, G. Dark-field/hyperspectral microscopy for detecting nanoscale particles in environmental nanotoxicology research. *Science of The Total Environment* **2021**, *772*, 145478.

34. Nigamatzyanova, L.; Fakhrullin, R. Dark-field hyperspectral microscopy for label-free microplastics and nanoplastics detection and identification in vivo: A Caenorhabditis elegans study. *Environmental Pollution* **2021**, *271*, 116337.

35. Monteleone, A.; Wenzel, F.; Langhals, H.; Dietrich, D. New application for the identification and differentiation of microplastics based on fluorescence lifetime imaging microscopy (FLIM). *Journal of Environmental Chemical Engineering* **2021**, *9*, 104769.

36. Olson, N. E.; Xiao, Y.; Lei, Z.; Ault, A. P. Simultaneous Optical Photothermal Infrared (O-PTIR) and Raman Spectroscopy of Submicrometer Atmospheric Particles. *Analytical Chemistry* **2020**, *92*, 9932–9939.

37. Marcott, C.; Kansiz, M.; Dillon, E.; Cook, D.; Mang, M. N.; Noda, I. Two-dimensional correlation analysis of highly spatially resolved simultaneous IR and Raman spectral imaging of bioplastics composite using optical photothermal Infrared and Raman spectroscopy. *Journal of Molecular Structure* **2020**, *1210*, 128045.

38. Meyns, M.; Primpke, S.; Gerdts, G. Library based identification and characterisation of polymers with nano-FTIR and IR-sSNOM imaging. *Analytical Methods* **2019**, *11*, 5195–5202.

39. Luo, H.; Xiang, Y.; Zhao, Y.; Li, Y.; Pan, X. Nanoscale infrared, thermal and mechanical properties of aged microplastics revealed by an atomic force microscopy coupled with infrared spectroscopy (AFM-IR) technique. *Science of The Total Environment* **2020**, *744*, 140944.

40. Weckhuysen, B.; ten Have, I.; Meirer, F.; Oord, R.; Zettler, E.; Van Sebille, E.; Amaral-Zettler, L. Nanoscale Infrared Spectroscopy Reveals Nanoplastics at 5000 m Depth in the South Atlantic Ocean. *Research Square (Preprint)* **2021**, DOI: 10.21203/rs.3.rs-955379/v1.

41. Mitrano, D. M.; Beltzung, A.; Frehland, S.; Schmiedgruber, M.; Cingolani, A.; Schmidt, F. Synthesis of metal-doped nanoplastics and their utility to investigate fate and behaviour in complex environmental systems. *Nature Nanotechnology* **2019**, *14*, 362–368.

42. Redondo-Hasselerharm, P. E.; Vink, G.; Mitrano, D. M.; Koelmans, A. A. Metal-doping of nanoplastics enables accurate assessment of uptake and effects on Gammarus pulex. *Environmental Science: Nano* **2021**, DOI: 10.1039/D1EN00068C.

43. Tian, L.; Chen, Q.; Jiang, W.; Wang, L.; Xie, H.; Kalogerakis, N.; Ma, Y.; Ji, R. A carbon-14 radiotracer-based study on the phototransformation of polystyrene nanoplastics in water versus in air. *Environmental Science: Nano* **2019**, *6*, 2907–2917.

44. Al-Sid-Cheikh, M.; Rowland, S. J.; Kaegi, R.; Henry, T. B.; Cormier, M.-A.; Thompson, R. C. Synthesis of 14 C-labelled polystyrene nanoplastics for environmental studies. *Communications Materials* **2020**, *1*, 1–8.

45. Keinänen, O.; Dayts, E. J.; Rodriguez, C.; Sarrett, S. M.; Brennan, J. M.; Sarparanta, M.; Zeglis, B. M. Harnessing PET to track micro-and nanoplastics in vivo. *Scientific Reports* **2021**, *11*, 1–12.

46. Ripken, C.; Kotsifaki, D. G.; Nic Chormaic, S. Analysis of small microplastics in coastal surface water samples of the subtropical island of Okinawa, Japan. *Science of The Total Environment* **2021**, *760*, 143927.

47. Ivleva, N. P.; Wiesheu, A. C.; Niessner, R. Microplastic in Aquatic Ecosystems. *Angewandte Chemie, International Edition* **2017**, *56*, 1720–1739.

48. Sobhani, Z.; Zhang, X.; Gibson, C.; Naidu, R.; Megharaj, M.; Fang, C. Identification and visualisation of microplastics/nanoplastics by Raman imaging (i): Down to 100 nm. *Water Research* **2020**, *174*, 115658.

49. Fang, C.; Sobhani, Z.; Zhang, X.; Gibson, C. T.; Tang, Y.; Naidu, R. Identification and visualisation of microplastics/ nanoplastics by Raman imaging (ii): Smaller than the diffraction limit of laser? *Water Research* **2020**, *183*, 116046.

50. Fang, C.; Sobhani, Z.; Zhang, X.; McCourt, L.; Routley, B.; Gibson, C. T.; Naidu, R. Identification and visualisation of microplastics / nanoplastics by Raman imaging (iii): algorithm to cross-check multi-images. *Water Research* **2021**, *194*, 116913.

51. Sarau, G.; Kling, L.; Oßmann, B. E.; Unger, A.-K.; Vogler, F.; Christiansen, S. H. Correlative Microscopy and Spectroscopy Workflow for Microplastics. *Applied Spectroscopy* **2020**, *74*, 1155–1160.

52. Schmidt, R.; Nachtnebel, M.; Dienstleder, M.; Mertschnigg, S.; Schroettner, H.; Zankel, A.; Poteser, M.; Hutter, H.-P.; Eppel, W.; Fitzek, H. Correlative SEM-Raman microscopy to reveal nanoplastics in complex environments. *Micron* **2021**, *144*, 103034.

53. Zhang, W.; Dong, Z.; Zhu, L.; Hou, Y.; Qiu, Y. Direct Observation of the Release of Nanoplastics from Commercially Recycled Plastics with Correlative Raman Imaging and Scanning Electron Microscopy. *ACS Nano* **2020**, *14*, 7920–7926.

54. Xu, G.; Cheng, H.; Jones, R.; Feng, Y.; Gong, K.; Li, K.; Fang, X.; Tahir, M. A.; Valev, V. K.; Zhang, L. Surface-Enhanced Raman Spectroscopy Facilitates the Detection of Microplastics <1 µm in the Environment. *Environmental Science & Technology* **2020**, *54*, 15594–15603.

55. Lv, L.; He, L.; Jiang, S.; Chen, J.; Zhou, C.; Qu, J.; Lu, Y.; Hong, P.; Sun, S.; Li, C. In situ surface-enhanced Raman spectroscopy for detecting microplastics and nanoplastics in aquatic environments. *Science of The Total Environment* **2020**, *728*, 138449.

56. Kooi, M.; Koelmans, A. A. Simplifying Microplastic via Continuous Probability Distributions for Size, Shape, and Density. *Environmental Science & Technology Letters* **2019**, *6*, 551–557.

57. Anger, P. M.; von der Esch, E.; Baumann, T.; Elsner, M.; Niessner, R.; Ivleva, N. P. Raman microspectroscopy as a tool for microplastic particle analysis. *Trends in Analytical Chemistry* **2018**, *109*, 214–226.

58. Von der Esch, E.; Kohles, A. J.; Anger, P. M.; Hoppe, R.; Niessner, R.; Elsner, M.; Ivleva, N. P. TUM-ParticleTyper: A detection and quantification tool for automated analysis of (Microplastic) particles and fibers. *PLOS ONE* **2020**, *15*, e0234766.

59. Brandt, J.; Bittrich, L.; Fischer, F.; Kanaki, E.; Tagg, A.; Lenz, R.; Labrenz, M.; Brandes, E.; Fischer, D.; Eichhorn, K.-J. High-Throughput Analyses of Microplastic Samples Using Fourier Transform Infrared and Raman Spectrometry. *Applied Spectroscopy* **2020**, *74*, 1185–1197.

60. Anger, P. M.; Prechtl, L.; Elsner, M.; Niessner, R.; Ivleva, N. P. Implementation of an open source algorithm for particle recognition and morphological characterisation for microplastic analysis by means of Raman microspectroscopy. *Analytical Methods* **2019**, *11*, 3483–3489.

61. Oßmann, B. E.; Sarau, G.; Holtmannspötter, H.; Pischetsrieder, M.; Christiansen, S. H.; Dicke, W. Small-sized microplastics and pigmented particles in bottled mineral water. *Water Research* **2018**, *141*, 307–316.

62. Schymanski, D.; Goldbeck, C.; Humpf, H.-U.; Fürst, P. Analysis of microplastics in water by micro-Raman spectroscopy: Release of plastic particles from different packaging into mineral water. *Water Research* **2018**, *129*, 154–162.

63. Thaysen, C.; Munno, K.; Hermabessiere, L.; Rochman, C. M. Towards Raman Automation for Microplastics: Developing Strategies for Particle Adhesion and Filter Subsampling. *Applied Spectroscopy* **2020**, *74*, 976–988.

64. Illian, J.; Penttinen, A.; Stoyan, H.; Stoyan, D., *Statistical analysis and modelling of spatial point patterns*; John Wiley & Sons: 2008; Vol. 70.

65. Brandt, J.; Fischer, F.; Kanaki, E.; Enders, K.; Labrenz, M.; Fischer, D. Assessment of Subsampling Strategies in Microspectroscopy of Environmental Microplastic Samples. *Frontiers in Environmental Science* **2021**, *8*, 288.

66. Imhof, H. K.; Laforsch, C.; Wiesheu, A. C.; Schmid, J.; Anger, P. M.; Niessner, R.; Ivleva, N. P. Pigments and plastic in limnetic ecosystems: A qualitative and quantitative study on microparticles of different size classes. *Water Research* **2016**, *98*, 64–74.

67. Käppler, A.; Fischer, D.; Oberbeckmann, S.; Schernewski, G.; Labrenz, M.; Eichhorn, K.-J.; Voit, B. Analysis of environmental microplastics by vibrational microspectroscopy: FTIR, Raman or both? *Analytical and Bioanalytical Chemistry* **2016**, *408*, 8377–8391.

68. Mintenig, S.; Kooi, M.; Erich, M.; Primpke, S.; Redondo- Hasselerharm, P.; Dekker, S.; Koelmans, A.; van Wezel, A. A systems approach to understand microplastic occurrence and variability in Dutch riverine surface waters. *Water Research* **2020**, *176*, 115723.

69. Koelmans, A. A.; Mohamed Nor, N. H.; Hermsen, E.; Kooi, M.; Mintenig, S. M.; De France, J. Microplastics in freshwaters and drinking water: Critical review and assessment of data quality. *Water Research* **2019**, *155*, 410–422.

70. Contado, C. Field flow fractionation techniques to explore the “nano-world”. *Analytical and Bioanalytical Chemistry* **2017**, *409*, 2501–2518.

71. Schwaferts, C.; Niessner, R.; Elsner, M.; Ivleva, N. P. Methods for the analysis of submicrometer- and nanoplastic particles in the environment. *Trends in Analytical Chemistry* **2019**, 52–65.

72. Gigault, J.; El Hadri, H.; Reynaud, S.; Deniau, E.; Grassl, B. Asymmetrical flow field flow fractionation methods to characterize submicron particles: Application to carbon-based aggregates and nanoplastics. *Analytical and Bioanalytical Chemistry* **2017**, *409*, 6761–6769.

73. Popp, J.; Mayerhöfer, T., *Micro-Raman Spectroscopy: Theory and Application*; De Gruyter: Berlin, Boston, 2020.

74. Kniggendorf, A.-K.; Wetzel, C.; Roth, B. Microplastics Detection in Streaming Tap Water with Raman Spectroscopy. *Sensors* **2019**, *19*, 1839.

75. Zhang, C.; Huang, K.-C.; Rajwa, B.; Li, J.; Yang, S.; Lin, H.; Liao, C.-s.; Eakins, G.; Kuang, S.; Patsekin, V.; Robinson, J. P.; Cheng, J.-X. Stimulated Raman scattering flow cytometry for label-free single-particle analysis. *Optica* **2017**, *4*, 103–109.

76. Suzuki, Y.; Kobayashi, K.; Wakisaka, Y.; Deng, D.; Tanaka, S.; Huang, C.-J.; Lei, C.; Sun, C.-W.; Liu, H.; Fujiwaki, Y.; Lee, S.; Isozaki, A.; Kasai, Y.; Hayakawa, T.; Sakuma, S.; Arai, F.; Koizumi, K.; Tezuka, H.; Inaba, M.; Hiraki, K.; Ito, T.; Hase, M.; Matsusaka, S.; Shiba, K.; Suga, K.; Nishikawa, M.; Jona, M.; Yatomi, Y.; Yalikun, Y.; Tanaka, Y.; Sugimura, T.; Nitta, N.; Goda, K.; Ozeki, Y. Label-free chemical imaging flow cytometry by high-speed multicolor stimulated Raman scattering. *Proceedings of the National Academy of Sciences* **2019**, *116*, 15842–15848.

77. Gillibert, R.; Balakrishnan, G.; Deshoules, Q.; Tardivel, M.; Magazzù, A.; Donato, M. G.; Maragò, O. M.; La Lamy de Chapelle, M.; Colas, F.; Lagarde, F.; Gucciardi, P. G. Raman Tweezers for Small Microplastics and Nanoplastics Identification in Seawater. *Environmental Science & Technology* **2019**, *53*, 9003–9013.

78. Zhang, S.; Sun, Y.; Liu, B.; Li, R. Full size microplastics in crab and fish collected from the mangrove wetland of Beibu Gulf: Evidences from Raman Tweezers (1–20 µm) and spectroscopy (20–5000 µm). *Science of The Total Environment* **2021**, *759*, 143504.

79. Gillibert, R.; Magazzù, A.; Callegari, A.; Ciriza, D. B.; Antonino, F.; Donato, M. G.; Maragò, O. M.; Volpe, G.; de La Chapelle, M. L.; Lagarde, F., et al. Raman Tweezers for Tire and Road Wear Micro-and Nanoparticles analysis. *ChemRxiv (preprint)* **2021**, DOI: 10.33774/chemrxiv-2021-h59n1.

80. Materić, D.; Ludewig, E.; Brunner, D.; Röckmann, T.; Holzinger, R. Nanoplastics transport to the remote, high-altitude Alps. *Environmental Pollution* **2021**, *288*, 117697.

81. Engel, A.; Plöger, M.; Mulac, D.; Langer, K. Asymmetric flow field-flow fractionation (AF4) for the quantification of nanoparticle release from tablets during dissolution testing. *International Journal of Pharmaceutics* **2014**, *461*, 137–144.

82. Tadjiki, S.; Assemi, S.; Deering, C. E.; Veranth, J. M.; Miller, J. D. Detection, separation, and quantification of unlabeled silica nanoparticles in biological media using sedimentation field-flow fractionation. *Journal of Nanoparticle Research* **2009**, *11*, 981–988.

83. Bousse, T.; Shore, D. A.; Goldsmith, C. S.; Hossain, M. J.; Jang, Y.; Davis, C. T.; Donis, R. O.; Stevens, J. Quantitation of influenza virus using field flow fractionation and multi-angle light scattering for quantifying influenza A particles. *Journal of Virological Methods* **2013**, *193*, 589–596.

84. Calzolai, L.; Gilliland, D.; Garcìa, C. P.; Rossi, F. Separation and characterization of gold nanoparticle mixtures by flow-field-flow fractionation. *Journal of Chromatography A* **2011**, *1218*, Flow-Field-Flow Fractionation, 4234–4239.

85. Hupfeld, S.; Ausbacher, D.; Brandl, M. Asymmetric flow field-flow fractionation of liposomes: 2. Concentration detection and adsorptive loss phenomena. *Journal of Separation Science* **2009**, *32*, 3555–3561.

86. Prata, J. C.; da Costa, J. P.; Fernandes, A. J. S.; da Costa, F. M.; Duarte, A. C.; Rocha-Santos, T. Selection of microplastics by Nile Red staining increases environmental sample throughput by micro-Raman spectroscopy. *Science of The Total Environment* **2021**, *783*, 146979.

87. Lyvén, B.; Hassellöv, M.; Haraldsson, C.; Turner, D. Optimisation of on-channel preconcentration in flow field-flow fractionation for the determination of size distributions of low molecular weight colloidal material in natural waters. *Analytica Chimica Acta* **1997**, *357*, 187–196.

88. Prestel, H.; Niessner, R.; Panne, U. Increasing the sensitivity of asymmetrical flow field-flow fractionation: Slot outlet technique. *Analytical Chemistry* **2006**, *78*, 6664–6669.

89. El Hadri, H.; Hackley, V. A. Investigation of cloud point extraction for the analysis of metallic nanoparticles in a soil matrix. *Environmental Science: Nano* **2017**, *4*, 105–116.

90. Zhou, X.-X.; Jiang, L.-W.; Wang, D.-J.; He, S.; Li, C.-J.; Yan, B. Speciation Analysis of Ag2S and ZnS Nanoparticles at the ng/L Level in Environmental Waters by Cloud Point Extraction Coupled with LC-ICPMS. *Analytical Chemistry* **2020**, *92*, 4765–4770.

91. Zhou, X.-X.; Lai, Y.-J.; Liu, R.; Li, S.-S.; Xu, J.-W.; Liu, J.-F. Polyvinylidene Fluoride Micropore Membranes as Solid-Phase Extraction Disk for Preconcentration of Nanoparticulate Silver in Environmental Waters. *Environmental Science & Technology* **2017**, *51*, 13816–13824.

92. Harris, P. T. The fate of microplastic in marine sedimentary environments: A review and synthesis. *Marine Pollution Bulletin* **2020**, *158*, 111398.

93. Li, C.; Busquets, R.; Campos, L. C. Assessment of microplastics in freshwater systems: A review. *Science of The Total Environment* **2020**, *707*, 135578.

94. Rillig, M. C.; Lehmann, A. Microplastic in terrestrial ecosystems. *Science* **2020**, *368*, 1430–1431.

95. Danopoulos, E.; Twiddy, M.; Rotchell, J. M. Microplastic contamination of drinking water: A systematic review. *PLOS ONE* **2020**, *15*, 1–23.

96. Barboza, L. G. A.; Dick Vethaak, A.; Lavorante, B. R.; Lundebye, A.-K.; Guilhermino, L. Marine microplastic debris: An emerging issue for food security, food safety and human health. *Marine Pollution Bulletin* **2018**, *133*, 336–348.

97. Baalousha, M.; Stolpe, B.; Lead, J. R. Flow field-flow fractionation for the analysis and characterization of natural colloids and manufactured nanoparticles in environmental systems: A critical review. *Journal of Chromatography A* **2011**, *1218*, 4078–4103.

98. Reschiglian, P.; Zattoni, A.; Roda, B.; Michelini, E.; Roda, A. Field-flow fractionation and biotechnology. *Trends in Biotechnology* **2005**, *23*, 475–483.

99. Yohannes, G.; Jussila, M.; Hartonen, K.; Riekkola, M.-L. Asymmetrical flow field-flow fractionation technique for separation and characterization of biopolymers and bioparticles. *Journal of Chromatography A* **2011**, *1218*, 4104–4116.

100. Zhang, X.; Li, Y.; Shen, S.; Lee, S.; Dou, H. Field-flow fractionation: A gentle separation and characterization technique in biomedicine. *Trends in Analytical Chemistry* **2018**, *108*, 231–238.

101. Wagner, M.; Holzschuh, S.; Traeger, A.; Fahr, A.; Schubert, U. S. Asymmetric Flow Field-Flow Fractionation in the Field of Nanomedicine. *Analytical Chemistry* **2014**, *86*, 5201–5210.